Measurement of the Higgs Boson Mass and Production Cross Section and Calibration of the Muon Momentum with the ATLAS Detector at the LHC



Siyuan Yan

New College

University of Oxford

A thesis submitted for the degree of

Doctor of Philosophy

2023

Acknowledgements

It is difficult to overestimate the effect of a prolonged global pandemic, and of the physical and mental isolation it has imposed on many of us. The shadow it would have cast over my DPhil journey would have been much gloomier, if not for the support and comradery I have received over such trying times. This thesis is dedicated to many people who guided, helped, and/or listened to me.

First and foremost, my gratitude goes to my supervisors, Ian Shipsey and Daniela Bortoletto. Thank you for creating such a vibrant group, for the fantastic discussions both online and offline, and for the helpful advice and lessons you've provided. I've learnt a lot from my DPhil journey in Oxford, and in no small parts thanks to you!

My gratitude also extends to the many present and past members of the Bortoletto/Shipsey group. Special thanks go to Giacomo for introducing me to ATLAS and MCP, for navigating through the puzzling features of athena and other software, and for the knowledge, insight and intuitions you have provided over the years! I could not have asked for a better guide for the start of my DPhil. Thanks also to the discussions and company with Elisabeth, Miha, Maria, Maxence, Simon, Gregor and Chunhao I've learnt a lot (physics, hardware, software, life, culture, politics, you name it!) from all of you! Lastly, a very personal thanks goes to Eleonora for her amazing work in muon calibration, as well as for being the inspiring physicist and person that you are. I will miss our coffee chats in R1!

My time at CERN has been an inspiring one and is defined by the people who I had the pleasure of interacting with. My most sincere gratitude goes to Haider Abidi for sparing my life, being a wonderful friend I (almost always) admire, introducing me to climbing, and being above the law. Thanks for being a great friend, person and colleague, let's see where life will take us! Thanks to Max Goblirsch for going along with my shenanigans against another HZZ convenor, lively discussions on reconstruction, HZZ and trigger, and being a wonderful person and a supportive friend! I thank Christos Anastopoulos for his leadership as the HZZ convenor during my time working on the mass analysis, and Chiara Arcangeletti and Guglielmo Frattari for being excellent analysis contacts for the fiducial cross-section measurement. There are also many people from whom

I've learnt a lot in the short time I've worked with them: RD Schaffer, Johannes Junggeburth, Federica Fabbri, Hongtao Yang, and many, many others.

My time in Oxford has been fractured by the pandemic. Still, I very much cherished the time spent with my cohort in 2019 and 2020, as well as the brief time when the university reopened between 2021 and 2022. My gratitude goes to Eimear, Iza and Ynyr, and the good old days daydreaming in the office! I also thank the great company I've had in my Oxford office, shared with Alessandro, Federico, Maggie and Olivier, you have brought normalcy back into my life after a turbulent two years, and I can't wait to hang out with you!

I thank my friends from the past and the present, for the beautiful times you have shared with me in the past, and I certainly wish to carry it to our futures! Special thanks need to be given to the two owners of zombie hit squad, Ayham and Jade, thank you for sticking with me through my moments of insanity, sadness and joy, I cannot thank you enough for keeping me sane and determined through my DPhil. I also thank Andrea for his support throughout the pandemic, let's have a drink in Liverpool! My personal thanks and thanks on behalf of my birds goes to Dara and Alex, for taking care of me and my birds in such trying times. To my friends Alberto and Hannah, thanks a lot for all your lessons in life, ornithology and only very occasionally physics. My time in Oxford would not be complete without the Sunday meet-ups with Mariona and MehRana. I will miss both of you, and all the times we've spent together!

Lastly, there are a few very special people and birds in my life. My family has always believed and supported me unconditionally, and nothing I write here could reflect how deeply I love them. I would like to think that my three birds, Skipper, Flakey and Minty, also believe in my ability to provide seeds for them, and I love them regardless. There are also some very special human persons who have unwaveringly believed in me, who have helped me realise who I am, and what I could achieve. Thanks to you, I know who I am, and I owe you everything.

Abstract

The ATLAS and CMS experiments at the Large Hadron Collider, located in CERN in Geneva, Switzerland announced the discovery of the Higgs boson on the 4th of July, 2012. Measurements of the Higgs boson properties provide stringent consistency tests for the Standard Model, and offer critical input parameters for theoretical models both within and beyond the Standard Model. Such measurements therefore require a precise understanding of the underlying detector throughout its operation. This thesis contributes to both aspects: measurements of the Higgs boson mass and cross-section, and studies of ATLAS detector performance through muon momentum calibration.

As the Higgs can decay to muons, improvements to the muon detector performance directly translate to the corresponding systematic uncertainties in the measurement of Higgs properties. This motivates the inclusion of new techniques in muon momentum calibration, including the addition of negative log-likelihood scans and generator reweighting. The calibration procedure is performed for both 2015-2018 and 2022 datasets, and reduces the leading systematic uncertainty in the Higgs mass measurement by 50%.

The measurements of Higgs boson properties are performed for the Higgs decaying into a pair of Z bosons, and subsequently decaying into two pairs of electrons or muons. This is a fully reconstructible final state with a high signal-to-background ratio, thus an ideal final state for precision measurements. The Higgs boson mass measurement utilises proton-proton collision data collected between 2015 - 2018 at the centre-of-mass energy $\sqrt{s} = 13$ TeV. A number of techniques, including per-event mass uncertainty, Z-mass constraint, and kernel estimation for background modelling, are included to reduce the statistical uncertainty of the measurement. The measured Higgs mass is 124.99 ± 0.18 (stat.) ± 0.04 (sys.) GeV using the 2015-2018 data. The Higgs boson fiducial cross-section measurement utilises proton-proton collision data collected in 2022 at the centre-of-mass energy $\sqrt{s} = 13.6$ TeV. The fiducial cross-section for its decay into a pair of Z bosons is measured to be $\sigma_{fid} = 2.80 \pm 0.74$ fb, and $\sigma_{tot} = 46 \pm 12$ pb once extrapolated to the full phase-space.

Statement of originality

Experimental particle physics is a collaborative and inter-disciplinary science. Taking the ATLAS collaboration as an example, with its approximately 6000 active members and 3000 scientific authors, it is one of the largest collaborative scientific efforts in history. It requires inputs from engineering (to build, maintain and operate the detector), statistics (to analyse the streams of data), and particle theory (to understand the underlying physical reality). This thesis benefits from such collaborative efforts, with Chapter 2 reviewing the theoretical framework, Chapter 3 and Section 6.1 describing the experimental setup of the ATLAS detector. The author's original contributions are summariesed below.

Muons in the ATLAS experiment Chapter 4 starts with an overview of muon reconstruction, identification and isolation in the ATLAS experiment, which are performed by collaborators. My contributions are on the development and derivation of scale and resolution calibration, and I derived the precision muon momentum calibration for the 2015-2018 dataset, which is implemented for all Run 2 ATLAS analyses involving muons. My specific contributions include:

- Development and implementation of a novel χ^2 in the fit procedure for faster convergence by targeting the mean and standard deviation of the dimuon mass spectrum.
- Development of a strategy to evaluate the systematic uncertainties of the fit procedure on the calibration parameters. This reduces systematics by a factor of four.
- Derivation of calibration parameters and systematic fits for each year of data taking - this is now the standard recommendation for muon momentum calibration in the ATLAS experiment.
- Updating and simplification of the software framework used for physics validation, thereby improving its stability and intuitiveness for future members of the calibration group.

Higgs mass measurement in $H \to ZZ^* \to 4\ell$ I was a main contributor to the Higgs mass analysis in $H \to ZZ^* \to 4\ell$ channel, and it is the subject of Chapter 5. My main contributions include:

- Validated numerous kinematic parameters associated with the four-lepton final state, and identification of the to source of mismodelling in the Z-mass constrain to be the mismodelling of muon track errors.
- Development of the kinematic reweighting method for the muon track errors, which is used as a basis for the quantile mapping method.
- Implementation of the continuous 2D background model. This reduces the systematic uncertainties associated with the background model compared to the previous iteration of this analysis.
- Performed simultaneous fits on the normalisation parameters for all background processes.
- Utilised bootstrapped simulation samples to study the impact of systematic uncertainties. Subsequently developed a strategy for combining systematic uncertainties in this analysis.
- Performed the final fit for both the bootstrapped simulation samples and the collected data, thus obtaining the expected and measured value of the Higgs mass.

Run 3 physics Chapter 6 begins with an overview of the upgrade activities to the ATLAS detector during the period between 2018 - 2022, which are performed by numerous engineers and scientists in the ATLAS collaboration. This is followed by two highlights of my contributions to the physics programs for the ATLAS collaboration after the upgrade, including muon calibration and the trigger studies for the Higgs fiducial cross-section measurement. My main contributions include:

- Developed the strategy for deriving Run 3 muon calibration parameters, and deriving and finalised muon calibration using the preliminary Run 3 data. This is used for all early Run 3 analyses involving muons.
- Investigated the muon resolution in Run 3 as a function of detector regions.
- Studied the trigger efficiency for $H \to ZZ^* \to 4\ell$ channel in Run 3, and finalising a trigger menu for this analysis.
- Implemented the Run 3 trigger scale factors into the $H \to ZZ^* \to 4\ell$ analysis framework.

Contents

List of Figures xiii

List of Tables xvii

1 Introduction 1

2 Standard Model of Particle Physics 3
- 2.1 Standard Model as a field theory . . . 3
  - 2.1.1 Elementary particles . . . 5
  - 2.1.2 Electroweak theory . . . 6
  - 2.1.3 The Higgs mechanism . . . 8
  - 2.1.4 Quantum chromodynamics . . . 11
- 2.2 The Higgs phenomenology at the LHC . . . 14
- 2.3 Limitations of the Standard Model . . . 14

3 The LHC and the ATLAS detector 19
- 3.1 Large Hadron Collider . . . 20
- 3.2 The ATLAS detector . . . 23
  - 3.2.1 The Inner Detector . . . 27
  - 3.2.2 Calorimeters . . . 30
  - 3.2.3 Muon spectrometer . . . 32
  - 3.2.4 Trigger system . . . 35
  - 3.2.5 The ATLAS Monte Carlo simulation . . . 37

4 Muons in the ATLAS experiment 39
- 4.1 Reconstruction . . . 40
- 4.2 Identification . . . 43
  - 4.2.1 Selection working points . . . 43
  - 4.2.2 Isolation working points . . . 47
- 4.3 Muon p_{T} correction . . . 49
  - 4.3.1 Data and simulation samples . . . 52
  - 4.3.2 Sagitta bias correction . . . 54

4.3.3 Scale and resolution calibration . . . 59
4.3.4 Performance studies for muon calibration . . . 66
4.4 Conclusion . . . 72

5 Measurement of the Higgs mass in $H \to ZZ^*$ decay 75
5.1 Data and Monte Carlo simulated samples . . . 76
5.1.1 Simulated signal samples . . . 77
5.1.2 Simulated background samples . . . 77
5.2 Physics objects . . . 79
5.2.1 Electrons . . . 80
5.2.2 Muons . . . 80
5.3 Event selection . . . 81
5.3.1 Impact parameter and vertex selection . . . 81
5.3.2 Quadruplet selection . . . 82
5.4 Analysis strategy . . . 83
5.4.1 Final-state radiation recovery . . . 84
5.4.2 Z-mass constraint . . . 84
5.4.3 Signal-background discriminant . . . 90
5.4.4 Per-event resolution . . . 92
5.5 Signal modelling . . . 94
5.6 Background modelling . . . 97
5.7 Results . . . 99

6 Physics beyond Run 2 107
6.1 Overview of the Run 3 ATLAS upgrades . . . 108
6.2 Muon scale and resolution calibration for early Run 3 data . . . 110
6.2.1 Data and simulated samples . . . 110
6.2.2 Calibration procedure . . . 110
6.2.3 Validation . . . 113
6.3 Higgs fiducial cross-section measurement . . . 115
6.3.1 Lepton trigger efficiencies in Run 3 . . . 116
6.3.2 Trigger ranking studies . . . 118
6.3.3 Event selection . . . 124
6.3.4 Background estimation . . . 124
6.3.5 Analysis strategy . . . 125
6.3.6 Results . . . 127

7 Conclusion and outlook 131

Appendices

A Trigger naming convention for Run 3 **137**

B Trigger ranking studies per channel **139**

C Kinematic distributions in the $H \to ZZ^* \to 4\ell$ channel in Run 3 **147**

References **153**

List of Figures

2.1 The shape of the SM Higgs potential. 10
2.2 The SM Higgs boson coupling strength. 12
2.3 Feynman diagrams for triple and quartic gluon self-interaction. 13
2.4 Leading order diagrams for the four main production modes for the SM Higgs boson at the LHC. 15
2.5 The SM Higgs boson production cross-section as a function of the centre-of-mass energy for proton-proton collisions for a Higgs boson with mass at 125 GeV. 16
2.6 The SM Higgs boson decay branching ratio as a function of Higgs mass for each final state. 17

3.1 A schematic diagram of the full LHC accelerator complex. 21
3.2 The delivered integrated luminosity recorded by the ATLAS experiment. 23
3.3 The recorded luminosity as a function of average number of interactions per bunch crossing. 24
3.4 A schematic illustration of the ATLAS detector. 24
3.5 The ATLAS coordinate system in relation to the LHC beam line. . 25
3.6 The ATLAS detector coverage in η for all sub-detectors. 27
3.7 A schematic showing the ID components. 28
3.8 A schematic, cross-sectional view of the ATLAS ID barrel. 29
3.9 A schematic overview of the ATLAS calorimeters. 31
3.10 A schematic overview of the ATLAS muon spectrometers. 34

4.1 The definition of track impact parameters. 41
4.2 Schematic diagram for the different types of muon reconstruction chains. 44
4.3 Muon identification efficiency for identification working points. . 48
4.4 Distribution of muon isolation variables. 50
4.5 Muon isolation efficiencies as a function of muon momentum. . . 51
4.6 Distributions of data and simulated $Z \to \mu\mu$ pair momentum and invariant mass distributions before and after kinematic reweighting. 55

4.7 Sagitta bias of combined muons. 57
4.8 Residual sagitta bias of combined muons. 58
4.9 Example comparison between uncorrected and corrected dimuon mass peak. 63
4.10 imuon invariant mass distribution of $J/\psi \to \mu\mu$ and $Z \to \mu\mu$ events with combined muons. 69
4.11 Fitted mean mass for the dimuon system as a function of the leading muon pseudorapidity. 71
4.12 Fitted dimuon mass resolution as a function of the leading muon pseudorapidity. 72
4.13 Dimuon invariant mass distribution of $\Upsilon \to \mu\mu$ candidate events . 73
4.14 Fitted mean dimuon mass and resolution for $\Upsilon \to \mu\mu$ events as a function of the leading muon pseudorapidity. 74

5.1 Composition of the Higgs boson production modes in the SM as a fraction of the total Higgs production cross-section at 13 TeV at the LHC. 79
5.2 The unconstrained four-lepton invariant mass distribution for Higgs candidates with and without final state radiation recovery. . . . 85
5.3 The four-lepton invariant mass distribution for simulated Higgs candidates with and without Z mass constrain. 86
5.4 The constrained di-lepton mass distributions in the control regions before track error correction. 87
5.5 The muon track error distributions before and after kinematic reweighting. 89
5.6 The muon track error distribution before and after quantile mapping method. 90
5.7 The di-lepton invariant mass distribution after Z mass constraint and track error correction. 91
5.8 The observed and expected four-lepton invariant mass distribution in the signal region of $H \to ZZ^* \to 4\ell$. 92
5.9 The observed and expected neural network output distributions in the signal region of $H \to ZZ^* \to 4\ell$. 93
5.10 The observed and expected per-event resolution distributions in the signal region of $H \to ZZ^* \to 4\ell$. 94
5.11 The signal fit for $H \to ZZ^* \to 4\ell$. 97
5.12 The probability density function for the non-resonant ZZ^* production. 99
5.13 The fitted four-lepton invariant mass from simulation and data distribution. 101

5.14 Systematic uncertainties on the Higgs mass. 102
5.15 The negative log-likelihood scan for the Higgs mass fit. 104
5.16 The Higgs mass fit result in each final state. 105

6.1 ME track resolution in Run 3. 111
6.2 Ratio of fractional CB track error between data and simulation in Run 3. 112
6.3 Scale and resolution of $J/\psi \to \mu\mu$ candidate events reconstructed with CB muons as a function of leading muon pseudorapidity. . 114
6.4 Scale and resolution of $Z \to \mu\mu$ candidate events reconstructed with CB muons as a function of leading muon pseudorapidity. . 114
6.5 Scale and resolution of $J/\psi \to \mu\mu$ candidate events reconstructed with CB muons as a function of leading muon momentum. 115
6.6 Scale and resolution of $Z \to \mu\mu$ candidate events reconstructed with CB muons as a function of leading muon momentum. 115
6.7 Ranking studies of single-electron triggers for all decay modes in $H \to ZZ^* \to 4\ell$. 119
6.8 Ranking studies of single-muon triggers for all decay modes in $H \to ZZ^* \to 4\ell$. 120
6.9 Ranking studies of double-muon triggers for all decay modes in $H \to ZZ^* \to 4\ell$. 120
6.10 Ranking studies of multi-muon triggers for all decay modes in $H \to ZZ^* \to 4\ell$. 121
6.11 Ranking studies of di-emu triggers for all decay modes in $H \to ZZ^* \to 4\ell$. 121
6.12 Ranking studies of multi-emu triggers for all decay modes in $H \to ZZ^* \to 4\ell$. 122
6.13 Trigger efficiency as a function of $p_{T,4l}$ for each of the 4 channels and the inclusive channel. 124
6.14 Data/MC comparison for lepton p_{T}. 126
6.15 The observed and expected four-lepton invariant mass distribution for Higgs boson candidates in Run 3. 128
6.16 Results for the $\sigma(pp \to H)$ measurements from ATLAS publications as a function of the pp centre-of-mass energy. 130

B.1 Ranking studies of single-electron triggers 140
B.2 Ranking studies of single-muon triggers 141
B.3 Ranking studies of double-muon triggers 142
B.4 Ranking studies of multi-muon triggers 143
B.5 Ranking studies of di-emu triggers 144

B.6 Ranking studies of multi-emu triggers 145

C.1 Data/MC comparison for lepton η. 148
C.2 Data/MC comparison for lepton ϕ. 149
C.3 Data/MC comparison for four-lepton system. 150
C.4 Data/MC comparison for on-shell and off-shell Z bosons. 151

List of Tables

4.1 Definitions of muon isolation working points. 51
4.2 Description of the simulated resonances used for muon momentum calibration. 53
4.3 Description of the background processes for $Z \to \mu\mu$. 54
4.4 The detector region definitions for the scale and resolution fit. . 64
4.5 Summary of ID momentum scale and resolution corrections. . . . 67
4.6 Summary of MS momentum scale and resolution corrections. . . 67
4.7 Summary of CB momentum scale and resolution corrections. . . 68

5.1 Description of the simulated signal processes. 78
5.2 Description of the production of simulated background samples. . 79
5.3 Summary of electron selection requirements for the $H \to ZZ^* \to 4\ell$ analysis. 80
5.4 Summary of muon selection requirements for the $H \to ZZ^* \to 4\ell$ analysis. 81
5.5 The expected and observed yields for 105$< m_{4\ell} <$160 GeV. 100
5.6 The expected and observed yields for 115$< m_{4\ell} <$130 GeV. 100

6.1 Summary of CB momentum resolution and scale corrections in Run 3. 113
6.2 Lowest unprescaled lepton triggers available during the 2022 pp data-taking period. 117
6.3 Summary of trigger efficiency with kinematic matching for 2022 unprescaled muon triggers as evaluated in ggH samples. 118
6.4 Summary of trigger efficiency with kinematic matching for 2022 unprescaled electron triggers as evaluated in ggH samples. . . . 118
6.5 Summary of trigger efficiency with kinematic matching for 2022 unprescaled mixed triggers as evaluated in ggH samples. 119
6.6 Lowest unprescaled lepton triggers available during the 2022 pp data-taking period used in the $H \to ZZ^* \to 4\ell$ fiducial cross-section analysis. 123

6.7 Summary of object selection for Run 3 $H \to ZZ^* \to 4\ell$ fiducial cross-section analysis. 125
6.8 Summary of event selection for Run 3 $H \to ZZ^* \to 4\ell$ fiducial cross-section analysis. 125
6.9 Summary of fiducial region definition for Run 3 $H \to ZZ^* \to 4\ell$ fiducial cross-section analysis. 126
6.10 The expected and observed yields for 115$< m_{4\ell} <$130 GeV. 127
6.11 The systematics breakdown in the fiducial $H \to ZZ^* \to 4\ell$ cross-section measurement. 129

Chapter 1

Introduction

Experimental particle physics is a discipline across energy scales and layers of complexity. Physics at the sub-MeV[1] scale is required for understanding multi-TeV collisions, as in the case for silicon detectors and collisions at the Large Hadron Collider. In a different layer of complexity, studies of the detector mechanical structure and its stability contribute to our knowledge of particle physics. This thesis depicts these layers, and bridges detector performance and physics analysis.

Modern particle physics is defined by the highly successful Standard Model (SM), a theoretical framework based on quantum field theory and the principle of symmetry. It describes three out of the four fundamental interactions, and through the introduction of spontaneous symmetry breaking and the Higgs mechanism, explains the origin of mass for massive gauge bosons and fermions. The SM has withstood stringent experimental tests, and most experimental results have shown good agreement with predicted parameters and theoretical modelling. The most recent triumph of the SM is the discovery of the Higgs boson in 2012, and the following decade saw the precise measurement of the Higgs boson properties.

One of the collaborations that first announced the Higgs boson discovery is the ATLAS collaboration at the Large Hadron Collider. The ATLAS detector is a general-purpose detector, with the design goal of detecting as many physics signatures as possible. As disassembling a 25 m detector can prove challenging,

[1] This thesis adopts natural units $c = \hbar = 1$.

especially once the detector is operational, other methods and studies are required to ensure the long-term operation and understanding of detector performance across time. One example of such studies is the calibration of muon momentum, which is specifically relevant to all physics processes involving muons as final states.

This thesis focuses on both the challenge of Higgs boson properties measurements, and muon performance for two periods of ATLAS operation: the data-taking period between 2015 and 2018 (colloquially known as *Run 2*), and the full dataset from 2022 (known as early *Run 3* data). The thesis is structured as follows: Chapter 2 presents a brief overview of the theoretical framework of the SM, and phenomenology relevant to the measurement of the Higgs boson at the LHC. Chapter 3 provides a short description of the Large Hadron Collider, the ATLAS detector and its sub-components. Chapter 4 delves into the intricacies of muon reconstruction, with a sharp focus on the muon momentum calibration. Chapter 5 describes the measurement of the Higgs mass in the $H \to ZZ^* \to 4l$ decay channel using Run 2 proton-proton collision at the centre-of-mass energy of 13 TeV. Chapter 6 includes preliminary muon momentum calibration, and trigger studies that contribute to the measurement of the Higgs fiducial cross section using the early Run 3 dataset. Finally, chapter 7 provides a conclusion, and a discussion of the future outlook for these measurements.

Chapter 2

Standard Model of Particle Physics

Currently, we do not have a unified theory of nature, but we can understand nature at vastly different scales of distance and energy. At the scale of the solar system, general relativity governs by its description of spacetime. General relativity explains that gravity originates from the motions of matter along geodesics of the spacetime curvature, and is substantiated through the observation of the perihelion precession of Mercury's orbit around the sun, the orbits of binary pulsars, and the direct observation of gravitational waves. On the other extreme, the Standard Model (SM) describes the subatomic scale, where the interaction strength of gravity becomes negligible compared to the other three fundamental interactions: electromagnetic, weak and strong interactions. The most successful quantum theory to date, the SM also offers descriptions of matter interactions and explanations for the origin of mass.

Section 2.1 provides an overview of the SM, its mathematical formulations and the resultant particles. Section 2.2 describes the discovery of the Higgs boson, and its production and decays at the LHC. Together, these sections establish the motivation and the notation used in the rest of this thesis.

2.1 Standard Model as a field theory

The Standard Model (SM) of particle physics describes the basic constituents of matter and their interactions through the language of quantum field theory (QFT). Fundamentally a field theory, QFT for particle physics combines quantum

mechanics and special relativity, and describes fundamental objects as fields with discrete (or *quantised*) energy, and obeys Lorentz transformation. Thus in the SM, both matter particles and fundamental force carriers are quantised excitations of quantum fields, and their evolution obeys the Euler-Lagrange equation:

$$\partial_\mu\left(\frac{\partial\mathcal{L}}{\partial(\partial_\mu\phi_i)}\right) - \frac{\partial\mathcal{L}}{\partial\phi_i} = 0, \tag{2.1}$$

where $\mathcal{L}$ is the Lagrangian and ϕ_i is a continuous quantum field in x^μ[1]. The dynamics of a system is therefore encapsulated by the Lagrangian, and transformations that leaves the system unchanged (commonly referred to as symmetries) result in conserved quantities in accordance with Noether's theorem [1]. In addition to Poincar$\acute{e}$ symmetries (translation, rotation and Lorentz boost), the SM is a non-abelian gauge field theory that obeys the following symmetry structure[2] [2] :

$$SU(3)_C \times SU(2)_L \times U(1)_Y. \tag{2.2}$$

The $SU(3)_C$ symmetry (with C referring to the colour charge) is the underlying symmetry for quantum chromodynamics (QCD), which describes the strong interaction between coloured objects, quarks and gluons. The $SU(2)_L \times U(1)_Y$ is the underlying symmetry of an unified interaction between electromagnetism and the weak interaction, the electroweak (EW) interaction. Here, L refers to the weak isospin coupling to the left-handed particles only. A left-handed particle refers to the chirality eigenstate meaning that the particle transforms in a left-handed representation of the Poincar$\acute{e}$ group. Y refers to the weak hypercharge, a single charge operator relating the electric charge and the third component of the weak isospin. The SM is locally gauge invariant by construction, namely that the theory is invariant under the following transformation:

$$\phi \rightarrow e^{i\alpha(x)}\phi, \tag{2.3}$$

[1]Here, the μ indices run over the spacetime dimensions. Einstein notation is used for the rest of this thesis, where repeated indices are summed over for all values of the index.

[2]Here we follow the group theory notion, where $U(N)$ is a set of $N \times N$ unitary matrices, and $SU(N)$ is a subset of $U(N)$ with unitary determinant.

where the transformation term, $\alpha(x)$ can be arbitrarily different at all points of spacetime. However, naive mass terms associated with the gauge fields are not locally invariant, thus preventing fundamental particles from acquiring mass. This sharply contrasts with our experimental measurements and experience of reality, and is resolved by the introduction of the Higgs mechanism. By interacting with the non-zero Higgs field, particles acquire mass, while maintaining the local gauge symmetry structure [2]. Further detail on the Higgs mechanism and its phenomenology at the LHC is discussed in Section 2.2.

2.1.1 Elementary particles

In quantum mechanics, the Pauli exclusion principle states that two or more identical particles, with half integer spins (fermions) cannot occupy the same quantum state within a quantum system simultaneously. This gives rise to the electronic structure of electron orbital in atoms. Fermions obey Fermi-Dirac statistics.

Particles with integer spin, bosons, are not subject to the Pauli exclusion principle. Any number can occupy the same quantum state, such as photons produced by a laser, or atoms in a Bose-Einstein condensate. Bosons obey Bose-Einstein statistics.

In the SM, all 'matter particles' are spin-1/2 fermions, and all 'force carriers' are bosons. Fermions are further divided into quarks and leptons. The former carry colour charge, and the latter are colourless, and thus not affected by strong interaction. Quarks are divided into two types based on their electrical charge (all quarks have fractional electrical charges with respect to that of an electron, which is denoted as e. The *up*-type quark has charge of +2/3 e and *down*-type quark has -1/3 e), and three generations based on their masses, making a total of six quark flavours. Similarly, leptons are categorised into charged leptons and neutral leptons (neutrinos), and three generations based on the mass of the charged leptons. Neutrinos possess non-zero mass, but

only upper limits on neutrino masses exist [3]. Additionally, the mass ordering of neutrinos is currently unknown [4].

The SM bosons are either vector bosons (spin 1) or a scalar boson (spin 0). All bosons are force mediators: the photon for electromagnetism, the W and Z bosons for weak interaction, and gluons for strong interaction. Only the W boson is charged with two variants: the W^+ and W^-, and all other bosons are electrically neutral. Both photons and gluons are massless, while the W and Z bosons are massive. Corresponding to the number of generators in $SU(3)$, gluons have 8 distinct variants. The Higgs boson, at the mass of 125 GeV, is the only known scalar boson, and is the result of spontaneous symmetry breaking [2].

Three of the twelve fermions (electron, up and down quarks) make up atoms. Protons and neutrons make up the atomic nucleus, and both are composite, colourless states of quarks and gluons. Electrons are bound at distinct energy levels around the nucleus, thus completing a electrically-neutral atom. Protons consist of two up quarks, one down quark and a sea of virtual quark-antiquark pairs, created by splitting of gluons. Each component in a proton, be it quarks or gluons, is referred to as parton, and each carries a fraction of the proton momentum. The probability of interacting with a specific parton is parameterised by parton distribution functions (PDF), for which an extensive literature [5] and parametrisations [6, 7] exist.

2.1.2 Electroweak theory

Quantum electrodynamics (QED) describes the interaction between charged fermions with the photon as its mediator, and is the precursor of the unified electroweak theory. It follows the $U(1)$ gauge symmetry described by Equation 2.3, and is described by the Dirac Lagrangian [2]:

$$\mathcal{L} = \bar{\phi}(i\gamma^\mu D_\mu - m)\phi, \tag{2.4}$$

where ϕ is the fermionic field for the charged leptons, and D_μ is the covariant derivative with the photon field A_μ:

$$D_\mu = \partial_\mu + iqA_\mu, \tag{2.5}$$

where A_μ is the photon field and transforms with the local gauge choice χ:

$$A_\mu \rightarrow A_\mu^{'} = \partial_\mu - \partial_\mu \chi. \tag{2.6}$$

The formulation of the weak interaction follows closely to that of QED, but with the addition of chirality, which relates to the relative direction between particle spin and momentum. The need for a chiral theory arises from the experimental observation of ^{60}Co decay, for which chirality of the emitted electron is maximally violated [8]. This requires the $SU(2)$ symmetry structure, and thus a different set of transformations. The fermionic field, ϕ, now encapsulates the left-handed weak isospin doublets of charged lepton and its corresponding neutrino, and infinitesimally transforms as:

$$\phi(x) = \begin{pmatrix} \nu_e(x) \\ e(x) \end{pmatrix} \rightarrow \phi^{'}(x) = \phi(x)(\mathbf{I} + ig_W \alpha(x) \cdot \mathbf{T}), \tag{2.7}$$

where $\mathbf{I}$ is the two dimensional identity matrix, g_W is the weak coupling constant, $\alpha(x)$ is the local choice of gauge, and $\mathbf{T} = \frac{1}{2}\sigma$, with σ as the Pauli spin-matrices, which are the three generators of the $SU(2)$ group. Similar to QED, the covariant derivative takes up the following form to preserve the gauge invariance of $SU(2)$:

$$D_\mu = \partial_\mu + ig_W \mathbf{T} \cdot \mathbf{W}_\mu, \tag{2.8}$$

where $\mathbf{W}_\mu$ refers to the three gauge fields of the weak interaction. These three gauge fields can be constructed into two fields with electrically-charged current, and one with neutral current, all of which only couple to left-handed particles or right-handed antiparticles. This theoretical assumption contrasts to the experimental observation that the weak neutral current couples to both chiral states [9].

This discrepancy was predicted by the unified model between electromagnetism and the weak interaction, which proposed by Glashow, Salam and

Weinberg (GSW) [10–12]. Starting from the observation that both the photon and Z boson field (A_μ and Z_μ respectively) carry neutral current, it is then possible to express the two bosons as a mixed state between the two fields. This gives rise to a new $U(1)_Y$ local gauge symmetry, with a new gauge field B_μ, which couples to a new weak hypercharge Y, with coupling strength $g^{'}$. The GSW model thus describes the four bosons: photons, Z and $W^{\pm}$ as the following fields:

$$A_\mu = +B_\mu \cos\theta_W + W_\mu^{(3)} \sin\theta_W, \tag{2.9}$$

$$Z_\mu = -B_\mu \sin\theta_W + W_\mu^{(3)} \cos\theta_W, \tag{2.10}$$

$$W_\mu^{\pm} = \frac{1}{\sqrt{2}}(W_\mu^{(1)} \mp i W_\mu^{(2)}), \tag{2.11}$$

with θ_W as the weak mixing angle defined as follows:

$$\begin{aligned} \sin\theta_W &= \frac{g_W}{\sqrt{g_W^2 + g^{'2}}} \\ \cos\theta_W &= \frac{g^{'}}{\sqrt{g_W^2 + g^{'2}}}, \end{aligned} \tag{2.12}$$

In this unified model, the couplings strength of the photon, the W and the Z boson are related by:

$$e = g_W \sin\theta_W = g_Z \sin\theta_W \cos\theta_W, \tag{2.13}$$

and with the weak hypercharge Y relating to the electric charge and weak isospin $I_W^{(3)}$ by $Y = 2(Q - I_W^{(3)})$. The bosonic fields in Equation 2.9-2.11 are without naive mass terms, and for fermions, only the kinetic terms are included, resulting in a theory with massless particles. This is due to the fact that naive mass terms, $-m\phi\bar{\phi}$ are not gauge invariant, and another mechanism is required to retrieve particle mass.

2.1.3 The Higgs mechanism

The $SU(2) \times U(1)$ symmetry considered in Section 2.1.2 is an exact one, and one that does not include an intrinsic mass term for gauge bosons and fermions. The Higgs mechanism recovers gauge boson and fermion masses through spontaneous

symmetry breaking by introducing a scalar field, such that the local gauge symmetry is broken, and mass terms are recovered through interacting with the field [13–15]. This is generated through the following isospin doublet with $Y_W = 1$ [2]:

$$\phi = \begin{pmatrix} \phi^+ \\ \phi^0 \end{pmatrix}, \tag{2.14}$$

with the following Lagrangian:

$$\mathcal{L} = \frac{1}{2}(\partial_\mu \phi)(\partial^\mu \phi) - V(\phi), \tag{2.15}$$

where the first term on the left hand side corresponds to the kinetic energy of the scalar field, with potential energy described by $V(x) = \frac{1}{2}\mu^2\phi^2 - \frac{1}{4}\lambda\phi^4$. The first term in the potential energy corresponds to the mass of the scalar boson, while the second term corresponds to the four-point self-interaction of the scalar boson.

Additionally, to preserve the $SU(2) \times U(1)$ gauge invariance of the Lagrangian in Equation 2.15, the following covariant derivative is used:

$$\partial_\mu \rightarrow D_\mu = \partial_\mu + ig_W \mathbf{T} \cdot \mathbf{W}_\mu + ig^{'}\frac{Y}{2}B_\mu, \tag{2.16}$$

where $g^{'}$ is the coupling strength of the gauge field B_μ to weak hypercharge Y.

The vacuum expectation value (VEV) refers to the value of the minimum of $V(x)$, and can be obtained by setting $\frac{\partial V(x)}{\partial \phi^2} = 0$. The sign of μ^2 determines the shape of $V(x)$ and its minima. For $\mu^2 > 0$, the minimum occurs only at $\phi = 0$. If $\mu^2 < 0$, a set of minima emerges:

$$\phi^2 = \frac{-\mu^2}{2\lambda} = \frac{v^2}{2}. \tag{2.17}$$

The physical vacuum, or ground state, can therefore be on any point along this curve, and introduces the spontaneous symmetry breaking. A schematic diagram for the Higgs potential for $\mu^2 < 0$ is shown in Figure 2.1 [16].

Under the $SU(2) \times U(1)$ unitary gauge transformation, we can choose the Higgs doublet to be:

$$\phi = \frac{1}{\sqrt{2}} \begin{pmatrix} 0 \\ v + h(x) \end{pmatrix}, \tag{2.18}$$

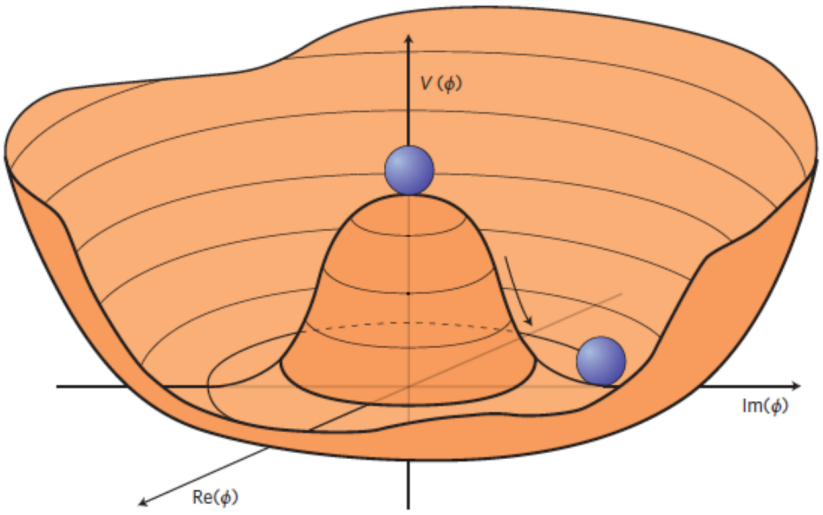

Figure 2.1: The shape of the SM Higgs potential and an illustration of electroweak symmetry breaking. The unstable minimum at $|\phi|^2 = 0$, and the degenerate minima at $|\phi|^2 = -\frac{\mu^2}{2\lambda}$ are indicated by the blue spheres. Reproduced from [16].

where $h(x)$ is explicitly the Higgs field, and is entirely real. The kinetic term in the SM Lagrangian then takes the form:

$$\begin{aligned} D^\mu\phi D_\mu\phi =& \frac{1}{2}(\partial_\mu h)(\partial^\mu h) + \\ & \frac{1}{8}g_W^2(W_\mu^{(1)} + iW_\mu^{(2)})(W^{(1)\mu} - iW^{(2)\mu})(v + h(x))^2 + \\ & \frac{1}{8}(g_W W_\mu^{(3)} - g^{'}B_\mu)(g_W W^{(3)\mu} - g^{'}B^\mu)(v + h(x))^2, \end{aligned} \tag{2.19}$$

For a gauge boson with mass m and field A_μ, its mass term appears in the kinematic term with the following form: $\frac{1}{2}m^2 A_\mu A^\mu$. Thus, the mass of $W^\pm$ bosons can be obtained from Equation 2.19:

$$m_W = \frac{1}{2}g_W v, \tag{2.20}$$

The mass terms of the photon and Z boson field can be obtained from the purely quadratic term of $W_\mu^{(3)}$ and B_μ with mixing described by Equation 2.9 and 2.10. With the proper transformation, the photon and Z mass are:

$$\begin{aligned} m_A &= 0, \\ m_Z &= \frac{1}{2}v\sqrt{g_W^2 + g'^2}, \end{aligned} \tag{2.21}$$

with the definition of the weak mixing angle in Equation 2.12, the ratio of the mass of the W and the Z boson is $\cos\theta_W$, and has been experimentally verified.

By measuring g_W and m_W, the VEV of the Higgs field is estimated at 246 GeV, leaving λ, the self-interaction term of the Higgs boson, to be constrained from the measurement of Higgs mass:

$$m_H = \sqrt{2\lambda v^2}, \tag{2.22}$$

Fermion masses can similarly be recovered using the Higgs mechanism through the Yukawa interaction, and the coupling strength between the Higgs boson and the fermions are proportional to the fermion masses. The relation between Higgs coupling strength and fermion masses can be seen in Figure 2.2.

2.1.4 Quantum chromodynamics

Quantum chromodynamics (QCD) describes the interaction between particles with colour charges with the gluon, which is the mediator for the strong interaction. It follows a $SU(3)$ symmetry transformation:

$$\psi(x) \rightarrow \psi^{'}(x) = exp[ig_s\alpha(x) \cdot \hat{(T)}(x)], \tag{2.23}$$

where g_s is the strong coupling, $\alpha(x)$ is the function of spacetime coordinate, and $\hat{T}(x) = T^a$ are the eight generators of $SU(3)$ group, and are related to the Gell-Mann matrices, λ^a, by $T^a = \frac{1}{2}\lambda^a$. The dimensionality of the wavefunction ψ therefore follows that of the $SU(3)$ generators (3×3 matrices), and corresponds to the three colour charges: red, blue, and green. The generators satisfy the commutator relation: $[T^a, T^b] = if_{abc}T^c$, where f_{abc} is the structure constant.

Following $SU(3)$ symmetry, the partial derivative is replaced by the covariant derivative:

$$D_\mu = \partial_\mu + ig_s G^a_\mu T^a, \tag{2.24}$$

where the G^a_μ is the gluon field, and transforms under the $SU(3)$ symmetry as:

$$G^a_\mu \rightarrow G^{a'}_\mu = G^a_\mu - \partial_\mu\alpha_a - g_s f_{cba}\alpha_c G^b_\mu, \tag{2.25}$$

with the resulting QCD Lagrangian:

$$\mathcal{L} = -\frac{1}{4}G^a_{\mu\nu}G^{\mu\nu}_a + \bar{\psi}(iD - m)\psi, \tag{2.26}$$

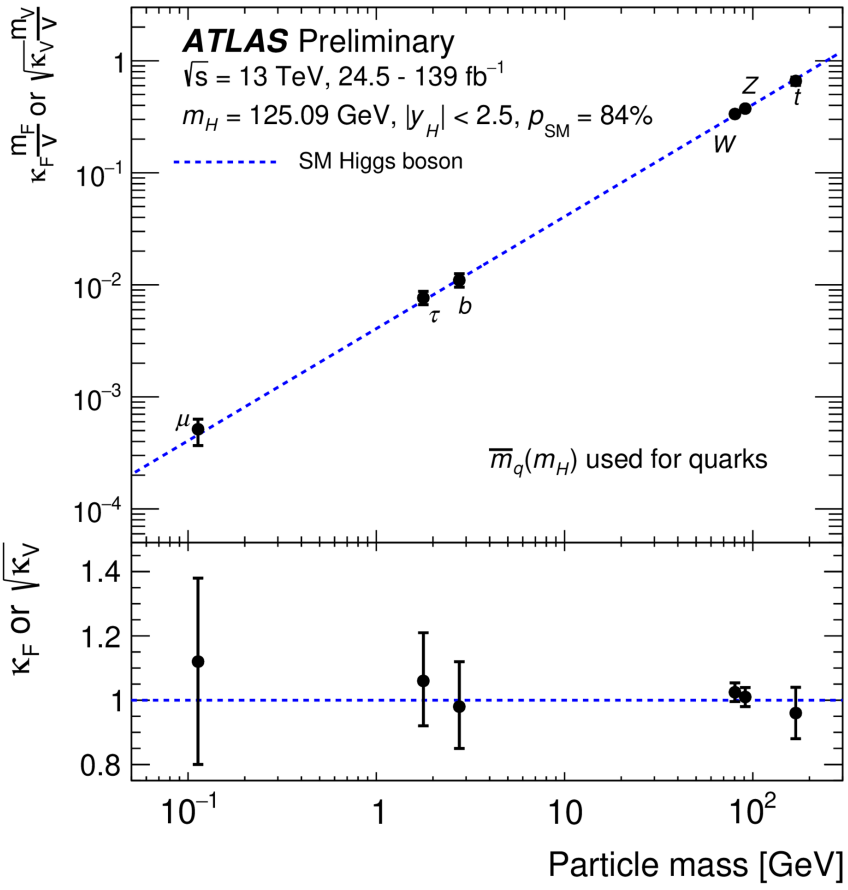

Figure 2.2: Reduced coupling-strength modifiers κ_F for fermions ($F = t, b, \tau, \mu$) and for weak gauge bosons ($V = W$, Z) as a function of their masses m_F and m_V, respectively, and the vacuum expectation value of the Higgs field $v = 246$ GeV. The SM prediction for both cases is also shown (dotted line). The black error bars represent 68% CL intervals for the measured parameters. The coupling modifiers are measured assuming no BSM contributions to the Higgs boson decays, and the SM structure of loop processes such as ggF and $H \to \gamma\gamma$. The lower inset shows the ratios of the values to their SM predictions. Reproduced from [17]

where the first term corresponds to the kinetic term for the gluon fields, and the second term corresponds to the Dirac Lagrangian. The gluon field strength in the first term, $G_a^{\mu\nu}$, is:

$$G_a^{\mu\nu} = \partial^\mu G_a^\nu - \partial^\nu G_a^\mu - g_s f^{abc} G_b^\mu G_c^\nu, \tag{2.27}$$

As the generators of $SU(3)$, $\hat{T}$ does not have a trivial commutation relation, QCD is known as a non-Abelian gauge theory, and the presence in the gluon field strength tensor gives rise to the gluon self-interaction, in the form of triple and quartic

gluon vertices (shown in Figure 2.3). This results in a phenomenon specific to QCD, the *colour confinement*, which states that the coloured objects are always confined to colour-less states, and no particles with non-zero colour charge can propagate as free particles. Combined with the running coupling of the strong force, the energy required to separate a coloured object increases rapidly to infinity:

$$\alpha_s(\mu^2) = \frac{g_s}{4\pi} = \frac{12\pi}{(33 - 2n_f)\ln(\frac{\mu^2}{\Lambda_{QCD}})}, \tag{2.28}$$

where μ is the energy scale, n_f is the number of quark flavours, and $\Lambda_{QCD} \approx 200$ MeV is the energy scale of divergence for the perturbative method. The potential energy required to separate a coloured object from a bound state increases until it is enough to spontaneously emit a gluon, which subsequently cascades into pairs of quarks and gluons to form new colour-less bound states, collectively known as hadrons. Such cascades of hadrons are referred to as a *jet*, and represents the kinematics of the initial hadron. The measurements of jet properties permits studies of non-perturbative QCD, and is an important aspect of the LHC physics program.

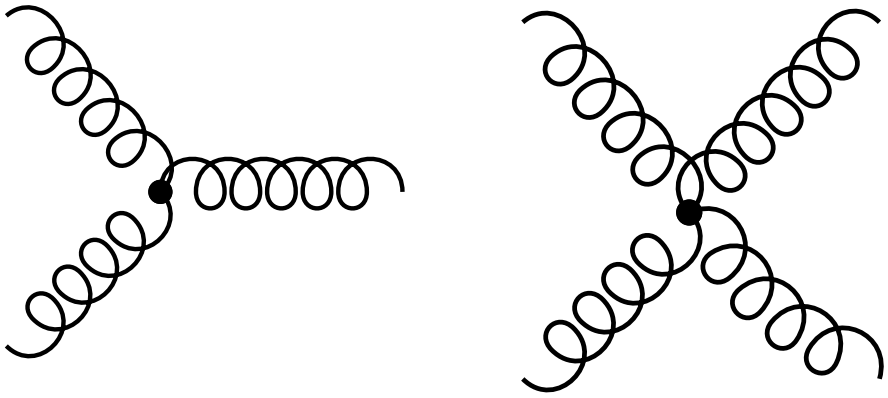

Figure 2.3: Feynman diagrams for triple and quartic gluon self-interaction.

2.2 The Higgs phenomenology at the LHC

The discovery of a scalar boson was announced by the ATLAS and CMS collaborations in July 2012 [18, 19]. At the time of discovery, its measured mass combining the ATLAS and CMS results was 125.09 ± 0.21 (stat.) ± 0.11 (syst.) GeV [20], and initial measurements of it CP and spin properties were consistent with the expectation of the SM Higgs boson. Since its discovery, further studies of the Higgs boson spin, parity, production channels and decay rates have found no deviation from the SM Higgs boson [21–23].

The four main Higgs boson production modes at the Large Hadron Collider (LHC) are gluon-gluon fusion (ggH), vector boson fusion (VBF), associated production with a vector boson (VH), and the associated production with a pair of top quarks ($t\bar{t}H$). The Feynman diagrams for these production modes are shown in Figure 2.4, and the production cross sections as a function of the centre-of-mass energy are shown in Figure 2.5. Other production modes, such as associated production with a pair of bottom quarks ($b\bar{b}H$) and with a single top quark (tH), are more difficult to detect experimentally.

The Higgs boson is an unstable particle, and decays to bosons and fermions if kinematically feasible. As discussed in Section 2.1.2, the Higgs boson preferentially decays to heavier particles. As the Higgs boson mass is smaller than twice that of the W and Z boson mass, its decay into di-vector boson results in at least one of the vector bosons being produced off mass shell. Figure 2.6 shows the Higgs boson decay branching ratio as a function of the Higgs mass for each final state.

2.3 Limitations of the Standard Model

So far we have examined the Standard Model as a gauge theory, and its predictions for the Higgs boson phenomenology at the LHC. Experimentally, the SM has been one of the most successful theoretical frameworks to date, and it has been tested to unprecedented numerical precision. However, it is not a complete description of nature, with a number of limitations hinting at new physics.

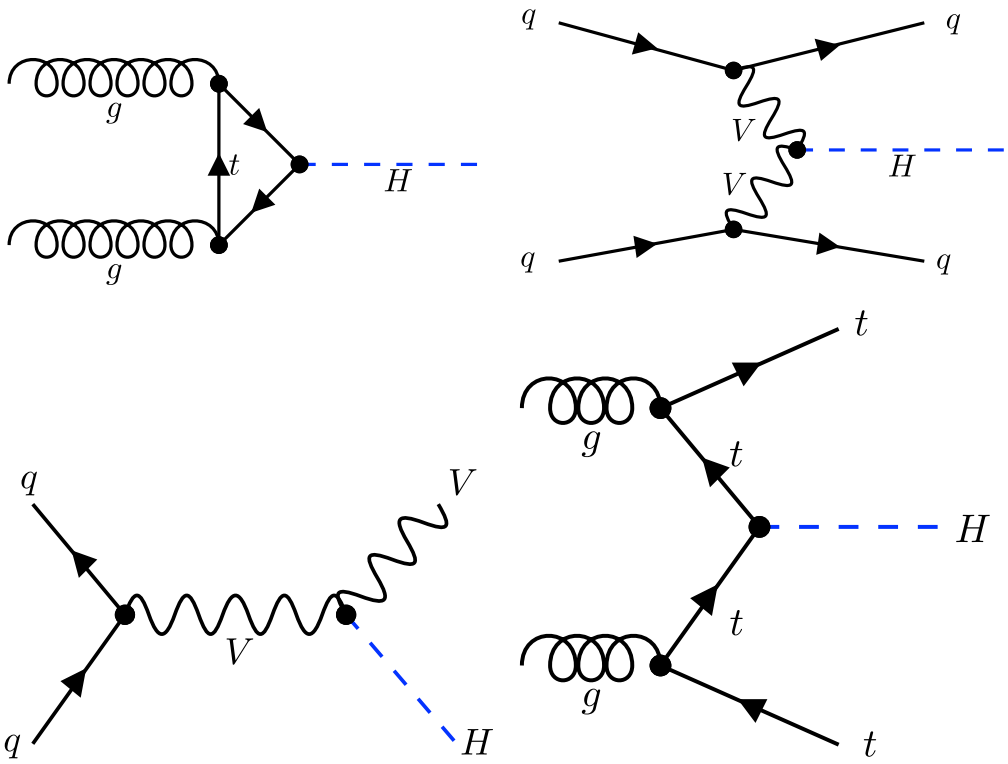

Figure 2.4: Leading order diagrams for the four main production modes (ggH top left, VBF top right, VH bottom left, and ttH bottom right) for the SM Higgs boson at the LHC.

The SM misses descriptions for both the extra matter and energy content and one fundamental interaction. The existence of dark matter is firmly established through cosmological observations, including the galactic rotation curves [25], the distribution of visible and total mass densities of the Bullet cluster [26], and the cosmic microwave background [27]. An additional source of mass-energy with unknown origin is the dark energy, supported by the observations of Type 1a supernovae [28], and the cosmological survey of the cosmic microwave background [27]. Neither dark matter nor dark energy has a corresponding candidate particle in the SM. There have been many experimental searches for potential dark matter candidates [29]. Similarly, gravity is not yet incorporated into the SM with a bosonic candidate, the graviton, as the force carrier [30]. Nor does the SM offer an explanation for the weakness of gravity compared to other fundamental forces of nature.

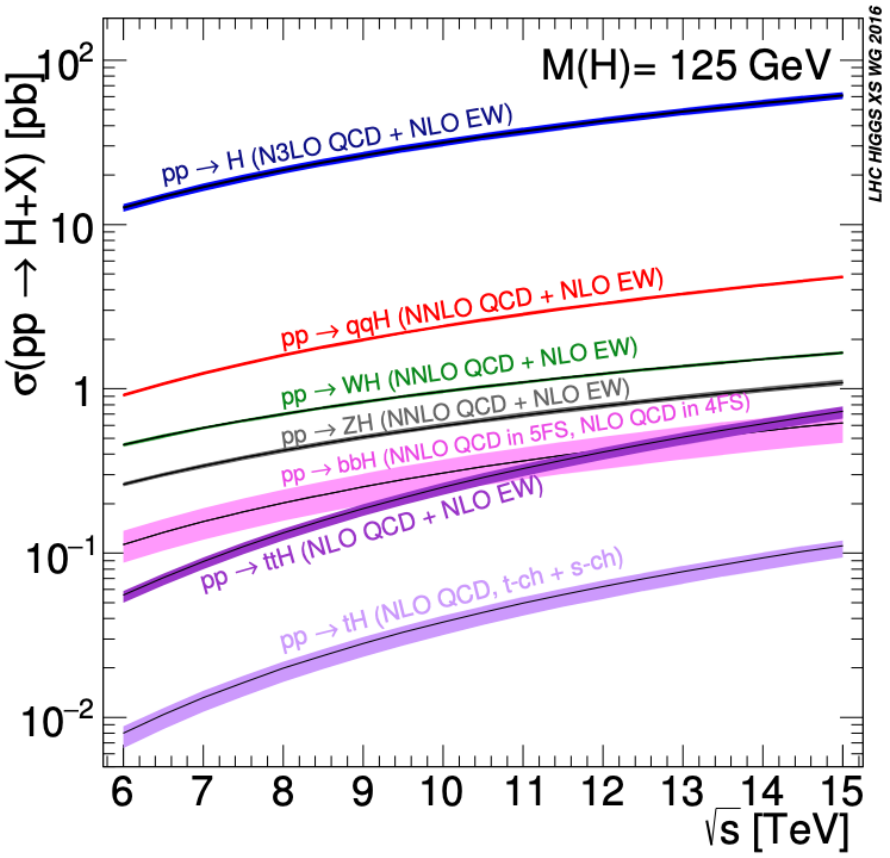

Figure 2.5: The SM Higgs boson production cross-section as a function of the centre-of-mass energy for proton-proton collisions for a Higgs boson with mass at 125 GeV. ggH production is shown in blue, denoted as $pp \to H$, VBF is shown in red, denoted as $pp \to qqH$, $t\bar{t}H$ is in dark purple, denoted as $pp \to ttH$, $b\bar{b}H$ is in pink, denoted as $pp \to bbH$, and tH is in light purple, denoted as $pp \to tH$. The two VH processes (WH and ZH) are shown separately in green and gray respectively. Reproduced from [24]

The SM also cannot account for the observed matter-antimatter asymmetry of the Universe, as matter and antimatter are created in equal parts in the early universe in the SM. While the SM does incorporate CP violation as measured experimentally [24, 31], it is not enough to produce the matter-antimatter asymmetry we observe in the universe today. This hints at new physics that can generate large CP-violation at energy scales that are beyond the current experimental reach.

The observation of neutrino oscillations [32] implies that neutrinos are massive particles, contrary to the SM prediction. This suggests the existence of another mass generation mechanism, such as neutrinos being their own antiparticles.

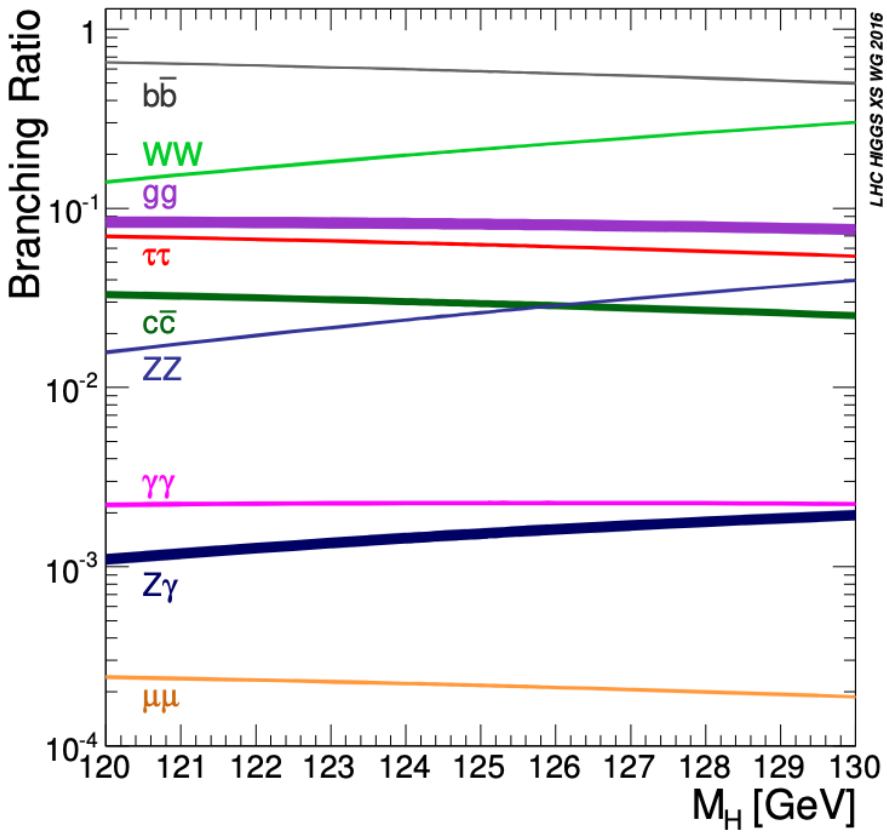

Figure 2.6: The SM Higgs boson decay branching ratio as a function of Higgs mass for each final state. The branching ratio to a Z boson pair is shown in light blue. The theoretical uncertainties are indicated as bands. Reproduced from [24].

Another striking puzzle is the fact that the Higgs is such a *light* particle. Being a scalar particle, the mass term of the Higgs receives corrections from self-interactions, bosonic and fermionic loops which are quadratically divergent. If there is no new physics until the Planck scale, and if Planck scale physics couples to the Higgs boson, it would receive enormous, fine-tuned quantum corrections for every single interaction, such that the Higgs mass remains the observed 125 GeV. This opens up the possibility that there exists new physics at higher energy scales [33], and a number of theoretical solutions (including supersymmetry, composite Higgs models, and extra dimensions) are explored both theoretically and experimentally. The measurement of the properties of the Higgs boson, including its mass, couplings, CP and width, is therefore crucial to further our understanding of the universe.

Chapter 3

The LHC and the ATLAS detector

The Large Hadron Collider (LHC) is located at the European Organization for Nuclear Research in Geneva, Switzerland. It is installed in the existing underground 26.7 km circumference tunnel which housed the Large Electron-Positron Collider. It is a hadron accelerator with and collider designed to operate at an energy of up to $\sqrt{s}$ =14 TeV, operating at an instantaneous luminosity of $\approx 10^{34}\text{cm}^{-2}\text{s}^{-1}$ for proton-proton collisions. The high centre-of-mass energy provides a probe for heavy particle production, and the high instantaneous luminosity allows for the measurements of low cross-section processes.

Hadrons are accelerated within the two beamlines in the LHC ring, and collide at four interaction points. The ATLAS experiment is located at one of these interaction points. A general-purpose detector, the ATLAS detector is able to withstand the harsh radiation environment of the LHC, and is designed to measure as many physics signatures as possible. The radiation hardness ensures the ATLAS detector's performance does not degrade (to the extent possible) over the lifetime of the LHC, and this enables the vast variety of physics, and the ability to perform internal cross-checks across different physics processes over the lifetime of the LHC.

This chapter is organised as follows: section 3.1 starts with a brief description of the LHC accelerators and the principles of proton-proton (pp) collisions. An overview of the design choices of the ATLAS detector is provided in Section 3.2,

with further details on the tracking, calorimetry, muon spectrometry, triggers and simulation in the subsequent sections.

3.1 Large Hadron Collider

The LHC inherits the underground tunnel and the existing injector chain from the LEP experiment, and is able to accelerate and collide protons and lead ions. For the proton-proton (pp) collisions, the LHC is designed to reach a centre-of-mass energy of 14 TeV, and an instantaneous luminosity of $10^{34}\text{cm}^{-2}\text{s}^{-1}$. In practice, the LHC reached 13 TeV between the 2015-2018 data-taking period, and 13.6 TeV in 2022.

The protons are produced by stripping electrons from hydrogen atoms using a duoplasmatron source [34]. The proton bunch is then accelerated by a linear accelerator (Linac 2 before 2020, which has since been upgraded to Linac4), and then a sequence of three magnet synchrotrons (Proton Synchrotron Booster, Proton Synchrotron, and Super Proton Synchrotron) which increase the proton energy to 450 GeV before they are injected into the main LHC ring [35]. A schematic diagram for the LHC accelerator complex is provided in Figure 3.1. The protons then circulate in two beams in opposite directions in separate beam pipes, limited by the space available from the LEP tunnel. The proton beams are bunched and accelerated by the radio-frequency (RF) cavities to a design energy of up to 7 TeV. The protons are guided by the superconducting NbTi magnet system, which is capable of reaching the current required (>11 kA) to maintain the protons in their orbits at these energies [36]. Around the four interaction points, superconducting quadrupole triplets are used to focus the beam prior to collision [37].

The two circulating proton beams each contain a maximum of 2808 bunches, with each bunch containing around 10^{11} protons. The spacing between each bunch in the beam is determined by the RF system, and at the interaction points, the two beams cross each other every 25 ns, a frequency of 40 MHz. Within each crossing, multiple proton-proton collisions occur, with the majority of these collisions being

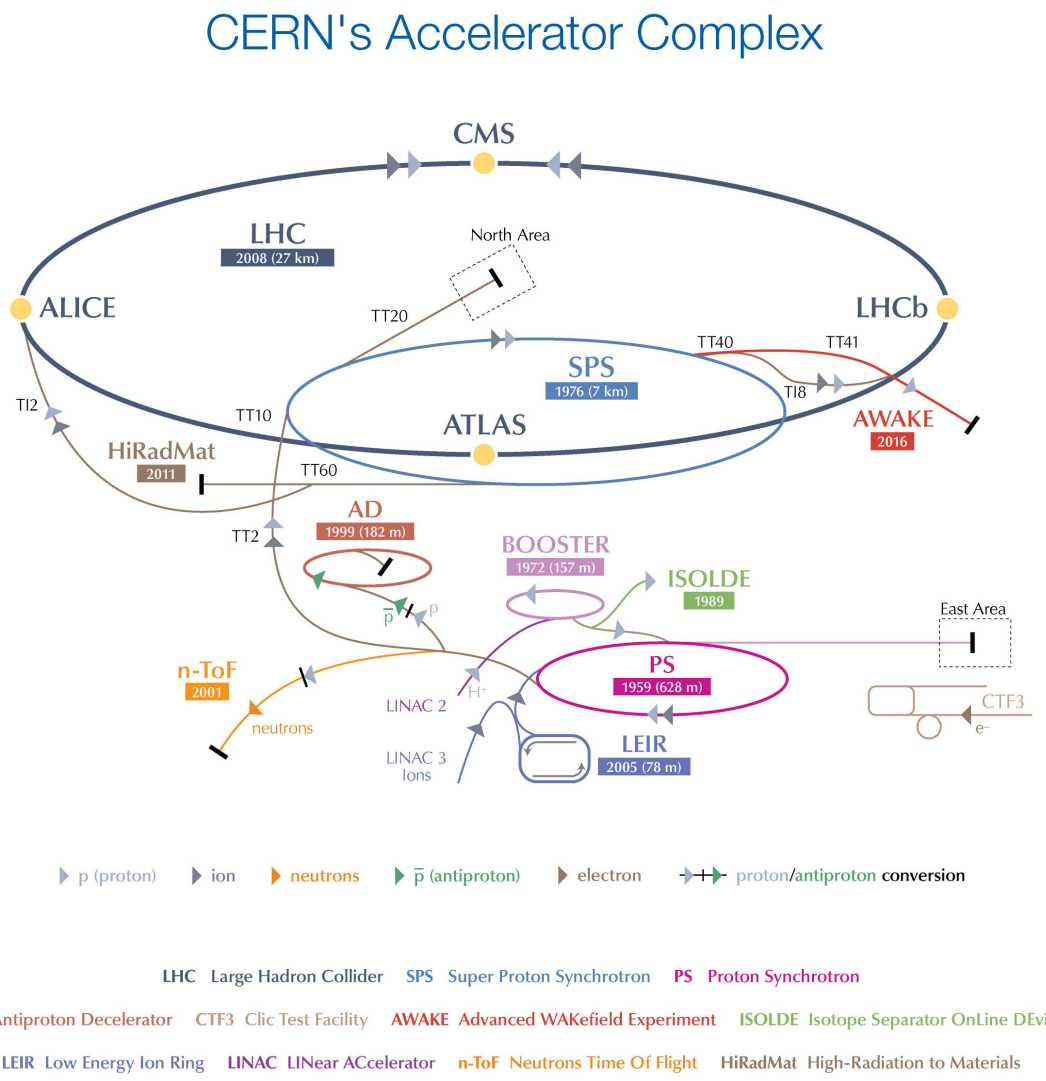

Figure 3.1: A schematic diagram of the full LHC accelerator complex. Reproduced from [38].

QCD interactions involving low momentum transfer, which are referred to as soft-scattering processes [37]. The total number of particle interactions per bunch-crossing is referred to as pile-up, and it increases the complexity of identifying and reconstructing hard-scattering processes involving high momentum transfer between partons. The increase in pile-up is an unavoidable consequence of increasing the LHC luminosity $\mathcal{L}$, as shown by the following equation:

$$\mathcal{L} = \frac{N_b^2 n_b f_{rev} \gamma F}{4\pi \epsilon_n \beta^*}, \tag{3.1}$$

where N_b is the number of particles per bunch, n_b is the number of bunches

per beam, f_{rev} is the frequency for the beam revolution, γ is the Lorentz factor, F is the reduction factor due to the angle between two colliding bunches, ϵ_n is the normalized transverse beam emittance, and β^* is the beta function at the collision point [2]. The increase in luminosity is however required to probe processes with cross-section σ_p, as the rate for these processes are

$$\frac{dN_p}{dt} = \mathcal{L}\sigma_p, \tag{3.2}$$

where N_p is the number of events for a given process. As a result, high luminosity is essential for probing rarer processes such as the production of the Higgs boson. The performance deterioration in a high pile-up environment is compensated by increasingly sophisticated hardware and software tools, such that hard-scattering collisions can be identified [39].

The LHC operated at $\sqrt{s} = 13$ TeV between 2015-2018 (known as Run 2), and the total delivered integrated luminosity for Run 2 was $\int \mathcal{L}dt \approx 156$ fb^{-1}. The centre-of-mass energy was then upgraded to 13.6 TeV after numerous upgrades to the LHC injector system and individual LHC experiments. These upgrade activities are collectively referred to as the Phase-I upgrade, and is described in Chapter 6. After restarting the LHC in 2022 (known as Run 3), the integrated luminosity for 2022 was ≈ 30 fb^{-1}. As a result, the average pile-up was 13 in 2015, 36 in 2018, and 42.5 in 2022. The integrated luminosity as a function of time can be seen in Figure 3.2, and the pileup profile is shown in Figure 3.3.

After the completion of Run 3 at the end of 2026, the LHC will undergo three years of Phase-II upgrade to sustain its discovery potential, and to withstand higher luminosity. The LHC will then re-emerge as the High-Luminosity LHC, or HL-LHC, and continue to deliver a total of 3000 fb^{-1} over ten years. From the machine point of view, this involves upgrades to the superconducting magnets, the RF system and other infrastructure [40]. For individual experiments, this translates to an increase in pileup and radiation damage to detector systems. As the result, the ATLAS experiment is actively anticipating its Phase-II upgrade, which includes the installation of a new Inner Tracker, implementation of new

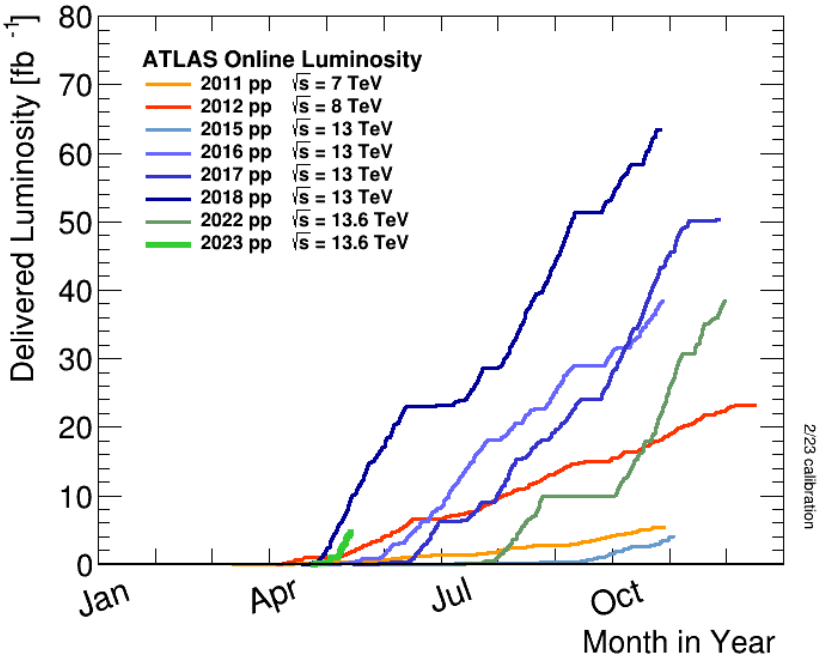

Figure 3.2: The delivered integrated luminosity recorded by the ATLAS experiment as a function of month in the year for each year of LHC operation. The operation period between 2011 and 2023 is displayed, with each year indicated by a different colour. Reproduced from [42].

trigger systems in the calorimeter and muon systems, and a new subsystem known as High Granularity Timing Detector in the forward region [41].

3.2 The ATLAS detector

ATLAS is an abbreviation for A Toroidal LHC ApparatuS, and is the largest volume detector ever built for accelerator-based particle physics. It is a general-purpose detector with the design goal of recording as many physics signatures as possible. The detector components are roughly cylindrical around the LHC beam pipe, and are longitudinally centred on the interaction point. Additionally, the detector components are immersed in magnetic fields generated by a central superconducting solenoid, and three superconducting toroids. A schematic of the detector apparatus is shown in Figure 3.4.

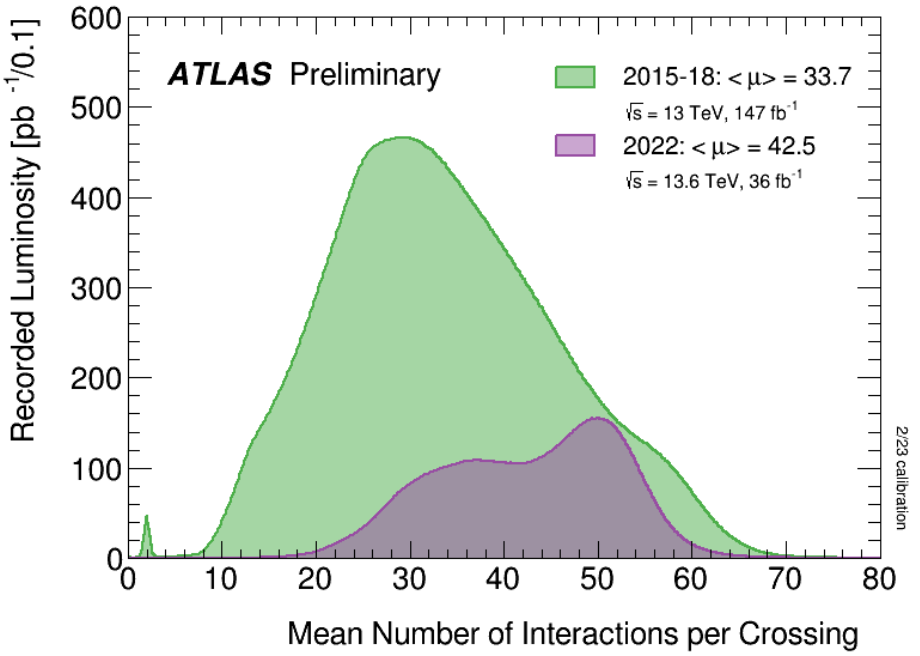

Figure 3.3: The recorded luminosity as a function of average number of interactions per bunch crossing for Run 2 (2015-2018) and Run 3 (2022) of ATLAS data-taking campaigns. Reproduced from [42].

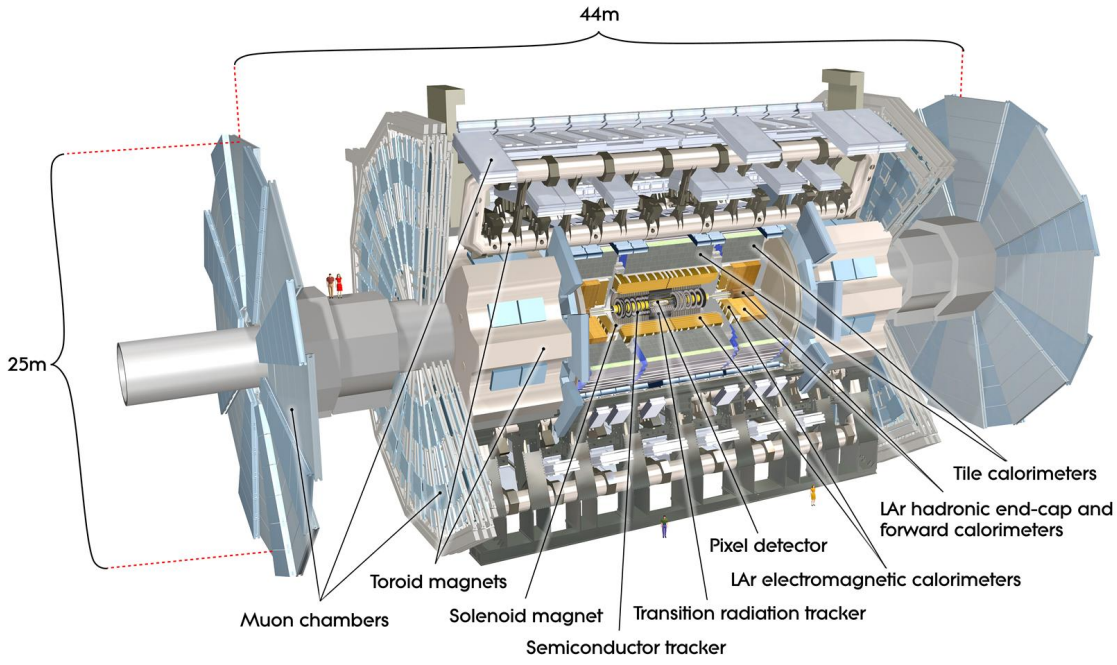

Figure 3.4: A schematic illustration of the ATLAS detector. Reproduced from [43].

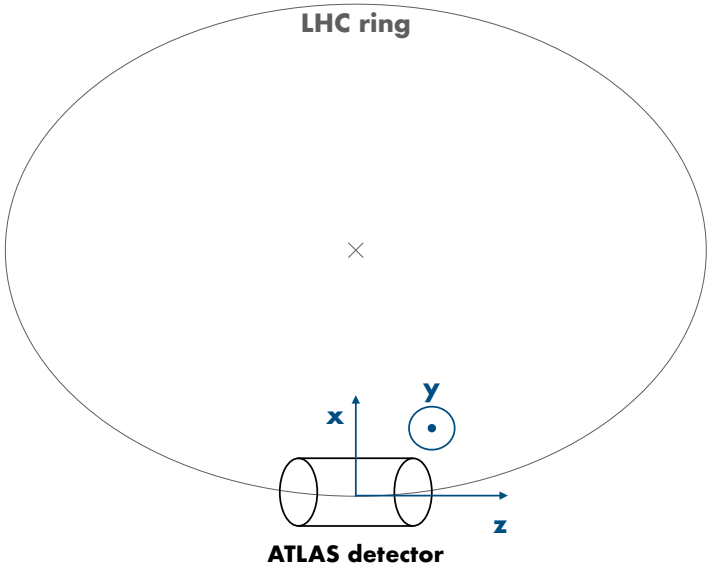

Figure 3.5: The ATLAS coordinate system in relation to the LHC beam line. The origin is the centre of the ATLAS detector. The x-axis points to the centre of the LHC ring, the y-axis vertically upwards, and the z-axis points to the beamline, completing the right-handed coordinate system. The side where z>0 is referred to as the A-side, and the C-side otherwise.

The ATLAS coordinate system

The ATLAS coordinate system in relation to the LHC beamline is shown in Figure 3.5. In this coordinate system, the azimuthal angle ϕ and polar angle θ are defined with respect to the z-axis. In the relativistic limit, pseudorapidity η is preferred over θ,

$$\eta = -\ln(\tan(\frac{\theta}{2})), \tag{3.3}$$

Incorporating these angular definitions, the separation between two particles can then be defined by their pseudorapidity-azimuthal separation ΔR:

$$\Delta R = \sqrt{(\Delta\eta)^2 + (\Delta\phi)^2}, \tag{3.4}$$

In the R-z plane, two additional impact parameters can be defined to describe how close a particle track is to the nominal beamline:

- d_0: transverse impact parameter, the radial distance between the point of the closest approach to the beam axis.
- z_0: longitudinal impact parameter, the z position of the track at the point of closest approach.

The ATLAS sub-detector systems

The main design criteria for the ATLAS detector are:

- High geometric coverage in η and full ϕ coverage, ensure the identification of different physics processes with varied kinematic topology.
- Efficient, high-precision tracking across particle momentum and energy. This is critical for the identification of charged particles in a high pile-up environment with multiple overlapping tracks, in addition to their full reconstruction at low luminosity. Track measurements can also be used in conjunction with measurements in the calorimeter for the identification of long-lived particles.
- Excellent calorimetry for measuring electromagnetic and hadronic activity for neutral and charged particles and for jet identification and reconstruction. Calorimetry also contributes to the measurement of transverse missing energy (E_T^{miss}), an important indicator for neutrinos and other weakly interacting particles.
- Ability to trigger and measure events at low-p_{T} thresholds, thus offering high precision and statistics for most physics processes of interest.

These design goals are addressed by the ATLAS sub-detectors: the Inner Detector (ID), the Electromagnetic calorimeter (ECAL), the Hadronic calorimeter (HCAL), and the muon spectrometer (MS). The detector coverage for each sub-detector, and its trigger system (where available) is shown in Figure 3.6.

The ATLAS system of magnets consists of a solenoid outside the tracker, providing a near uniform 2 T magnetic field along the z-axis for momentum

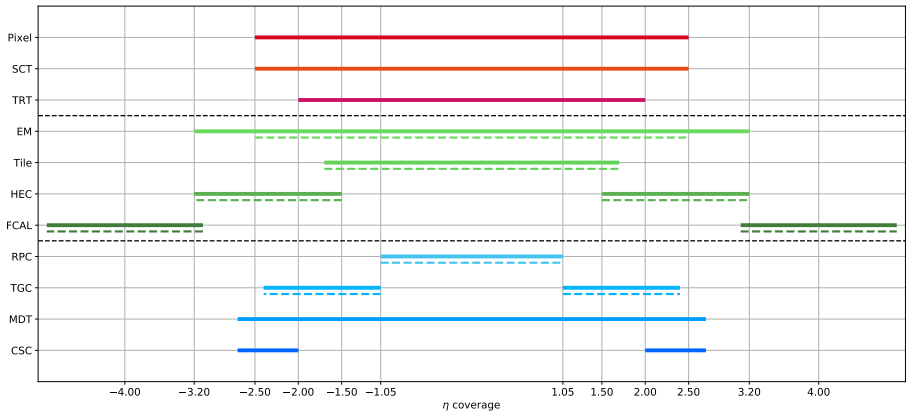

Figure 3.6: The ATLAS detector coverage in η for all sub-detectors. The three main sub-detectors (ID, calorimeters and MS) are separated by black dashed lines. The geometric coverage for each sub-detector is shown in coloured solid lines, while the trigger coverage for each sub-detector system is shown in coloured dashed lines (where applicable). The inner detector components (Pixel, SCT and TRT) are highlighted in red, the calorimeter components (EM, Tile, HEC and FCAL) are highlighted in green, and the muon spectrometer components (RPC, TGC, MDT and CSC) are highlighted in blue.

determinations, and a toroidal magnetic system outside the calorimeters which produces a magnetic field in the azimuthal direction for the muon spectrometer.

3.2.1 The Inner Detector

The Inner Detector (ID) is the closest sub-detector to the LHC beam pipe, and withstands the highest density of particle tracks as a result. Therefore excellent temporal and spatial resolution throughout the detector volume is critical for momentum measurement and vertex identification.

The ID registers the trajectories of charged particles in the solenoidal magnetic field. Charged particles travel in a helical trajectory under the near-uniform solenoidal field at 2 T. The ID registers the particle trajectory through layers of distinct detector modules, and records a series of 'hits' along the track of the particle. The particle charge can be inferred through the direction of track curvature, while the momentum can be measured from the following equation:

$$p_T = \frac{0.3BL^2}{8s}. \tag{3.5}$$

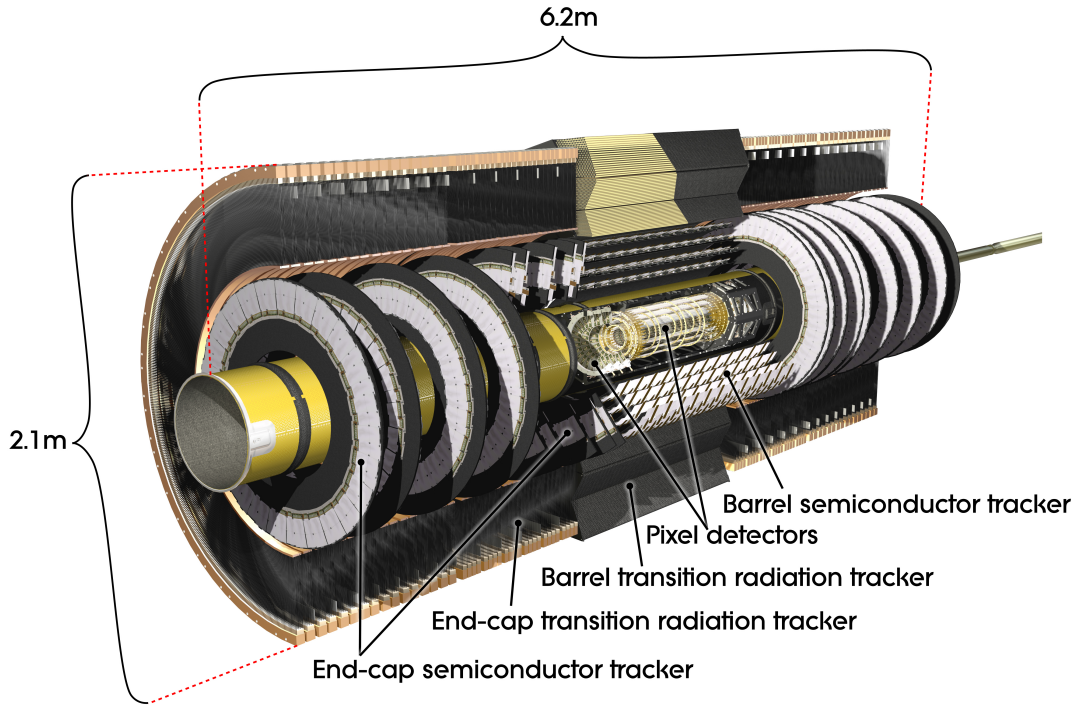

Figure 3.7: A schematic showing the ID components. Reproduced from [43].

In the limit where $L << R$, where L is the length of the tracker, R is the radius of the track, B is the magnetic field strength, and s is sagitta, the maximum perpendicular length between the curvature and the chord [44].

The ID combines three distinct detector technologies to ensure the high-granularity and high number of hits for track reconstruction and particle identification. At the smallest radius, the silicon pixel detector (Pixel) and surrounding it the semiconductor tracker (SCT) provide high precision space points and granularity for vertex reconstruction and precision measurement of the trajectories, while the transition radiation tracker (TRT) offers a large number of hits at larger radius with lower granularity, and hence lower spatial resolution. A schematic diagram of the ID can be seen in Figure 3.7 and 3.8.

- **The Pixel detector** is the inner-most layer of ID, and consists of three layers of silicon pixel detectors with a minimum pixel size of 50 μm $\times$ 400 μm in $r\phi \times z$ over the range of $|\eta| < 2.5$. As charged particles traverse a pixel detector, which is a reverse-biased silicon sensor, electron-hole

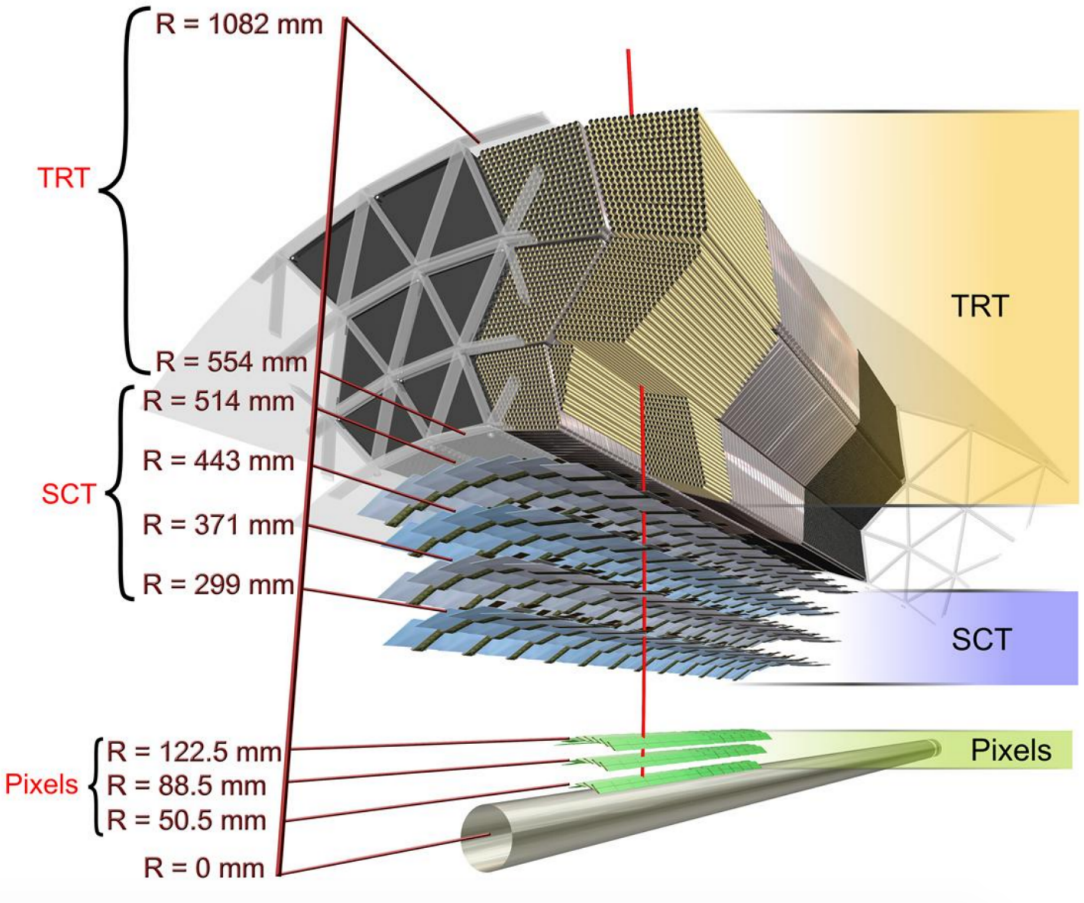

Figure 3.8: A schematic, cross-sectional view of the ATLAS ID barrel. Particle track crossing the ID is shown in red line. Reproduced from [45].

pairs are created. The subsequent collection of these pairs creates an electric signal, indicating the position at a given radius along the trajectory of a charged particle. In the barrel region, the sensors are arranged on concentric cylinders around the beam axis at radii between 50.5 mm and 122.5 mm, and on disks perpendicular to the beamline in the end-cap region, consisting of a total of around 80.4 million readout channels. During the long shutdown of LHC between 2013-2015, an insertible B-layer (IBL) was installed at 33 mm from the IP, the closest layer to the beam line [46]. The typical size of the silicon sensor is 50 μm $\times$ 250 μm in $r\phi \times z$, thereby providing the highest spatial resolution in the tracking system.

- **The SCT** is the intermediate layer of the ID, and consists of eight concentric

layers of silicon-strip detectors that surround the Pixel detector over the range $|\eta| < 2.5$, providing four space points for each track. The strips have a mean pitch of 80 μm, and are arranged perpendicular to the beamline in the barrel, and radially perpendicular to the beamline in the endcap. To measure both coordinates, the neighbouring strips are arranged at a stereo angle of 40 mrad. This results in the intrinsic resolution of 17 μm in $r\phi$, and 580 μm in z. The total number of readout channels in the SCT is approximately 6 million, and provides the second-best spatial resolution.

- **The TRT** is the largest and outer-most layer of the ID, providing a large number of hits (typically 36 per track) using 4 mm straw tubes, with gold plated anode wires at their centre, covering $|\eta| < 2.0$. The straw tubes are filled with a gas mixture of Xenon, carbon dioxide and oxygen, to maximise the capture rate of transition radiation photons, which are emitted from charged particles traversing media with distinct dielectric constants. The straws are parallel to the beamline in the barrel region, and radially in wheels in the endcap. The total number of TRT readout channels is approximately 351,000. Unlike the other sub-detectors of the ID, the TRT does not record the z-position of the hit, and the position resolution is 130 μm in $r\phi$, sufficient to contribute to the momentum resolution. Additionally, the straws are interspersed with hydrocarbon fibres, thus the TRT is able to contribute to electron identification performance through the detection of transition radiation from relativistic charged particles.

3.2.2 Calorimeters

While the Inner Detector aims to measure particle momentum with minimum disruption to the trajectory of the particle, the calorimeter system is designed to measure particle energy by absorbing the energy deposited from all particles that traverse it. With the exception of muons and neutrinos, the calorimeter system provides good containment for all traversed particles. This is crucial for energy

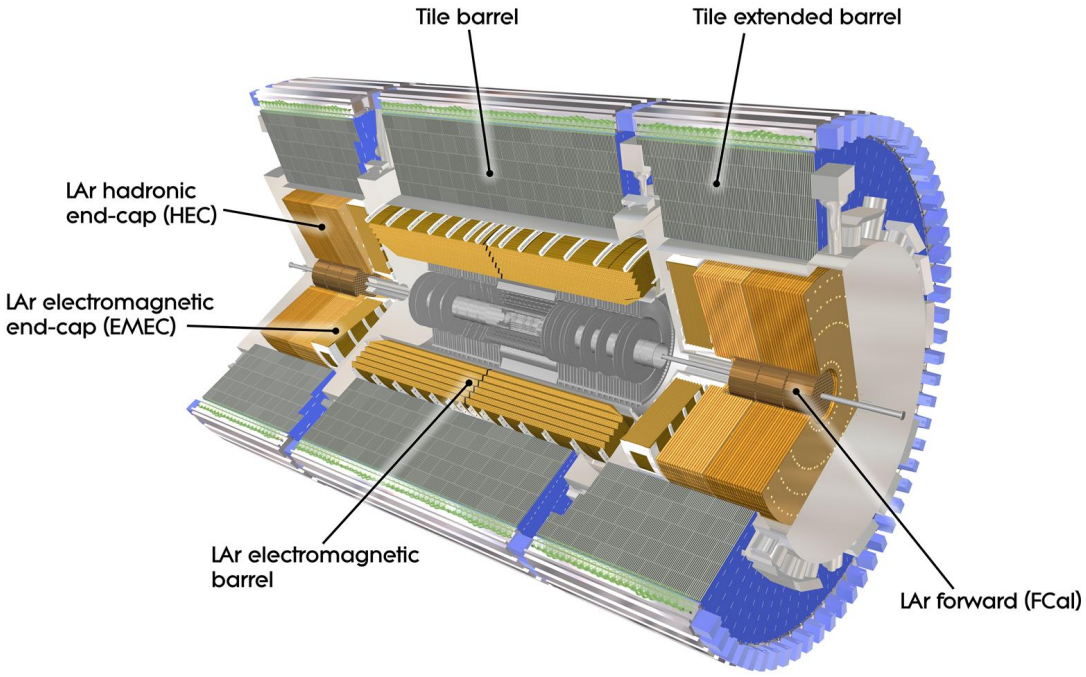

Figure 3.9: A schematic overview of the ATLAS calorimeters. Reproduced from [43].

measurement, while the large detector coverage allows for the measurement of missing transverse momentum.

As a particle interacts with the calorimeter material, it creates a cascade of secondary particles (typically referred to as a shower). As a particle showers, its energy decreases. The distance that a high-energy electron traverses in matter before its energy decreases to $1/e$ of its initial energy is referred to as radiation length, X_0. This occurs through photon conversion and bremsstrahlung. Similarly, the nuclear interaction length (λ) is the mean distance traversed by a hadron before an inelastic nuclear interaction.

Based on the characteristics of showers, the calorimeter system has two sub-detectors: the electromagnetic (ECAL) and the hadronic calorimeter (HCAL). Both calorimeters are sampling calorimeters, meaning that they utilise alternating layers of dense materials (producing showers) and active detecting materials (measuring energy deposits). A schematic diagram is shown in Figure 3.9.

- **The ECAL** is the inner layer of the calorimeter system, covering regions

up to $|\eta| < 3.2$. It consists of the barrel and two endcaps, with a small gap at $z = 0$. It uses lead as the passive material (thanks to its short radiation length), and liquid argon (LAr) cooled to 88 K as the active material. Particles traversing the LAr ionise it, and under the action of an electric field drift towards the electrodes. The collected charge is amplified and is proportional to the initial energy of the charged particles. Overall, a particle traverses 22 X_0 in the barrel, and 24 X_0 in the endcap.

- **The HCAL** is the outer layer of the calorimeter system, covering regions up to $|\eta| < 4.9$. The central region is covered by the **tile** calorimeter, which uses steel and plastic scintillator tiles as the passive and active materials respectively. As a charged particle traverses the plastic scintillator, it produces excitations in the atoms, and results in scintillation photons when the atoms de-excite. This signal is proportional to the initial energy of the charged particle. Wavelength shifting fibers, which are attached to either cell edge, transmit the collected light to the photomultiplier tubes where the signal is amplified and readout. The **hadronic end cap (HEC)** covers high η regions, and uses copper and tungsten as passive material (for hadronic shower), and liquid argon as the active material. Furthermost out in η, the **forward calorimeter (FCAL)** extends the calorimeter coverage to $|\eta| = 4.9$. Similarly, FCAL utilises liquid argon as active material, and the first layer of passive material is copper (efficient heat dissipation), followed by two layers of tungsten. The HCAL provides approximately 11 interaction lengths of hadronic depth.

3.2.3 Muon spectrometer

Similar to the tracker, the muon spectrometer (MS) measures the momentum of muon tracks by measuring their sagitta in a toroidal magnetic field. With most other particles absorbed by the calorimeter system, the MS is capable of identifying and measuring muons in a low-noise environment, while providing

signatures for the underlying physics process of interest. By measuring muon track momentum, MS also completes the measurement of missing energy.

The MS consists of a barrel sector and two endcaps, each immersed in the magnetic field provided by toroidal magnets. In both barrel and endcaps, the MS is arranged in a 16-fold azimuthal segmentation, to follow the 8-fold azimuthal symmetry of the toroidal magnet structure. The segments that are encased in the toroidal magnets are colloquially referred to as the Large Sectors, and Small Sectors otherwise. Unlike the solenoidal field for the ID, the toroidal magnet system bends the particle trajectory in the $R - z$ plane. At $|\eta| < 2.7$, monitored drift tubes (MDTs) and cathode strip chambers (CSCs) provide at least three precision positional measurements. The very central region $|\eta| < 0.1$, is reserved for cooling and service cables, for which complementary measurements from the calorimeter systems are required to identify and reconstruct muons. Within $|\eta| < 2.4$, the trackers are also complemented with resistive plate chambers (RPCs) in the barrel and thin-gap chambers (TGCs) in the endcaps for triggering events of interest. An overview of the MS is shown in Figure 3.10.

- **The MDT** chambers consist of several layers of aluminium drift tubes for positional reconstruction covering $|\eta| < 2.7$. The drift tubes in the MDT operate on the same principle as the drift tubes in the TRT, ionised electrons are collected at a central tungsten-rhenium wire operating at a 3080 V. The tubes are filled with an argon-carbon dioxide gas mixture at high pressure. Each drift tube in the MDT is able to achieve a spatial resolution of 80 μm, corresponding to 16% accuracy for a muon with $p_{\mathrm{T}} = 1$ TeV. Additionally, as each MDT chamber consists of 3-8 layers of drift tubes, it is possible to register multiple hit information for the transversed particle, and this enables an axial position resolution of 35 μm. Spatial accuracy for the MDT is therefore crucial for track reconstruction, and an optical system is installed in place to measure and account for the change in muon chamber positions in real-time. Due to the long drift time compared to the 25 ns

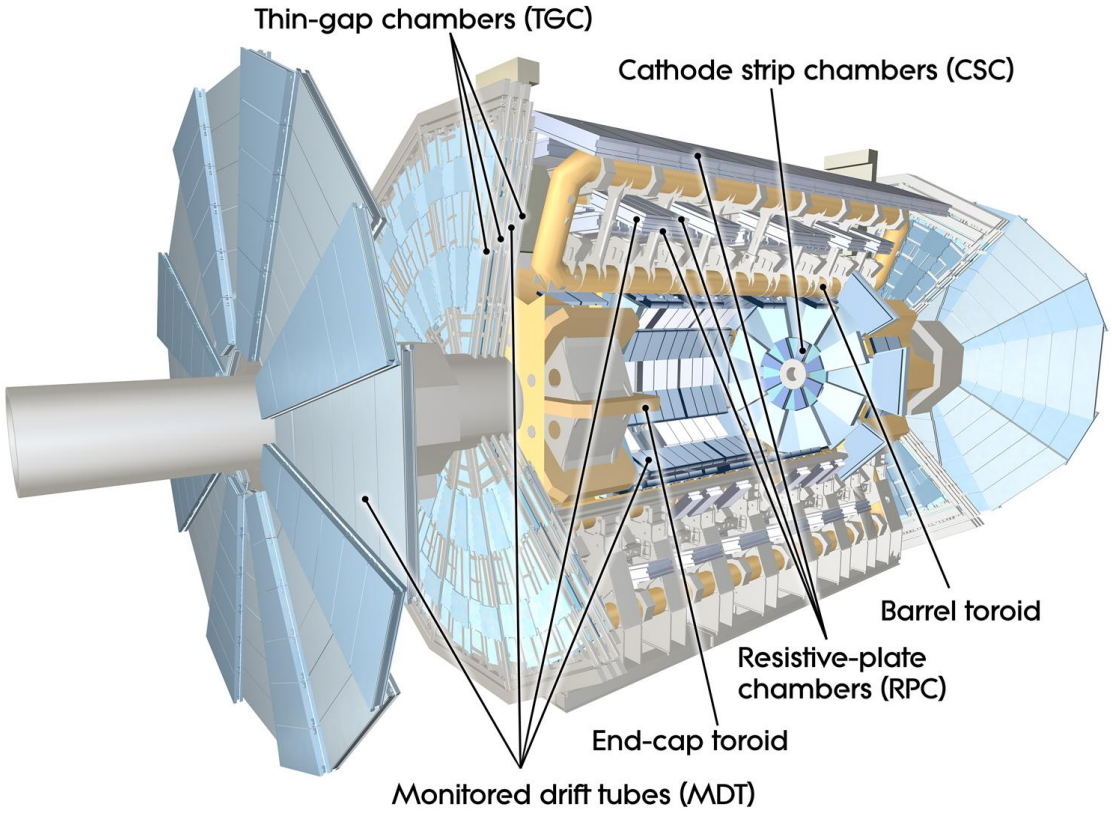

Figure 3.10: A schematic overview of the ATLAS muon spectrometers. Reproduced from [43].

interval between bunch crossings, the CSCs and the trigger chambers are used to resolve ambiguities.

- **The CSCs** are multi-wire proportional chambers that cover $2.0 < |\eta| < 2.7$ to account for the high particle flux in the forward region. They use an array of wires (anodes) operating at 1900 V that are arranged in the radial direction, and two sets of cathode strips, one running parallel to, and the other one perpendicular to the anodes to provide a two-dimensional coordinate. Each CSC is filled with an argon-carbon dioxide gas mixture, and a transversing ionising particle emits ionising radiation, which results in a cascade in ionisation particles (commonly referred to as an avalanche) due to the high electric field across the chamber. The position of the track is obtained by interpolating the charges induced on neighbouring

cathode strips. It provides an excellent time resolution of 7 ns, and a spatial resolution of 60 μm in the bending plane and 4 mm in ϕ.

- **The RPC** is a three-layer gaseous detector covering $|\eta| < 1.05$. It is a gaseous parallel electrode-plate detector, and two resistive plates are kept parallel to each other at a distance of 2 mm, which is filled with an insulating gas mixture. Ionising tracks traversing the RPC form avalanches in the high electric field (4.9 kV/mm) between the two resistive plates, and the signals are read out on the outer faces of the resistive plates. The signal response is produced within 25 ns, but with a reduced spatial resolution of 10 mm in the z direction, and an ϕ resolution of 10 mm.

- **The TGCs** are multi-wire proportional chambers used in the endcaps for $1.05 > |\eta| > 2.4$ and have a similar signal response time to the RPCs. The TGCs operate under the same principle as the CSCs, but with a different geometry (smaller wire-to-cathode distance than wire-to-wire distance), a different gas mixture and a higher operating voltage (2900 V) than the CSC. These factors suppress the formation of secondary avalanches (which is crucial for high-rate environments), and provide a better time resolution. They achieve a spatial resolution of 2-6 mm in the R direction and a ϕ resolution of 7 mm.

3.2.4 Trigger system

As discussed in Section 3.1, the proton-proton bunches cross each other at an interval of 25 ns, translating to a frequency of 40 MHz. This sharply contrasts with the target event record rate of ≈1 kHz, which is limited by the available computational resources. The trigger and data acquisition system is therefore crucial for the operation and physics analyses of the ATLAS experiment. It makes real-time decisions on whether a given collision should be recorded, reduces event rate, and preserves events that may contain physics of interest.

A two-tiered approach is adopted for the ATLAS trigger system: the Level 1 (L1) trigger and the High-Level Trigger (HLT) system. The L1 trigger system is a hardware-based trigger system, and the relevant detector sub-system and detector coverage are seen in Figure 3.6. It utilises custom electronics and information with reduced granularity to first identify candidates for photon, electron, jet and muon, and to select events based on event-level quantities, such as total energy in the calorimeter and the multiplicity of a certain object. The L1 trigger system reduces the event rate from 40 MHz to 100 kHz [47].

The HLT system is a software-based system, which utilises fast trigger algorithms for early rejection. This is followed by full reconstruction algorithms, similar to those used for offline analysis for the final selection. Partial, or full information from the detector is used to reconstruct physics objects. This further reduces the event rate to an average of 1 kHz, and the events that pass the HLT selection criteria are sent to permanent storage for offline reconstruction [48].

Trigger chains are developed to select events with physics of interest. Each chain is designed to select a set of physics signatures, such as leptons, photons, jets, particle lifetimes, total energy and missing energy. To control the rate of accepted events, a prescale value is applied to reduce the number of accepted events. The value of the prescale corresponds to the inverse of the probability that an event is accepted. In the case when the prescale for a trigger chain is 1, all events passing the trigger chain are stored, and this trigger chain is referred to as an *unprescaled* trigger [49].

Trigger chains are separated into two groups, or *streams*. The main physics stream covers all signatures relevant to ATLAS physics analyses, and occupies the bulk of the trigger rate at an average of 1.0 kHz. A separate dedicated stream covers muons with lower transverse momentum, which is essential for the B-physics program [49].

3.2.5 The ATLAS Monte Carlo simulation

The Monte Carlo simulation is a crucial part of both the ATLAS experiment and its physics programs. It is used widely for the design, development, implementation and validation of identification, reconstruction and calibration algorithms, and to evaluate their performance. For physics programs, the MC simulations are widely used to evaluate experimental sensitivity, and to estimate the impact of statistical and systematic uncertainties.

The MC events are first generated with the calculation of matrix element amplitudes and scattering processes. A plethora of external software and libraries are available, and examples include Powheg [50–52] and Sherpa [53]. Parton showering, hadronisation, and the simulation of the underlying event are simulated by Pythia [54]. The simulation of interaction of particles with the ATLAS detector, the digitisation of the detector response, and any changes in detector condition are handled by the Athena framework [55, 56], and utilises Geant4 simulation [57–59].

To simulate pile-up in normal ATLAS operation, randomised events are read-in, and their hits are overlaid to simulate detector response in a busy environment. As the pile-up profile is not generally known at the time of MC generation, the MC events are subsequently reweighted to match the pile-up distribution.

Chapter 4

Muons in the ATLAS experiment

Upon the discovery of muons in 1936, Isidor Isaac Rabi famously remarked: *'Who ordered that?'*, echoing the surprise that he, as well as his contemporaries, experienced on the seemingly ad-hoc nature of this new particle. Decades later, while a flourishing theoretical framework seeks to address the origin of lepton flavours [60, 61], experimental particle physicists of today offer a set of pragmatic answers. Muons are ingrained in many facets of ATLAS operations and studies: as signatures for event triggers, as backgrounds to be vetoed, or as final states for many ATLAS analyses.

Unlike the cloud chamber observation that led to Rabi's exclamation, the ATLAS experiment cannot observe the entire muon trajectory within the fiducial volume. Instead, it combines hit and energy deposit information that is spatially well-separated from the trackers, calorimeters, and the muon spectrometer to reconstruct the muon trajectory. These muons then satisfy a set of identification criteria, which define different levels of purity, and systematic uncertainty, for a wide range of ATLAS physics analyses. To satisfy the level of precision required by physics measurements and beyond SM searches, it is critical to calibrate the reconstructed muon kinematics (most notably the transverse momentum) in simulation to that in data. This agreement between data and simulation is also necessary for muon reconstruction efficiency, vertex association efficiency, and isolation variables, and relevant calibrations are derived for these quantities as well.

This chapter offers an overview of muon combined performance in the ATLAS experiment, with a strong focus on the muon momentum calibration for ATLAS Run 2 data. Section 4.1 offers a technical overview of how muons are reconstructed from measurements in ATLAS sub-detectors, and introduces the quantities used for the rest of this thesis. Section 4.2 describes the process of identifying muons produced at the interaction point, and differentiating against fake muons from secondary decays. Lastly, Section 4.3 focuses on muon momentum calibration including charge-dependent and charge-independent effects.

4.1 Reconstruction

As a minimum-ionising particle, muons leave the following signatures in the ATLAS detector: the presence of ID and MS tracks, and characteristic energy deposits in the calorimeters. Due to modest energy resolution in the calorimeters, tracks from the ID and MS detectors (wherever available) are used for muon reconstruction. Due to the high interaction lengths of the calorimeters (minimum of 26.9 X_0 for ECAL and approximately 10 X_0 for HCAL), the hadronic punch-through in the muon system is negligible.

In the ID, all charged particle tracks are reconstructed indiscriminately. First, information from the Pixel and SCT are converted into 3-dimensional space points. A set of space points form a 'seed', with varying requirements on the silicon layers [62]. These seeds are then used to build 'roads', for which additional hits are found by moving towards the outer edge of the ID. This provides a crude estimate of track parameters (explained below). Additional steps, including extrapolating hits to the TRT using a Kalman filter [1], and a final fit with all hits are required to obtain the final track parameters [64].

Track qualities are then evaluated using a number of criteria, such as χ^2 of the track fit, and if the track is measured at every layer of the detector at the

[1] The Kalman filter processes a series of discrete measurements subjected to statistical uncertainties. By combining the hits measured from the Pixel sub-detector and subsequent measurements in the TRT, the Kalman filter minimises the statistical uncertainties on the trajectory [63]

location it is expected to traverse. High-quality tracks with $p_{\mathrm{T}} > 400$ MeV and other additional requirements [39] are used to reconstruct the primary vertex. This is divided into two stages: vertex finding and fitting. Once the primary vertex of the event is determined, it is then associated to tracks, allowing for the computation of five track parameters and their covariance matrices. These track parameters include two impact parameters (d_0 and z_0, the shortest distance between track and beamline, and the difference in z coordinate between track and primary vertex), two angular parameters (θ and ϕ, the polar angle and the azimuthal angle respectively), and measurement of charge over momentum (q/p). A schematic illustration of d_0 and z_0 is shown in Figure 4.1.

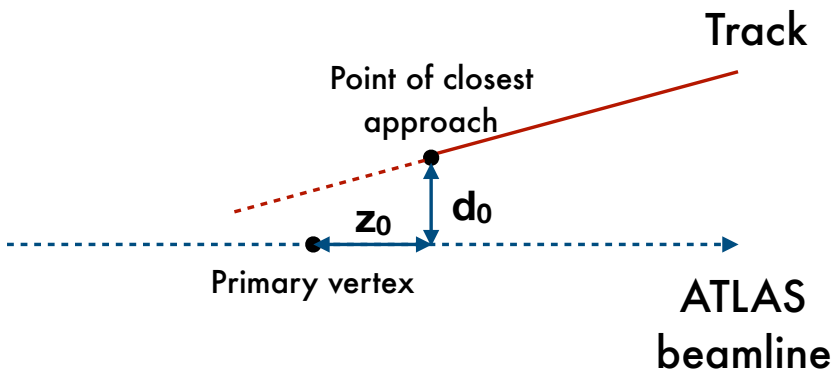

Figure 4.1: A schematic illustration of the two impact parameters, d_0 and z_0. The transverse impact parameter, d_0, is the shortest distance between the track and the beamline. The longitudinal impact parameter, z_0, is the difference in z coordinate between the primary vertex and the point of closest approach.

In the MS, hits in each station are identified as 'segments' through a Hough transform [65]. Combining measurements orthogonal to the bending plane (from the RPC and TGC), segments in different MDT and CSC stations are then constructed into three-dimensional track candidates, for which loose constraints on the IP and magnetic field bending are imposed. An iterative global χ^2 fit is then performed in three steps. First, the muon trajectory is constrained by the magnetic field, material interaction, and the misalignment of all detector chambers. Hits with a large contribution to global χ^2 are then removed from the following

fits, and the second iteration is performed to remove overlaps between tracks. A final iteration is performed for backward extrapolation to the beamline, such that a loose IP constraint and energy loss in the calorimeters can be accounted for.

With information from each sub-detector, five reconstruction strategies are developed, leading to the corresponding muon *types*. A schematic of these muon types is shown in Figure 4.2, and they are described in the following:

- Combined (CB) muons are reconstructed by associating MS tracks to associated ID tracks, then performing a combined track fit using ID and MS hits, with constraints on the energy loss in the calorimeters. This is the most common type of muons used in most ATLAS analyses. At $|\eta| > 2.5$, MS tracks can also be combined with segments reconstructed in the pixel and SCT endcap detectors to increase ID coverage. These are referred to as Silicon-Forward (SiF) muons.

- Inside-out (IO) combined muons are reconstructed using an inside-out algorithm. For IO muons, ID tracks are extrapolated to the MS to search for at least three hits that are loosely aligned. The ID track, calorimeter energy deposit, and the MS hits are then combined into IO muons. Since this type of muon does not rely on the presence of a reconstructed MS track, IO muons recover some efficiency in regions of low MS coverage, and for low p_{T} muons.

- Muon-spectrometer Extrapolated (ME) muons use a complementary approach to the IO muons, it extrapolates the MS track to the beamline. These muons are used in cases where MS tracks cannot be matched to an ID track, thus fully exploiting the MS coverage up to $|\eta| = 2.7$.

- Segment-tagged (ST) muons are similar to IO muons, but impose a looser constraint on the number of MS segments. ST muons extrapolate ID tracks to the MS, and impose tight angular matching requirements to at least one MS segment. The ST muon type provides sensitivity for muons in regions with limited MS coverage, such as $|\eta| < 0.1$.

- Lastly, the calorimeter-tagged (CT) muons are identified by extrapolating the ID tracks to the calorimeter to search for energy deposits that are consistent with a muon. Similar to ST muon, the CT muon type is mainly used for regions with limited MS coverage, such as the wiring and service region at $|\eta| < 0.1$.

Overlaps between different muons are defined by the available MS segments, and the order of precedence starts with CB muons, followed by IO muons, then ST muons, and finally CT muons. The overlap with ME muons is resolved by selecting tracks with better fit quality and a larger number of hits.

A schematic representation of these muon types is shown in Figure 4.2

4.2 Identification

Defining muon types ensures that muons can be reconstructed throughout the detector acceptance. However, they are not indicators of the origin of these muons, such as whether they originated from a short-lived SM or BSM particle (prompt), or a secondary decay of a hadron or a long-lived BSM particle (non-prompt). Therefore a set of requirements, referred to as a *working point* (WP), is defined to suit the requirements of a wide variety of ATLAS physics analyses. Two sets of separate WP definitions are used to distinguish prompt muons: the *selection* WPs target the rejection of non-prompt muons from light hadron decays by analysing the quality of muon tracks, while the *isolation* WPs target the rejection of non-prompt muons from b and c quark decays, which produces good quality muon tracks, but can be distinguished using information from the calorimeter and location of the primary vertex.

4.2.1 Selection working points

The selection working points (WPs) are optimised for two metrics: maximising prompt muon efficiency and minimising the light-hadron misidentification rate. The former refers to the probability that a prompt muon is reconstructed as a

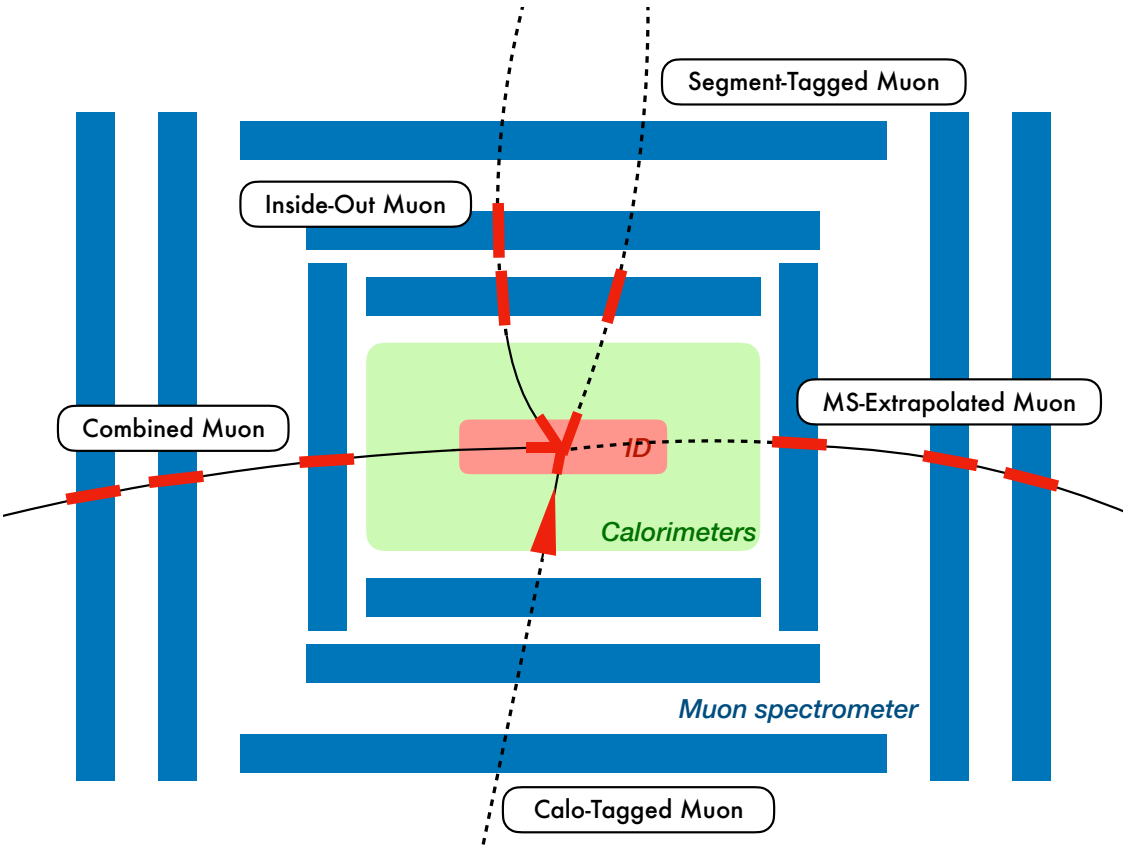

Figure 4.2: Schematic diagram for the different types of muon reconstruction chains. This illustrates a cross-section along the beamline for the ATLAS detector, with the Inner Detector (light red), Calorimeters (light green) and Muon Spectrometers (blue) labelled in the diagram. The solenoid and toroid systems are omitted from the diagram. The solid lines represent the muon tracks reconstructed in the sub-detector, the red segments represent the hits (or energy deposits in the case of calorimeter) being registered in the sub-detector, and dotted lines in a sub-detector represent that this particular muon type does not rely on the information in that sub-detector.

muon and passes the WP selection criteria, while the latter is the fraction of light hadrons reconstructed as muons that pass the WP selection criteria. Light hadron decays generally lead to lower-quality muon tracks due to in-flight decay, therefore a number of variables are defined to exploit this feature to maximise the prompt muon efficiency. These include detector level quantities (the number of *precision stations*, defined as the number of MS stations that a muon has at least three hits in the MDT or CSC; the number of *precision hole stations* [2], the number of stations that a muon has less than three hits, and is missing at least

[2]Here, a *hole* refers to an active sensor traversed by the track that contains no hit and is between two layers with hits assigned to the track.

three expected hits), as well as track variables reconstructed from the ID and MS sub-detectors. One such quantity is the q/p compatibility:

$$q/p \text{ compatibility} = \frac{|q/p_{\text{ID}} - q/p_{\text{MS}}|}{\sqrt{\sigma^2(q/p_{\text{ID}}) - \sigma^2(q/p_{\text{MS}})}}, \tag{4.1}$$

where q/p_{ID} and q/p_{MS} are the measurements of charge over momentum in the ID and MS respectively, and $\sigma(q/p_{\text{ID}})$ and $\sigma(q/p_{\text{MS}})$ are their corresponding uncertainties. For CB and IO muons, q/p compatibility is useful as it corresponds to the compatibility between the ID and MS measurements. Similarly, another quantity $\rho^{'}$, is defined as follows:

$$\rho^{'} = \frac{|p_{\text{T,ID}} - p_{\text{T,MS}}|}{p_{\text{T,CB}}}, \tag{4.2}$$

where $p_{\text{T,ID}}$, $p_{\text{T,MS}}$ and $p_{\text{T,CB}}$ correspond to the muon p_{T} measured in the ID, MS, and from the combined track fit respectively. The energy loss when muon traverses the calorimeter systems is accounted for in $p_{\text{T,MS}}$. Based on these quantities, three cut-based WPs are defined in order of least to most stringent: *Loose*, *Medium* and *Tight*. The *Loose* WP has the highest prompt muon efficiency with less purity and larger systematic uncertainties (hereinafter denoted by systematics), and is optimal for the reconstruction of Higgs boson decays into four-leptons. The *Medium* WP balances prompt muon efficiency and purity while keeping systematics small, and is suitable for a wide range of ATLAS analyses. Finally, the *Tight* WP provides the highest purity at the cost of prompt muon efficiency, and is therefore used for analyses that are limited by backgrounds from non-prompt muons. The selection criteria for these WPs are summarised as follows:

- *Medium* WP: within $|\eta| < 2.5$ (ID acceptance region), only CB and IO muons are included. They are required to have a q/p compatibility smaller than seven for a loose agreement between ID and MS measurements. In addition, these muons are required to have at least two precision stations, except for the very central region with cabling and limited MS coverage ($|\eta| < 0.1$). For these central muons, a looser requirement is imposed (one precision

station, and at most one precision hole station). For muons outside of the ID coverage, ME and SiF muons are used, and are required to have at least three precision layers.

- *Loose* WP: all muons passing the *Medium* WP are accepted. Additionally, CT and ST muons are used within $|\eta| < 0.1$ to recover the efficiency in the MS gap region. The *loose* WP also aims to recover lost efficiency for low-p_{T} muons ($p_{\mathrm{T}} < 7$ GeV), which lose most of their energy when traversing the calorimeter, therefore significantly reducing their likelihood of having two precision stations. This loss of efficiency for low-p_{T} muons is recovered by loosening the requirement for the number of precision stations to one for IO muons within $|\eta| < 1.3$, provided they are independently reconstructed as ST muons to increase their purity.

- *Tight* WP: all CB and IO muons are required to have at least two precision stations. The normalised χ^2 is required to be less than eight to reject in-flight hadronic decays. Further requirements are placed on q/p compatibility and $\rho^{'}$ to reject low-p_{T} muons.

Two WPs are defined for analyses targeting extreme p_{T} ranges: the *High-*p_T and *Low-*p_T WP. As the name suggests, the *High-*p_T WP is optimised for muons with $p_{\mathrm{T}} > 100$ GeV, and provides the best momentum resolution and rejection of tracks with large track uncertainties. The *Low-*p_T WP targets muons with p_{T} down to 3 GeV, which are less likely to be reconstructed as full tracks in the MS. It uses a set of detector and track-based variables that provides good separation between prompt muons and light-hadron decays.

The fraction of prompt muons that are reconstructed and identified is referred to as the reconstruction efficiency, and it varies in p_{T} and detector regions for both data and simulation. The efficiencies for *Loose*, *Medium*, and *Tight* as a function of p_{T} and η can be found in Figure 4.3. The reconstruction efficiency is generally different between data and simulation due to the simulated detector geometry not perfectly describing the real detector geometry, inaccuracies in

magnetic field modelling and energy loss. These discrepancies are resolved by applying correction weights, or scale factors (SF) to simulation, such that the efficiencies match up between simulation and data in regions of p_{T}, η and ϕ. With the application of SF, the muons are suitable to be used in ATLAS physics analyses. The efficiency SF for a particular algorithm X is defined as:

$$\mathrm{SF}(X) = \frac{\epsilon^{\mathrm{Data}}(X)}{\epsilon^{\mathrm{MC}}(X)}, \tag{4.3}$$

where $\epsilon^{\mathrm{Data}}(X)$ and $\epsilon^{\mathrm{MC}}(X)$ corresponds to the efficiencies in data and simulation for reconstruction algorithm X. As the efficiency in data cannot be measured directly, an alternative method utilises the high purity of $Z \to \mu\mu$ and $J/\psi \to \mu\mu$ decays, and estimates the reconstruction efficiency in both data and simulation within an ID coverage of $|\eta| < 2.5$. This is referred to as the tag-and-probe method. The *tag*, referring to one leg of the muon pair, is required to satisfy stringent identification criteria. This is done such that the second muon, the *probe*, can be reliably identified as another muon candidate (since the invariant mass between the *tag* and *probe* is consistent with originating from a $Z \to \mu\mu$ or $J/\psi \to \mu\mu$ decay), and can be used to test the efficiency of a reconstruction algorithm. At regions outside of ID acceptance, a separate double-ratio method is used to estimate reconstruction SF [66].

4.2.2 Isolation working points

Isolation WPs target the separation between prompt and non-prompt muons from in-flight decays from hadrons, τ leptons, or heavy quarks. This is performed by measuring the hadronic activity in the vicinity of muons. This can be measured either in the ID (using ID track related variables), in the calorimeter (using topological cell clusters), or through the combination of the two (using a particle flow algorithm).

Track-based isolation is defined as the scalar sum of p_{T} inside a cone of radius ΔR around the muon, excluding the muon track itself, where $\Delta R = \min(R, 10\ \mathrm{GeV}/p_T^{\mu})$, $R = \sqrt{\delta\eta^2 + \delta\phi^2}$, and $\delta\eta$ and $\delta\phi$ are the magnitudes of the

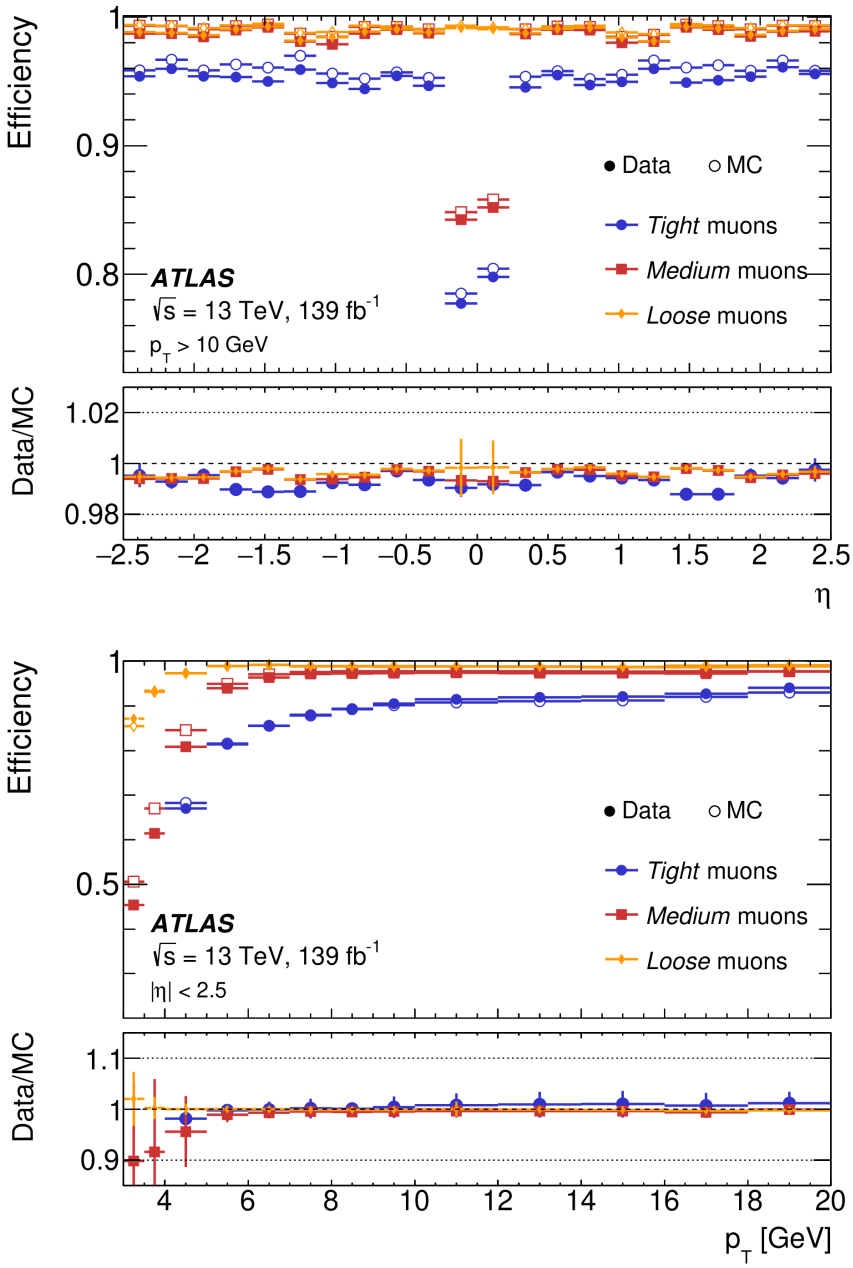

Figure 4.3: Muon identification efficiency for *Loose* (yellow), *Medium* (red) and *Tight* (blue) WPs. The identification efficiency is measured for events passing trigger requirements. The measured efficiency in data is plotted in solid markers, and in hollow markers for simulated efficiency. The upper plot shows the muon identification efficiencies measured in $Z \to \mu\mu$ events as a function of η, using muons with $p_{\mathrm{T}} > 10$ GeV. The lower plot shows the muon identification efficiencies measured in $J/\psi \to \mu\mu$ events as a function of p_{T}. Each plot displays a ratio plot at the bottom, which shows the ratio between measured and simulated efficiencies for each WP, and the corresponding statistical and systematic uncertainties. Reproduced from [66].

the differences of pseudorapidity and azimuthal angle between the reconstructed muon and the ID track. Depending on the WPs, ΔR is either 0.2 (referred to as p_T^{cone20}), or min(10 GeV/p_T^{μ}, 0.3) (labelled as $p_T^{\text{varcone30}}$). In the latter case, the cone size is chosen to vary with p_{T}^{μ} for highly boosted systems. The minimum track p_{T} used in the isolation WP is either 500 MeV or 1 GeV.

Similarly, calorimeter-based isolation ($E_T^{\text{topocone20}}$) is defined as the transverse energy of topological cell clusters in a cone of size $\Delta R = 0.2$, after subtracting muon energy deposits in the calorimeter and pileup effects. While track-based variables are constrained by the track constraint on its primary vertex, calorimeter-based isolation is much more sensitive to pile-up, and results in degraded energy resolution. Therefore, combining track-based and calorimeter-based isolation is often used, such that the former provides reduced pileup dependency and better momentum resolution, and the latter offers sensitivity to neutral particles and low p_{T} muons. For this purpose, a particle-flow-based algorithm is introduced to remove overlaps between track-based and calorimeter-based isolation.

The particle-flow-based isolation variable is defined as the sum of track-based isolation (using $p_T^{\text{varcone30}}30$ for $p_{\text{T}}^{\mu} < 50$ GeV and p_T^{cone20} for $p_{\text{T}}^{\mu} > 50$ GeV), in addition to the transverse energy of a neutral particle-flow object in a $\Delta R = 0.2$ cone, which is labelled as E_T^{neflow20}. The distributions for these variables for prompt and non-prompt muons are shown in Figure 4.4.

A multivariate discriminant, *prompt lepton BDT*, is also developed to achieve the highest rejection rate of non-prompt muons. It utilises track and calorimeter information, as well as computed likelihoods of a muon originating from a b-hadron decay [67]. The definitions of the isolation WPs are summarised in Table 4.1, and the efficiencies of the loose WPs are shown in Figure 4.5.

4.3 Muon p_{T} correction

The ATLAS simulation provides an accurate but idealised description of the geometry and material distribution for the detector and the toroids. The simulation does not account for detector deformations, local inhomogeneity

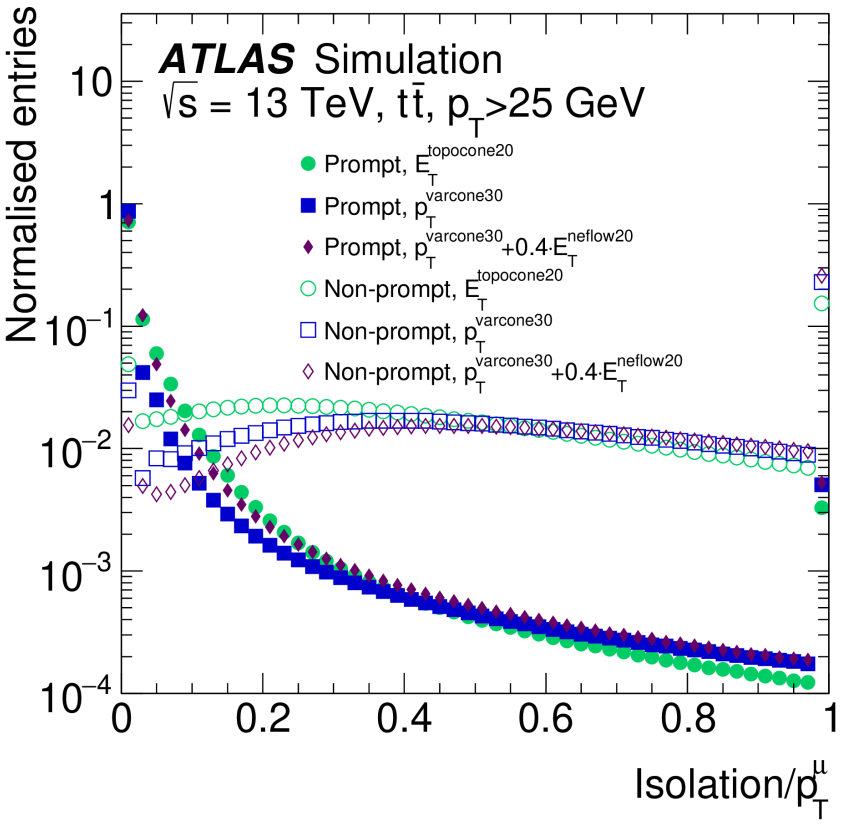

Figure 4.4: Distribution of track-based ($p_T^{\text{varcone30}}$, in blue square markers), calorimeter-based ($E_T^{\text{topocoe20}}$, in green circular markers) and particle-flow-based ($p_T^{\text{varcone30}} + 0.4E_T^{\text{neflow20}}$, in purple diamond markers) variables, after dividing their value by the muon p_{T}. The prompt muon isolation distribution is shown in closed markers, and the non-prompt muon isolation distribution is shown in open markers. These distributions are measured from simulated $t\bar{t}$ events, and each is normalised to unit area. Reproduced from [66].

of the magnetic field and differences in the amount of detector material in the simulation and detector, and inaccuracies in physics modelling. Therefore, additional calibrations are needed to achieve per-mille level precision for the muon momentum scale, and percent level precision for muon momentum resolution.

Such calibration is derived in a two-fold process. The charge-dependent bias, known as sagitta bias, is derived and corrected for in data events. Subsequently, charge-independent corrections for scale and resolution are derived with simulated events.

Isolation WP	Definition
*PflowLoose**	$(p_T^{\text{cone20}} + 0.4 \cdot E_T^{\text{neflow20}}) < 0.16 \cdot p_{\text{T}}^{\mu}$
*PflowTight**	$(p_T^{\text{cone20}} + 0.4 \cdot E_T^{\text{neflow20}}) < 0.045 \cdot p_{\text{T}}^{\mu}$
*Loose**	$p_T^{\text{varcone30}} < 0.15 \cdot p_{\text{T}}^{\mu}$, $E_T^{\text{topocone20}} < 0.3 \cdot p_{\text{T}}^{\mu}$
*Tight**	$p_T^{\text{varcone30}} < 0.04 \cdot p_{\text{T}}^{\mu}$, $E_T^{\text{topocone20}} < 0.15 \cdot p_{\text{T}}^{\mu}$
HighPtTrackOnly	$p_T^{\text{cone20}} < 1.25$ GeV
*TightTrackOnly**	$p_T^{\text{varcone30}} < 0.06$ GeV
PLBDTLoose (PLBDTTight)	$p_T^{\text{varcone30}} < \max(1.8 \text{ GeV}, 0.15 \cdot p_{\text{T}}^{\mu})$
	BDT cut to mimic *TightTrackOnly* efficiency

Table 4.1: Definitions of the muon isolation WPs. The name of the WP is listed in the first column, and the isolation criteria are listed in the second column. The minimum p_{T} required for all WPs are 1 GeV except for *PflowLoose* and *PflowTight* WP, for which the minimum p_{T} requirement is 500 MeV. WPs marked with * have two variations in the definition of ΔR: one with constant $\Delta R = 0.2$ for $p_{\text{T}}^{\mu} > 50$ GeV, and the other with ΔR decreasing with p_{T} as $\min(10 \text{ GeV}/p_T^{\mu}, 0.3)$.

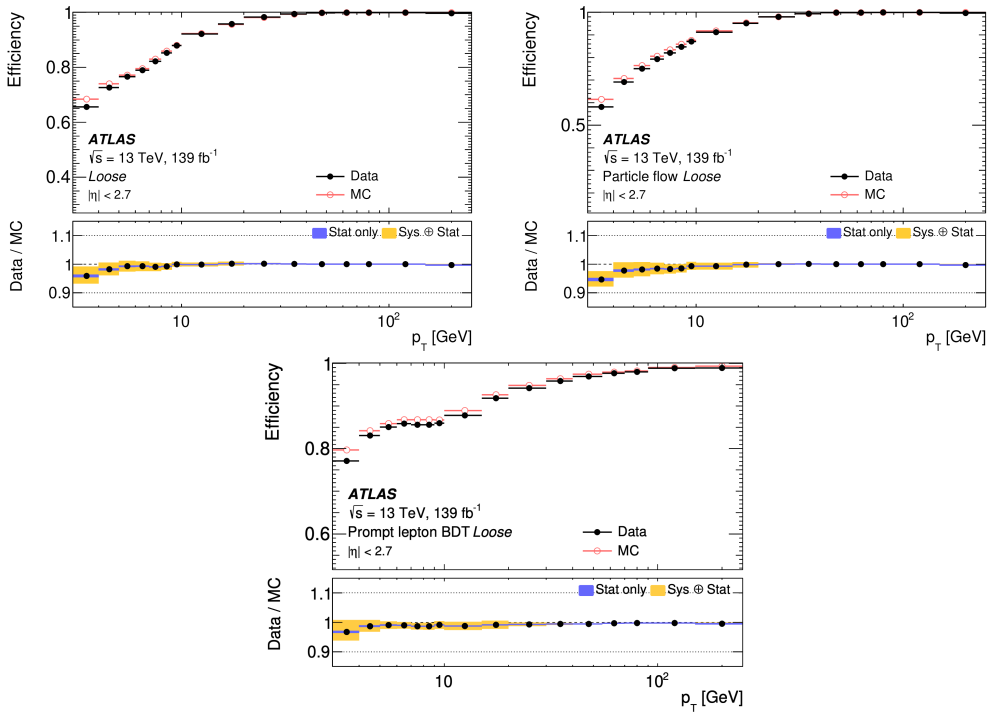

Figure 4.5: Muon isolation efficiency for *Loose* (top left), *PflowLoose* (top right) and *PLBDTLoose* (bottom) WPs as a function of muon p_{T}. The identification efficiency measured in data is represented by black markers, and the simulated efficiency is represented by hollow red markers. These efficiencies are measured in $Z \to \mu\mu$ events, using muons with $p_{\text{T}} > 3$ GeV and $|\eta| < 2.7$. The bottom panel shows the ratio between measured efficiency and simulated efficiency, with statistical and systematic uncertainties indicated by the error bars. Reproduced from [66].

4.3.1 Data and simulation samples

The sagitta bias correction utilises the $Z \to \mu\mu$ decay to measure the charge-dependent momentum bias, while the scale and resolution correction uses both $Z \to \mu\mu$ and $J/\psi \to \mu\mu$ peaks to study behaviour across ranges of p_{T}. Both types of corrections are validated on $Z \to \mu\mu$, $J/\psi \to \mu\mu$ and $\Upsilon \to \mu\mu$ peaks. This section describes the data and simulation sample used to derive these calibrations.

Data sample

This analysis utilises the pp collision sample collected between 2015-2018. Only events collected under stable beam conditions, with all relevant ATLAS sub-systems fully operational are used in this analysis. A combination of single-muon triggers (dedicated to $Z \to \mu\mu$ collection) and specialised triggers for $J/\psi \to \mu\mu$ and $\Upsilon \to \mu\mu$ are used. A dedicated stream for B-physics was deployed in 2016 due to the increased LHC instantaneous luminosity, such that abundant low-p_{T} events can be reconstructed at a later time after reconstructing the main physics stream. This additional stream greatly increased the $J/\psi \to \mu\mu$ and $\Upsilon \to \mu\mu$ statistics available for 2016-2018. The integrated luminosity is 139 fb^{-1} after trigger and data quality requirements, with an average pile-up per bunch crossing of 33.7.

Simulated samples

For the signal samples, the following resonances are considered: $Z \to \mu\mu$, $J/\psi \to \mu\mu$, $\Psi(2S) \to \mu\mu$, and $\Upsilon \to \mu\mu$ (where Υ represents $\Upsilon(1S)$, $\Upsilon(2S)$ and $\Upsilon(3S)$). To increase the number of events, additional selection criteria are imposed. $J/\psi \to \mu\mu$ events require at least one muon to have $p_{\mathrm{T}} > 6$ GeV and $|\eta| < 2.5$, while $\Upsilon \to \mu\mu$ events require both muons to have $p_{\mathrm{T}} > 4$ GeV and $|\eta| < 2.7$. Alternative samples of $Z \to \mu\mu$ are used to evaluate the impact of generator mismodelling. The generators used for the simulated backgrounds are listed in Table 4.2.

Table 4.2: Description of the simulated resonances. The resonance process is defined in the first column, with the Monte Carlo generators, the parton distribution functions (PDFs) and the accuracy for the calculations listed in the following columns.

Process	Generator	PDF	Fixed order accuracy
$Z \to \mu\mu$	POWHEG-BOX v1 [50–52, 68] , interfaced to Pythia 8.186 with AZNLO [69]	CT10nlo [70]	NLO
$Z \to \mu\mu$ (alternative)	Sherpa 2.2.1 [53]	NNPDF3.0nnlo [71]	NNLO
$J/\psi \to \mu\mu$	Pythia 8.186	CTEQ6L1 with A14 generator parameters [72]	LO
$\Psi(2S) \to \mu\mu$ $\Upsilon \to \mu\mu$	Pythia 8.186	CTEQ6L1	LO

The main background for the low-p_{T} resonances is the combinatorial background from other physics processes. This is challenging to simulate and is therefore estimated from an exponential fit to the data. For $Z \to \mu\mu$ decays, the main backgrounds are a Z boson decaying to a τ ($Z \to \tau\tau$), fakes from muonic decay of the W boson ($W \to \mu\nu$), Drell-Yan production ($Z^*/\gamma^*(\to \mu\mu)$), diboson productions (VV), and top-pair production ($t\bar{t}$). The generators used for the simulated backgrounds are listed in Table 4.3.

Specific to the scale and resolution corrections, a large data/simulation discrepancy in the reconstructed kinematics of the Z p_{T} is observed. As the effect of single muon p_{T} mismodelling is at the per-mille level, the dimuon p_{T} discrepancies are the results of theoretical and PDF modelling uncertainty.

The effects of Z p_{T} mismodelling also differ for each generator. To correct for this effect, 2D maps of Z η and p_{T} are derived for Pythia+POWHEG, Sherpa and MadGraph. Additional weights are interpolated from 2D maps and assigned for each event. The effect of Z p_{T} mismodelling on kinematic distributions, and the effect of applying Z p_{T} corrections are shown in Figure 4.6.

Table 4.3: Description of the background processes for $Z \to \mu\mu$. The process is defined in the first column, with the Monte Carlo generators and parton distribution functions (PDFs) listed in the following columns. Note that the $t\bar{t}$ background has the h_{damp} parameter set to 1.5 m_{top} [73]. The h_{damp} parameter is a re-summation damping factor and one of the parameters that effectively regulates high-p_{T} radiation against which the $t\bar{t}$ system recoils.

Process	Generator	PDF
$Z \to \tau\tau$, $W \to \mu\nu$, $Z^*/\gamma^*(\to \mu\mu)$	POWHEG-BOX v1, interfaced to Pythia 8.186 with AZNLO	CT10nlo
$Z \to \tau\tau$, $W \to \mu\nu$, $Z^*/\gamma^*(\to \mu\mu)$	POWHEG-BOX v1, interfaced to Pythia 8.186 with AZNLO	CT10nlo
VV	POWHEG-BOX v2 [74], interfaced to Pythia 8.210 with AZNLO	CT10nlo
$t\bar{t}$	POWHEG-BOX v2 [50–52, 75], interfaced to Pythia 8.210 with A14	NNPDF3.0nlo [71]

4.3.2 Sagitta bias correction

Dedicated detector alignment by the ATLAS experiment removes the bulk of charge-dependent bias, but a residual bias persists. This residual effect results in biases in the worsened p_{T} resolution, leading to a degradation of the invariant mass resolution in the Higgs to four-lepton final state. Therefore, an additional correction is developed for muon tracks to capture such charge-dependent effects, and is referred to as the *sagitta bias correction*.

Sub-detector alignment

Accurate knowledge of detector geometry is critical to improving the resolution of reconstructed track parameters, and by extension, physical observables. Systematic and periodic detector alignment studies are therefore performed to ensure its mechanical and temporal stability.

The ID alignment is based on global χ^2 minimisation of the track-hit residuals [76]. Additional constraints on the IP and track parameters measured from external

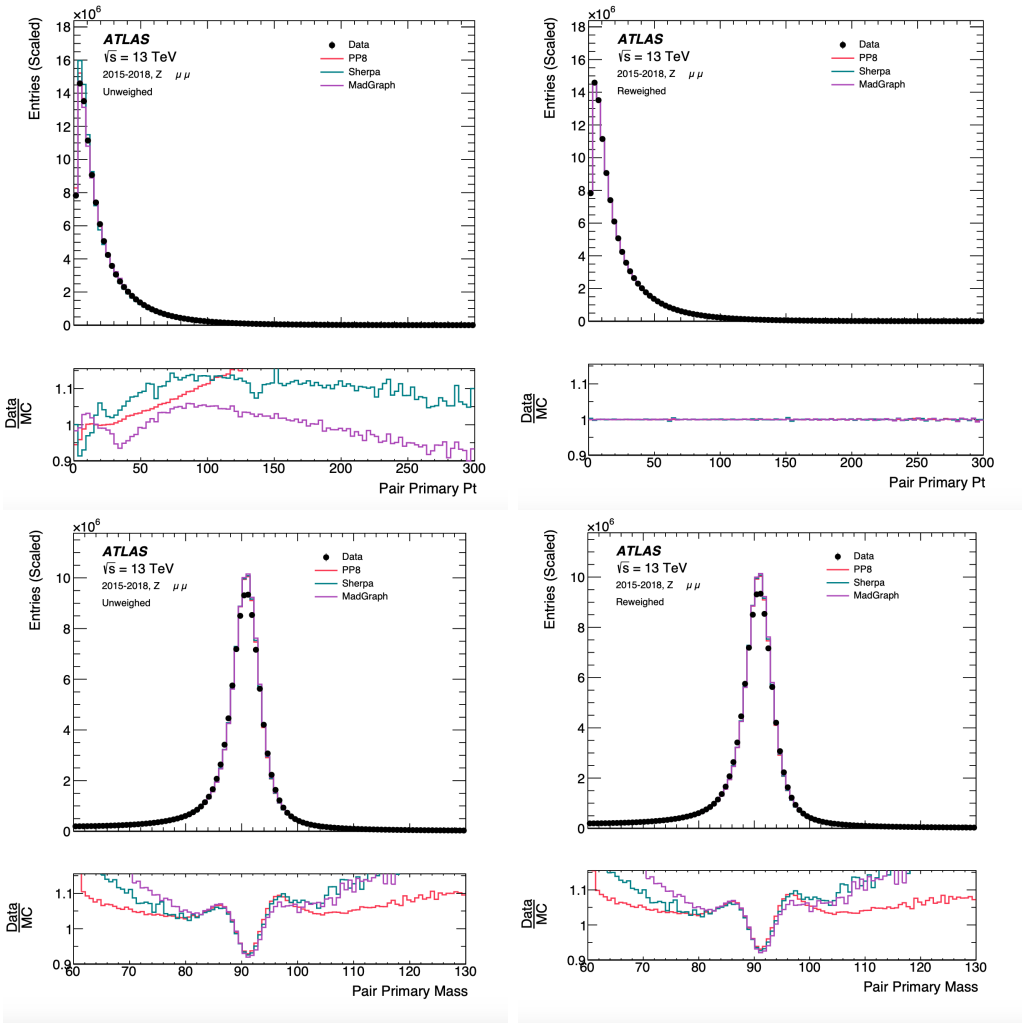

Figure 4.6: Distributions of data and simulated $Z \to \mu\mu$ pair p_{T} (first row) and invariant mass distributions (second row) before (first column) and after (second column) kinematic reweighting for three generators. Samples generated with POWHEG-BOX interfaced with PYTHIA are represented by red lines. Samples generated with SHERPA and MADGRAPH are shown in green and purple respectively. The kinematic weight is derived from the pair p_{T} ratio between data and each simulated sample, and interpolated based on the pair p_{T} of each event.

sub-detectors are imposed to reduce systematic biases. However, this procedure is insensitive to a number of biases, including radial detector deformation and ill-defined alignment solutions in the alignment software. These effects are collectively referred to as *weak modes*, which leaves the global χ^2 invariant.

The MS alignment utilises its optical monitoring system to correct for the 3D movements of muon chambers relative to other muon chambers and reference markers. The accuracy of the optical alignment is limited by operational accuracy

and construction precision. Additional dedicated data collection runs are also used to improve the MS alignment, including cosmic-ray events, and proton-proton collision events with the toroidal field off. This leads to precision at the $\mathcal{O}(10\ \mu\text{m})$ for the bulk of the detector, and $\mathcal{O}(100\ \mu\text{m})$ in specific detector regions.

Deriving sagitta bias

These detector effects are largely independent, therefore sagitta bias corrections are derived separately for ID, CB and MS muon tracks. Additionally, sagitta bias is derived for each ATLAS data-taking period to be combined with the yearly released alignment parameters. The sagitta bias is approximated as:

$$\frac{q}{\hat{p}} = \frac{q}{p} + q \times \delta_s, \tag{4.4}$$

where q is the charge of the muon, p and $\hat{p}$ are the corrected and uncorrected muon momentum respectively, and δ_s (shorthand for $\delta_s(\eta, \phi)$) is the impact of sagitta mismodelling on track momentum, measured in units of TeV^{-1}. To estimate this bias, $Z \to \mu\mu$ events are used for its precise modelling. The invariant mass, $m_{\mu\mu}$ of the dimuon system is expressed as the following:

$$m_{\mu\mu}^2 = 2p_T^+ p_T^-(\text{cosh}(\Delta\eta) - \text{cos}(\Delta\phi)), \tag{4.5}$$

where p_T^+ and p_T^- refer to the transverse momenta of positively and negatively charged muons respectively, and $\Delta\eta$ and $\Delta\phi$ are the differences between the pseudorapidity and the azimuthal angle of the two muons. Ignoring second order terms in δ_s, the biased invariant mass, $\hat{m}_{\mu\mu}$ can obtained by combining Equation 4.4 and 4.5, yielding the following parametrisation:

$$m_{\mu\mu}^2 = \hat{m}_{\mu\mu}(1 + \delta_s p_\text{T}^+ - \delta_s p_\text{T}^-). \tag{4.6}$$

As the number of positive muons equates to the number of negative muons in Z decays, the overall effect of δ_s cancels out, leaving $< m_{\mu\mu} >$ unaffected, but broadens the resolution of the $Z \to \mu\mu$ mass peak. Therefore, the variance of the $Z \to \mu\mu$ mass peak is sensitive to the sagitta bias.

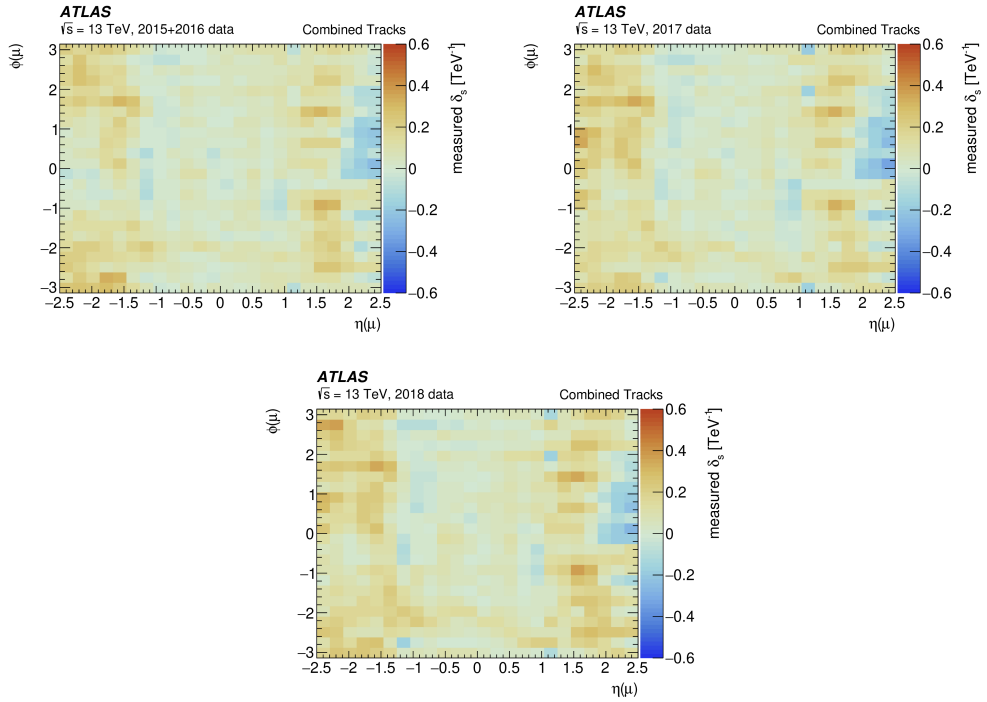

Figure 4.7: Sagitta bias on the CB muon p_{T} measured in bins of η and ϕ before applying sagitta bias correction. The biases are shown separately for the three data-taking periods: years 2015 and 2016 (upper left), 2017 (upper right), and 2018 (bottom). Large bias is observed in the region of $\eta \approx 2.5$ and $0 < \phi < 2.0$. The distribution of measured sagitta bias is similar in different years of data-taking. The bias is defined in Equation (4.4).

The sagitta bias is evaluated by minimising the variance of the $Z \to \mu\mu$ mass peak in a grid of 24×24 $\eta - \phi$ detector regions. An iterative method is used, and the sagitta bias correction δ_s derived from the previous iterations is applied to the muon p_{T} for the next iteration. The residual sagitta bias before and after correction for different data-taking campaigns are shown in Figure 4.7 and 4.8.

The typical values of sagitta bias are around $\mathcal{O}(0.1)$ TeV^{-1} in the barrel region. The iterative method terminates after the residual sagitta bias in each region is less than $\mathcal{O}(10^{-3})$ TeV^{-1}.

The systematic uncertainties associated with the non-closure of the fit procedure are estimated by two methods. The first method injects the residual δ_s in the last iteration back to simulation, which has perfectly aligned geometry. The difference in p_{T} before and after the bias is then taken as a systematic uncertainty. In the second method, the systematic related to the fit procedure is

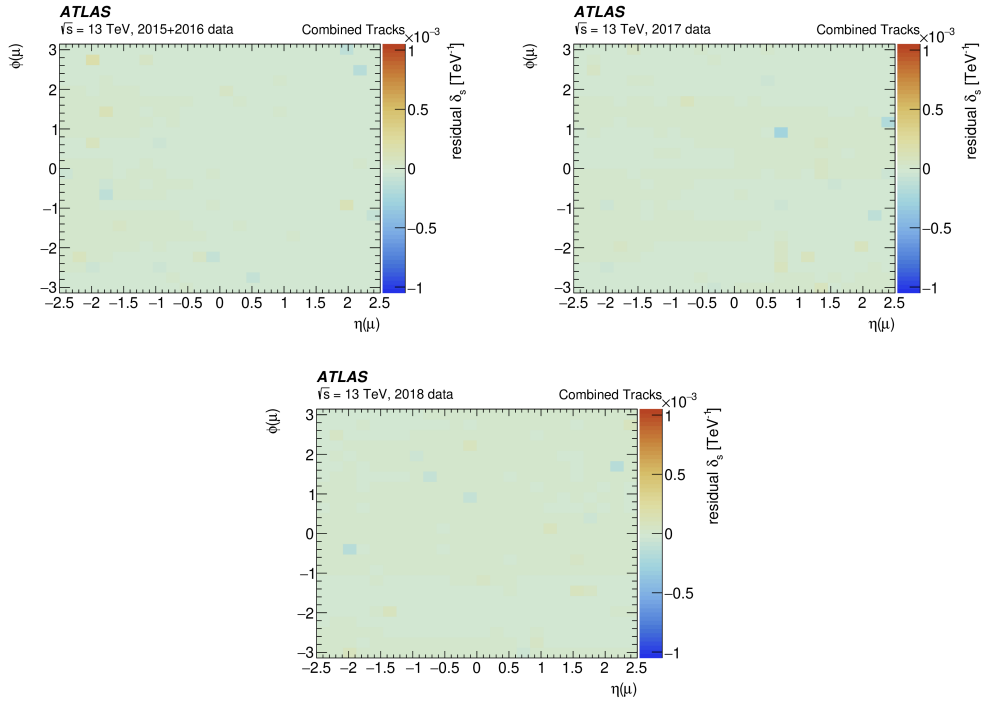

Figure 4.8: Residual sagitta bias on the CB muon p_T measured in bins of η and ϕ after applying sagitta bias correction. The biases are shown separately for the three data-taking periods: years 2015 and 2016 (upper left), 2017 (upper right), and 2018 (bottom). The bias is defined in Equation (4.4). The average residual bias are $\mathcal{O}(10^{-4})$ TeV^{-1}.

estimated by injecting a known set of sagitta bias to perfectly aligned simulated events. The fitted sagitta bias from the biased events is then compared to the injected bias, and the difference is then taken as the source of systematic bias. The two methods are consistent for a full range of injected biases, and the larger systematic between the two methods is taken as the fit uncertainty. These non-closures are of the order of $\mathcal{O}(0.02)$ TeV^{-1}, with precise values region dependent.

The second source of uncertainty originates from extrapolating from the Z peak decay muons to the high p_T (up to 450 GeV) and high η (up to $|\eta| < 2.7$) regions due to a lack of sufficient $Z \to \mu\mu$ decays in data. To account for this effect, the difference between measured sagitta bias in data and simulation in bins of p_T and η are assigned as systematic uncertainties. Additionally, sagitta bias is not extrapolated for events with dimuon mass above 450 GeV, and a non-closure uncertainty (similar to the one described above) is applied, resulting

in an uncertainty of up to $\mathcal{O}(0.4)$ TeV^{-1}.

4.3.3 Scale and resolution calibration

After the charge-dependent bias correction is applied to data, the muon momentum scale and resolution calibration is determined in simulation. This is the procedure to correct the p_{T} of the MC simulated events to precisely reproduce the characteristics of the muon momentum reconstructed in experimental data, specifically from the di-muon decays of the $Z \to \mu\mu$ and $J/\psi \to \mu\mu$ resonances.

$Z \to \mu\mu$ decays are used for the p_{T} scale and resolution extraction as they provide an abundant source of muons at intermediate momenta, i.e. p_{T} ∼20-100 GeV. As discussed in Section 4.3.1, generator-level Z p_{T} mismodelling, which is the result of theoretical and PDF modelling uncertainty is corrected in the simulation. Z p_{T} mismodelling is irrelevant to the detector deformities and physics mismodelling in muon reconstruction.

The $J/\psi \to \mu\mu$ decay events are also used to derive the scale and resolution corrections for several reasons. First, J/ψ mesons are abundantly produced at the LHC, leading to more than 1.3 billion reconstructed $J/\psi \to \mu\mu$ events with muons of transverse momentum above 5 GeV in 2015-2018 data. These events represent a very clean sample of muons with a relatively low background, and with momentum in the region complementary to the one covered by $Z \to \mu\mu$ decays. Furthermore, J/ψ mesons are boosted, and consequently the distance between the muons in the η–φ plane is small. The invariant mass of these pairs can be used to detect local imperfections such as magnetic field mismodelling, as well as the mismodelling of the intrinsic resolution of the ATLAS sub-detectors. Independent calibrations are derived for ID and MS muons and their combination (CB muons), as they are sensitive to distinct detector and magnetic field mismodelling.

The following parametrisation for the corrected transverse momentum, p_T^{Cor},

is used to derive correction parameters:

$$p_T^{Cor,Det} = \frac{p_T^{MC,Det} + \sum_{n=0}^{1} \Delta s_n^{Det}(\eta,\phi)(p_T^{MC,Det})^n}{1 + \sum_{m=1}^{2} \Delta r_m^{Det}(\eta,\phi)(p_T^{MC,Det})^{m-1} g_m}, \tag{4.7}$$

where the $\Delta s_n^{Det}(\eta,\phi)$ and $\Delta r_n^{Det}(\eta,\phi)$ are scale and resolution correction terms with different p_T dependencies, and g_m is a normally distributed random variable with zero mean and unit width. Each calibration parameter is derived in specific $\eta-\phi$ regions, where detector types and material are comparatively homogeneous. All corrections are divided into 18 η regions. Additionally, two ϕ bins are divided for CB and MS calibration to separate the small and large sectors.

The numerator of Equation 4.7 describes the mismodelling of the muon momentum scales. The $\Delta s_0^{Det}(\eta,\phi)$ term accounts for the inaccuracy in energy loss modelling between the IP and the material traversed by the muon. Due to the negligible energy loss between the IP and the ID, $\Delta s_0^{ID}(\eta,\phi)$ is set to zero. The $\Delta s_1^{Det}(\eta,\phi)$ term then accounts for the inaccuracy in the magnetic field integral and the dimension of the detector in the direction perpendicular to the magnetic field.

The denominator of Equation 4.7 describes mismodelling of the muon p_T resolution, $\frac{\sigma(p_\mathrm{T})}{p_\mathrm{T}}$. This is parameterized by the quadratic sum of three terms [77, 78]:

$$\frac{\sigma(p_\mathrm{T})}{p_\mathrm{T}} = r_0/p_\mathrm{T} \oplus r_1 \oplus r_2 \cdot p_\mathrm{T}, \tag{4.8}$$

with each term accounting for a physics effect influencing the experimental resolution as follows:

- r_0: fluctuations of the energy loss in the traversed material,
- r_1: multiple scattering and any other effects of angular deviation along the muon trajectory,
- r_2: intrinsic resolution mismodelling caused by the spatial resolution of the hit measurements and by any residual misalignment between sub-detectors.

Equation 4.8 is expected to be valid in a wide range of p_{T}, from $\mathcal{O}(1)$ GeV to $\mathcal{O}(1)$ TeV. Similar to the scale correction terms, $\Delta r_0^{ID}(\eta, \phi)$ is set to zero due to the negligible impact of energy loss in the traversed material. For the MS correction, $\Delta r_2^{MS}(\eta, \phi)$ is set to the alignment parameters determined from dedicated runs, such as the cosmic-ray, toroid-off [79] and alignment [80] data, as no charge-dependent effects were included in the simulation.

Derivation of calibration parameters

When extracting calibration parameters, muons are assigned to η–ϕ regions of fit (ROFs). The calibration parameters are then obtained from the dimuon mass spectrum through a χ^2 minimisation fit. In addition, dimuon mass spectra are divided based on muon momenta to increase the sensitivity to p_{T} dependent correction effects. For $J/\psi \to \mu\mu$ decays, the fit is performed in two categories defined by the subleading muon transverse momentum: $6.25 < p_{\mathrm{T}}^{\mathrm{Det,sublead}} < 9$ GeV and $p_{\mathrm{T}}^{\mathrm{Det,sublead}} > 9$ GeV. Similarly for the Z, the two categories are defined by the leading muon transverse momentum: $20 < p_{\mathrm{T}}^{\mathrm{Det,lead}} < 50$ GeV and $p_{\mathrm{T}}^{\mathrm{Det,lead}} > 50$ GeV.

The templates for $m_{\mu\mu}^{\mathrm{Det}}$ for $J/\psi \to \mu\mu$ and $Z \to \mu\mu$ are built using simulated samples. Firstly, the background contribution in each template is estimated. For $Z \to \mu\mu$ templates, a small background component (approximately 0.1%) is extracted from simulation and added to the templates. A much larger (up to 15%) non-resonant background from decays of light and heavy hadrons and from continuum Drell–Yan production is present for events selected in the $J/\psi \to \mu\mu$ channel, which is estimated with a data-driven approach due to the difficulty in simulating a large number of processes with the correct weights. The dimuon invariant mass distribution in data is fit in each ROF using a Crystal Ball function [81] convolved with an exponential background distribution. This background model is then combined with the simulated signal templates used in the fit.

A multi-iteration fitting procedure is performed to estimate the scale and resolution parameters. The fitting procedure begins with a coarse detector region

definition for six $|\eta|$ regions, and uses increasingly granular region definitions at later iterations. The finest region definition includes 18 η regions for ID fits. For CB and MS calibrations, the small and large sectors of the MS are studied separately to isolate any effects in overlaps between different sectors. This results in a splitting in ϕ, referred to as the two-fold ϕ splitting. To estimate the scale and smearing parameters, a multi-stage procedure is used. A two-step random walk minimisation is first performed where the parameters are sampled within a specified range. The parameter configuration that leads to the best agreement for the invariant mass distribution between simulation and data is kept. In the first step, the best agreement is defined by a simplified metric, high level χ^2 (referred to as HL χ^2), where the compatibility between the means and standard deviations of the distributions is compared. In the second step, a binned χ^2 is computed that compares the dimuon mass spectrum in simulation to that of data. Around this best-agreement parameter configuration, signal templates are then generated at discrete intervals and interpolated using moment morphing [82]. Using this signal model, a full minimisation using the binned χ^2 is performed. This procedure is iteratively repeated, where the second muon outside the ROF definition is calibrated using results from the previous iteration, until the change of each parameter stays within the root mean square of its values as estimated from the last five iterations. A comparison between the uncorrected and the corrected dimuon mass peak can be seen in Figure 4.9. The definition of the regions is given in the Table 4.4.

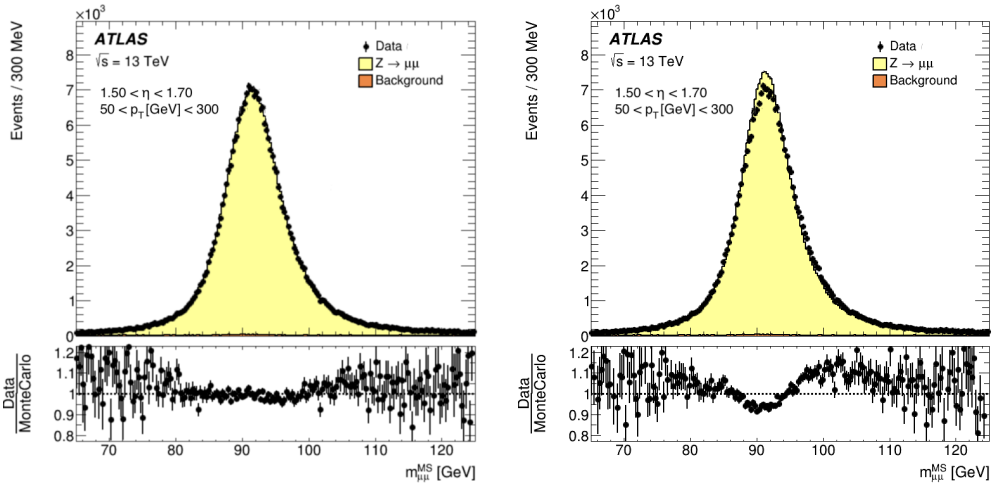

Figure 4.9: Dimuon mass distributions before (left) and after (right) correction in selected kinematic regions for 2017 data-taking period. The leading muon in the dimuon pair is required to have $1.5 < \eta < 1.7$, and $50 < p_{\mathrm{T}} < 300$ GeV. The top panel shows the dimuon mass distribution in data and in simulation, and the bottom panel shows the ratio between data and simulation, with statistic error displayed in error bars.

The calibration parameters obtained from the fits to the data are summarised in Tables 4.5, 4.6, and 4.7, and are averaged over the three η regions. The statistical and systematic uncertainties are summed in quadrature, with the systematic uncertainties dominating the total uncertainty. All sources of uncertainties are evaluated by varying the parameters of the template fit. The higher uncertainty for Δr_1^{ID} in the second bin is associated with the region of the ID with the largest amount of material, corresponding to the transition between the barrel and endcap region sub-detectors. The increase in uncertainty as a function of $|\eta|$ for s_1^{ID} is due to the decrease of the magnetic field integral of the solenoid as a function of $|\eta|$. The larger uncertainties for some of the MS terms in the $1.05 \leq |\eta| < 2.0$ region are associated with the low bending power of the magnet system of the MS in part of that region.

Systematic uncertainties on the correction terms were obtained by repeating the ID, CB and MS fits with variations of the fit procedure at different iterations. The main contributions to systematic uncertainties are:

- J/ψ only and Z only fit: the correction fit is repeated using only the $J/\psi \to \mu\mu$ or $Z \to \mu\mu$ event candidates. Because of the limited statistical

Table 4.4: The region definitions for the scale and resolution fit. Note that for the MS and CB fit, a two-fold split in ϕ between large and small sectors is adopted for the Final region definition, thus increasing the number of regions to 36.

Iteration	Regions	$\|\eta\|$ Min	$\|\eta\|$ Max
Initial regions	Region 1	0.00	0.40
	Region 2	0.40	0.80
	Region 3	0.80	1.25
	Region 4	1.25	1.70
	Region 5	1.70	2.00
	Region 6	2.00	2.60
Intermediate regions	Region1	0.00	0.40
	Region2	0.40	0.80
	Region3	0.80	1.05
	Region4	1.05	1.25
	Region5	1.25	1.50
	Region6	1.50	1.70
	Region7	1.70	2.00
	Region8	2.00	2.30
	Region9	2.30	2.60
Final regions	Region 1	0.00	0.40
	Region 2	-0.40	0.00
	Region 3	0.40	0.80
	Region 4	-0.80	-0.40
	Region 5	0.80	1.05
	Region 6	-1.05	-0.80
	Region 7	1.05	1.25
	Region 8	-1.25	-1.05
	Region 9	1.25	1.50
	Region 10	-1.50	-1.25
	Region 11	1.50	1.70
	Region 12	-1.70	-1.50
	Region 13	1.70	2.00
	Region 14	-2.00	-1.70
	Region 15	2.00	2.30
	Region 16	-2.30	-2.00
	Region 17	2.30	2.60
	Region 18	-2.60	-2.30

power of this configuration, only the Δs_1 parameter is left free in the fit, with the resolution parameters and Δs_0 correction term fixed to nominal values. The resulting uncertainty accounts for the uncertainty in extrapolating between low and high p_{T} regimes.

- Z p_{T} reweighting: new templates of $m_{\mu\mu}^{ID}$, $m_{\mu\mu}^{CB}$ and $m_{\mu\mu}^{ME}$ are generated for the $Z \to \mu\mu$ sample using a different scheme of Z kinematics reweighting. As discussed in Section 4.3.1, the reweighting map is derived separately for each generator. For this systematic uncertainty, correction parameters are derived without kinematic reweighting, with SHERPA-derived reweighting, and MadGraph-derived reweighting. This covers the theory uncertainty when deriving correction parameters.

- J/ψ and Z p_{T} template range: the p_{T} range of the J/ψ and Z templates are varied. For J/ψ, the two nominal p_{T} templates are $p_T^{J/\psi,nom} \in [6.3, 9]$GeV and $p_T^{J/\psi,nom} \in [9, 20]$GeV. For the Z, the two templates are $p_T^{Z,nom} \in [20, 50]$GeV and $p_T^{Z,nom} \in [50, 300]$GeV. The boundary of the two templates for the J/ψ is varied between 8 and 12 GeV, and for the Z is varied between 40 and 80 GeV. This preserves the statistics, and estimates the systematic uncertainty arising from a possible p_{T} dependency.

- Mass binning of J/ψ and Z: the number of bins for the $m_{\mu\mu}$ templates is reduced from 200 to 150 for the Z, and from 90 to 60 for the J/ψ. This systematic covers any binning effect in generating templates.

- Z mass window: new templates of $m_{\mu\mu}$ are generated for the $Z \to \mu\mu$ sample after a variation of the m_Z window selection of $\pm$ 10 GeV, i.e. using $75 < m_{\mu\mu} < 115$ GeV for all track types. This region is more sensitive to the shape variations of the ISR and FSR contributions, the running of α_Z^{EM} and other specific choices of the MC generators used in the $Z \to \mu\mu$ simulation.

- J/ψ mass window: new templates of $m_{\mu\mu}$ are generated for the $J/\psi \to \mu\mu$ sample after a variation of the $m_{J/\psi}$ window selection, i.e. using $2.75 < m_{\mu\mu} < 3.4$ GeV for all track types. The region farther from the $m_{J/\psi}$ peak is more sensitive to the shape variation of the combinatorial background, and the specific choices of the MC generators used in the $J/\psi \to \mu\mu$ simulation.

- J/ψ background: new $m_{\mu\mu}$ templates are generated for $J/\psi \to \mu\mu$ samples using a background parametrisation different from the exponential function. For this systematic uncertainty, background parametrisation including a combination of two crystal ball functions, and a Chebyshev function are used.

- Statistical variation: the standard deviation of the last five iterations of each calibration is used as an extra uncertainty for each calibration parameter. This captures any instabilities in the fit, and the correlations between different fit parameters.

- J/ψ resolution non-closure: the performance studies detailed in Section 4.3.4 showed non-closure of the mass resolution in J/ψ, particularly in the transition region ($1<|\eta|<2$). This is the result of Z-J/ψ extrapolation, and additional uncertainties are assigned to the resolution parameters to cover this non-closure. This is only applied to the ID and MS calibration.

The positive and negative differences between the nominal result and the systematic variations of the correction parameters are added in quadrature to provide a total systematic variation. The largest component of the total uncertainty in the momentum scale originates from the comparison of the J/ψ and Z-only fits. The remaining components are smaller by about a factor of two. For the resolution smearing terms, in the same kinematic region, the largest uncertainty comes from the J/ψ and Z p_{T} template fit range. At significantly higher momenta the uncertainty in the J/ψ and Z p_{T} template fit range still dominates the resolution uncertainty in $p_{\mathrm{T}}^{Cor,CB}$.

4.3.4 Performance studies for muon calibration

The derived calibration constants are validated using $J/\psi \to \mu\mu$, $\Upsilon \to \mu\mu$, and $Z \to \mu\mu$ decays. The $\Upsilon \to \mu\mu$ events are the most sensitive to intermediate p_{T} values between the two other resonances, with p_{T} centred around 20 GeV. The validation studies are performed with finer bins in detector segmentation and in

Table 4.5: Summary of ID muon momentum resolution and scale corrections used in Equation 4.7, averaged over the three main detector regions. The corrections are derived in 18 pseudorapidity regions and averaged, with each region assigned a weight proportional to its η width. The uncertainties represent the sum in quadrature of the statistical and systematic uncertainties.

Region	$\Delta r_1^{\mathrm{ID}}(\times 10^{-3})$	Δr_2^{ID} [TeV^{-1}]	$s_1^{\mathrm{ID}}(\times 10^{-3})$
$\lvert\eta\rvert < 1.05$	$4.4^{+3.0}_{-2.7}$	$0.12^{+0.03}_{-0.03}$	$-0.82^{+0.19}_{-0.06}$
$1.05 \leq \lvert\eta\rvert < 2.0$	$6.7^{+19.5}_{-3.1}$	$0.31^{+0.03}_{-0.03}$	$-0.86^{+0.36}_{-0.21}$
$\lvert\eta\rvert \geq 2.0$	$9.4^{+3.6}_{-5.3}$	$0.08^{+0.02}_{-0.02}$	$-0.45^{+1.19}_{-0.55}$

Table 4.6: Summary of MS momentum resolution and scale corrections for small and large MS sectors, averaged over three main detector regions. The corrections for large and small MS sectors are derived in 18 pseudorapidity regions, and averaged, with each region assigned a weight proportional to its η width. The uncertainties represent the sum in quadrature of the statistical and systematic uncertainties. The larger uncertainties for some terms in the $1.05 \leq \lvert\eta\rvert < 2.0$ region are associated with the low bending power of the magnet system of the MS in part of that region.

Region	Δr_0^{MS} [MeV]	$\Delta r_1^{\mathrm{MS}}(\times 10^{-3})$	Δr_2^{MS} [TeV^{-1}]	s_0^{MS} [MeV]	$s_1^{\mathrm{MS}}(\times 10^{-3})$
$\lvert\eta\rvert < 1.05$ (large)	71^{+41}_{-10}	$13.5^{+3.1}_{-2.6}$	$0.11^{+0.02}_{-0.02}$	-27^{+18}_{-14}	$2.33^{+0.61}_{-0.61}$
$\lvert\eta\rvert < 1.05$ (small)	63^{+35}_{-23}	$17.2^{+2.3}_{-3.6}$	$0.12^{+0.02}_{-0.02}$	-18^{+14}_{-24}	$-1.51^{+1.15}_{-0.45}$
$1.05 \leq \lvert\eta\rvert < 2.0$ (large)	42^{+401}_{-53}	$26.7^{+19.5}_{-2.8}$	$0.14^{+0.02}_{-0.02}$	-29^{+43}_{-57}	$-0.9^{+2.8}_{-1.9}$
$1.05 \leq \lvert\eta\rvert < 2.0$ (small)	44^{+437}_{-59}	$29.2^{+8.2}_{-1.5}$	$0.18^{+0.02}_{-0.02}$	-28^{+39}_{-43}	$-1.3^{+2.0}_{-1.6}$
$\lvert\eta\rvert \geq 2.0$ (large)	61^{+48}_{-27}	$16.8^{+3.2}_{-4.3}$	$0.11^{+0.02}_{-0.02}$	-1^{+43}_{-29}	$1.7^{+1.3}_{-1.4}$
$\lvert\eta\rvert \geq 2.0$ (small)	47^{+32}_{-40}	$17.8^{+1}_{-1.9}$	$0.16^{+0.02}_{-0.02}$	-8^{+14}_{-12}	$1.94^{+0.76}_{-0.54}$

momentum, compared to the bins used for deriving the calibration. Additionally, the momentum requirements for validation are lower than those used for calibration. This allows for an extensive validation of the calibration procedures, for both detector segmentation and extrapolation to extreme regions of p_{T}.

The invariant mass distributions for the $J/\psi \to \mu\mu$ and $Z \to \mu\mu$ events in each detector region are shown in Figure 4.10. The lineshapes of the two resonances in simulation agree with the data within the systematic uncertainties, demonstrating the overall effectiveness of the p_{T} calibration.

The systematic band shape in Figure 4.10 shows the effect of varying scale and resolution parameters. The sinusoidal-like systematic shape (most prominently observed in the $J/\psi \to \mu\mu$ distribution) is the result of the scale parameter

Table 4.7: Summary of CB momentum resolution and scale corrections for small and large MS sectors, averaged over the three main detector regions. The corrections for large and small MS sectors are derived in 18 pseudorapidity regions and averaged, with each region assigned a weight proportional to its η width. The energy loss term Δr_0^{CB} is negligible and therefore fixed to zero in the fit for all η. The uncertainties represent the sum in quadrature of the statistical and systematic uncertainties.

Region	$\Delta r_1^{\text{CB}}(\times 10^{-3})$	Δr_2^{CB} [TeV^{-1}]	s_0^{CB} [MeV]	$s_1^{\text{CB}}(\times 10^{-3})$
$\lvert\eta\rvert < 1.05$ (large)	$6.7^{+1.4}_{-0.9}$	$0.08^{+0.04}_{-0.05}$	$-5.0^{+2.9}_{-4.0}$	$0.35^{+0.24}_{-0.22}$
$\lvert\eta\rvert < 1.05$ (small)	$6.5^{+1.3}_{-1.0}$	$0.11^{+0.05}_{-0.05}$	$-0.9^{+2.5}_{-3.6}$	$-0.83^{+0.25}_{-0.14}$
$1.05 \leq \lvert\eta\rvert < 2.0$ (large)	$10.3^{+2.6}_{-2.7}$	$0.24^{+0.10}_{-0.07}$	$-2.0^{+5.7}_{-6.7}$	$-0.83^{+0.39}_{-0.30}$
$1.05 \leq \lvert\eta\rvert < 2.0$ (small)	$8.9^{+1.7}_{-2.7}$	$0.29^{+0.08}_{-0.03}$	$-3.0^{+3.3}_{-4.0}$	$-0.80^{+0.26}_{-0.21}$
$\lvert\eta\rvert \geq 2.0$ (large)	$10.6^{+2.2}_{-2.7}$	$0.21^{+0.10}_{-0.07}$	$2.3^{+13}_{-9.3}$	$0.80^{+1.09}_{-0.42}$
$\lvert\eta\rvert \geq 2.0$ (small)	$11.5^{+2.2}_{-2.1}$	$0.26^{+0.08}_{-0.06}$	$-12.6^{+8.2}_{-9.7}$	$1.59^{+0.47}_{-0.43}$

variation. As shown in Equation 4.7, shifting scale parameters directly impacts muon p_{T}, therefore changing the position of dimuon mass peak. The different momentum dependency of Δs_0 and Δs_1 is observed from the asymmetry in the systematic impact on either side of the dimuon mass peak, as the Δs_1 term dominates at larger p_{T}, resulting in increased systematic variation in $m_{\mu\mu} > 3.1$ GeV. The cosinusoidal-like systematic shape (most prominently observed in the zmm distribution) is the result of the resolution variation, which changes the width of the dimuon mass distribution. Similar to the scale variation, the momentum dependency is observed from the asymmetry in the systematic variation in the dimuon mass peak.

The p_{T} calibration can be further tested using parameters derived from the reconstructed resonance peaks, as the mass of a dimuon system, $m_{\mu\mu}$ is described by:

$$m_{\mu\mu}^2 = 2p_T^1 p_T^2[\cosh(\Delta\eta) - \cos(\Delta\phi)]. \tag{4.9}$$

For muon pairs with similar momentum resolution, the relative mass resolution, $\sigma_{\mu\mu}/m_{\mu\mu}$ is directly proportional to the relative muon momentum resolution (ignoring angular effects):

$$\frac{\sigma_{\mu\mu}}{m_{\mu\mu}} = \frac{1}{\sqrt{2}}\frac{\sigma_\mu}{p_\mu}. \tag{4.10}$$

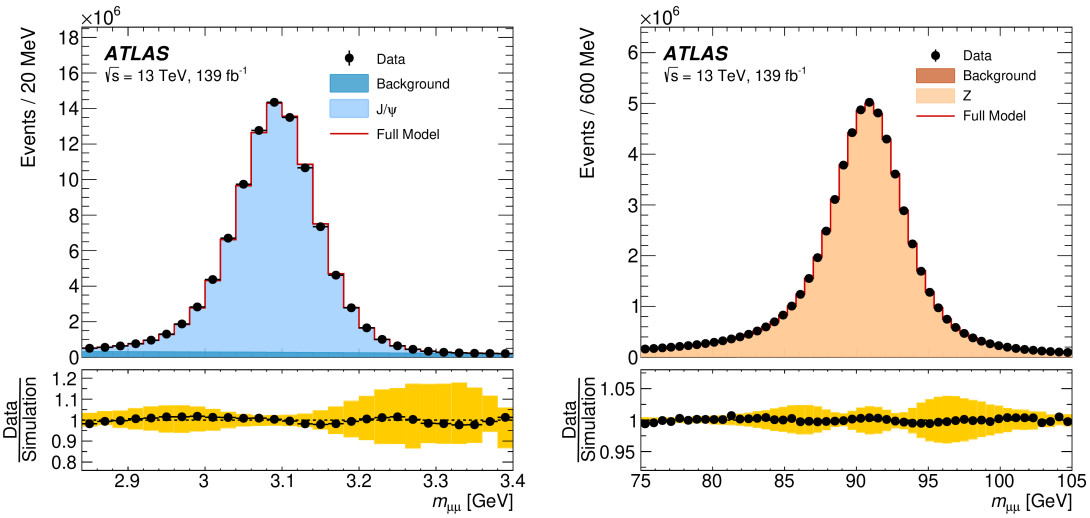

Figure 4.10: Dimuon invariant mass distribution of $J/\psi \to \mu\mu$ (left) and $Z \to \mu\mu$ (right) candidate events reconstructed with CB muons. The upper panels show the invariant mass distribution for data and the signal simulation plus the background estimate. The points show the data. The continuous line corresponds to the simulation with the MC momentum corrections applied. Background estimates are added to the signal simulation. The lower panels show the ratios of the data to the MC simulation. The bands represent the effect of the systematic uncertainties in the MC momentum corrections. In the Z sample, the MC background samples are added to the signal sample according to their expected cross-sections. In the J/ψ sample, the background is estimated from a fit to data. The sum of background and signal MC distributions is normalised to data.

Similarly, the total muon momentum scale ($s =< \frac{p^{reco}-p^{true}}{p^{true}} >$) is directly related to the di-muon mass scale, $s_{\mu\mu}$:

$$s_{\mu\mu} = \sqrt{s_{\mu 1} s_{\mu 2}}, \tag{4.11}$$

where $s_{\mu 1}$ and $s_{\mu 2}$ are the momentum scales of the two muons in the decay.

Therefore, the effectiveness of the momentum calibration can also be measured by comparing the mean $m_{\mu\mu}$, and resolution $\sigma(m_{\mu\mu})$ of the dimuon mass resonances, rather than the measurements from single muons. As a first pass, the mean and standard deviation from the $J/\psi \to \mu\mu$ and $Z \to \mu\mu$ templates are used as an estimation for dimuon mass scale and resolution, with the background components estimated from data, and subtracted from templates. In the subsequent studies, fully analytical fits are performed for each resonance, allowing for cross-checks between different kinematic regimes. The fitting procedure and the fit parameters are optimised for each resonance.

The mass window for J/ψ decays is chosen to be $2.8 < m_{\mu\mu} < 3.9$ GeV. The increased lower bound removes the kinematic sculpting effects from low-p_{T} triggers, which is challenging to model analytically. The upper bound is increased to include the $\Psi(2S)$ peak to provide a second resonance, thus providing an upper limit for the fitted J/ψ resolution. This is especially relevant in the high η region where the detector mass resolution is lower. The intrinsic widths of J/ψ and $\Psi(2S)$ decays are negligible compared to the experimental resolution, and are therefore modelled by a double-sided crystal ball (DSCB) function. A DSCB has one Gaussian core (capturing the convolution effect from detector resolutions), and two power-law tails, each with two free parameters. For both J/ψ and $\Psi(2S)$, the parameters describing the Gaussian core are allowed to float when fitting to data, while the four parameters for power-law tails are extracted from simulation, and kept fixed in the fits to data. In this kinematic region, the main backgrounds are the non-resonant combinatoric background and the misidentified muons, which are modelled by an exponential function.

The mass window for Z decays is chosen to be $75 < m_{\mu\mu} < 105$ GeV. For $Z \to \mu\mu$ validation, the true Z lineshape is convolved with a DSCB as the fit function. Similar to the J/ψ, the main backgrounds for Z decay are the non-resonant processes, and are described by an exponential function.

For both resonances, the peak position and width of the Crystal Ball function are used as estimators of the $m_{\mu\mu}$ and $\sigma(m_{\mu\mu})$ variables in each of the η and p_{T} bins. Figure 4.11 and 4.12 display the mean ($< m_{\mu\mu} >$) and resolution ($\sigma(m_{\mu\mu})$) of the dimuon mass fit as a function of the leading-muon η for the two resonances. The dimuon mass resolution is about 1.3% and 1.6% at small η values for the J/ψ and Z bosons, respectively, and increases to 2.1% and 2.4% in the endcaps. This corresponds to a relative muon p_{T} resolution of 1.8% and 2.3% in the centre of the detector and 3.0% and 3.4% in the endcaps for J/ψ and Z boson decays, respectively. Uncertainties in the dimuon mass resolution range between 2% and 5% for the J/ψ and between 3% and about 6% for the Z boson.

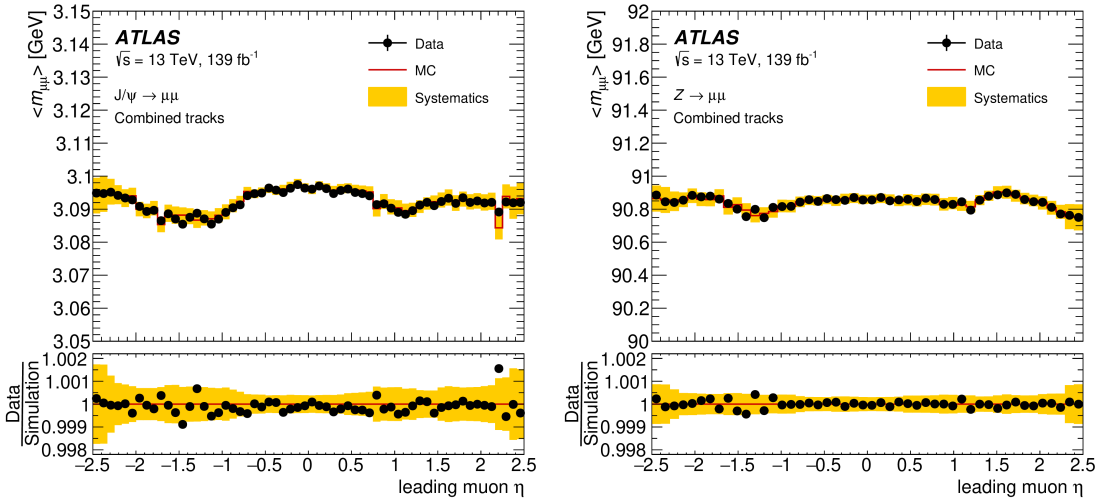

Figure 4.11: Fitted mean mass of the dimuon system for CB muons for (a) J/ψ and (b) $Z \to \mu\mu$ events for data and corrected simulation as a function of the pseudorapidity of the highest-p_{T} muon. The upper panels show the fitted mean mass value for data and corrected simulation. The small variations of the invariant mass estimator as a function of pseudorapidity are due to imperfect energy loss corrections and the magnetic field description in the muon reconstruction. Both effects are well reproduced in the simulation. The lower panels show the ratios of the data to the MC simulations. The error bars represent the statistical uncertainty; the shaded bands represent the systematic uncertainty in the correction method and the systematic uncertainty in the extraction method added in quadrature.

The same methodology used for the $J/\psi \to \mu\mu$ fit is applied to $\Upsilon \to \mu\mu$ decays. The three resonances ($1S$, $2S$ and $3S$) are all modelled by DSCBs, with the background processes modelled by a polynomial fit rather than an exponential function. As done for the $J/\psi \to \mu\mu$ and $Z \to \mu\mu$ decays, the momentum scale dependency and the resolution are extracted as a function of the pseudorapidity of the leading muon in the event. Figure 4.13 compares the data and simulation after all corrections. The data agree with the simulation within the systematic uncertainties. The uncertainty in the momentum scale is up to 0.05% in the central region and up to 0.1% in the forward region. Figure 4.14 displays the fitted mean mass and the dimuon invariant mass resolution for $\Upsilon \to \mu\mu$ events, and the resolution is in agreement within about 3%.

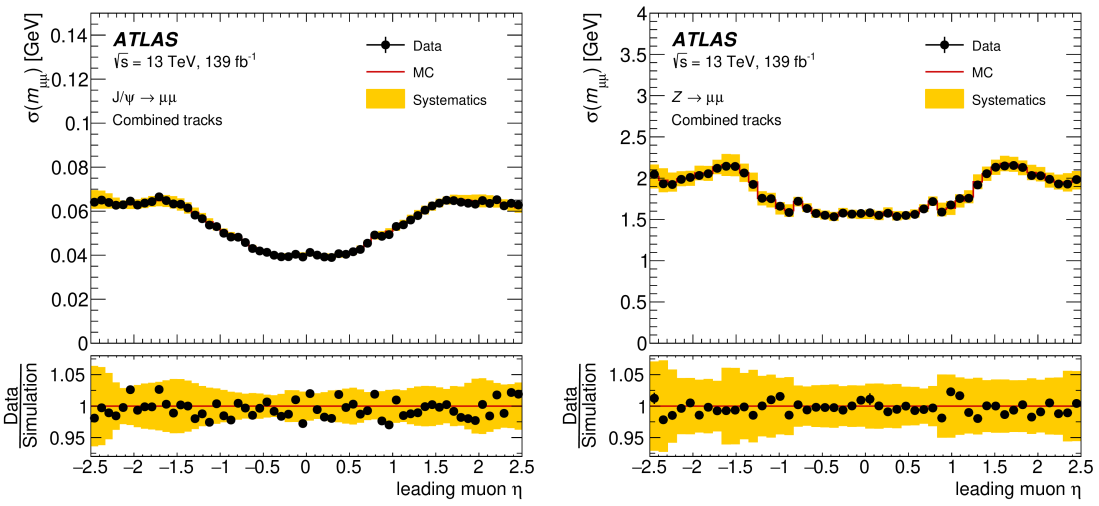

Figure 4.12: Dimuon invariant mass resolution for CB muons for (a) J/ψ and (b) $Z \to \mu\mu$ events for data and corrected simulation as a function of the pseudorapidity of the highest-p_{T} muon. The upper panels show the fitted resolution value for data and corrected simulation. The lower panels show the ratios of the data to the MC simulations. The error bars represent the statistical uncertainty; the shaded bands represent the systematic uncertainty in the correction method and the systematic uncertainty in the extraction method added in quadrature. For the $Z \to \mu\mu$ the estimator shown in the plot is only sensitive to the detector resolution and not to the natural width of the Z boson, as discussed in the text.

4.4 Conclusion

This chapter presented the state-of-the-art technique for muon reconstruction, identification, isolation and calibration, derived from the pp dataset corresponding to 139 fb^{-1} at $\sqrt{s} = 13$ TeV. The well-understood resonances $Z \to \mu\mu$, $J/\psi \to \mu\mu$ and $\Upsilon \to \mu\mu$ are used for its derivation and validation.

For reconstruction and identification, a precision better than per-mille level is achieved for muons with $p_{\mathrm{T}} > 10$ GeV in most detector regions, and better than 1% for muons with p_{T} down to 3 GeV.

Both charge-dependent and charge-independent momentum biases are corrected for. For charge-dependent bias, $Z \to \mu\mu$ events are used, and the bias is reduced from an average of up to 0.4 TeV^{-1} to $2 \cdot 10^{-4}$ TeV^{-1} for muons with $p_{\mathrm{T}} < 450$ GeV. The scale and resolution are studied using $J/\psi \to \mu\mu$ and $Z \to \mu\mu$ decays, where the B-physics stream introduced in 2016 increased the recorded number of low-p_{T} events. The combined uncertainties on the scale and resolution

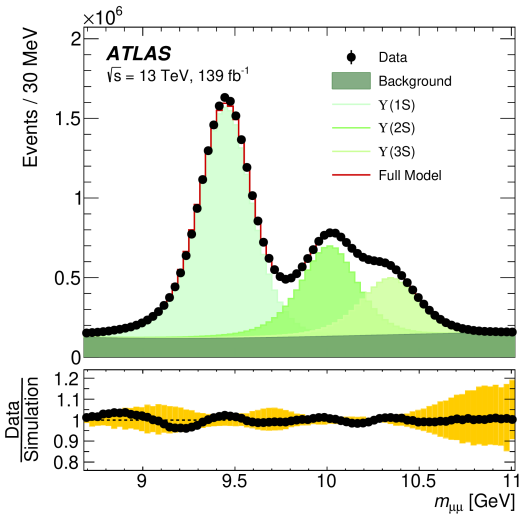

Figure 4.13: Dimuon invariant mass distribution of $\Upsilon \rightarrow \mu\mu$ candidate events reconstructed with CB muons. The upper panels show the invariant mass distribution for data and for the signal simulation plus the background estimate. The background is estimated from a fit to the data as described in the text. The lower panel shows the ratio of the data to the MC simulations. The points show the data. The continuous line corresponds to the sum of simulation and background with the MC momentum corrections applied. The band represents the effect of the systematic uncertainties in the MC momentum corrections. The sum of background and signal MC distributions is normalised to the data. Reproduced from [83].

correction parameters are reduced by **a factor of two** relative to the previous calibration parameters reported in Ref. [84], which is the result of improved calibration techniques, and the additional statistics for the $J\psi$ resonance. The improved calibration techniques include generator reweighting, HL χ^2, and moment morphing. The relative muon p_{T} resolution is of the order of a few percent. This improvement benefits all ATLAS analyses with muons in the final state.

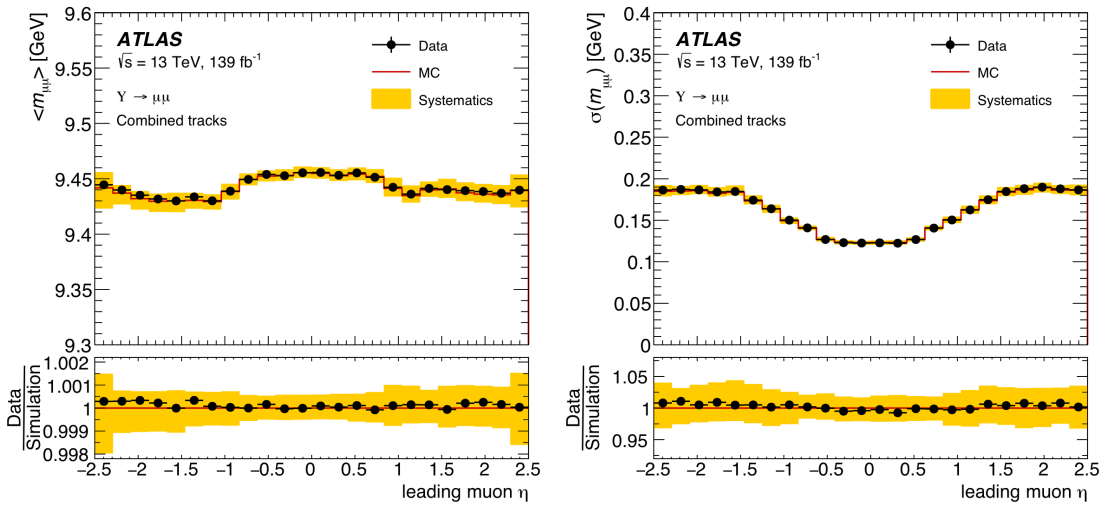

Figure 4.14: Left: Fitted mean mass of the dimuon system for CB muons for $\Upsilon \to \mu\mu$ events for data and corrected simulation as a function of the pseudorapidity of the highest-p_{T} muon. Right: Dimuon mass resolution of the dimuon system for CB muons for $\Upsilon \to \mu\mu$ events for data and corrected simulation as a function of the pseudorapidity of the highest-p_{T} muon. The upper panels show the fitted mean mass value for data and corrected simulation. The lower panels show the ratios of the data to the MC simulations. The error bars represent the statistical uncertainty; the shaded bands represent the systematic uncertainty in the correction method and the systematic uncertainty in the extraction method added in quadrature.

Chapter 5

Measurement of the Higgs mass in $H \to ZZ^*$ decay

The Higgs boson mass (m_H) is a free parameter in the Standard Model (SM). As no theoretical predictions for the value of m_H are available, its value must be determined experimentally. Within the SM, the value of m_H uniquely defines the coupling and cross-section between the Higgs boson and charged fermions [2]. Combined with the measurement of the top quark and W boson mass, it offers a window for stringent tests for the electroweak theory [85]. Both the Higgs and top mass are connected to the shape of the Higgs potential, and therefore the stability of the electroweak vacuum [86, 87]. An unstable electroweak vacuum can decay by nucleation of bubbles, reaching the new vacuum, and expanding to the entire universe. Some of our current theoretical calculation indicates that we live in a metastable universe based on the precision measurements of m_H and m_t [88, 89]. Improving m_H precision contributes to the prediction of the Higgs self-coupling, which has not been observed experimentally at the time of writing this thesis. These factors theoretically motivate a high-precision measurement of the Higgs boson mass. This can be achieved experimentally in the $H \to ZZ^* \to 4l$ decay channel, which has fully-reconstructable final states and a high signal-to-background ratio.

Using the pp collision data from 2011 and 2012, the ATLAS and CMS collaborations independently measured m_H [90, 91], using a dataset with centre-of-mass energies of 7 and 8 TeV, corresponding to an integrated luminosity

of 25 fb^{-1}. The two measurements are combined, resulting in the measured $m_H = 125.09 \pm 0.24$ GeV [20]. For Run 2, the ATLAS collaboration combined its Run 1 measurement with the early Run 2 dataset (with an integrated luminosity of 36.1 fb^{-1}) to obtain $m_H = 124.97 \pm 0.24$ GeV [92]. The equivalent combination using dataset collected by the CMS collaboration (with an integrated luminosity of 35.9 fb^{-1}) resulted in the measured $m_H = 125.38 \pm 0.14$ GeV [93].

This chapter outlines the measurement of m_H using the full Run 2 dataset (with integrated luminosity at 139 fb^{-1}) collected by the ATLAS experiment, and its combination with the Run 1 measurement in the $H \to ZZ^* \to 4l$ decay channel. This analysis improves on the earlier ATLAS Higgs mass measurements by using the Z-mass constraint method, per-event resolution and a signal-background discriminant to improve the mass resolution.

5.1 Data and Monte Carlo simulated samples

The proton-proton collision data used for this analysis were collected between 2015 to 2018 at the centre-of-mass energy of 13 TeV using single-lepton, di-lepton and trilepton triggers. The combined efficiency in the kinematic acceptance region (described in Section 5.2 and 5.3) of these triggers averages at around 98%, inclusive of all final states. After checks for detector live time and data quality checks, this corresponds to an integrated luminosity of 139 fb^{-1}. The mean number of proton-proton interactions in each bunch crossing is 33.7 [94].

MC simulated samples are used for several purposes. The signal samples are used to estimate the trigger efficiency, optimise event selection criteria, and determine the shape and normalisation of the signal model. Additionally, simulated signal samples are generated at different values of m_H to reduce the dependency on the Higgs mass at several stages of this analysis. Background samples are used to evaluate the shape of each background component. In processes where the background components are too small, normalisations are also extracted directly from simulation.

Generated events are processed through the ATLAS detector simulation [95] within the GEANT4 framework [96] and reconstructed in the same way as collision data. Additional pp interactions in the same and nearby bunch crossings, referred to as pile-up, are included in the simulation. The pile-up events are generated using PYTHIA 8 with the A3 set of tuned parameters [97] and the NNPDF2.3LO PDF set [98]. The simulated samples are weighted to reproduce the observed distribution of the mean number of interactions per bunch crossing in the data.

5.1.1 Simulated signal samples

For simulated signal samples, the following production modes are considered: gluon-gluon fusion (ggH), vector boson fusion (VBF), with associated vector boson (VH, where V is either a W or a Z boson), with a top quark pair (ttH), in association with a bottom quark pair (bbH), or in association with a single top quark (tH). With the exception of $gg \to ZH$, which is simulated at leading order (LO), all other production modes are simulated at the next-to-leading-order (NLO) or better. For all signal processes, PYTHIA 8 [54] was used for the $H \to ZZ^* \to 4\ell$ decay as well as for parton showering, hadronisation and the underlying event. PYTHIA 8 was interfaced to EVTGEN v1.2.0 [99] for simulation of the bottom and charm hadron decays. For the ggH, VBF and VH processes, the AZNLO [69] set of tuned parameters was used, while the A14 [72] set was used for the ttH, bbH and tH processes. For ggH, VBF, and VH production, samples are simulated with a range of m_H values from 123 to 127 GeV, while other production modes are simulated assuming m_H=125 GeV. The generators used to simulate signal processes are listed in Table 5.1, while the composition of these production modes as a fraction of the total Higgs production cross section in the SM is shown in Figure 5.1.

5.1.2 Simulated background samples

The main background for this analysis is non-resonant ZZ^* production, and the following modes are considered: quark-initiated ($qqZZ$), gluon-initiated ($ggZZ$)

Table 5.1: Description of the simulated signal processes. The name of the signal production process is given in the first column, with the Monte Carlo generators, the parton distribution functions (PDFs) and the accuracy for the calculations listed in the following columns. Note that the ggH sample reweights the Higgs y spectrum from HJ-MINLO [100, 101] to NNLOPS [102]

Process	Generator	PDF	Fixed order accuracy
ggH	NNLOPS [50–52, 103, 104]	PDF4LHC [105] (NNLO)	N^{3}LO, NLO EW corrections [106–116]
VBF	POWHEG-BOX v2 [50–52, 117]	PDF4LHC (NLO)	NLO, NLO EW corrections [118, 119]
VH	POWHEG-BOX v2	PDF4LHC (NLO)	NNLO [120–123], NLO EW corrections [124–126]
$gg \to ZH$			NLO [120, 121, 127] with NLL QCD corrections [128]
$t\bar{t}H$	POWHEG-BOX v2 [129]	PDF4LHC (NLO)	NLO [130–133]
$b\bar{b}H$	MADGRAPH5_AMC@NLO v.2.3.3 [134]	CT10 NLO [70]	five-flavour scheme: NNLO, four-flavour scheme: NLO [135–137]
tH	MADGRAPH5_AMC@NLO v2.6.0	NNPDF3.0nnlo [71]	NLO [138, 139]

and vector boson scattering (EWZZ) production of ZZ^*. All sources of ZZ^* continuum background are generated using SHERPA v2.2.2 [53, 140–142], and alternative $qqZZ$ samples are produced for generator systematic studies using POWHEG-BOX v2 and MADGRAPH5_AMC@NLO.

The secondary background sources include backgrounds from WZ production, Z bosons produced in association with jets, and $t\bar{t}$ events, and also the small backgrounds originating from production processes with three electroweak bosons, or a $t\bar{t}$ pair and one or more top quarks or electroweak bosons (referred to as VVV and tXX, respectively). The details for all background processes are shown in Table 5.2.

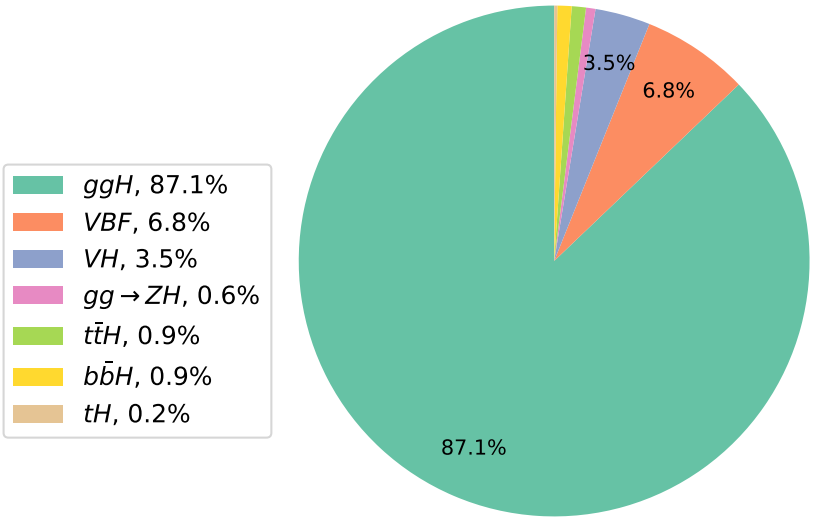

Figure 5.1: Composition of the Higgs boson production modes in the SM as a fraction of the total Higgs production cross-section at 13 TeV at the LHC.

Table 5.2: Description of the production of simulated background samples. The name of the background process is listed in the first column, with Monte Carlo generators and the parton distribution functions (PDFs) listed in the columns after.

Process	Generator	PDF
$qqZZ$	Sherpa v2.2.2 [53, 140–142]	NNPDF3.0nnlo
$qqZZ$ (alternate)	Powheg-Box v2	CT10
$qqZZ$ (alternate)	MadGraph5_aMC@NLO	PDF4LHC (NLO)
$ggZZ$	Sherpa v2.2.2	NNPDF3.0nnlo
EW ZZ	Sherpa v2.2.2	NNPDF3.0nnlo
WZ	Powheg-Box v2	CT10
Z+jets	Sherpa v2.2.1	NNPDF3.0nnlo
$t\bar{t}$	Powheg-Box v2	NNPDF3.0nnlo
tXX	MadGraph5_aMC@NLO	NNPDF3.0nnlo
VVV	Sherpa v2.2.2	NNPDF3.0nnlo

5.2 Physics objects

To measure the Higgs mass in a four-lepton final state, one needs an excellent understanding of electrons and muons in the ATLAS detector to select candidate Higgs events from the ZZ^* continuum background. Photons are used to recover

final-state radiation in the leading lepton to improve the mass resolution.

5.2.1 Electrons

Similar to muon reconstruction, electron reconstruction starts from ID tracks [143], which are then matched to energy clusters in the electromagnetic calorimeter. A Gaussian-sum filter algorithm corrects for the radiative energy loss [144], and a topological cell-clustering-based algorithm is used to further improve energy resolution, in particular for bremsstrahlung photons [145].

Electron identification is based on a likelihood discriminant, which utilises measured properties from the tracking system, calorimeter shower shapes, and quantities that combine information from both sub-detectors [143]. Identification efficiencies and background rejection rates are optimised in bins of η and E_T. For this analysis, the *Loose* working point is used, providing an electron reconstruction and identification efficiency of 90% for electrons with $p_{\mathrm{T}} > 30$ GeV. Electron tracks are required to have $p_{\mathrm{T}} > 7$ GeV, and $\eta < 2.47$. The electron energy scale and resolution are calibrated using $Z \to ee$ events, with more details in [146]. The selection criteria for electrons are shown in Table 5.3.

Table 5.3: Summary of electron selection requirements for the $H \to ZZ^* \to 4\ell$ analysis.

Electron selection criteria	
Identification selection	*Loose*
IP selection	$\lvert d_0\rvert < 1$ mm and $\lvert z_0 \cdot \sin(\theta)\rvert < 0.5$ mm (if ID track is available)
E_T	$E_T > 7$ GeV
η	$\lvert\eta\rvert <$2.47

5.2.2 Muons

Techniques for muon reconstruction, identification, isolation and calibration are detailed in Chapter 4. The majority of muons used in this analysis are CB muons. In regions with limited detector coverage, CT, ME and SiF muons are included for additional statistics. The selection criteria for differing muon types are shown in Table 5.4.

Table 5.4: Summary of muon selection requirements for the $H \to ZZ^* \to 4\ell$ analysis, and geometrical acceptance regions for different muon types.

Global muon selection criteria	
Identification selection	*Loose*
Isolation selection	*PflowLoose*
IP selection	$\lvert d_0\rvert < 1$ mm and $\lvert z_0 \cdot \sin(\theta)\rvert < 0.5$ mm (if ID track is available)
p_{T}	$p_{\mathrm{T}} > 5$ GeV
η	$\lvert\eta\rvert < 2.7$
Muon selection criteria for certain reconstruction types	
CB and ST muons	$\lvert\eta\rvert < 2.5$
ME muons	$\lvert\eta\rvert < 2.7$
SiF muons	$2.5 < \lvert\eta\rvert < 2.7$
CT muons	$p_{\mathrm{T}} > 15$ GeV for $\lvert\eta\rvert < 0.1$

Charge-dependent and charge-independent corrections, as described in Section 4.3.2 and 4.3.3, are applied to data and simulation respectively. When applied to data, the charge-dependent correction improves the resolution of the $Z \to \mu\mu$ mass peak by approximately 1%. The charge-independent correction derived from the CB tracks is used for this analysis, and reduces the associated uncertainty by a factor of four.

5.3 Event selection

5.3.1 Impact parameter and vertex selection

To suppress the background from heavy flavour hadrons, the impact parameter significance ($|d_0|/\sigma(d_0)$) is required to be lower than 5 (3) for electrons (muons). An additional cut on the muon transverse impact parameter ($|d_0| < 1$ mm) is applied to reduce the cosmic muon background.

These backgrounds are reduced further by constraining the common vertex of the four-lepton system. Collision vertices are reconstructed from ID tracks with transverse momentum $p_{\mathrm{T}} > 500$ MeV. Events are required to have at least one collision vertex with at least two associated tracks. The primary vertex used in the analysis is selected to be the vertex with the largest p_{T} sum in the event after refitting with a beam-spot constraint. To ensure that all four leptons

originate from the same vertex, they are all required to be within $|z_0 \cdot \sin(\theta)|$ < 0.5 mm of the primary vertex along the proton beam pipe. The quality of the vertex fit, defined by χ^2/ndof, is required to be less than 5 for a 4μ final state due to its higher track resolution, and less than 9 for all other final states. Further detail can be found in Ref. [147].

5.3.2 Quadruplet selection

Higgs candidates in $H \to ZZ^* \to 4\ell$ have four possible final states: (4μ, $2\mu 2e$, $4e$, $2e2\mu$). The difference between the $2\mu 2e$ and $2e2\mu$ final states arises from the mass ordering of the lepton pair. In each quadruplet, the di-lepton pair with mass (m_{12}) closest to the on-shell Z boson mass is referred to as the leading di-lepton pair, and the other di-lepton pair is referred to as the sub-leading pair with mass m_{34}. Both lepton pairs must contain two opposite-sign, same-flavour leptons.

Additional constraints on lepton p_{T} and di-lepton mass are imposed for background suppression. The three leading leptons are required to have minimal p_{T} of 20, 15 and 10 GeV respectively. To target on-shell Z boson production, the leading lepton pair must have 50 GeV $< m_{12} <$ 106 GeV, while a looser requirement is imposed on the sub-leading lepton pair. The sub-leading lepton pair are required to have a mass of $m_{threshold} < m_{34} < 115$ GeV, where $m_{threshold} =$ 12 GeV for events with four-lepton invariant mass $m_{4l} <$ 140 GeV, and increasing linearly to 50 GeV at m_{4l} = 190 GeV, and remains at 50 GeV for events with larger m_{4l}. J/ψ events are further suppressed in the $4e$ and 4μ channels by requiring the alternative lepton pairing to have a minimal di-lepton mass of 5 GeV. All leptons in the quadruplet are required to be well-separated with $\Delta R(\ell, \ell') > 0.10$ [1].

The high lepton-multiplicity in the final state results in a large combinatoric background. In cases where multiple quadruplets pass these selection criteria, the preference is first given to quadruplets with m_{12} closest to the Z boson mass. If there is more than one quadruplet with identical m_{12}, the quadruplet with

[1] The angular distance between two objects, ΔR is defined as $\Delta R = \sqrt{(\Delta\eta)^2 + (\Delta\phi)^2}$, where $\Delta\eta$ is their difference in pseudorapidity, and $\Delta\phi$ is their difference in azimuthal angle.

m_{34} closest to the Z boson mass is selected as the candidate quadruplet. For VH and ttH production modes, where the vector boson and the top quark could decay into additional high p_{T} prompt leptons, a matrix element for the Higgs boson decay is computed at LO using MadGraph5_aMC@NLO [134], with the lepton kinematics as inputs. The quadruplet with the largest matrix element is then identified as the Higgs boson candidate. [147].

5.4 Analysis strategy

The goal of this analysis is to measure the Higgs boson mass precisely by improving background rejection and quadruplet mass resolution, which are achieved by recovering final-state radiation (FSR), imposing a Z-mass constraint (ZMC), inclusion of a signal-background discriminant, and a per-event resolution estimate. The FSR recovery improves the mass resolution for events with photon emission, while the ZMC improves the mass resolution further using a likelihood constraint for the leading lepton pair mass. The four-lepton invariant mass with FSR recovery and ZMC applied is referred to as $m_{4l}^{constrained}$. In the previous iteration of this analysis, a large discrepancy between data and simulation was observed for $m_{4l}^{constrained}$ in final states involving muons. This was identified to be the result of muon track error mismodelling in the simulation, which is corrected by using a Cumulative Distribution Function (CDF) mapping method. The signal-background discriminant is updated with the output of a deep neural-network (DNN), further improving the background rejection. After implementing the final likelihood model described in Section 5.5 and 5.6, the expected sensitivity on m_H is improved by 0.5 % compared to the previous iteration of this analysis using early Run 2 data [92]. The per-event resolution uses lepton kinematics to estimate the width of the Higgs mass peak, which is used to optimise the signal model for this analysis.

5.4.1 Final-state radiation recovery

The leptons in the $H \to ZZ^* \to 4\ell$ decay can emit Final-State Radiation (FSR) when interacting with the detector material or when bending in a magnetic field. If the FSR is energetic enough, the four-lepton invariant mass will show degradation in resolution, resulting in events shifting out of the mass window requirement. As a result, FSR recovery is needed to increase the yield in the signal region, and improve four-lepton mass resolution.

While the default ATLAS reconstruction algorithm for electrons recovers nearby FSR candidates, FSR from muons and FSR that are non-collinear to (or far from) electrons are not recovered. In this analysis, an explicit recovery algorithm is used to target and recover these FSR particles. For final states involving muons, FSR recovery is only applied to the leading pair of muons, and if the angular separation between photon and muon satisfies $\Delta R < 0.15$. Non-collinear FSR is considered for all leptons in all final states if the photons are sufficiently energetic (p_{T}>10 GeV) and are well separated from lepton (ΔR>0.15). A maximum of one FSR is recovered per quadruplet, and if multiple FSR candidates are identified, the preference is given to the one with the highest p_{T}.

From simulation, it is estimated that 3% of signal events are affected by FSR. By including these events and applying FSR recovery, the four-lepton invariant mass resolution is improved by about 1%. The m_{4l} distribution before and after FSR recovery for those signal events with an FSR photon is shown in Figure 5.2.

5.4.2 Z-mass constraint

In the SM $H \to ZZ^*$ decay, the Z with higher mass is more likely to be produced on-shell, while the other one is off-shell. Therefore, the Higgs mass resolution can be improved by imposing a Gaussian constraint on the kinematics of the leading lepton pair to the Breit-Wigner lineshape of the Z boson, and performing a likelihood fit based on the lepton kinematics and their associated errors. This methodology is referred to as the Z-mass constraint (ZMC), and it changes the momenta of the leading lepton pair within their uncertainties, such that the

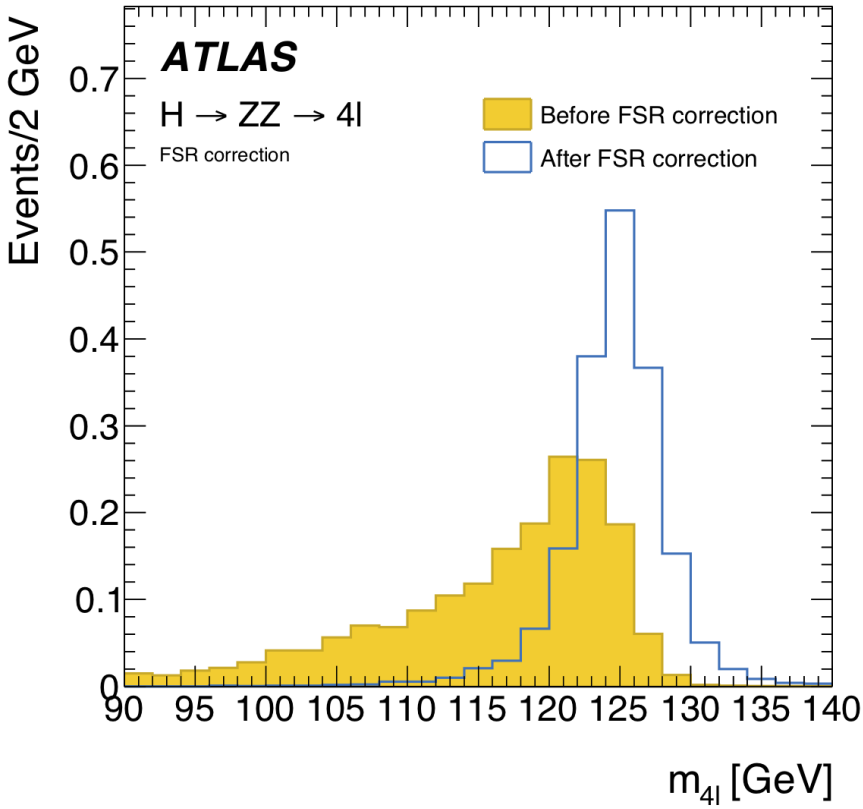

Figure 5.2: The unconstrained four-lepton invariant mass distribution for simulated Higgs candidates with FSR before (in yellow histograms) and after (in blue) FSR recovery. Only simulated events with an identified FSR are shown in this plot, which account for 3% of all signal events.

invariant mass is closer to that of the Z boson. For muons, ZMC uses the muon track covariance matrix, which contains the uncertainties on the fit parameters. The inclusion of the ZMC improves the resolution of m_{4l} by 17%. The resolution improvement after FSR recovery and subsequent ZMC can be seen in Figure 5.3.

Muon track error correction

The previous iteration of this analysis [148] saw a discrepancy between observed and simulated $m_{12}^{constrained}$ mass distribution. This effect is studied in $Z+l$ control regions [2], and is only observed in events where the Z boson decays into a pair of muons. The effect of the ZMC in the $Z+l$ control region is seen in Figure 5.4.

[2] This is a sample of leptons (e, μ) accompanying an on-shell Z boson decay to either electrons or muons. Further detail can be found in Ref [149]

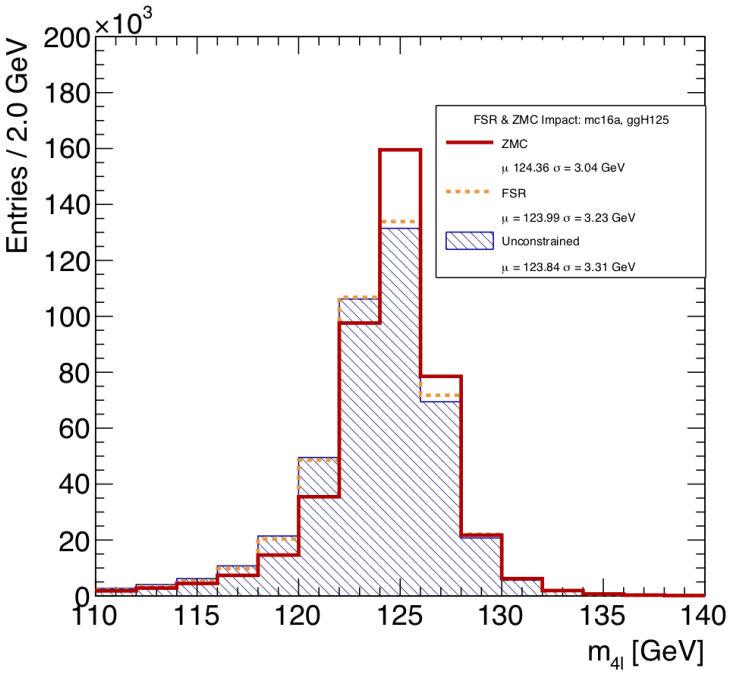

Figure 5.3: The m_{4l} distributions and the Gaussian fitted mean and resolution in a simulated ggH sample using 2015-2016 geometry with m_H set to 125 GeV. The unconstrained distribution (shaded blue histogram) shows the m_{4l} distribution for all events passing physics object and event selection as described in Section 5.2 and 5.3. The m_{4l} distribution after the FSR recovery is shown in the dashed yellow histogram, and shows $\tilde{2}$% improvement over the unconstrained m_{4l}. The m_{4l} distribution with both the FSR recovery and ZMC is shown in the solid red histogram, and shows $\tilde{8}$% improvement over the unconstrained m_{4l}. Reproduced from [148].

Each input variable to the ZMC is studied by comparing its data and MC distribution. This includes the individual kinematic variables and their associated uncertainties. The largest source of discrepancy is found in the uncertainty of the track momentum, $\sigma(q/p)$ (expressed as charge over momenta). For electrons, an energy resolution estimate is used as a ZMC input instead of $\sigma(q/p)$, resulting in no discrepancy between observed and simulated $m_{12}^{constrained}$.

Similar mismodelling of $\sigma(q/p)$ is observed in the $Z \to \mu\mu$ phase space. This in turn biases the ZMC method, resulting in a data/MC discrepancy in the leading di-muon mass. The source of $\sigma(q/p)$ mismodelling is currently being

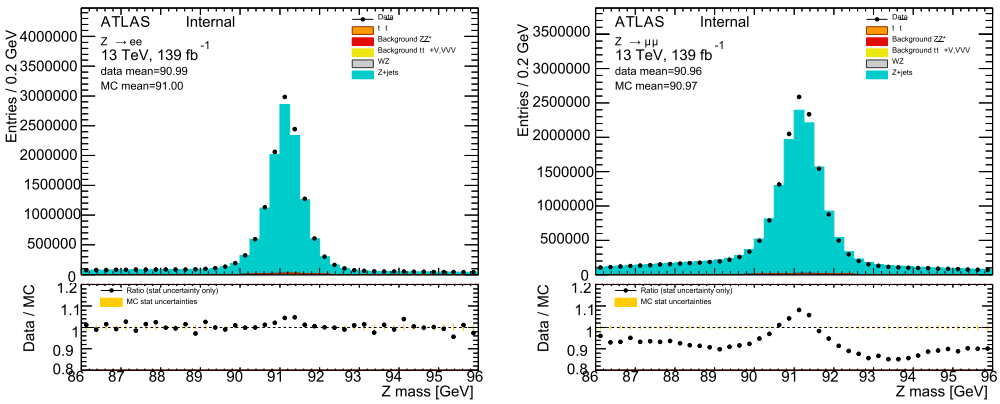

Figure 5.4: The constrained di-lepton mass distributions for the leading lepton pair in $(Z \to ee) + l$ (left) and $(Z \to \mu\mu) + l$ (right) control regions. The top panel shows the di-lepton mass distribution for data and simulated background processes, and the bottom panel shows the ratio between data and simulation with statistical uncertainty only. While the discrepancy in data and simulation remains lower than 4% for $(Z \to ee) + l$ events, it exceeds 10 % for $(Z \to \mu\mu) + l$ events, where a clear resolution mismodelling can be observed in the ratio plot. Reproduced from [148].

investigated by the tracking and muon combined performance group in ATLAS. For this analysis, practical solutions are developed to reduce $\sigma(q/p)$ mismodelling, and the following sections focus on the ones which the author contributed to.

Track error correction

A first attempt to correct $\sigma(q/p)$ is performed by deriving additional weights from the ratio between data and simulated muon $\sigma(q/p)$ distributions. This ratio is then interpolated for muon $\sigma(q/p)$ to obtain the associated weights to avoid the binning effect. To reduce any residual bias on muon kinematics, weights are derived in bins of p_T, η and ϕ. The binning is optimised to account for any local detector or kinematics effects, and ensure sufficient statistics in each bin for the study. The p_T-η-ϕ binning described in Equation 5.1-5.6 are therefore adopted.

$$p_T = \{10, 25, 35, 40, 45, 50, 60, 100, 300\} \text{ GeV}, \tag{5.1}$$

$$|\eta| = \{0, 0.4, 0.8, 1.05, 1.15, 1.25, 1.5, 1.7, 2.0, 2.1, 2.3, 2.5, 2.6\}. \tag{5.2}$$

For ϕ binning, the definition of small and large sector boundaries are used, where the large sectors are defined as:

$$(0.180+k\times0.785<\phi<0.180+k\times0.785)\vee(\phi>2.960\wedge\phi<2.960), \text{ for } |\eta|<1.05, \tag{5.3}$$

$$(0.131+k\times0.784<\phi<0.131+k\times0.784)\vee(\phi>3.011\wedge\phi<3.011), \text{ for } |\eta|>1.05, \tag{5.4}$$

where $k\in\mathbb{Z}\cap[-3,3]$. The small sector boundaries are defined as:

$$0.180+k\times0.785<\phi<0.605+k\times0.785, \text{ for } |\eta|<1.05, \tag{5.5}$$

$$0.131+k\times0.784<\phi<0.655+k\times0.784, \text{ for } |\eta|>1.05, \tag{5.6}$$

where $k\in\mathbb{Z}\cap[-4,3]$. The data/MC $|\sigma(q/p)|$ distribution before and after reweighting is shown in Figure 5.5. Additionally, the p_T distribution after $|\sigma(q/p)|$ reweighting is also studied for any potential bias on the lepton p_T, which is also shown in Figure 5.5.

As shown in Figure 5.5, the muon-level reweighting method reduces the data/MC $\sigma(q/p)$ mismodelling to sub % level, without distorting the p_T distribution. Muon-level reweighting ultimately was not used in this analysis iteration, but it sets the basis for the method that was ultimately adopted: the quantile mapping method.

The principle for quantile mapping follows that of inverse transform sampling, which is a non-parametric method that utilises the CDF to transform any given distribution. For the $\sigma(q/p)$ correction, the CDF of MC is matched to that of data:

$$CDF_{MC,corr}(\sigma(q/p))=CDF_{data}(\sigma(q/p)). \tag{5.7}$$

To obtain the value of the corrected $\sigma(q/p)$ from uncorrected $\sigma(q/p)$, a map is constructed using CDF_{data} and $CDF_{MC,uncorr}$ as follows:

$$\sigma(q/p)_{corr}=CDF^{-1}_{data}(CDF_{MC,uncorr}(\sigma(q/p)_{uncorr})), \tag{5.8}$$

where the function composition $CDF^{-1}_{data}(CDF_{MC,uncorr})$ maps the uncorrected $\sigma(q/p)$ to that of data. Therefore, the uncorrected $\sigma(q/p)$ would be assigned to

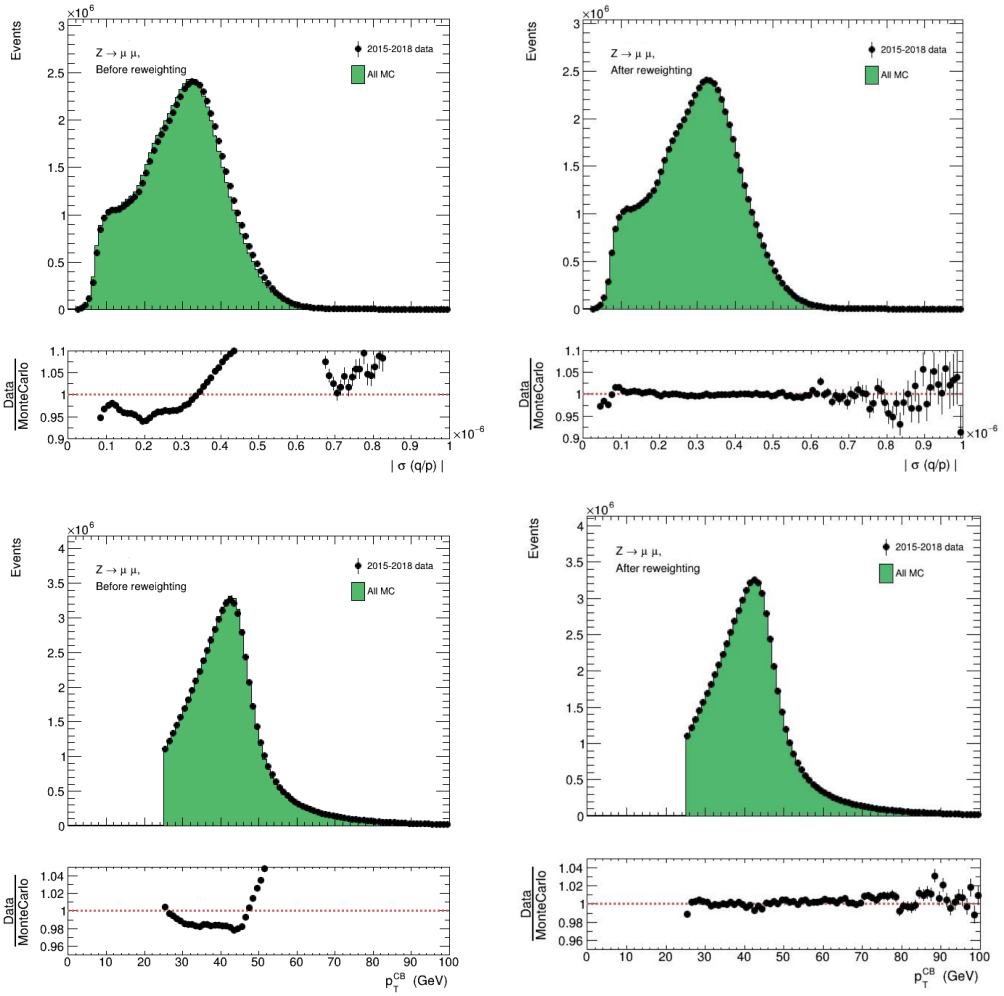

Figure 5.5: The $|\sigma(q/p)|$ (top) and leading muon p_{T} (bottom) distributions for combined muon track before (left) and after (right) kinematic reweighting. The cut at 25 GeV in p_{T} is a result of the event selection applied for the $Z+l$ control region. The top panel shows the distributions of each variable in data and simulation, and the bottom panel shows the ratio between data and simulation with their combined statistical error. The $|\sigma(q/p)|$ discrepancy after reweighting is reduced to below percent level without distorting the p_{T} distribution of the leading muon.

the $\sigma(q/p)$ in data with corresponding quantiles. This map is derived in intervals of 0.25% and interpolated for each muon. Additionally, as $\sigma(q/p)$ strongly depends on momentum, the relative track error, $\sigma(q/p)^{rel} = \frac{\sigma(q/p)}{(q/p)}$ is used for map derivation. The p_T, η and ϕ binning defined in Equation 5.1-5.3 are adopted to derive the maps. An illustrated example of quantile mapping is shown in Figure 5.6

This method corrects the constrained Z mass peak, and the remaining discrepancies are understood to arise from the generator-level kinematic mismodelling.

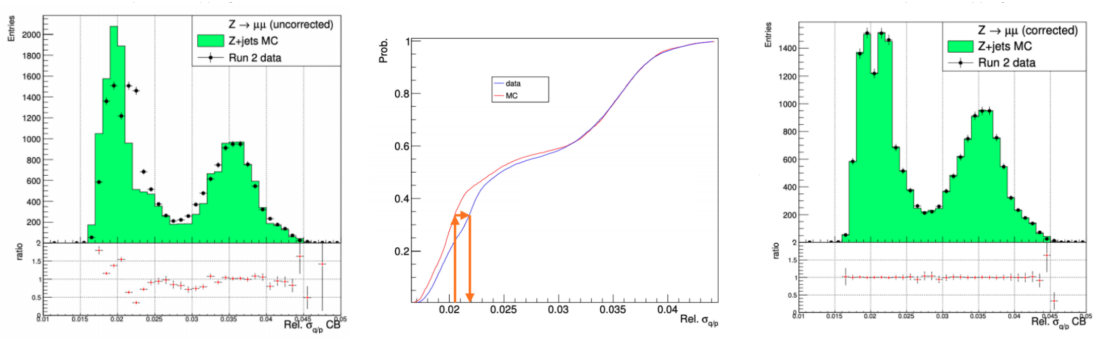

Figure 5.6: The $\sigma(q/p)^{rel}$ distributions in 2015-2018 data and simulated samples in $Z \rightarrow \mu\mu + l$ control regions. The right-most and the left-most plots show the distribution of $\sigma(q/p)^{rel}$ before and after quantile mapping along with the ratio between data and simulated events. The middle plot shows the cumulative distribution function for data and simulation, along with an illustration (orange arrows) for how the correction is derived as described in Equation. 5.8.

After the correction is applied (as shown in Figure 5.7), the mean of the m_{4l} uncertainties increases compared to when the uncorrected track errors were used, which suggests that the previous iteration of the HZZ mass measurement underestimated the impact of $\sigma(q/p)$. The other kinematic variables are unaffected by the correction. The four-lepton invariant mass peak with the FSR and corrected ZMC method applied is shown in Figure 5.8.

5.4.3 Signal-background discriminant

A high signal-background ratio can reduce the uncertainty on m_H by removing the impact of the statistical fluctuations in the background model. The use of machine learning algorithms can aid in this by creating a discriminant that can improve the signal-background ratio.

Deep learning refers to a large class of machine learning algorithms that use multiple layers of nonlinear processing units, or nodes, to discriminate and or to regress an output. An introduction and review of deep learning's application in particle physics can be found in Ref [151]. Tensorflow [152] is an open-source library that can be used for deep learning and Keras [153] is a Python API capable of running it that allows for rapid experimentation with different network architectures and hyper-parameters. These tools were used

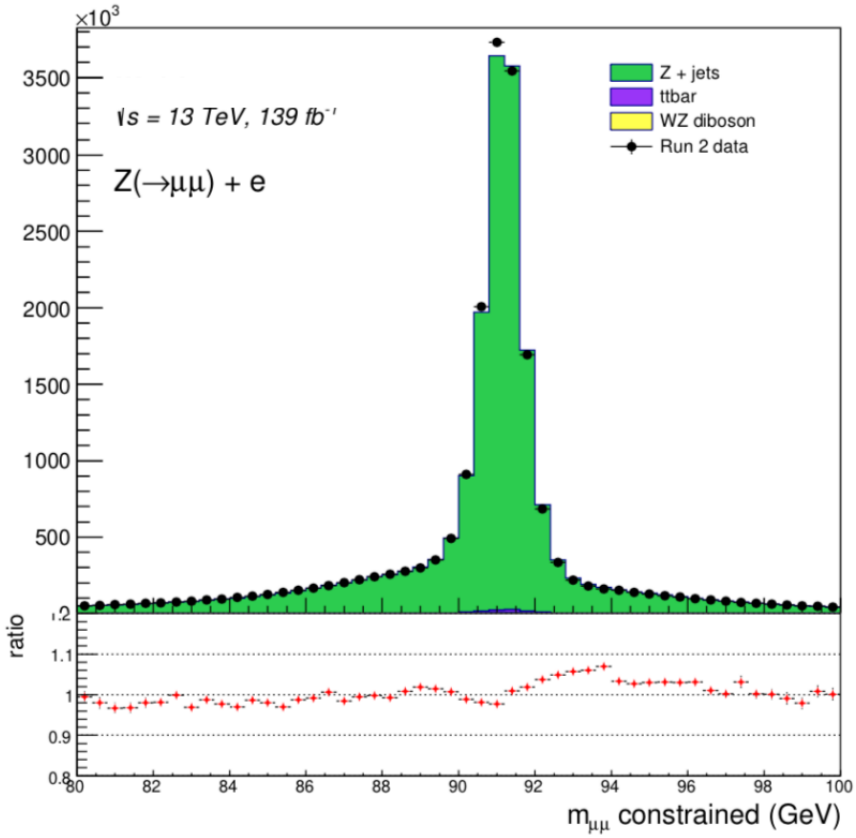

Figure 5.7: The di-lepton mass distributions in 2015-2018 data and simulated samples in $Z \to \mu\mu + e$ control regions after ZMC correction and quantile mapping. The top panel shows the di-muon mass distributions in data and simulation, and the bottom panel shows the ratio between data and simulation with their combined uncertainty.

to train the Neural Network (NN) to classify signal and background to further improve the signal-background ratio in this analysis.

The classifier NN_{ZZ}^{disc} was trained separately for same-flavour (4μ and $4e$) and opposite-flavour ($2\mu 2e$ and $2e2\mu$) final states. The training variables were the four-lepton transverse momentum, $p_T^{4\ell}$, four-lepton pseudorapidity, $\eta_{4\ell}$, and $KD\,(ZZ^*)$. The definitions for both $p_T^{4\ell}$ and $\eta_{4\ell}$ at training and evaluation account for the FSR recovery but exclude the ZMC. $KD\,(ZZ^*)$ is a kinematic discriminant based on the calculated matrix elements, accurate to leading order, for ggH production and SM ZZ production using MadGraph5_aMC@NLO:

$$KD\,(ZZ^*) = ln\left(\frac{|M_{ggH}|^2}{|M_{ZZ}|^2}\right). \tag{5.9}$$

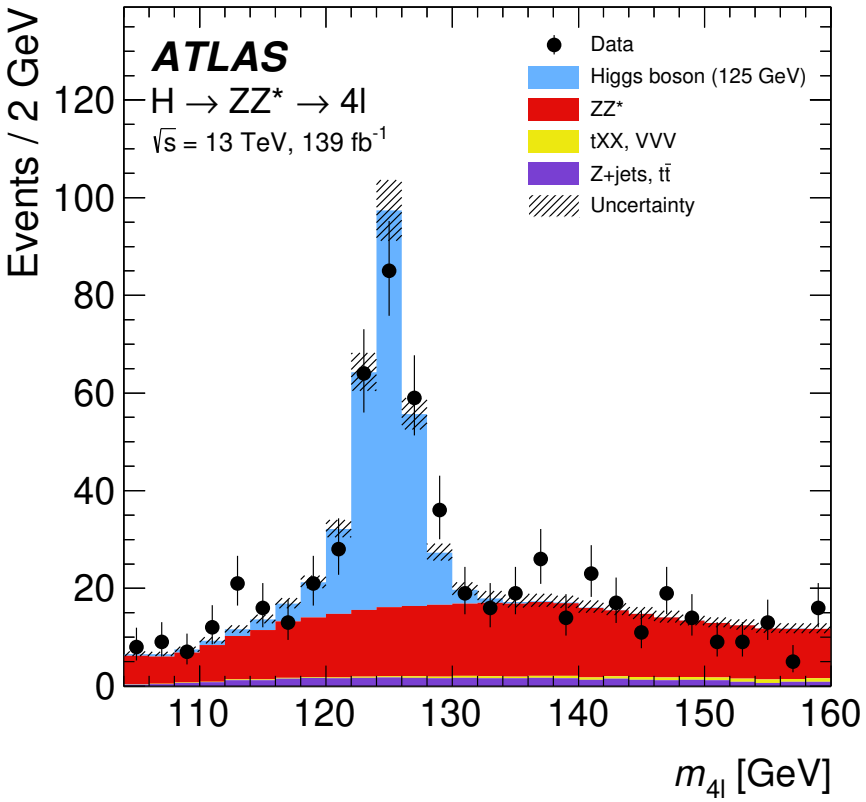

Figure 5.8: The observed and expected $m_{4\ell}$ distributions in the signal region. The simulated events are taken from simulation of $H \to ZZ^* \to 4l$ (at $m_H = 125$ GeV), ZZ^*, tXX and VVV processes, and from a data-driven estimate for the Z+jets and $t\bar{t}$ backgrounds. The hatched band shows the total uncertainty in the simulated events, which includes the theoretical uncertainty of the SM cross-section for the signal and the ZZ^* background. Reproduced from [150].

This discriminant enhances the signal significance in the m_H measurement as it separates signal and background events based on decay properties and the enhancement is comparable across all Higgs production modes. The distributions of D_{NN} in the signal region are shown in Figure 5.9.

5.4.4 Per-event resolution

Each Higgs candidate differs in its event topology and detector response, which further increases the error on m_{4l}. In addition, the error on m_{4l} is propagated from the lepton kinematic measurements, which are poorly modelled in the simulation as discussed in Section 5.4.2. To improve on these sources of m_{4l}

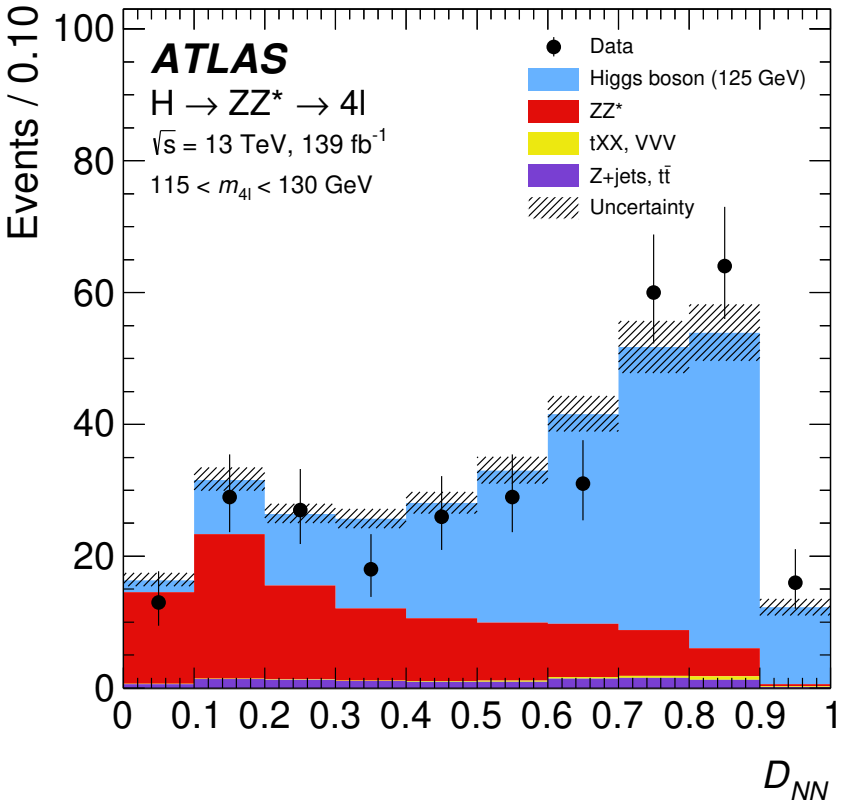

Figure 5.9: The observed and expected D_{NN} distributions in the signal region. The simulated events are taken from simulation of $H \to ZZ^* \to 4l$ (at $m_H = 125$ GeV), ZZ^*, tXX and VVV processes, and from a data-driven estimate for the Z+jets and $t\bar{t}$ backgrounds. The hatched band shows the total uncertainty in the simulated events, which includes the theoretical uncertainty of the SM cross-section for the signal and the ZZ^* background.

error, a per-event resolution σ_i is derived based on a quantile-regression neural network (QRNN). This network is trained on simulated signal events using the Tensorflow library and the Keras python interface, and it aims to predict a given quantile of the $|m_{4l}^{constrained} - m_{4l}^{truth}|$ distribution, where m_{4l}^{truth} is the truth-level information from the simulated events. The target quantile is calibrated by scanning 10 target quantiles between 56% and 68%, and deriving a scale factor which produces 68% confidence-level intervals on the simulated events. The QRNN is trained separately for each final state, and the inputs are p_{T}, η and ϕ of the individual leptons, as well as constrained four-lepton momentum and its uncertainty. The distribution of σ_i in the signal region is shown in Figure 5.10.

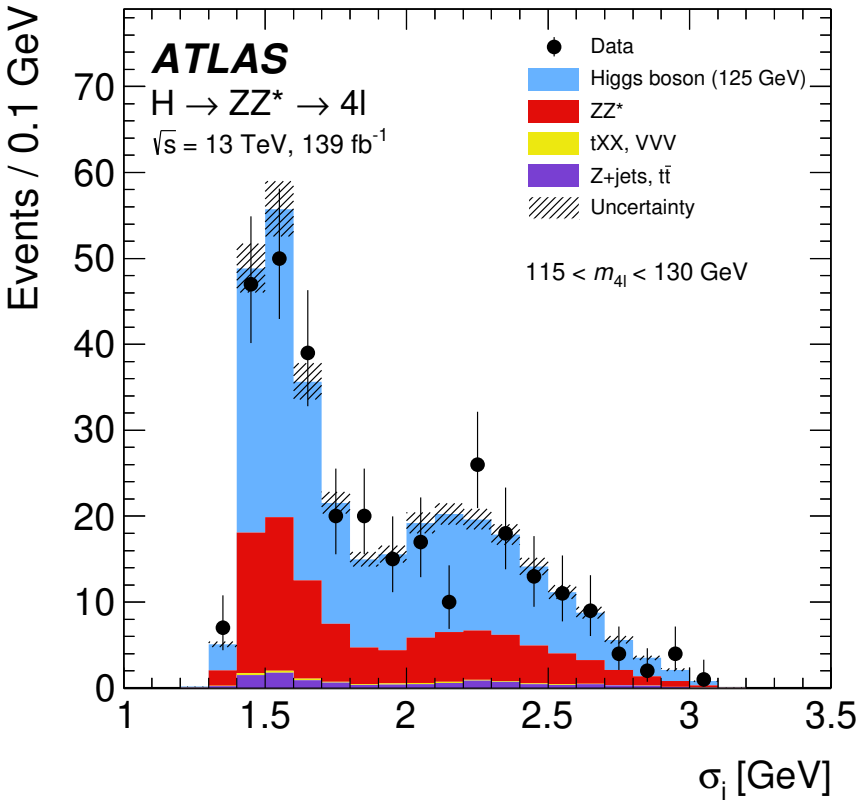

Figure 5.10: The observed and expected σ_i distributions in the signal region. The simulated events are taken from simulation of $H \to ZZ^* \to 4l$ (at $m_H = 125$ GeV), ZZ^*, tXX and VVV processes, and from a data-driven estimate for the Z+jets and $t\bar{t}$ backgrounds. The hatched band shows the total uncertainty in the simulated events, which includes the theoretical uncertainty of the SM cross-section for the signal and the ZZ^* background. The double peak structure in the σ_i distribution originated from the difference in resolution for each final state. The 4μ and $2\mu 2e$ events typically have σ_i 1.5 GeV, while the $2e2\mu$ and $4e$ events typically have σ_i 2.1 GeV due to the difference between electron resolution and muon resolution.

5.5 Signal modelling

The $H \to ZZ^* \to 4\ell$ signal is modelled using a combination of analytical function for the m_{4l} shape, with a histogram-based shape estimation for D_{NN}. Parameters for the analytical function are determined from a maximum-likelihood fit to the simulated events. The normalisation for this signal analytical function is then determined with the background normalisation by fitting to data. The signal model is derived separately for each final state.

As the main aim of this analysis is to further reduce the statistical uncertainty

on m_H, it is useful to include implicit and explicit dependencies of other variables in the signal modelling. These variables include the true Higgs mass m_H, signal-background discriminant D_{NN}, and per-event resolution σ_i as described in Section 5.4.

The signal probability density function is defined as:

$$P(m_{4l}, D_{NN}, \sigma_i | m_H) = P(m_{4l} | D_{NN}, \sigma_i, m_H) \times P(D_{NN} | \sigma_i, m_H) \times P(\sigma_i | m_H)$$

$$\approx P(m_{4l} | D_{NN}, \sigma_i, m_H) \times P(D_{NN} | m_H), \tag{5.10}$$

where the following approximations are made:

1. $P(D_{NN}|\sigma_i, m_H) \approx P(D_{NN}|m_H)$ as the discriminant has no explicit dependencies of σ_i.

2. $P(\sigma_i|m_H) \approx P(\sigma_i)$ as the per-event resolution does not depend on m_H.

3. $P(\sigma_i)$ is omitted from the signal model as its distributions are similar in signal and background regions.

The first term in Equation 5.10 describes the signal shape projected in the four-lepton invariant mass. Since the width of the Higgs boson (4.1 MeV) is 300 times smaller than the detector resolution at the Higgs peak, the signal shape is dominated by the detector response. This simplifies the signal model to a detector response function with a shifted mean to model the shape.

The convolved Higgs peak is modelled with a double-sided crystal ball (DSCB) function, with a Gaussian peak and power law tails on both sides,

$$DSCB = N \times \left\{ \begin{array}{ll} exp(\left(- \frac{(m_{4\ell} - \mu)^2}{2\sigma^2} \right)), & \text{for } \alpha_{low} \leq \frac{(m_{4\ell} - \mu)}{\sigma} \leq \alpha_{hi} \\ A_{low} \times B_{low}, & \text{for } \frac{(m_{4\ell} - \mu)}{\sigma} < \alpha_{low} \\ A_{high} \times B_{high}, & \text{for } \frac{(m_{4\ell} - \mu)}{\sigma} > \alpha_{hi} \end{array} \right\}, \tag{5.11}$$

where N is the normalisation constant of the function, μ and σ are the mean and sigma of the central Gaussian distribution. A and B are the exponential and the power-law tails respectively,

$$A = \frac{n}{|\alpha|} \times exp\left(- \frac{|\alpha|^2}{2} \right), \tag{5.12}$$

$$B = (\frac{n}{|\alpha|} - |\alpha| - \frac{(m_{4\ell} - \mu)}{\sigma})^{-n}, \tag{5.13}$$

where α and n are fit parameters on either the low or the high side. α_{low} (α_{hi}) is the point where the function transitions from the core to the tails, which is defined by n_{low} (n_{high}) power laws on the lower (higher) mass spectrum. The low-mass tail of the $m_{4\ell}$ spectrum is typically longer, due to the additional uncertainty in energy loss for low momentum leptons. The higher mass tail is typically sharper due to the application of FSR recovery and ZMC.

Additionally, the mean of the Gaussian core μ is parametrised as a function of m_H and D_{NN} as follows:

$$\mu = a^{\mu}(m_H - 125 \text{ GeV}) + b^{\mu}(D_{NN}) \text{ GeV}, \tag{5.14}$$

where a^{μ} and $b^{\mu}(D_{NN})$ are fitted parameters from simulated m_H mass points ranging from 123 GeV to 127 GeV as described in Section 5.1, calculated for each final state. The a^{μ} term reduces the dependency of $m_{4\ell}$ on m_H, while $b^{\mu}(D_{NN})$ absorbs the sub-channel dependency on D_{NN}. The dependency of b^{μ} on D_{NN} is parametrised as a linear function for $2e2\mu$ and $4e$, and a combination of linear and exponential decay for the other two final states.

The dependency in D_{NN} is explicitly isolated in the second term of equation 5.10. $P(D|m_H)$ accounts for any residual dependencies of the discriminant on m_H. This PDF is created by interpolating the discriminant distribution from m_H mass points between 123 GeV to 127 GeV using ggH, VBF and VH simulated samples. This is interpolated using a non-linear moment morphing method [82] at intervals of 200 MeV.

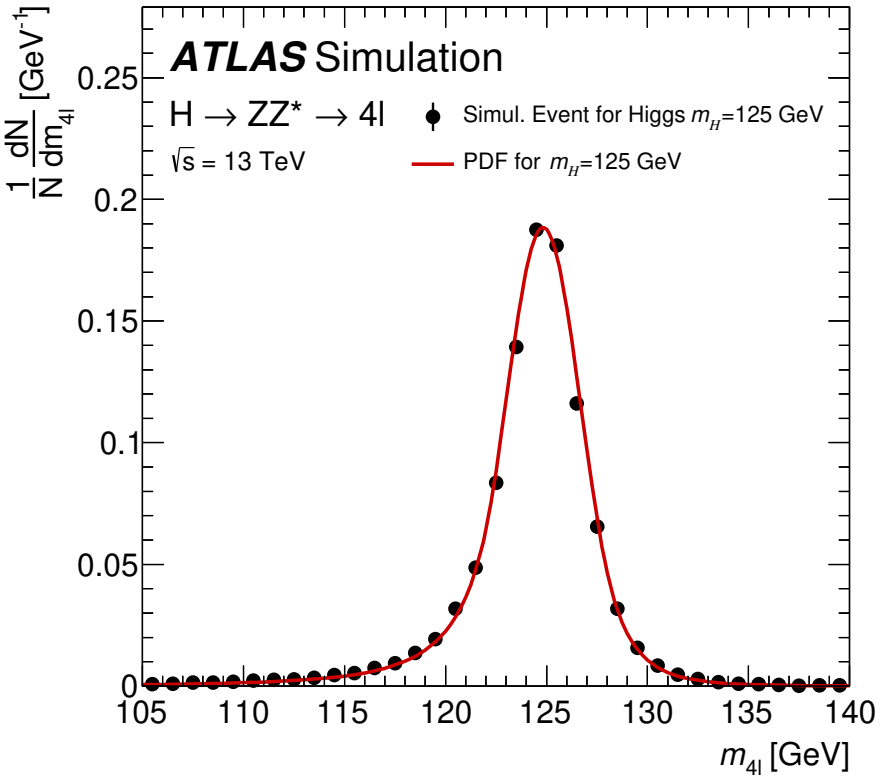

Figure 5.11: The probability density function derived from simulation (red line) and the distribution of simulation (black dots) in m_{4l} for $H \to ZZ^* \to 4\ell$ with $m_H = 125$ GeV. The probability density functions are derived separately for each final state, and summed together using the predicted yields. Both the probability density function and the distribution are normalised to unity.

The signal normalisation is determined through a maximum likelihood fit to data, with the four final states treated independently. The signal model can be seen in Figure 5.11.

5.6 Background modelling

Despite the large S/B ratio in the $H \to ZZ^* \to 4\ell$ channel, it is crucial to model the background processes accurately to reduce biases on the measured value of m_H. Since the signal-background discriminant D_{NN} is trained against the non-resonant ZZ^* background, the background modelling must include the D_{NN} variable to account for any residual correlation between D_{NN} and m_{4l}. Similar

to the signal model, the background processes can be modelled as:

$$\begin{aligned} P(m_{4l}, D, \sigma_i | m_H) &= P(m_{4l}, D | \sigma_i, m_H) \times P(\sigma | m_H) \\ &\approx P(m_{4l}, D) \times P(\sigma) \\ &\approx P(m_{4l}, D), \end{aligned} \tag{5.15}$$

where the following assumptions are made:

1. Minimum interference between background and signal processes, which leads to negligible m_H dependencies.

2. Neither D nor m_{4l} depends on σ_i in the background region, which leads to negligible σ_i dependencies.

3. $P(\sigma_i)$ is omitted from the background model as its distributions are similar in the signal and background regions.

The background processes in this analysis consist of a wide, non-resonant peak around m_{4l} and D_{NN} due to the kinematic selection and application of ZMC, they are therefore difficult to model analytically. As a result, an adaptive Kernel Estimation technique is used to generate 2D probability density functions (PDFs) for each background process and each final state.

2D PDFs for the ZZ^* and $tXX + VVV$ are constructed using simulated events for each final state. For Z+jets, data from dedicated control regions are used to reconstruct 2D PDFs [154]. The PDFs are generated using an adaptive kernel estimation technique with Gaussian kernels [155] to reduce fluctuations and boundary effects.

Gaussian kernels are used for the adaptive kernel estimation. The parameter ρ corresponds to the width of each Gaussian kernel, and therefore controls how much feature from the original dataset is captured by the 2D PDF. ρ is tuned by minimising the residual error between the PDF and simulation, which is performed separately for each process and final state. An example background model for the $qqZZ$ process is shown in Figure 5.12.

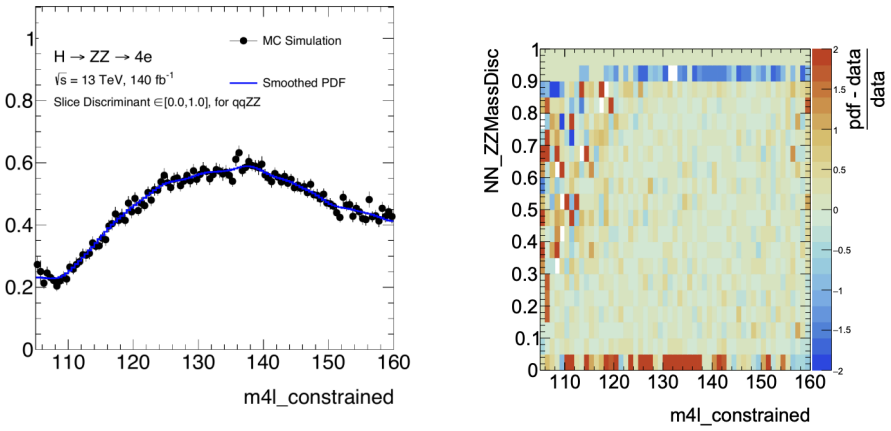

Figure 5.12: The probability density function for the $qqZZ$ process in the $4e$ final state. The left plot shows the 1D projection on $m_{4\ell}$ of the PDF (blue lines) and the simulated distribution. The right plot shows the fractional difference between the PDF and the simulated distribution in bins of $m_{4\ell}$ and D_{NN}.

The normalisation of the non-resonant ZZ^* background is extracted from directly fitting the 2D PDF to data for each sub-channel. The normalisation for reducible backgrounds, including $Z + jets$, $t\bar{t}$ and WZ, are estimated using data-driven estimation techniques [149]. Lastly, the tVV and VVV backgrounds contribute less than 0.5% of the signal region, and their normalisations are taken directly from simulation.

5.7 Results

The Higgs mass is measured by maximising the profile-likelihood ratio:

$$\lambda(m_H) = \frac{\mathcal{L}\left(m_H, \hat{\hat{\theta}}(m_H)\right)}{\mathcal{L}\left(\hat{m}_H, \hat{\theta}\right)}, \tag{5.16}$$

where $\hat{m}_H$ and $\hat{\theta}$ denote the unconditional maximum-likelihood estimates of the parameters of the likelihood function $\mathcal{L}$, while $\hat{\hat{\theta}}$ is the conditional maximum-likelihood estimate of the parameters θ for the parameter of interest, m_H.

The estimate of m_H is extracted using an unbinned maximum-likelihood method to the four sub-channels in m_{4l} for 105< $m_{4\ell}$ <160 GeV, with the free parameters being m_H and signal and background normalisation parameters.

The nuisance parameters are also allowed to float, albeit constrained by their priors. Tables 5.5 and 5.6 show the expected and observed events for signal and background processes in the extended region of 105< $m_{4\ell}$ <160 GeV, and the signal region of 115< $m_{4\ell}$ <130 GeV respectively.

Table 5.5: The expected and observed yields for 105< $m_{4\ell}$ <160 GeV.

Final state	signal	ZZ*	Reducible backgrounds	tXX	Total	Observed
4μ	81 ± 5	124 ± 9	7.5 ± 0.5	3.4 ± 0.4	215 ± 9	217
$2e2\mu$	56.0 ± 3.3	83 ± 6	8.8 ± 0.6	2.40 ± 0.22	151 ± 6	169
$2\mu2e$	43.1 ± 3.1	64 ± 7	9.3 ± 1.6	2.27 ± 0.29	119 ± 6	115
$4e$	38.9 ± 2.9	55 ± 7	7.5 ± 1.0	2.11 ± 0.25	104 ± 6	103
Total	219 ± 13	326 ± 28	33.5 ± 2.9	10.2 ± 1.0	589 ± 25	604

Table 5.6: The expected and observed yields for 115< $m_{4\ell}$ <130 GeV.

Final state	signal	ZZ*	Reducible backgrounds	tXX	Total	Observed
4μ	78 ± 5	38.7 ± 2.8	2.23 ± 0.16	0.61 ± 0.07	120 ± 5	115
$2e2\mu$	53.4 ± 3.2	26.7 ± 1.8	2.62 ± 0.19	0.40 ± 0.04	83.1 ± 3.5	94
$2\mu2e$	41.2 ± 3.0	17.9 ± 1.7	3.0 ± 0.5	0.36 ± 0.05	62.5 ± 3.3	59
$4e$	36.2 ± 2.7	15.8 ± 2.0	2.45 ± 0.34	0.38 ± 0.04	54.8 ± 3.2	45
Total	209 ± 13	99.1 ± 8.0	10.5 ± 0.9	1.75 ± 0.18	321 ± 14	313

The combined measurement of m_H in the $H \to ZZ^* \to 4\ell$ channel is:

$$m_H = 124.99 \pm 0.19 = 124.99 \pm 0.18(\text{stat.}) \pm 0.04(\text{syst.}) \quad \text{GeV}. \tag{5.17}$$

The statistical uncertainty is estimated by fixing all nuisance parameters associated with systematic uncertainties, and leaving all other parameters unconstrained. Figure 5.13 shows the distribution of data together with the fitted lineshapes. The small fluctuation is the result of the 1D projection of the background models, and has negligible impact on the m_H fit value.

Systematic uncertainties originate from two primary sources: the experimental uncertainty and the modelling uncertainties. The experimental uncertainties incorporate the limited understanding of the detector, the reconstruction of events, and the calibration of relevant kinematics quantities The modelling uncertainties parametrises the error in simulating the signal and background processes. Both types of systematic uncertainties are modelled by introducing nuisance parameters θ_i (one for each source of systematic uncertainty) in the likelihood

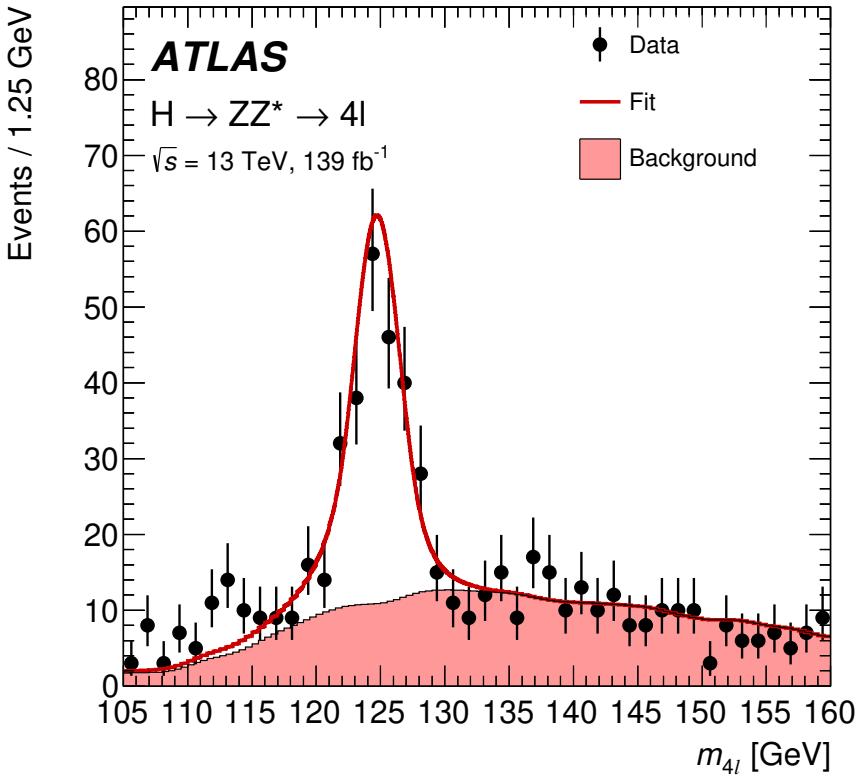

Figure 5.13: The fitted probability density function from simulation (red line) and the data distribution in $m_{4\ell}$ for all subchannels combined. The probability density function is projected to $m_{4\ell}$ for display purposes. The background component is shown separately (shaded red).

function, with Gaussian or log-normal functions that reflect the uncertainties associated with the nuisance parameters. The number of nuisance parameters is determined by recommendations from individual combined performance groups. For muon momentum calibration, 5 nuisance parameters are used, including contribution from sagitta bias, scale and resolution correction. The full systematic scheme for electron energy scale and resolution is used, which includes 74 nuisance parameters, covering effects in different regions of the ATLAS detector.

The impact for each source of systematic uncertainty is then evaluated by shifting θ to $\pm 1\Delta\theta$, performing the fit on m_H, and calculating the difference in m_H between nominal θ ($\hat{\theta}$) and the shifted θ. The impact of each uncertainty is evaluated both before fitting the normalisation parameters for each signal and background process (known as the pre-fit effect), and after fitting the

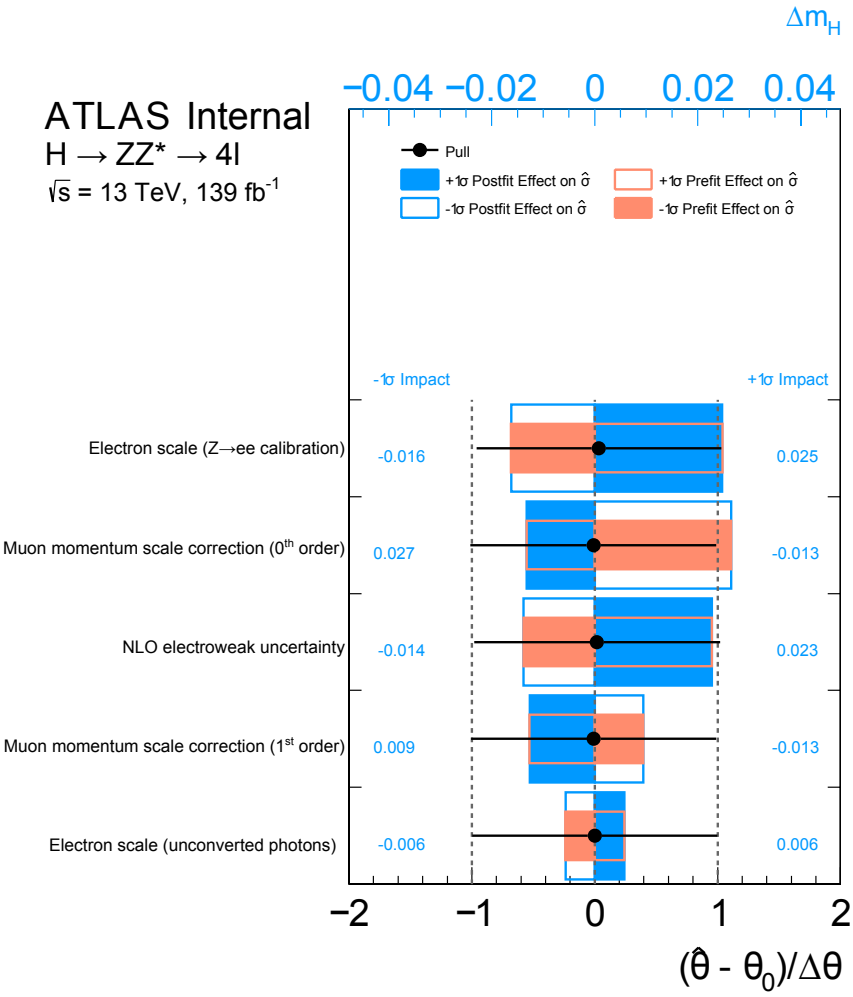

Figure 5.14: Systematic uncertainties on m_H ranked by their magnitude. The orange (blue) bars show the pre-fit (post-fit) effect of the systematics, and the size of their impact is shown at the top of the figure. The black dotted lines show the mean and error on the pull, with their impact indicated by the scale at the bottom of the figure. Systematics with less than 5 MeV impact on m_H are omitted from this plot.

normalisation parameters (known as the post-fit effect). The full systematic uncertainty ranking can be seen in Figure 5.14.

As shown in Figure 5.14, the main sources of systematic uncertainties are the electron energy scale measurement, the muon momentum scale measurement, and the signal modelling associated with the electroweak process.

For electron energy scale, the largest source of uncertainty is correlated to the method used to extract the scale correction using $Z \to ee$ decays. This includes the mass window variation, event and electron selection, efficiencies

associated with the trigger, identification and reconstruction, and modelling uncertainties for the $Z \to ee$ process. The second largest electron energy scale uncertainty is associated with misidentifying unconverted photons (those which did not convert into an electron-positron pair before entering the calorimeter) as electrons. Further details on the electron energy scale calibration can be found in Ref. [146]-[143].

The muon momentum scale uncertainty has been discussed extensively in Chapter 4. Here, the two systematic uncertainties are associated with the parameterisation of the muon momentum scale correction and its p_{T} dependency, whether it is the 0th, or the 1st order correction. These both include uncertainties associated with the fit procedure, including mass window variation, impact of using only the J/ψ or Z peak to perform the calibration, p_{T} binning, and generator effects.

An additional systematic uncertainty is included as the NLO electroweak uncertainty in the Higgs decay. This accounts for the uncertainty in electroweak corrections in the FSR emission, which induce variations in the measured value of m_H. The impact of this systematic uncertainty is evaluated by producing alternative simulated samples from Prophecy4f [156] and Hto4l [157, 158].

The measured value of m_H in each subchannel and their negative log-likelihood scans are shown in Figure 5.16. Overall, good agreement is observed between each subchannel, with the p-value between each fit measured at 0.8. The result of this measurement is combined with the same measurement in Run 1 of ATLAS operation to further constrain the uncertainty on m_H, and is shown in Figure 5.16. Only the lepton measurement systematics are considered to be correlated, due to the sustained detector condition. In this combination, the electron calibration uncertainty is correlated between the two runs, while the muon calibration uncertainty is treated independently due to the improvement in Run 2 as described in 4.3.3.

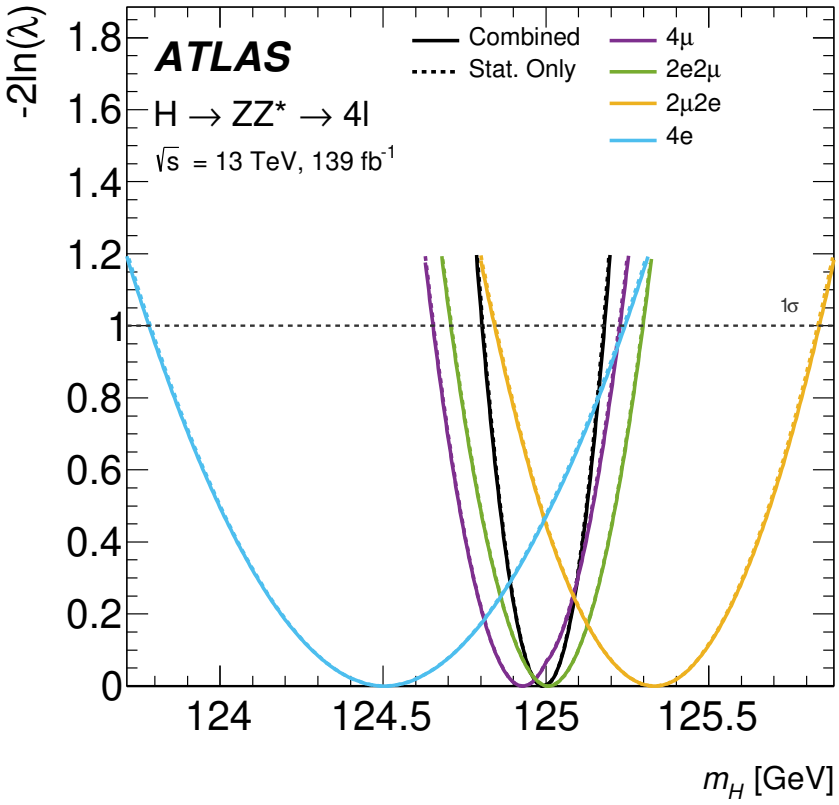

Figure 5.15: The negative log-likelihood scan in each subchannel of the fit, along with the combined fit. The scan with only the statistical uncertainty for each subchannel is shown by a dashed line, and the fit with both statistical and systematic uncertainty is shown by a solid line. The horizontal line represents 1σ uncertainty.

The combined result, calculated by combining the likelihoods of the two measurements is:

$$m_H = 124.94 \pm 0.18 = 124.94 \pm 0.17(\text{Stat.}) \pm 0.03(\text{Sys.}) \quad \text{GeV}. \tag{5.18}$$

which has slightly smaller statistical and systematic uncertainties than the Run 2 result alone. The p-value from combining the two measurements is 0.4.

This compares to the CMS full Run 2 measurement of the m_H of $m_H = 125.04 \pm 0.12$ GeV $= 125.04 \pm 0.11(\text{stat.}) \pm 0.05(\text{syst.})$ GeV, with the Run 1 and Run 2 combination result at $m_H = 125.08 \pm 0.12$ GeV $= 125.08 \pm 0.10(\text{stat.}) \pm 0.05(\text{syst.})$ GeV [159]. This measurement benefited the larger magnetic field of the CMS solenoid, translating directly to a better mass resolution for four lepton system and thus a reduced statistical uncertainty compared to the ATLAS

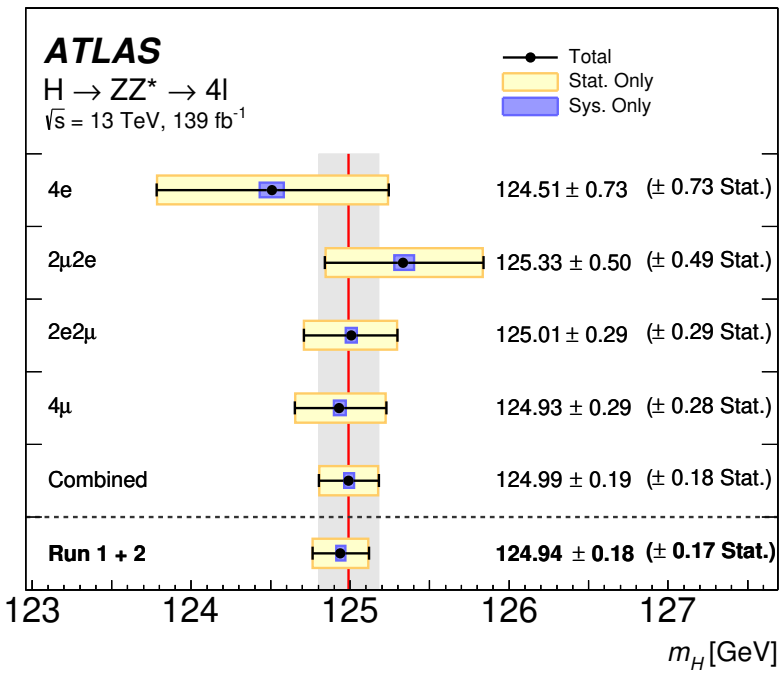

Figure 5.16: The fit result in each final state, along with the combined result. The coloured bars on each point show the combined statistical and systematic uncertainty, while the results in brackets show the statistical uncertainty only. The vertical red line represents the combined Run 2 result, with the grey band as its total uncertainty.

measurement. In contrast, the fraction of the total uncertainty budget that is due to systematic uncertainty is reduced by 20% in the ATLAS measurement compared to the CMS result, indicating the effectiveness of ATLAS muon momentum and electron energy scale calibrations.

Chapter 6

Physics beyond Run 2

The physics results discussed presented in the preceding chapters, including the muon combined performance (Chapter 4) and the Higgs mass measurement (Chapter 5), use the 139 fb^{-1} dataset collected during ATLAS Run 2. Run 2 was succeeded by Long shutdown 2 (LS2), during which the accelerator complex was not operating, thus allowing for maintenance activities and upgrades to be carried out to the LHC and the LHC experiments. This is especially important for the experiments to anticipate the challenges in the planned High-Lumi LHC (HL-LHC) upgrade, which will see a much higher pileup, leading to additional challenges of greater radiation hardness and faster electronics. These challenges are anticipated and partially addressed by the ATLAS experiment during LS2, by activities including partial upgrades to the readout electronics, upgrades to the tracking software, and the installation of the New Small Wheel (NSW).

For ATLAS analyses, it is crucial to understand the impact of these activities on the measurements of reconstructed objects, ranging from reconstructed tracks to reconstruction of Higgs boson candidates. The upgrades to the magnet systems of the LHC also allowed for safe operation at an increased centre-of-mass energy of $\sqrt{s} = 13.6$ TeV, allowing for measurements of Higgs boson cross-section at an unprecedented energy. The following sections provide a brief overview of the ATLAS LS2 activities, especially the ones most relevant to physics analyses. The data-taking period after LS2 was completed commenced in July 2022, and is referred to as Run 3. The following sections also highlight the author's

main contribution towards muon calibration for the 2022 data and an early measurement of the fiducial cross-section for $H \to ZZ^*$.

6.1 Overview of the Run 3 ATLAS upgrades

The Run 3 peak luminosity is expected to reach 2×10^{34} cm^{-2}s^{-1}, corresponding to an average pileup between 55 to 65 with 25 ns bunch spacing [160]. The level of pileup, as well as the level of radiation damage, are well beyond the original design goals of the ATLAS experiment, therefore extensive hardware and software upgrades are required for physics measurements in Run 3 and HL-LHC [160]. This is referred to as the Phase-I upgrade of ATLAS, with the main upgrade activities highlighted below:

- *Installation of muon New Small Wheels (NSW)*: The NSW is the upgrade to the Small Wheel system in Run 2. This is necessitated by the higher than expected cavern background radiation level in the Small Wheel region, the high rate of low momentum fake triggers, and the need for precision tracking, specifically in anticipation of HL-LHC. The NSW has two chamber technologies, with one devoted to the Level-1 trigger function (small-strip Thin Gap Chambers, or sTGC), and the other to precision tracking (micromegas detectors, or MM). Both technologies are capable of trigger function, and withstanding high background radiation up to 15 kHZ/cm^2. The NSW also utilises the FELIX readout system [161] to avoid saturation in the readout links [160, 162]. The NSW was in the commissioning phase in the 2022 data-taking period. As a result, the NSW is not included in the trigger system in 2022. In the context of object reconstruction, the NSW hits are used for muon track reconstruction, with more stringent requirements imposed on those muons that traversed the NSW. Further details are discussed in Section 6.2.

- *Installation of new muon chambers*: In addition to the NSW, new muon chambers are installed in the barrel of the MS, including 8 small Monitored Drift Tube (sMDT) systems and 16 Resistive Plate Chambers (RPC) [163].

- *Liquid Argon Calorimeter (LAr)*: The Phases-I upgrade for the LAr is performed in anticipation of the HL-LHC. This mainly consists of upgrades of the readout electronics, and deployment of a new trigger algorithm, allowing for much finer granularity in the measurement of energy deposits [164]. Similar to the NSW, the LAr upgrade also utilises the FELIX readout system [161]. In Run 3, both the new and legacy trigger systems were included in the physics runs, and the electromagnetic triggers are set to use the legacy system by default.

- *Updates to the Trigger system*: The detector upgrades mentioned above are accompanied by multiple improvements in both the trigger hardware and software. For the L1 muon triggers, the main upgrade is to the Muon-Central-Trigger-Processor Interface (MUCTPI) [165], allowing more trigger candidates to be sent and received, and taking into account the geometrical overlap between MS chambers. The L1 calorimeter trigge is augmented by three modules: the electron feature extractor (eFEX), the jet feature extractor (jFEX) and the global feature extractor (gFEX).

- *ATLAS Forward Proton (AFP) spectrometers*: The AFP spectrometers are designed to detect particles at about 200 m upstream and downstream of the ATLAS interaction point at very small scattering angles. First installed in 2017, the AFP detectors have been upgraded to maintain an out-of-vacuum solution for the photomultipliers, providing a safer environment for the AFP to operate. Several AFP electronic motherboards have also been replaced due to radiation damage [166].

6.2 Muon scale and resolution calibration for early Run 3 data

As a result of LS2 upgrade activities described in Section 6.1, a new set of muon momentum calibrations is required for Run 3 physics analyses involving muons. The hardware upgrades introduce new localised material effects and mismodelling in simulation, while the software upgrade to both L1 and HLT introduces changes that the calibration procedure is sensitive to. The commissioning phase of the NSW introduces additional challenges for the calibration, and studies of the NSW are critical for its long-term integration.

The following section describes the dataset used for 2022 muon calibration, preliminary studies of the muon momentum resolution using simulated samples, as well as the methodology and results for muon momentum calibration for 2022 data.

6.2.1 Data and simulated samples

The data sample consists of pp collision data collected at $\sqrt{s} = 13.6$ TeV during 2022, passing the trigger and detector quality requirements. This corresponds to a total integrated luminosity of 29 fb^{-1}. The average number of pp interactions per bunch crossing for the 2022 dataset is 42.5. Additionally, the dedicated B-physics stream is used for J/ψ events. The simulated samples take the average number of pp interactions per bunch crossing, and the data-taking conditions in 2022 into account.

6.2.2 Calibration procedure

At the start of Run 3, a few studies were performed on simulation to understand the changes in muon resolution as a result of the change in simulated geometry. Two estimators for muon momentum resolution are investigated, with one utilising the truth information from simulation, and the other relying on track errors from reconstruction, and thus is able to be applied to data.

The former method uses the simulated events to measure the width of the fractional difference between the reconstructed and truth p_{T}, defined by $(p_T^{reco} -$

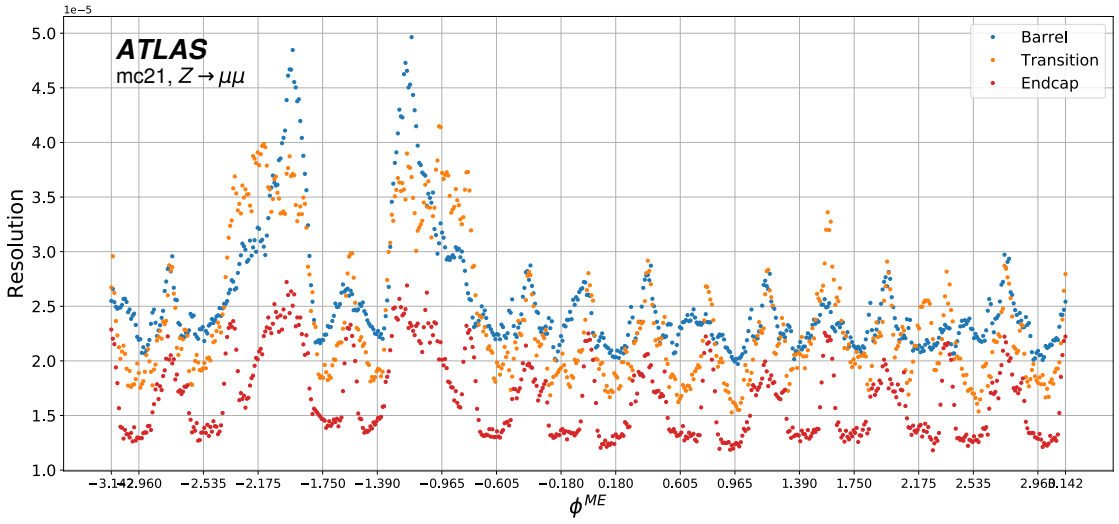

Figure 6.1: ME track resolution with respect to ϕ in simulated $Z \to \mu\mu$ events. The x-axis shows the track resolution, which is estimated by the width of $(p_T^{reco} - p_T^{truth})/p_T^{reco}$ for all muons in the ϕ region. The muon distributions are displayed separately for the three η regions, with Barrel corresponding to the $|\eta| < 1.05$ (in blue), Transition corresponding to $1.05 < |\eta| < 1.5$ (in orange), and Endcap corresponding to $|\eta| > 1.5$ (red). The y-axis corresponds to the measured ϕ of the muons, with the separation of MS sectors shown in the minor grid lines. The detector resolution degradation due to additional material of the ATLAS support structure, can be observed in $-2.175 > \phi > -1.75$ and $-1.390 > \phi > -0.965$. The periodic structure in the track resolution corresponds to the structure of the MS sectors. The hit quality at the centre of each sector deteriorates due to the gap between each sector, thus worsening track resolution. The tracks which traverse sector boundaries register more hits due to the geometric overlap between adjacent sectors, thus improving track resolution.

$p_T^{truth})/p_T^{reco}$, as a function of ϕ. The resultant distribution is shown in Figure 6.1. The latter utilises the factional track error, $\sigma(q/p)/(q/p)$, which allows for comparisons to be made between data and simulation. An example of the difference between data and simulation is shown in Figure 6.2.

As an early attempt at understanding Run 3 data, the calibration procedure is largely unchanged compared to the methodology in Run 2. The scale and resolution parametrisation follows Equation 4.7. The parameterisation for the scale and resolution mismodelling in ID, CB and ME tracks remains the same as in Run 2, as discussed in 4.3.3. For ID tracks, δs_1, δr_1 and δr_2 are free parameters. For CB tracks, δs_0, δs_1, δr_1 and δr_2 are free parameters. For ME tracks, δs_0, δs_1, δr_0, δr_1 and δr_2 are free parameters. Due to the lack of Run 3 alignment

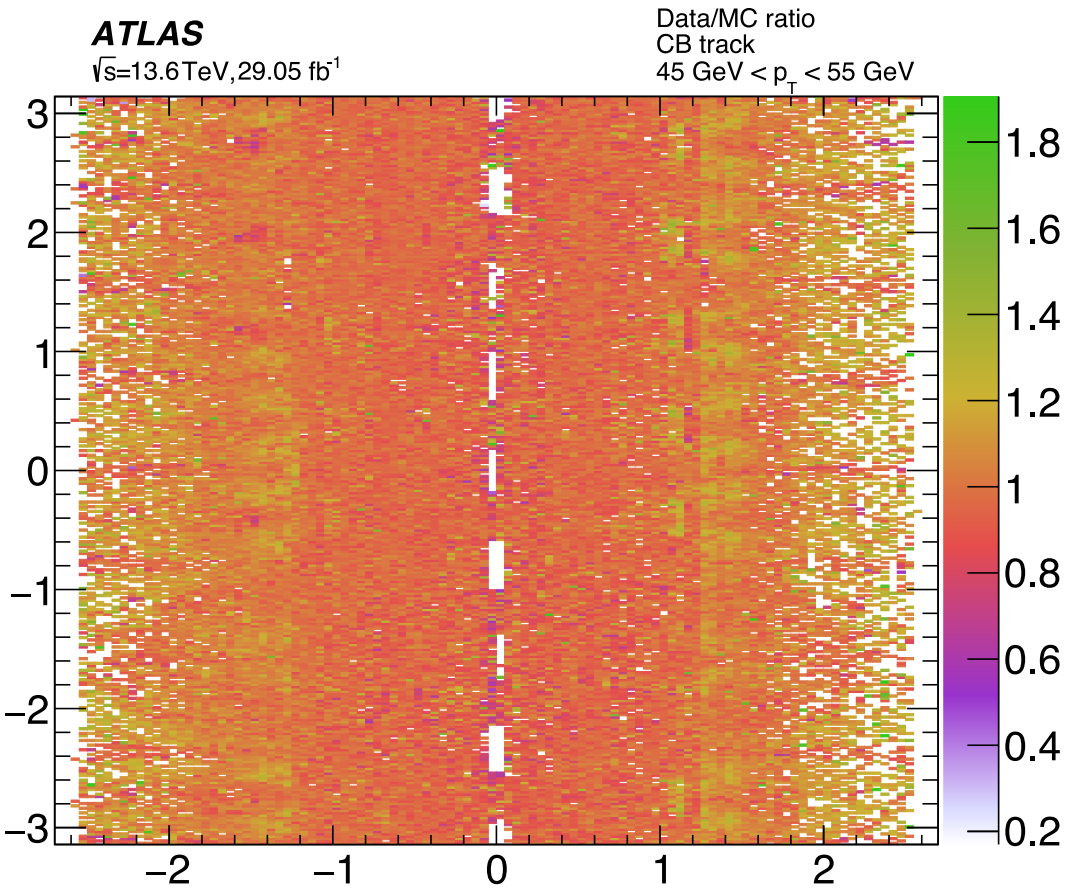

Figure 6.2: Ratio of fractional CB track error ($\sigma(q/p)/(q/p)$) between data and simulation in bins of η and ϕ for muons with p_{T} between 45 and 55 GeV. Within each bin, the mean track error was used as the estimator of the muon momentum resolution, and is shown as the heat map. The central η region where detector coverage is limited due to service cables are shown in white. The asymmetry in positive and negative η is due to operational issues of the side A of NSW, which worsens resolution in data, and increases the difference between data and simulation.

parameters, δr_2 is not externally constrained. Geometrically, the region definition now separates the NSW from an earlier stage of the iterations, such that its correlation with the rest of the detector can be reduced. Moment morphing and interpolation around the best-fit parameter is not performed due to the overall lower fit quality, which is attributed to the lack of alignment parameters. The same systematics scheme as described in Section 4.3.3 is calculated, with the envelope for the systematics as the uncertainties on the calibration parameters.

It is observed from the calibration fits that the ME track fit fails to converge, rendering the ID+ME combination scheme unusable at this stage. The CB

Table 6.1: Summary of CB momentum resolution and scale corrections for small and large MS sectors, averaged over the three main detector regions. The corrections for large and small MS sectors are derived in 18 pseudorapidity regions, as described in Section 4.3.3, and averaged, with each region assigned a weight proportional to its η width. The energy loss term Δr_0^{CB} is negligible and therefore fixed to zero in the fit for all η. The uncertainties represent the sum in quadrature of the statistical and systematic uncertainties.

Region	$\Delta r_1^{\text{CB}}(\times 10^{-3})$	Δr_2^{CB} [TeV^{-1}]	s_0^{CB} [MeV]	$s_1^{\text{CB}}(\times 10^{-3})$
$\lvert\eta\rvert < 1.05$ (large)	$7.1^{+2.1}_{-2.1}$	$0.2^{+0.1}_{-0.4}$	$-6.2^{+1.8}_{-1.6}$	$0.4^{+0.9}_{-0.4}$
$\lvert\eta\rvert < 1.05$ (small)	$6.3^{+1.5}_{-6.3}$	$0.2^{+0.1}_{-0.1}$	$-0.6^{+1.9}_{-1.9}$	$-0.7^{+0.8}_{-0.5}$
$1.05 \leq \lvert\eta\rvert < 2.0$ (large)	$11.2^{+5.5}_{-5.6}$	$0.3^{+0.1}_{-0.3}$	$-4.3^{+1.9}_{-1.5}$	$0.2^{+0.9}_{-0.4}$
$1.05 \leq \lvert\eta\rvert < 2.0$ (small)	$12.0^{+3.3}_{-2.7}$	$0.4^{+0.1}_{-0.2}$	$-0.1^{+1.7}_{-1.7}$	$-0.7^{+0.8}_{-0.4}$
$\lvert\eta\rvert \geq 2.0$ (large)	$14.0^{+7.5}_{-9.1}$	$0.2^{+0.1}_{-0.9}$	$-2.3^{+2.0}_{-1.7}$	$-0.1^{+1.0}_{-0.5}$
$\lvert\eta\rvert \geq 2.0$ (small)	$12.3^{+4.1}_{-13.8}$	$0.3^{+0.1}_{-0.2}$	$0.4^{+1.9}_{-2.1}$	$-0.8^{+0.9}_{-0.5}$

tracks are heavily constrained by the ID tracks, thus the resolution mismodelling can be captured by the calibration procedure. The results of CB calibration are summarised in Table 6.1.

Similarly, the Run 3 sagitta bias correction follows the same procedure as described in Section 4.3.3, and only the results derived for the CB track are used in the recommendation for the ATLAS physics analyses.

6.2.3 Validation

The Run 3 momentum calibration validation follows the procedure described in 4.3.4. The validations for leading muon p_{T} and η are shown in Figure 6.3-6.6.

The Run 3 calibration is sensitive to non-closure in the high p_{T} regime, and the over-smearing of the simulated sample compared to that of data. As seen in Figure 6.6, the tension between data and simulation increases dramatically with high p_{T}, and the dimuon mass resolution is better in data for $Z \to \mu\mu$ decays. As a result, additional systematics are assigned to both sagitta bias and scale and resolution for the non-closure at high p_{T}. For sagitta bias, this corresponds to increasing the residual bias related to fit non-closure by approximately 20 % across detector regions. For scale and resolution uncertainty, the non-closure

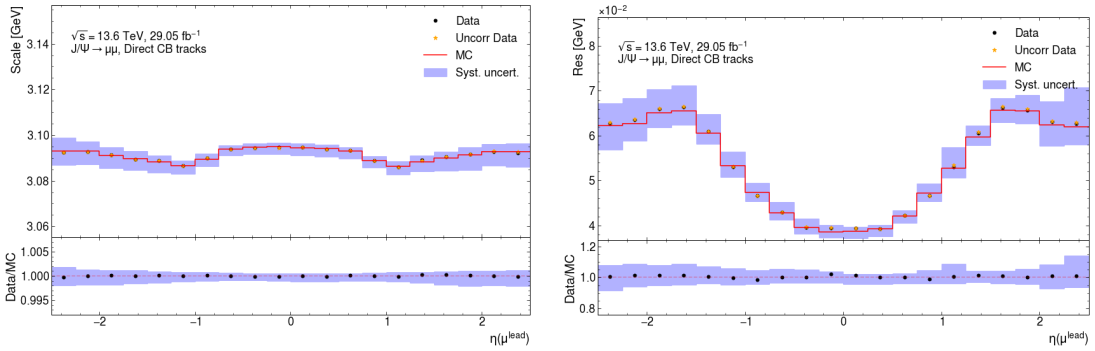

Figure 6.3: Scale (left) and resolution (right) of $J/\psi \to \mu\mu$ candidate events reconstructed with CB muons as a function of leading muon η. The scale and resolution are estimated through a fit to a double-sided crystal ball function, and the y-axis in the upper panel shows the dimuon mass scale (μ) and resolution (σ). The data before (black dots) and after (in yellow stars) sagitta bias correction is applied are shown in the plot. The background is estimated from a fit to data. In the bottom panel, the ratio between the corrected data and the corrected simulation is shown. The sum of background and signal MC distributions is normalised to data. The systematic uncertainties are indicated in purple in both the upper and lower panels.

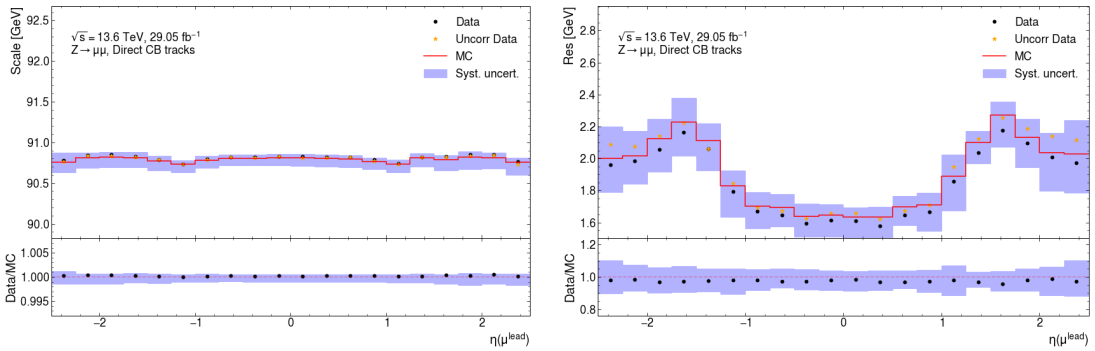

Figure 6.4: Scale (left) and resolution (right) of $Z \to \mu\mu$ candidate events reconstructed with CB muons as a function of leading muon η. The scale and resolution are estimated through a fit to a double-sided crystal ball function, and the y-axis in the upper panel shows the dimuon mass scale (μ) and resolution (σ). The data before (black dots) and after (in yellow stars) sagitta bias correction is applied are shown in the plot. The background is estimated from a fit to data. In the bottom panels, the ratio between the corrected data and the corrected simulation is shown. The sum of background and signal MC distributions is normalised to data. The systematic uncertainties are indicated in purple in both the upper and lower panels.

in validation is addressed by increasing the uncertainty associated with Δs_1, Δr_1 and Δr_2 in targeted detector regions.

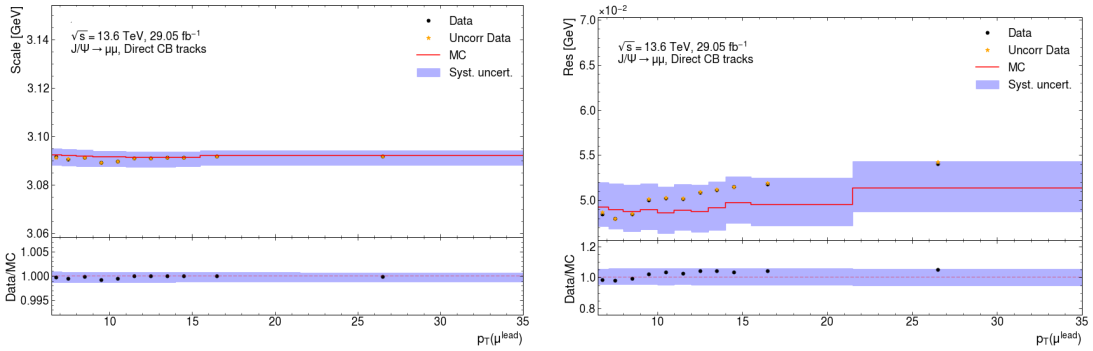

Figure 6.5: Scale (left) and resolution (right) of $J/\psi \to \mu\mu$ candidate events reconstructed with CB muons as a function of leading muon p_{T}. The scale and resolution are estimated through a fit to a double-sided crystal ball function, and the y-axis in the upper panel shows the dimuon mass scale (μ) and resolution (σ). The data before (black dots) and after (in yellow stars) sagitta bias correction is applied are shown in the plot. The background is estimated from a fit to data. In the bottom panels, the ratio between the corrected data and the corrected simulation is shown. The sum of background and signal MC distributions is normalised to data. The systematic uncertainties are indicated in purple in both the upper and lower panels.

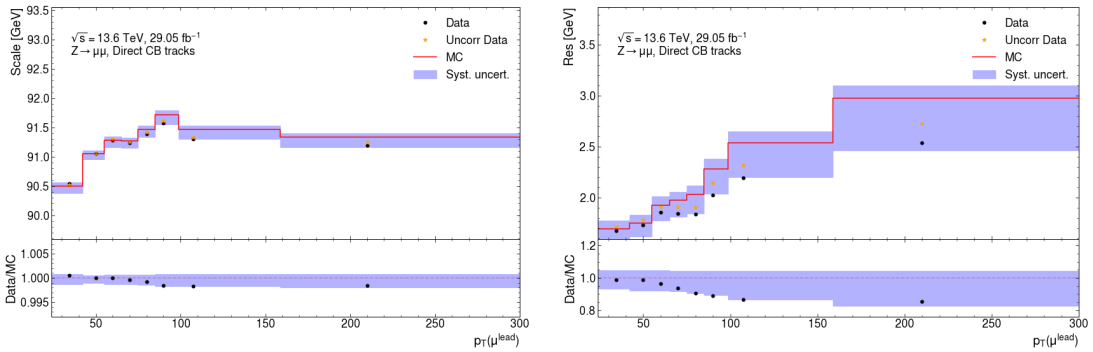

Figure 6.6: Scale (left) and resolution (right) of $Z \to \mu\mu$ candidate events reconstructed with CB muons as a function of leading muon p_{T}. The scale and resolution are estimated through a fit to a double-sided crystal ball function, and the y-axis in the upper panel shows the dimuon mass scale (μ) and resolution (σ). The data before (black dots) and after (in yellow stars) sagitta bias correction is applied are shown in the plot. The background is estimated from a fit to data. In the bottom panels, the ratio between the corrected data and the corrected simulation is shown. The sum of background and signal MC distributions is normalised to data. The systematic uncertainties are indicated in purple in both the upper and lower panels.

6.3 Higgs fiducial cross-section measurement

The Higgs boson couplings to other gauge bosons and charged fermions are fully calculable once the Higgs mass is fixed. The Higgs coupling measurement

then allows for stringent tests of the electroweak sector of the Standard Model (SM), as any deviation from the SM prediction serves as an indicator for physics beyond the SM. Additionally, the Higgs boson cross-section is dependent on the centre-of-mass energy of the pp collision. With the centre-of-mass energy of 13.6 fb^{-1}, the LHC Run 3 offers a unique data point for testing the SM.

The Higgs cross-section is measured in the *fiducial phase space* (also called fiducial volume) in the $H \to ZZ^* \to 4l$ final state with an analytical fit to the four-lepton invariant mass spectrum. The fiducial volume definition is chosen to match object selection criteria (as described in Section 5.2) to minimise the model dependence from reconstructing signal events. The fiducial cross-section is then extrapolated to the entire phase space to obtain the total cross-section.

6.3.1 Lepton trigger efficiencies in Run 3

Only leptonic (electron and muons) triggers are used for $H \to ZZ^* \to 4\ell$. In Run 2, the combined efficiency for all lepton triggers borders 100 % in both data and simulation. Due to the change in run conditions in Run 3 as described in Section 6.1, the combined trigger efficiencies deteriorate compared to Run 2. This is a result of increased fake rate in data, due to issues in acceptance problem from non-functional gas gaps and leaks in the RPC.

This necessitates the application of kinematic matching between L1 objects and the refined selection from the HLT, as well as applying simulation-to-data scale factors for each trigger used. As some triggers do not have the corresponding L1 object available for kinematic matching, these triggers are removed from the analysis. Additionally, the scale factors for the `4mu4_L14MU3V` trigger are not yet supported and are therefore removed from this analysis. The full list of unprescaled lepton triggers is shown in Table 6.2. Further details for the naming conventions of Run 3 triggers are found in Appendix A.

The trigger efficiency is studied extensively in the simulated gluon-gluon fusion (ggH) sample. All signal samples, including ggH, VBF, VH and $t\bar{t}H$ are

generated using the POWHEG MC generator at NLO in QCD, and matched to PYTHIA parton shower. This sample is generated at $\sqrt{s} = 13.6$ TeV and $m_H = 125.09$ GeV.

Single electron triggers	Single muon triggers
e26_lhtight_ivarloose_L1EM22VHI	mu24_ivarmedium_L1MU14FCH
e60_lhmedium_L1EM22VHI	mu50_L1MU14FCH
e140_lhloose_L1EM22VHI	mu60_0eta105_msonly_L1MU14FCH
e300_etcut_L1EM22VHI	mu60_L1MU14FCH
	mu80_msonly_3layersEC_L1MU14FCH

Di-electron triggers	Di-muon triggers
2e17_lhvloose_L12EM15VHI	2mu10_l2mt_L1MU10BOM
	2mu14_L12MU8F
	mu20_ivarmedium_mu8noL1_L1MU14FCH
	mu22_mu8noL1_L1MU14FCH

Multi-electron triggers	Multi-muon triggers
e24_lhvloose_2e12_lhvloose_L1EM20VH _3EM10VH	3mu6_L13MU5VF
	3mu6_msonly_L13MU5VF
	4mu4_L14MU3V
	mu20_2mu4noL1_L1MU14FCH

Di-emu triggers	Multi-emu triggers
e7_lhmedium_mu24_L1MU14FCH	e9_lhvloose_mu20_mu8noL1_L1MU14FCH
e17_lhloose_mu14_L1EM15VH_MU8F	2e12_lhloose_mu10_L12EM8VH_MU8F
e26_lhmedium_mu8noL1_L1EM22VHI	e12_lhloose_2mu10_L12MU8F

Table 6.2: Lowest unprescaled lepton triggers available during the 2022 pp data-taking period. The triggers in blue type are the ones for which trigger matching information was lost. The scale factors for the 4mu4_L14MU3V trigger are not supported by the trigger group.

Additionally, triggers with a high-efficiency drop (>90%) after applying trigger matching are also removed from the trigger list, as this implies incomplete kinematic information for trigger matching. The summary of individual trigger efficiencies, and the logical OR between the trigger decision and kinematic matching, are shown in Table 6.3-6.5.

Table 6.3: Summary of trigger efficiency with kinematic matching for 2022 unprescaled muon triggers as evaluated in ggH samples.

N_{lep}	Triggers	ϵ_{Trig}	$\epsilon_{TrigANDMatched}$	$\Delta\epsilon/\epsilon_{Trig}$ (%)
Single	mu24_ivarmedium_L1MU14FCH	0.591208	0.591188	0.003
	mu50_L1MU14FCH	0.247394	0.247361	0.013
	mu60_0eta105_msonly_L1MU14FCH	0.098895	0.002664	97.306
	mu60_L1MU14FCH	0.145665	0.145644	0.014
	mu80_msonly_3layersEC_L1MU14FCH	0.060413	0.002377	96.065
Di	2mu10_l2mt_L1MU10BOM	0.001809	0.001800	0.498
	2mu14_L12MU8F	0.534645	0.534436	0.039
Tri	3mu6_L13MU5VF	0.320727	0.318490	0.697
	3mu6_msonly_L13MU5VF	0.324958	0.005702	98.245

Table 6.4: Summary of trigger efficiency with kinematic matching for 2022 unprescaled electron triggers as evaluated in ggH samples.

N_{lep}	Triggers	ϵ_{Trig}	$\epsilon_{TrigANDMatched}$	$\Delta\epsilon/\epsilon_{Trig}$ (%)
Single	e26_lhtight_ivarloose_L1EM22VHI	0.449847	0.449799	0.011
	e60_lhmedium_L1EM22VHI	0.106891	0.106863	0.026
	e140_lhloose_L1EM22VHI	0.006245	0.006219	0.004
	e300_etcut_L1EM22VHI	0.000251	0.0	100
Di	2e17_lhvloose_L12EM15VHI	0.385498	0.385194	0.079
Tri	e24_lhvloose_2e12_lhvloose _L1EM20VH_3EM10VH	0.140633	0.139326	0.929

6.3.2 Trigger ranking studies

To further simplify the combinatorics in applying the trigger scale factors, the relevance of each trigger is evaluated on the ggH sample with $m_H = 125$ GeV. This analysis uses an iterative procedure to investigate the impact of each trigger, and this procedure is outlined as follows:

1. A trigger category (single-, di-, multi-electrons; single-, di-, multi-muons; di-, multi-emu) is identified in accordance with Table 6.2.

2. For a given trigger A, the efficiency of the logical *or* of all the triggers excluding trigger A is evaluated.

3. In the first iteration, the triggers are sorted in the plots with respect to the drop in efficiency.

Table 6.5: Summary of trigger efficiency with kinematic matching for 2022 unprescaled mixed triggers as evaluated in ggH samples.

N_{lep}	Triggers	ϵ_{Trig}	$\epsilon_{TrigANDMatched}$	$\Delta\epsilon/\epsilon_{Trig}$ (%)
Di	`e7_lhmedium_mu24_L1MU14FCH`	0.256850	0.255141	0.666
	`e17_lhloose_mu14_L1EM15VH_MU8F`	0.339232	0.0	100
	`e26_lhmedium_mu8noL1_L1EM22VHI`	0.313590	0.0	100
Tri	`2e12_lhloose_mu10_L12EM8VH_MU8F`	0.316380	0.315813	0.179
	`e12_lhloose_2mu10_L12MU8F`	0.261072	0.260162	0.349

4. The trigger with the lowest efficiency drop is removed.

This procedure is repeated until only one trigger remains and has been performed independently for each category of triggers in each final state. The plots summarising the ranking studies are shown in Figure 6.7-6.12. The ranking plots per-channel can be found in Appendix B.

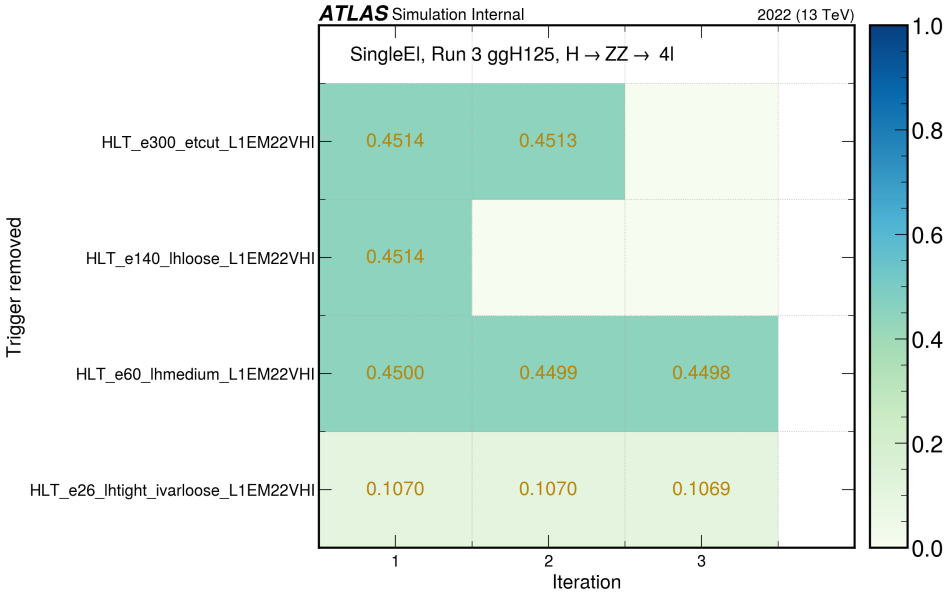

(a) 4e+4μ+2e2μ+2μ2e channel

Figure 6.7: Ranking studies of single-electron triggers for all decay modes in $H \to ZZ^* \to 4\ell$.

The summary of the study is the following:

- single-electron triggers: the most important trigger is found to be the `e26_lhtight_ivarloose_L1EM22VHI` as expected, being the trigger with

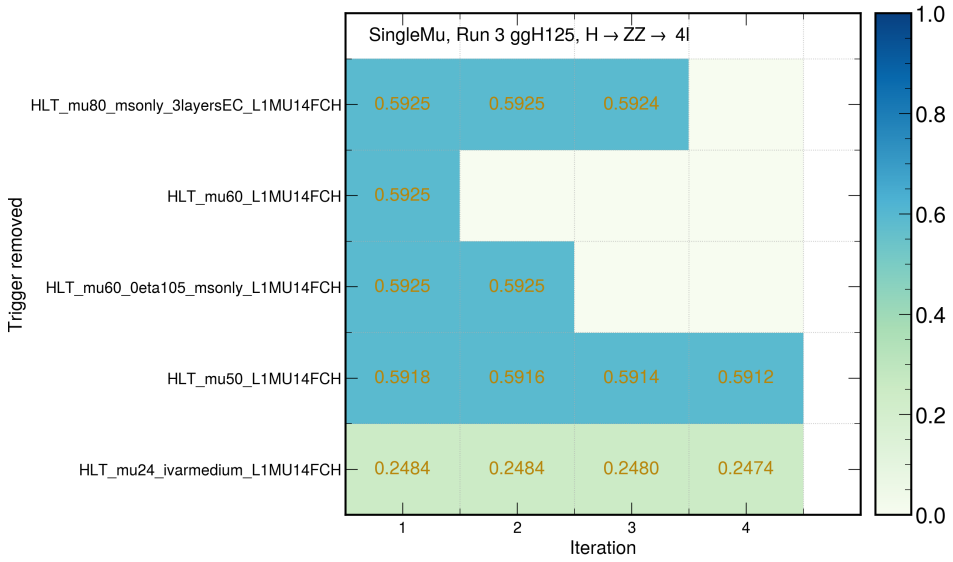

(a) 4e+4μ+2e2μ+2μ2e channel

Figure 6.8: Ranking studies of single-muon triggers for all decay modes in $H \to ZZ^* \to 4\ell$.

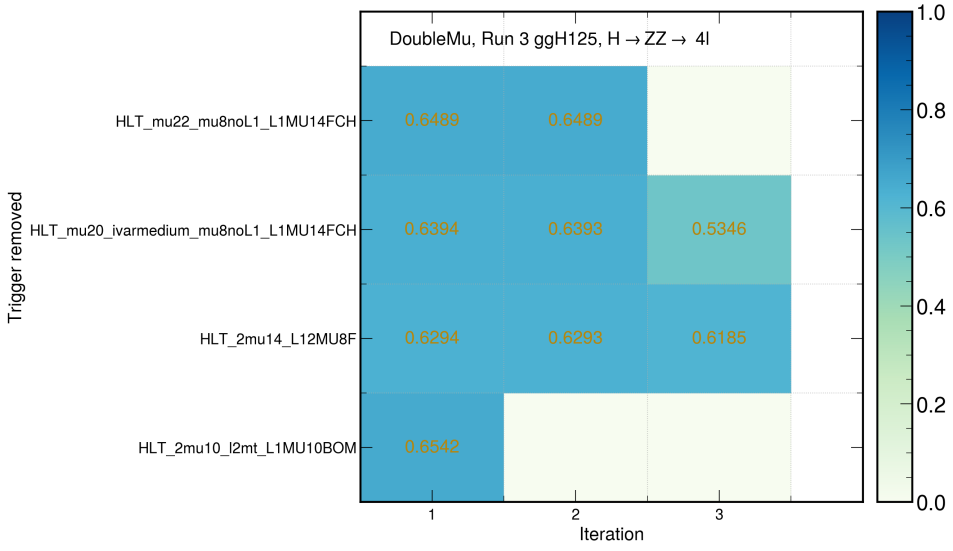

(a) 4e+4μ+2e2μ+2μ2e channel

Figure 6.9: Ranking studies of double-muon triggers for all decay modes in $H \to ZZ^* \to 4\ell$.

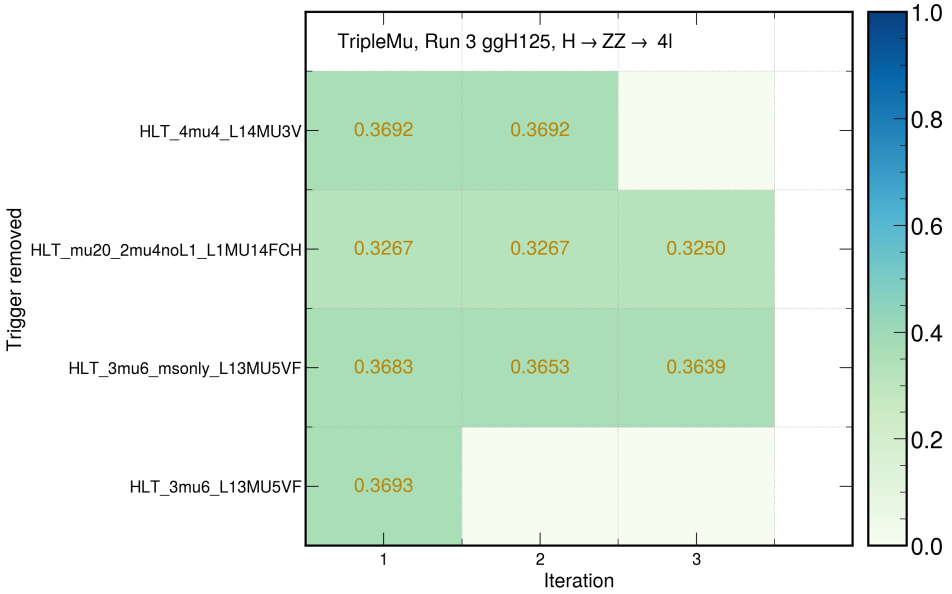

(a) 4e+4μ+2e2μ+2μ2e channel

Figure 6.10: Ranking studies of multi-muon triggers for all decay modes in $H \to ZZ^* \to 4\ell$.

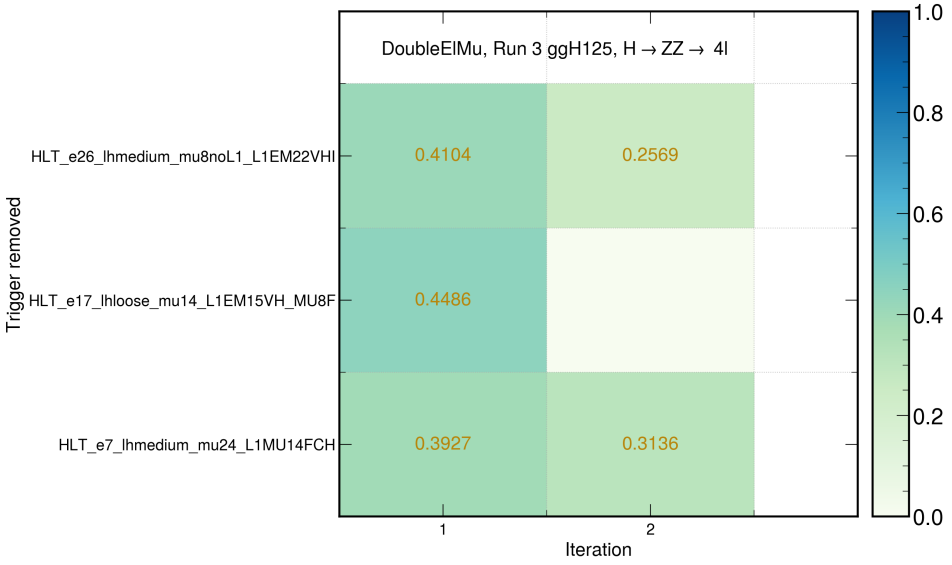

(a) 4e+4μ+2e2μ+2μ2e channel

Figure 6.11: Ranking studies of di-emu triggers for all decay modes in $H \to ZZ^* \to 4\ell$.

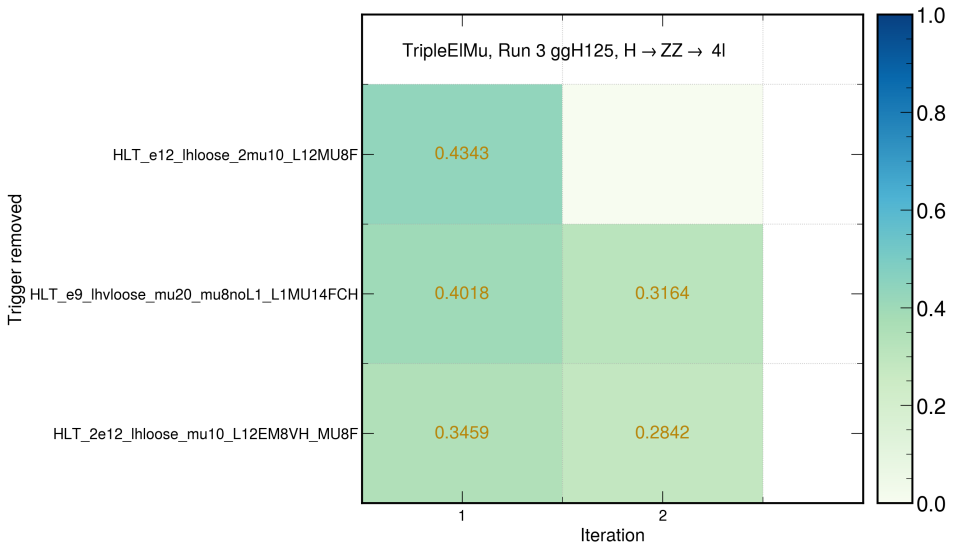

(a) 4e+4μ+2e2μ+2μ2e channel

Figure 6.12: Ranking studies of multi-emu triggers for all decay modes in $H \to ZZ^* \to 4\ell$.

the lowest E_T threshold. The `e300_etcut_L1EM22VHI` is instead found to have a negligible contribution to the total efficiency, as expected given the nature of the signal;

- single-muon triggers: `mu24_ivarmedium_L1MU14FCH` is the most relevant trigger in all channels involving muons, as expected again given the nature of the signal;
- di-electron: only one trigger is available;
- di-muon: the most relevant triggers are `2mu14_L12MU8F`
- di-emu triggers: the most relevant trigger is found to be `e7_lhmedium_mu24_L1MU14FCH`, whose importance is especially highlighted in the 2μ2e channel, as can be seen in Figure B.5(d). Furthermore, from the 4e and 4μ channels, it is possible to observe how the lower threshold of multi-lepton triggers plays an important role.
- multi-emu triggers: the most relevant triggers of this category are found to be

e9_lhvloose_mu20_mu8noL1_L1MU14FCH and the 2e12_lhloose_mu10_L12EM8VH_MU8F ones. Similar to di-emu triggers, it is possible to observe the effect of the lower threshold of multi-lepton triggers.

Combining the outcome of the kinematic matching and relevance ranking, the final trigger list used is shown in Table 6.6. The summary plot for the trigger efficiency as a function of $p_{T,4l}$ in the ggH sample is shown in 6.13.

Single electron triggers	Single muon triggers
e26_lhtight_ivarloose_L1EM22VHI e60_lhmedium_L1EM22VHI	mu24_ivarmedium_L1MU14FCH mu50_L1MU14FCH

Di-electron triggers	Di-muon triggers
2e17_lhvloose_L12EM15VHI	2mu14_L12MU8F

Multi-electron triggers	Multi-muon triggers
e24_lhvloose_2e12_lhvloose_L1EM20VH_3EM10VH	3mu6_L13MU5VF

Di-emu triggers	Multi-emu triggers
e7_lhmedium_mu24_L1MU14FCH e17_lhloose_mu14_L1EM15VH_MU8F	e12_lhloose_2mu10_L12MU8F 2e12_lhloose_mu10_L12EM8VH_MU8F

Table 6.6: Lowest unprescaled lepton triggers available during the 2022 pp data-taking period used in the $H \to ZZ^* \to 4\ell$ fiducial cross-section analysis.

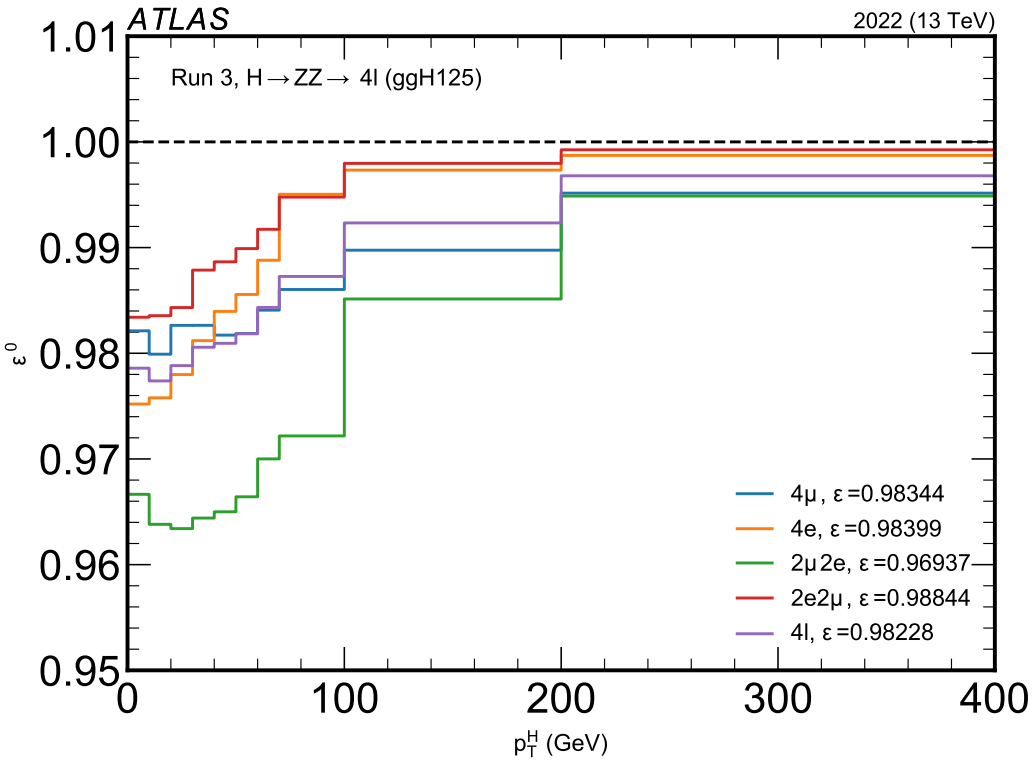

Figure 6.13: Trigger efficiency as a function of $p_{T,4l}$ for each of the 4 channels and the inclusive channel.

6.3.3 Event selection

The criteria for physics object and event selection are listed in Table 6.7 and 6.8 respectively. These selection criteria follow closely the selection criteria defined in Run 2 (see Section 5.2-5.3). The fiducial definition follows closely to that of event selection, which is shown in Table 6.9.

6.3.4 Background estimation

Similar to the Run 2 mass analysis, the main background processes are the non-resonant ZZ^* production. The signal and non-resonant ZZ^* normalisation are free parameters in the fit to $m_{4\ell}$. Other background contributions, including Z+jets, $t\bar{t}$ and WZ, pass event selection criteria due to the presence of jets, photons and non-prompt leptons, which are misidentified as prompt leptons. The normalisation factors for these processes are estimated by performing fits

Table 6.7: Summary of object selection for Run 3 $H \to ZZ^* \to 4\ell$ fiducial cross-section analysis.

Electron selection criteria	
Identification selection	*Loose*
E_T	$E_T > 7$ GeV
η	$\|\eta\| < 2.47$
Global muon selection criteria	
Identification selection	*Loose*
Isolation selection	*PflowLoose*
p_{T}	$p_{\mathrm{T}} > 5$ GeV
η	$\|\eta\| < 2.7$
Muon selection criteria for CT muons	
CT muons	$p_{\mathrm{T}} > 15$ GeV for $\|\eta\| < 0.1$, no more than 1 CT muon per event
Primary vertex selection	
ID track p_{T}	at least two ID tracks with $p_{\mathrm{T}} > 500$ MeV
Transverse impact parameter, d_0	$\|d_0\| < 1$ mm
Longitudinal impact parameter, z_0	$\|z_0 \cdot \sin(\theta)\|$

Table 6.8: Summary of event selection for Run 3 $H \to ZZ^* \to 4\ell$ fiducial cross-section analysis. The mass threshold for the off-shell Z pair, $m_{\text{threshold}}$ is 12 GeV for $m_{4\ell} < 140$ GeV, and rises linearly to 50 GeV for $m_{4\ell} = 190$ GeV.

Lepton selection criteria	
Lepton p_{T}	$p_{\mathrm{T}} >$20, 15, 10 GeV
Lepton separation for all lepton pairs	$\Delta R > 0.1$
Impact parameter	$\|d_0/\sigma(d_0)\| < 5(3)$ for electrons (muons)
Vertex selection	$\chi^2/N_{dof} < 6(9)$ for 4μ (other channels)
Quadruplet selection	
On-shell Z pair, m_{12}	$50 < m_{12} < 106$ GeV
Off-shell Z pair, m_{34}	$m_{\text{threshold}} < m_{12} < 115$ GeV
Four-lepton invariant mass, $m_{4\ell}$	$105 < m_{4\ell} < 160$ GeV
J/ψ suppression	$m_{ll} > 5$ GeV for alternative pairing of leptons
If an extra lepton presents with $p_{\mathrm{T}} > 12$ GeV	Select quadruplet with largest matrix element value

in dedicated relaxed control regions, and further detail can be found in Ref [167]. The other rare processes, including $t\bar{t}Z$, $t\bar{t}W$ and VVV are estimated from simulation directly due to their small contribution.

The kinematic distributions in the signal region for $115 < m_{4\ell} < 130$ GeV are shown in Figure 6.14. Additional kinematics distributions can be found in Appendix C.

6.3.5 Analysis strategy

The total cross-section, σ_{total} for a certain process is defined as:

$$\sigma_{total} = \frac{N_s}{\epsilon_{total} \times BR \times \mathcal{L}_{int}}, \tag{6.1}$$

Table 6.9: Summary of fiducial region definition for Run 3 $H \to ZZ^* \to 4\ell$ fiducial cross-section analysis.

Object selection criteria	
All leptons	$p_T > 5$ GeV, $\lvert\eta\rvert < 2.7$
Lepton kinematics	$p_T > 20, 15, 10$ GeV
Event selection criteria	
On-shell Z pair, m_{12}	$50 < m_{12} < 106$ GeV
Off-shell Z pair, m_{34}	$m_{\text{threshold}} < m_{12} < 115$ GeV
J/ψ suppression	$m_{ll} > 5$ GeV for alternative pairing of leptons
Four-lepton invariant mass, $m_{4\ell}$	$105 < m_{4\ell} < 160$ GeV
If an extra lepton presents with $p_T > 12$ GeV	Select quadruplet with largest matrix element value

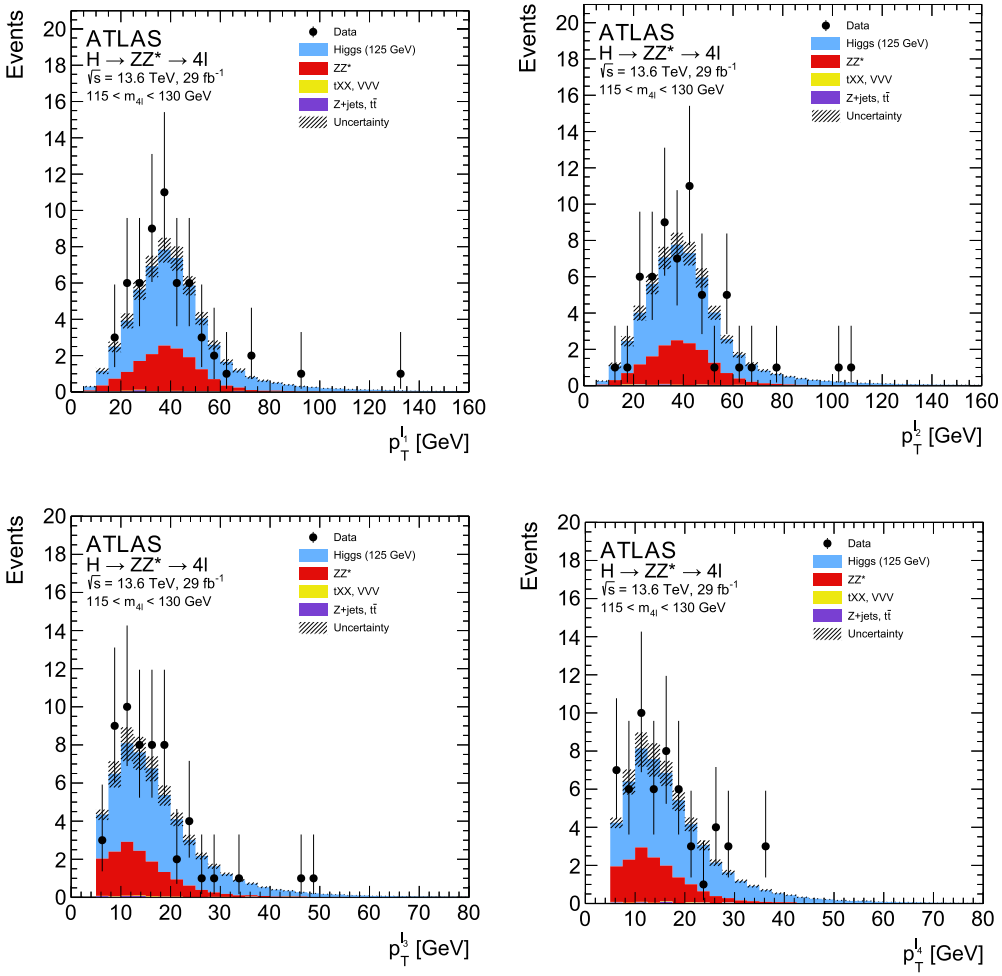

Figure 6.14: Pre-fit data/MC comparison in the signal region, $115 < m_{4\ell} < 130$ GeV, for the lepton p_T. Lepton 1 (top-left) is the positive lepton from the on-shell Z boson candidate, and lepton 2 (top right) is the negative lepton from the on-shell Z boson candidate. Lepton 3 (bottom left) is the positive lepton from the off-shell Z boson candidate, and lepton 4 (bottom right) is the negative lepton from the off-shell Z boson candidate.

where N_s is the number of observed events, ϵ_{total} is the total efficiency for detecting signal, and is the product of the detector acceptance A and reconstruction efficiency ϵ_{reco}. The branching ratio, BR is $1.25 \pm 0.03 \times 10^{-4}$ for $H \to ZZ^* \to 4\ell$ final state [168], and $\mathcal{L}_{int}$ is the integrated luminosity. This definition is intuitive, but highly model-dependent due to the finite detector acceptance. Once the total cross-section is extrapolated outside of the region where the detector has any sensitivity, the cross-section measurement becomes sensitive to different assumptions for the detector acceptance. Therefore, a model-independent definition for cross-section measurement, the fiducial cross-section σ_{fid} is defined as:

$$\sigma_{fid} = \sigma_{total} \times A \times BR = \frac{N_s}{\epsilon_{reco} \times \mathcal{L}_{int}}. \tag{6.2}$$

The fiducial phase space is defined closely to match the event selection criteria in Table 6.7 and 6.8. To extract the number of signal events, the combination of simulated $H \to ZZ^* \to 4\ell$ and the background processes are fit to the $m_{4\ell}$ distribution observed in data.

6.3.6 Results

The numbers of expected and observed events in each final state are shown in Table 6.10. The events used in this table are selected from a narrower mass window ($115 < m_{4\ell} < 130$ GeV) than that of the signal region definition ($105 < m_{4\ell} < 160$ GeV). The post-fit $m_{4\ell}$ distribution is shown in Figure 6.15.

Table 6.10: The expected and observed yields for 115< $m_{4\ell}$ <130 GeV.

Final state	Signal	ZZ*	Other backgrounds	Total	Observed
4μ	14.8 ± 0.8	8.3 ± 0.6	1.0 ± 0.3	20.6 ± 1.0	23
$2e2\mu$	8.5 ± 0.6	6.5 ± 0.4	1.0 ± 0.3	16.0 ± 0.8	13
$2\mu2e$	5.4 ± 1.0	3.2 ± 0.6	0.9 ± 0.1	9.4 ± 1.2	12
$4e$	5.7 ± 1.1	3.1 ± 0.7	0.8 ± 0.2	9.6 ± 1.4	9
Total	30.9 ± 2.9	21.1 ± 2.0	3.6 ± 0.7	55.6 ± 4.4	57

This analysis is primarily limited by the available statistics, which accounts for 25.1 % uncertainty. The main sources of systematic uncertainties are experimental uncertainties from the lepton reconstruction, identification, trigger selections, and

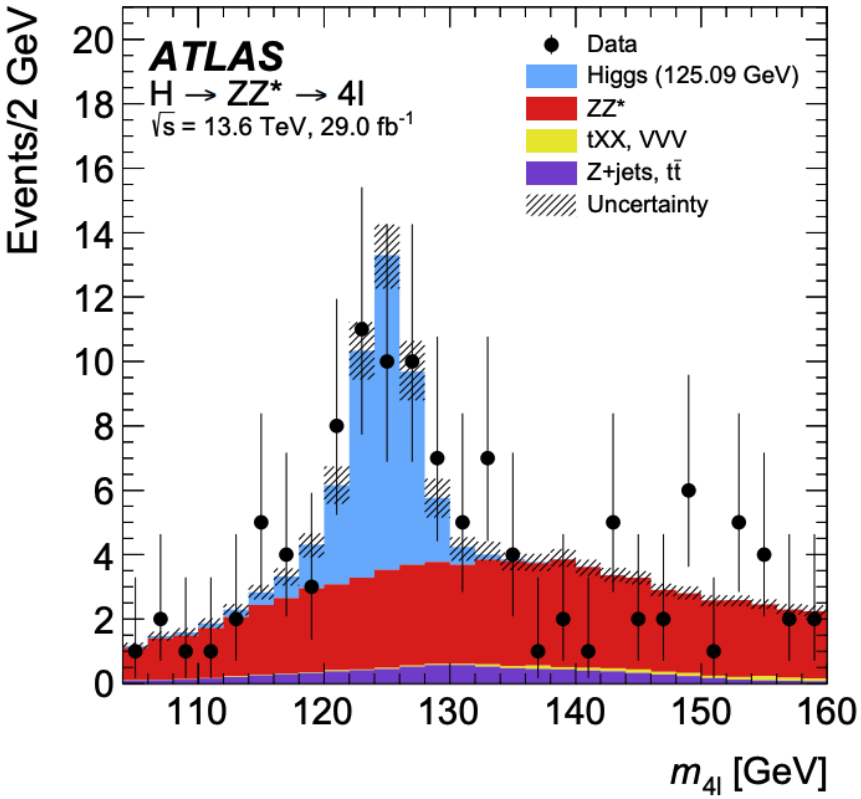

Figure 6.15: The observed and expected $m_{4\ell}$ distributions for Higgs boson candidates. The uncertainty in simulation is shown by the hatched band, and includes theoretical uncertainties in the SM cross-section for the signal and main background processes. The tXX label includes ttW and ttZ processes.

their energy calibrations. Other experimental systematics, including luminosity, pile-up modelling and the background estimation technique, contribute at the percent level. The main theoretical uncertainty originates from the modelling of the non-resonant ZZ^* background. The systematic uncertainty breakdown is shown in Table 6.11.

The fiducial cross-section measurement performed in $H \to ZZ^* \to 4\ell$ is measured to be $\sigma_{\text{fid}4\ell} = 2.80 \pm 0.74$ fb. This result is combined with the measurement in $H \to \gamma\gamma$ channel result. As the two decay channels do not share the same fiducial region definitions, a combination is performed by first extrapolating both results into the full phase space, and performing a likelihood combination. The total Higgs boson production cross-section at 13.6 TeV is measured to be $\sigma(pp \to H) = 45 \pm 11(\text{stat.}) \pm 3(\text{syst.})$ pb for $H \to ZZ^* \to 4\ell$

Table 6.11: The systematics breakdown in the fiducial $H \to ZZ^* \to 4\ell$ cross-section measurement.

Source	Uncertainty (%)
Electron uncertainties	6.3
Muon uncertainties	3.8
Luminosity	2.2
ZZ^* theoretical uncertainties	0.7
Reducible background estimation	0.6
Other uncertainties	<1.0
Total	7.9

channel, and $\sigma(pp \to H) = 67 \pm 9(\text{stat.}) \pm 6(\text{syst.})$ pb for $H \to \gamma\gamma$ channel. The p-value between the two measurements is 20%.

Through a likelihood combination of the two decay channels, the combined measurement of the Higgs boson production cross section is $\sigma(pp \to H) = 58.2 \pm 8.7 = 58.2 \pm 7.5(\text{stat.}) \pm 4.5(\text{syst.})$ pb at 13.6 TeV. The values of the total cross-section obtained from this analysis, and from past analysis from ATLAS, are shown in Figure 6.16. Overall, good agreement is observed between SM prediction and the measurement at the new centre-of-mass energy of 13.6 TeV. Further details for the combination between channels, and extrapolation to the total cross-section can be found in Ref. [167].

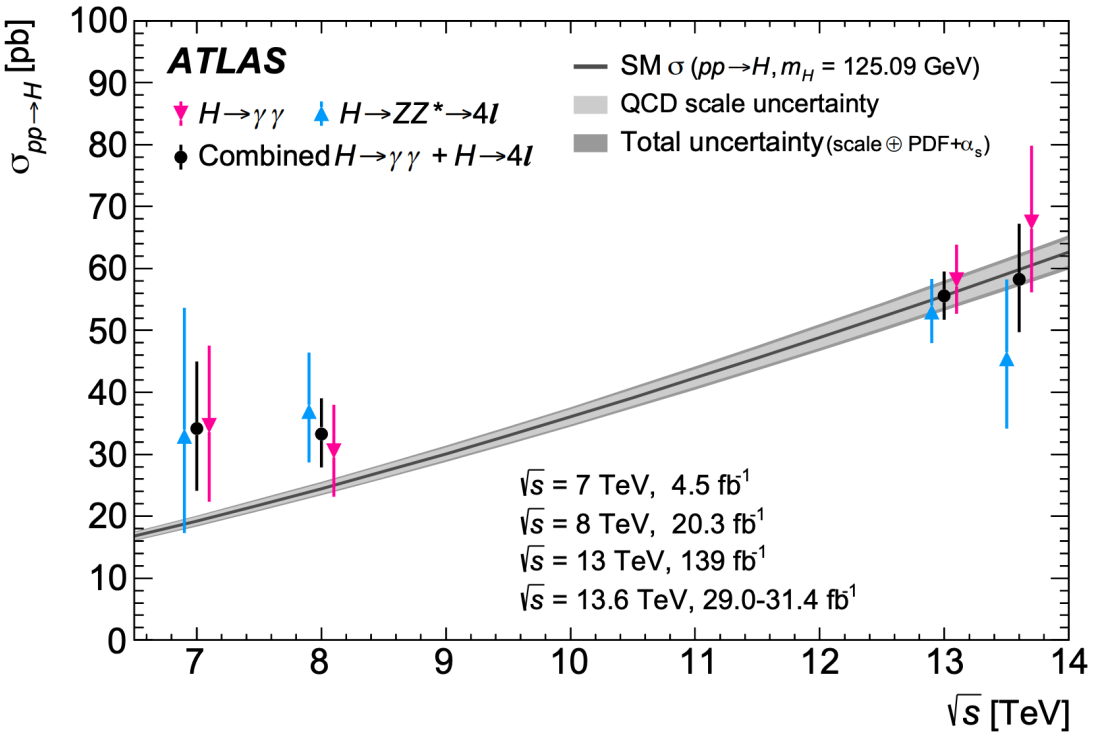

Figure 6.16: Results for the $\sigma(pp \to H)$ measurements from ATLAS publications [169, 170] as a function of the pp centre-of-mass energy. The SM predicted value and its uncertainties are shown in the grey band. The individual channel results of offset along the x-axis for display purposes.

Chapter 7

Conclusion and outlook

The measurement of the Higgs boson properties, including its mass and cross-sections, is crucial for advancing particle physics. Such measurements are made possible using the proton-proton collisions collected at the ATLAS detector, and the continuous studies and improvements in the analysis techniques and detector performance. Essential to both of these aspects is the reconstruction of muons, which is a key theme of this thesis, linking detector performance and the measurement of the Higgs mass and Higgs production cross-section. The results presented in this thesis are summarised below.

Chapter 5 presents the measurement of the Higgs boson mass using the full Run 2 pp collision dataset at the centre-of-mass energy of 13 TeV with an integrated luminosity of 139 fb^{-1}. This is performed in the $H \to ZZ^* \to 4l$ channel, and the Higgs mass is extracted from a maximum-likelihood fit to the invariant mass of the four-lepton system, the predicted invariant-mass resolution, and a discriminant score based on the kinematic variables of the four leptons. The final measured value of the Higgs boson mass is $m_H = 124.99 \pm 0.18\text{(stat.)} \pm 0.04\text{(syst.)}$ GeV. A combination with the Run 1 result was performed, and the combined Higgs mass is $m_H = 124.94 \pm 0.17\text{(stat.)} \pm 0.03\text{(syst.)}$ GeV.

The Higgs boson mass analysis greatly benefited from the improvements to the muon momentum calibration, and the specifics of this procedure are outlined in chapter 4. The scale and resolution mismodelling of the muon momentum measurement is investigated in $Z \to \mu\mu$ and $J/\psi \to \mu\mu$ decays collected in Run 2

pp collisions. For $Z \to \mu\mu$ decays, the uncertainty in the muon momentum scale is between 0.05 % and 0.15 % for the full p_{T} range. For the dimuon mass peak, the dimuon mass resolution ranges between 1.3 % to 2.4 % depending on the detector region. Overall, a factor of two improvement is observed in the precision of the muon momentum scale and resolution compared to the previous calibration.

Run 3 of the LHC provided access to an unprecedented centre-of-mass energy of 13.6 TeV for pp collisions. The author's contribution to the Run 3 analyses, including muon calibration and trigger performance studies, are outlined in chapter 6. The total Higgs boson production cross-section is extrapolated from the fiducial cross-section, and is measured at $\sigma(pp \to H) = 58.2 \pm 8.7$ pb $= 58.2 \pm 7.5$(stat.) $\pm$4.5 (syst.), which is consistent with the prediction from the Standard Model.

At the time of writing this thesis, one of the biggest obstacles for precision Higgs boson measurements is the limited statistics. This will be partially addressed by LHC Run 3 and the High-Luminosity LHC upgrades, albeit at the expense of higher pile-up, additional radiation damage and challenges in event reconstruction. Such challenges naturally call for advances in analysis techniques, and particle physics provides a multi-disciplinary playground for experimentation and innovation. Studies and applications of multivariate techniques, including graph neural networks, Bayesian optimisation and optimal transport, are suitable candidates to further our understanding of physics and detector performance, especially with their applications in tagging jets with different flavours, and distinguishing signal candidates with a large number of final state particles. The increasing statistics from Run 3 and subsequently High-Luminosity LHC upgrades also open up the possibility to probe the Higgs self-coupling term directly through the search for di-Higgs production, in addition to the search for Higgs coupling to lighter fermions, including charm quarks and muons.

To understand the level of precision attainable by the HL-LHC, one can extrapolate the Higgs boson mass measurement referenced in chapter 5 to 3000 fb^{-1} under two different scenarios. The first scenario (S1) assumes the current

systematic uncertainties and detector performances, and the second scenario (S2) assumes a 30% improvement in the total systematic uncertainties. The reduction in systematic uncertainty can be justified by the deployment of the Inner Tracker, and the improvement in muon calibration from additional statistics. The extrapolated systematic uncertainty is 0.04 GeV (S1) and 0.03 GeV (S2), while the extrapolated statistic uncertainty is 0.04 GeV, resulting in a total uncertainty of ≈0.05 GeV [171].

Ultimately, to fully measure the diverse couplings of the Higgs boson in a fully reconstructible environment, another machine succeeding the LHC will be needed. Such machines, usually called 'Higgs factories', will open up exciting possibilities for both beyond the Standard Model searches, and for precision electroweak measurements. Candidate machines include both linear (such as ILC [172]) and circular electron-positron colliders (such as FCC-ee [173] and CEPC [174]). These machines are capable of reducing the QCD modelling uncertainties, which are the largest theoretical uncertainties at the LHC, and the kinematics of each event can be precisely determined, thanks to the precision with which the initial-state energy is known. As an example, the FCC-ee will operate at the ZH pole, which allows for a model-independent determination of the ZH cross section by measuring the Higgs boson recoiling against the Z boson. This offers a significant uncertainty reduction in the Higgs coupling to the Z boson, from a projected 1.5 % by the end of HL-LHC, to 0.18 % by the end of FCC-ee [175]. With improvements in the systematic and theory uncertainties, the uncertainty in the measured Higgs boson mass can be reduced further to 2-3 MeV [176]. Similar improvements can be achieved for various physics programs, ranging from precision measurements of the top and W mass, searches for the Higgs coupling to light fermions (e.g. charm and electrons), and constraints on the Higgs self-coupling, in addition to signs of new physics at higher energies that could be studied at future energy frontier machines.

Appendices

Appendix A

Trigger naming convention for Run 3

The Run 3 HLT trigger naming convention specific to lepton triggers is summarised as follows:

- HLT reconstructed electron (muons) are labelled as `e` (`mu`), directly followed by the HLT p_{T} threshold for this trigger, and any non-default cuts on the HLT object. For example, `e140_lhloose` corresponds to requiring one electron with $p_{\mathrm{T}} > 140GeV$, while satisfying the *Loose* likelihood definition as defined in Ref [143].

- For multi-lepton triggers, the HLT trigger strings are concatenated for leptons with differing cuts. If n leptons have identical kinematic requirements, n is prefixed before the HLT string, instead of concatenating two identical HLT strings. For example, `mu20_2mu4noL1` corresponds to requiring one muon with $p_{\mathrm{T}} > 20$ GeV, and two other muons with $p_{\mathrm{T}} > 4$ GeV and reconstructed without requiring a L1 trigger.

- Each HLT object is selected from events that pass certain L1 trigger requirements unless stated otherwise (e.g. `noL1`). These requirements are appended at the end of each trigger name, starting with `L1`. The number of L1 objects required, if larger than 1, is appended immediately after `L1`. This is followed by the trigger sub-system name, which for electrons (muons) corresponds to `EM` (`MU`), and the value of the L1 threshold. Finally, the last

few strings correspond to the special requirements for L1, and are listed below:

  - `V`: **V**ariable thresholds with η;
  - `F`: require **F**ull-station (three-station) big-wheel coincidence for endcap;
  - `C`: require additional **C**oincidence for endcap;
  - `H`: require only events satisfying the good magnetic field flag;
  - `BO`: require central (**B**arrel **O**nly) muons;
  - `M`: **M**ultiple muon candidates in the same RPC pad.

- For multi-lepton triggers, the `L1` string only appears at the start of L1 trigger strings.

Appendix B

Trigger ranking studies per channel

The full set of trigger ranking studies can be found in Figure B.1-B.6.

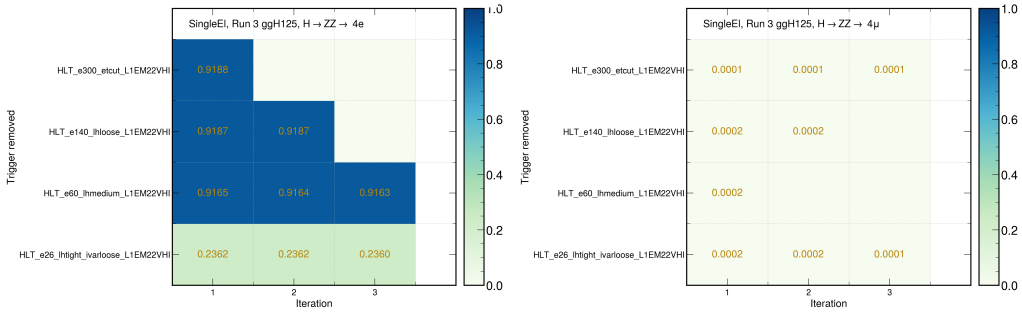

(a) 4e channel

(b) 4μ channel

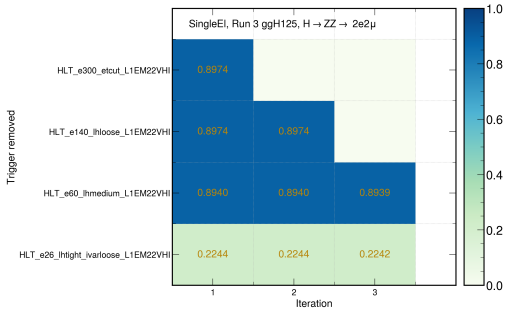

(c) 2e2μ channel

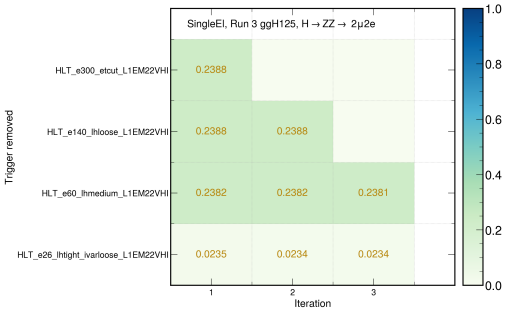

(d) 2μ2e channel

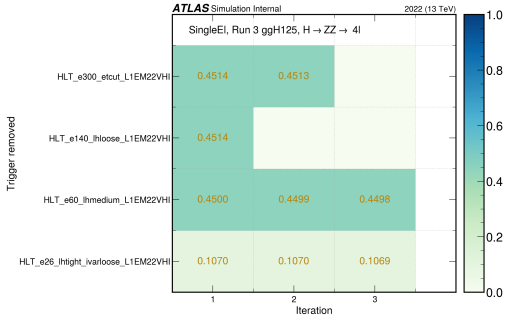

(e) 4e+4μ+2e2μ+2μ2e channel

Figure B.1: Ranking studies of single-electron triggers

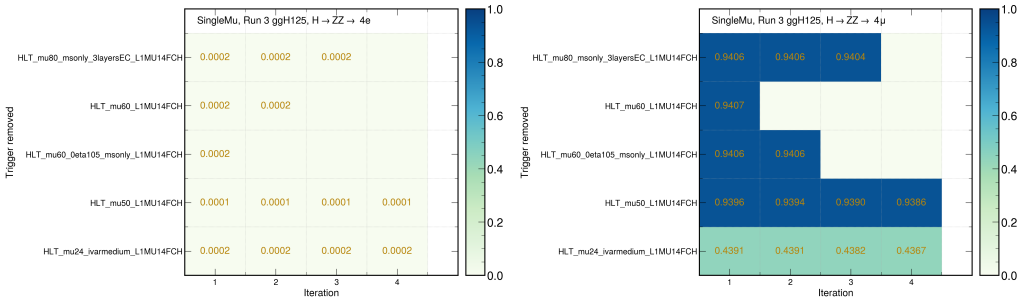

(a) 4e channel

(b) 4μ channel

(c) $2e2\mu$ channel

(d) $2\mu2e$ channel

(e) $4e+4\mu+2e2\mu+2\mu2e$ channel

Figure B.2: Ranking studies of single-muon triggers

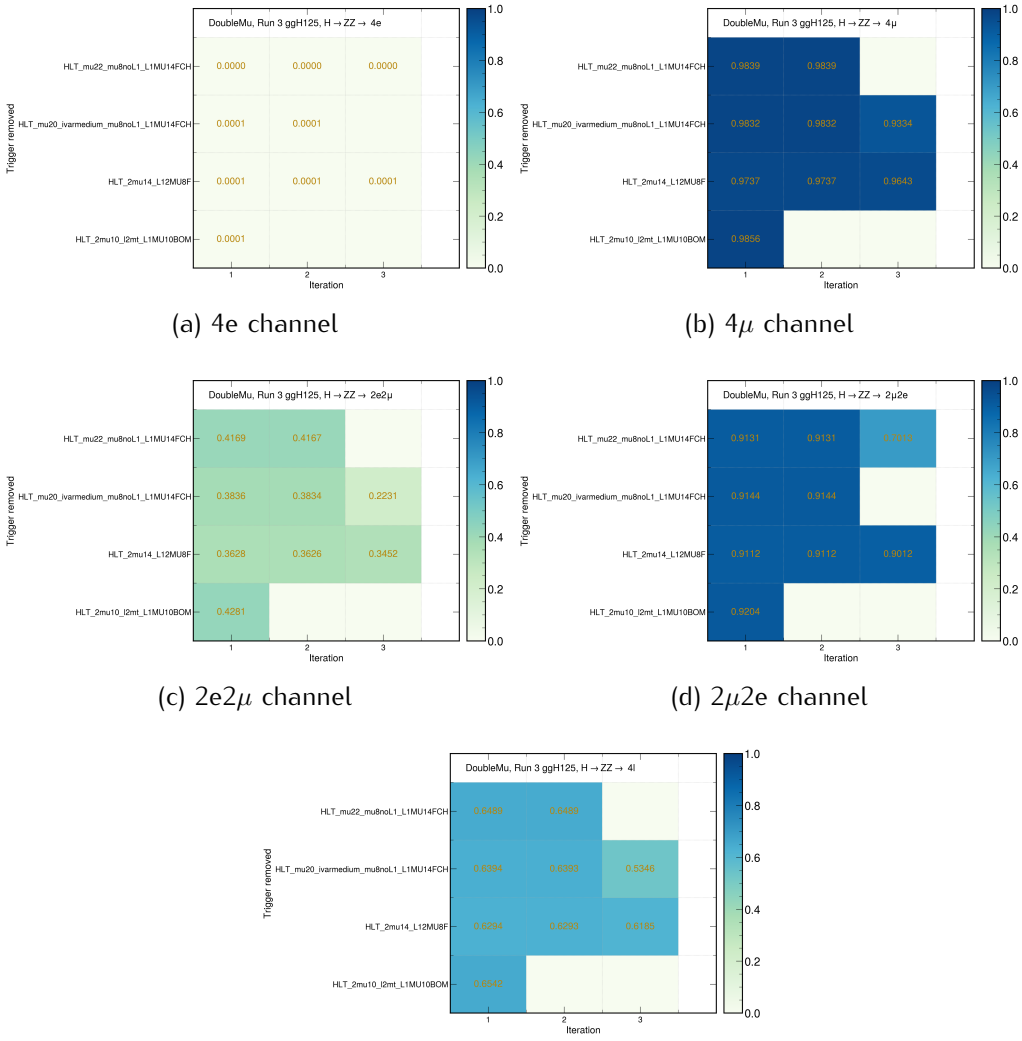

(a) 4e channel

(b) 4μ channel

(c) 2e2μ channel

(d) 2μ2e channel

(e) 4e+4μ+2e2μ+2μ2e channel

Figure B.3: Ranking studies of double-muon triggers

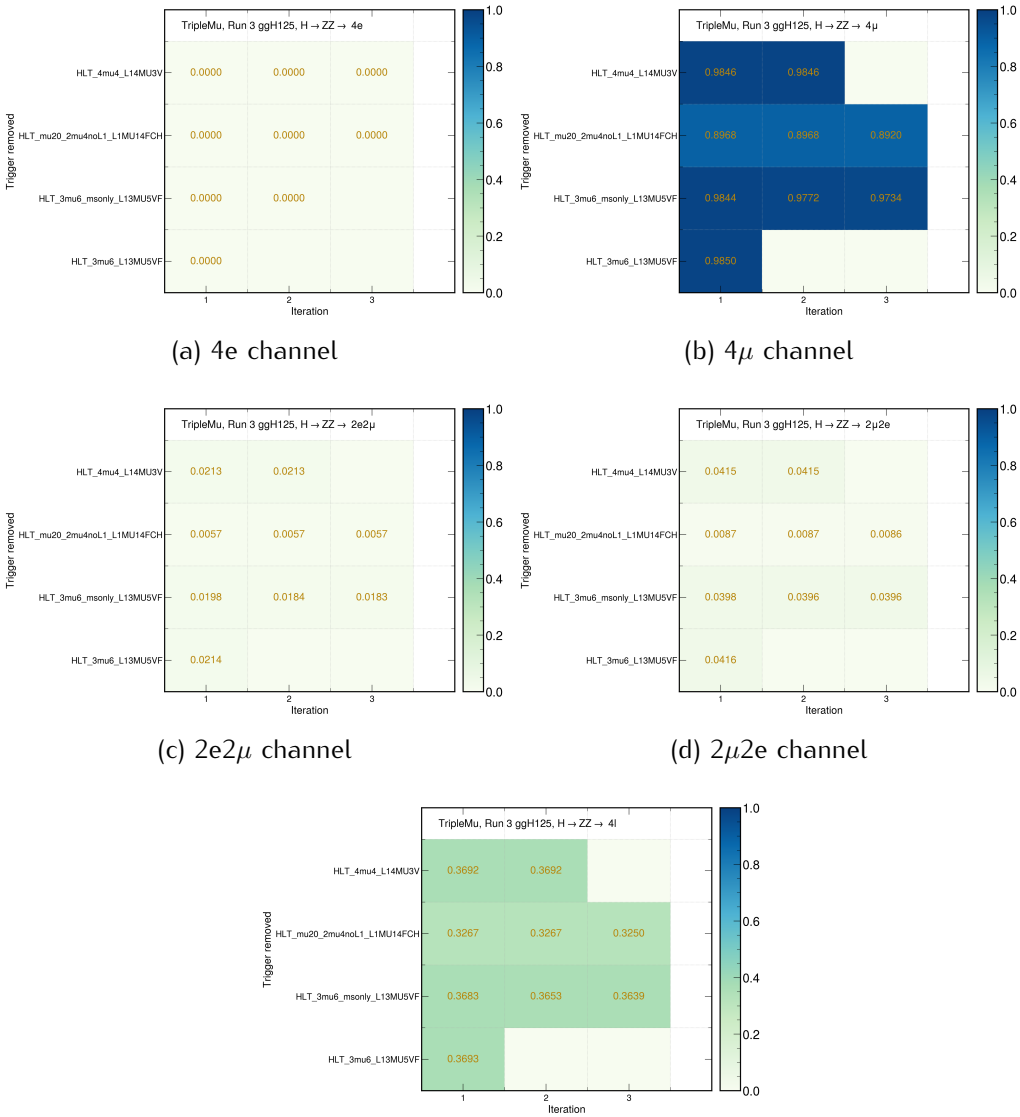

(a) 4e channel

(b) 4μ channel

(c) 2e2μ channel

(d) 2μ2e channel

(e) 4e+4μ+2e2μ+2μ2e channel

Figure B.4: Ranking studies of multi-muon triggers

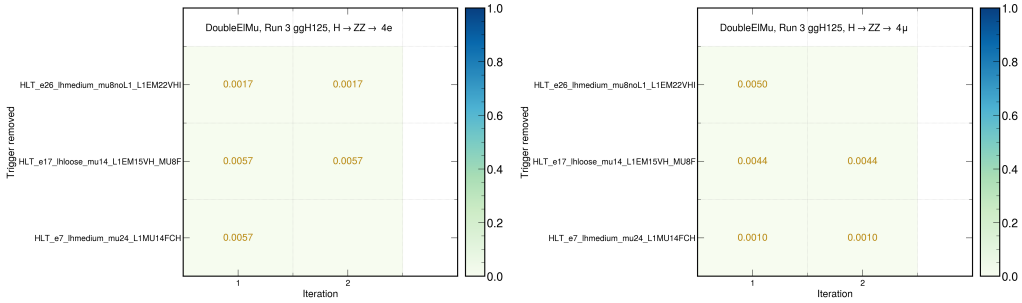

(a) 4e channel

(b) 4μ channel

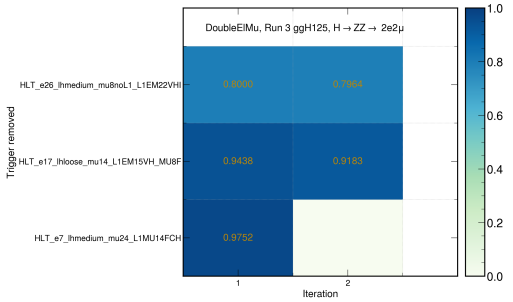

(c) 2e2μ channel

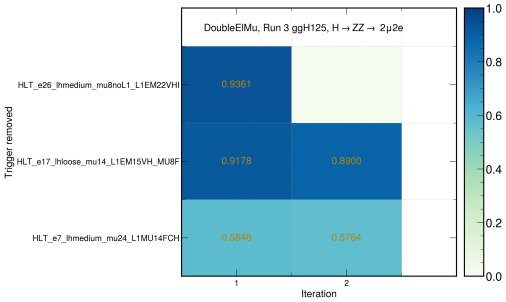

(d) 2μ2e channel

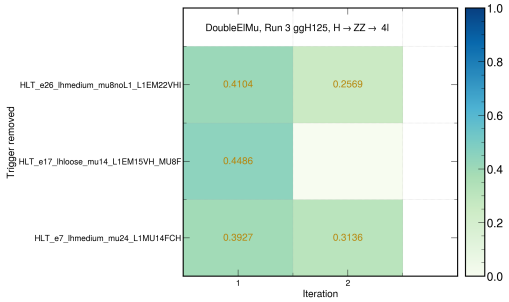

(e) 4e+4μ+2e2μ+2μ2e channel

Figure B.5: Ranking studies of di-emu triggers

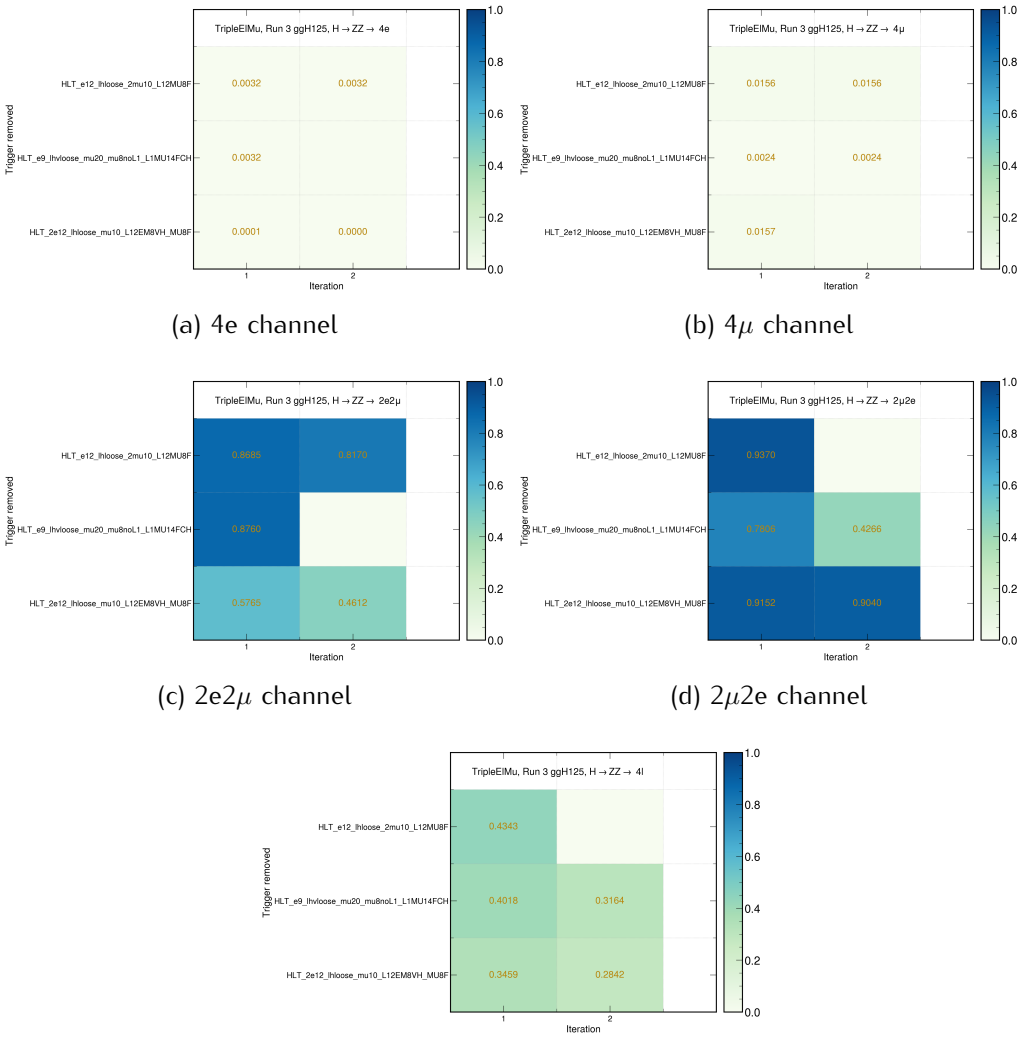

(a) 4e channel

(b) 4μ channel

(c) 2e2μ channel

(d) 2μ2e channel

(e) 4e+4μ+2e2μ+2μ2e channel

Figure B.6: Ranking studies of multi-emu triggers

Appendix C

Kinematic distributions in the $H \to ZZ^* \to 4\ell$ channel in Run 3

Figure C.1-C.2 show the pre-fit lepton kinematic distributions for the $H \to ZZ^* \to 4\ell$ final state in Run 3 data and simulation. The four-lepton kinematic variables are shown in Figure C.3, and the mass distributions for the Z bosons are shown in Figure C.4.

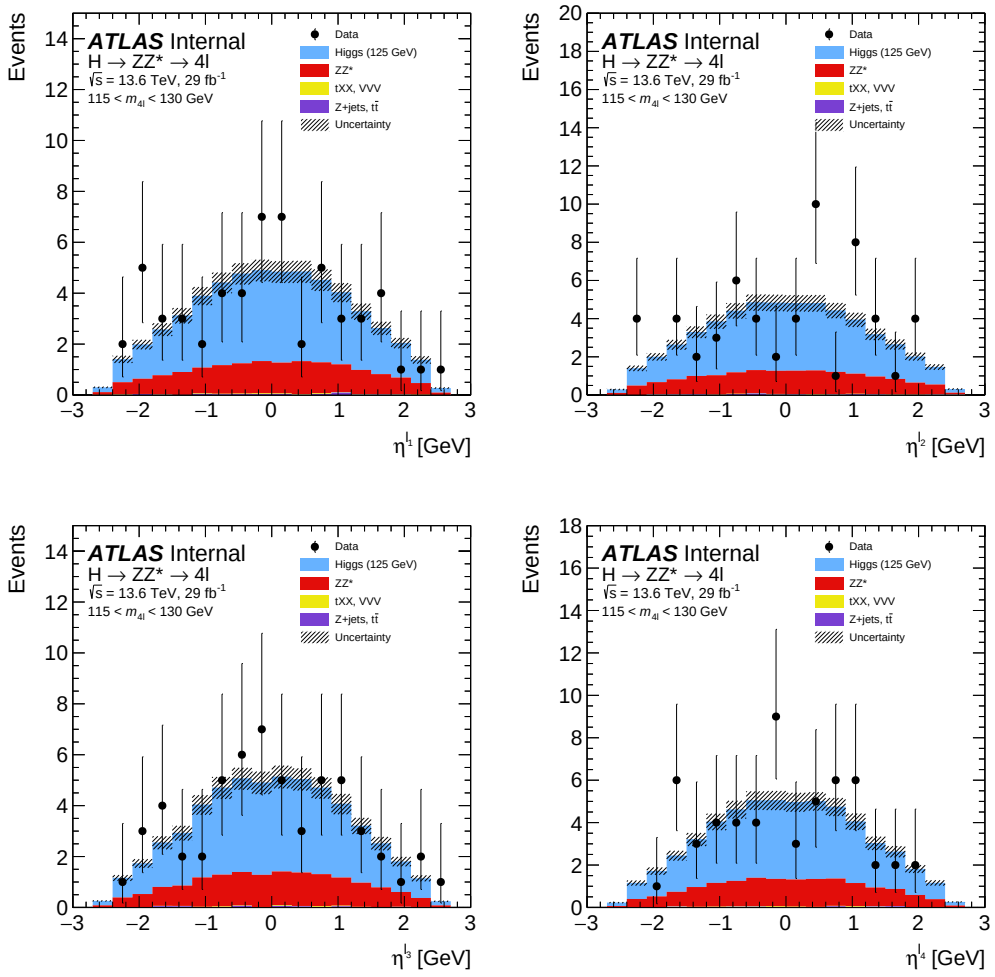

Figure C.1: Pre-fit data/MC comparison in the signal region, $115 < m_{4\ell} < 130$ GeV, for the lepton η. Lepton 1 (top-left) is the positive lepton from the on-shell Z boson candidate, and lepton 2 (top right) is the negative lepton from the on-shell Z boson candidate. Lepton 3 (bottom left) is the positive lepton from the off-shell Z boson candidate, and lepton 4 (bottom right) is the negative lepton from the off-shell Z boson candidate.

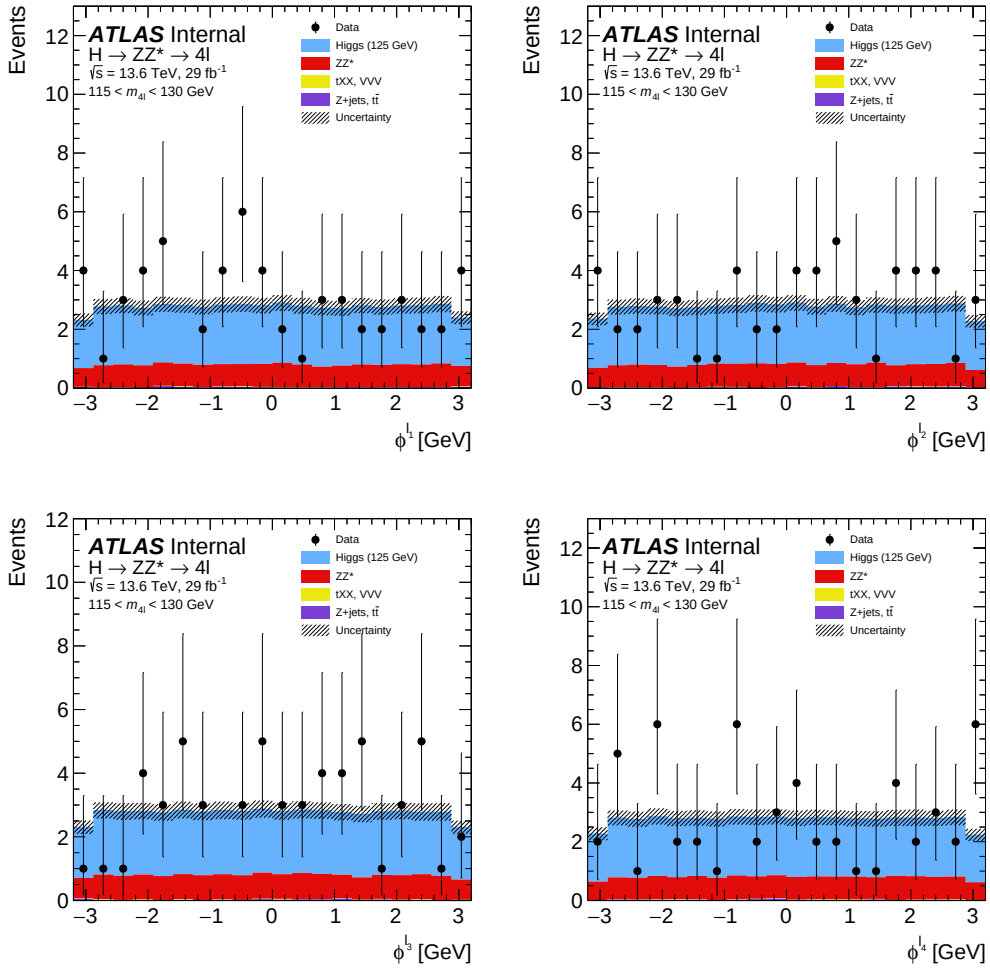

Figure C.2: Pre-fit data/MC comparison in the signal region, $115 < m_{4\ell} < 130$ GeV, for the lepton ϕ. Lepton 1 (top-left) is the positive lepton from the on-shell Z boson candidate, and lepton 2 (top right) is the negative lepton from the on-shell Z boson candidate. Lepton 3 (bottom left) is the positive lepton from the off-shell Z boson candidate, and lepton 4 (bottom right) is the negative lepton from the off-shell Z boson candidate.

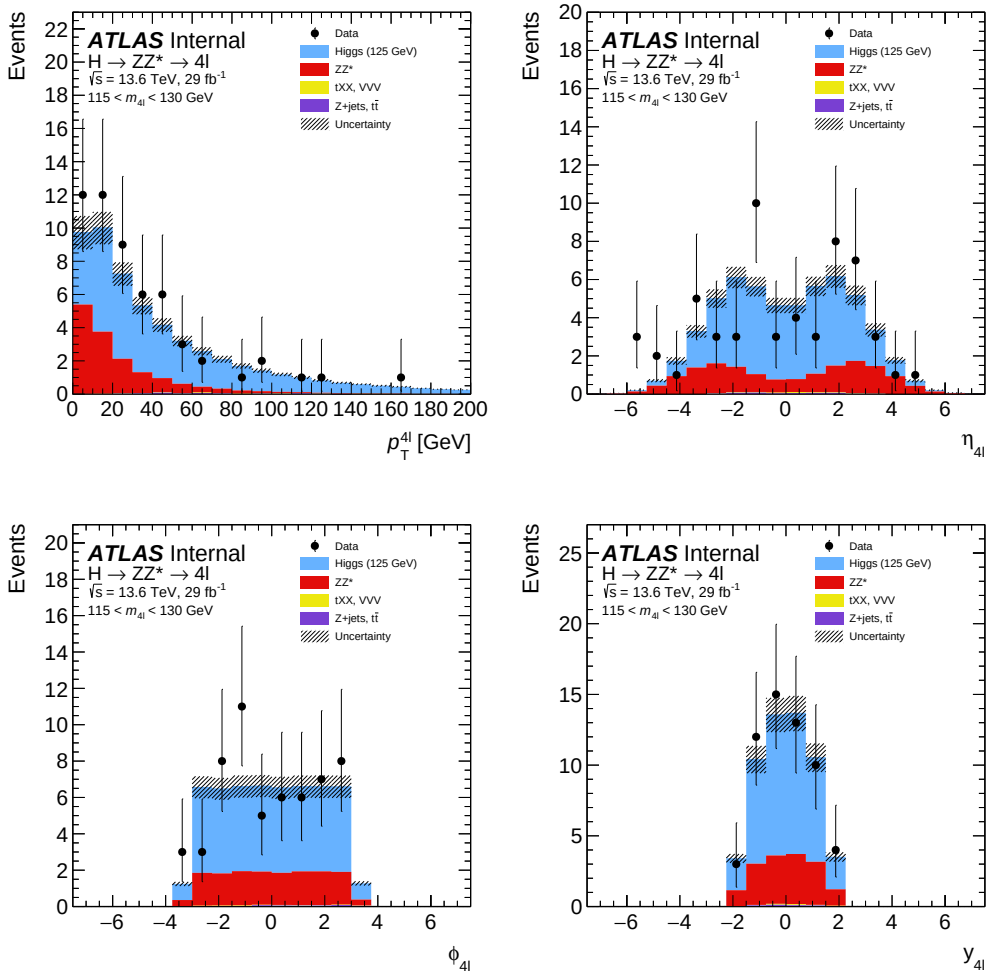

Figure C.3: Pre-fit data/MC comparison in the signal region, $115 < m_{4\ell} < 130$ GeV, for the four-lepton system quantities. Top-left shows the p_{T} distribution of the four-lepton system, and top right shows the η distribution of the four-lepton system. Bottom left shows the ϕ distribution, and bottom right shows the rapidity of the four-lepton system.

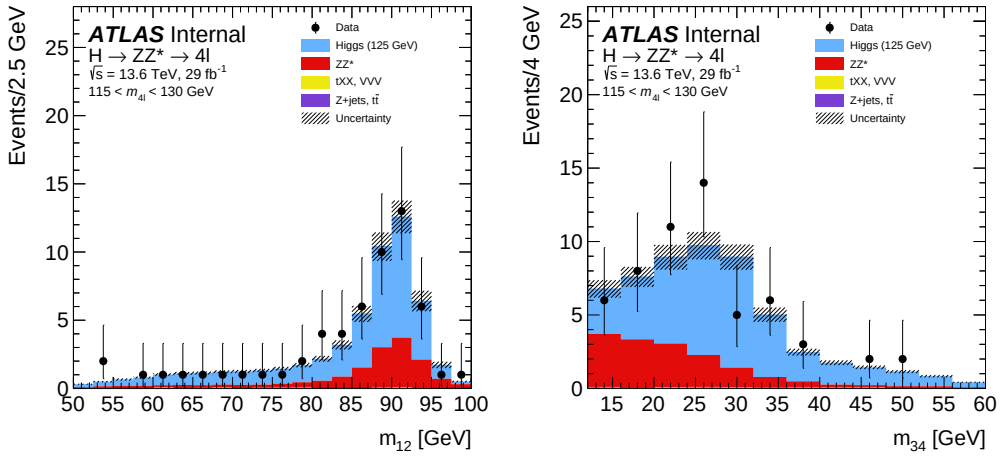

Figure C.4: Pre-fit data/MC comparison in the signal region, $115 < m_{4\ell} < 130$ GeV, for the Z boson mass distributions. The left plot shows the on-shell Z mass distribution after applying FSR recovery, and the right plot shows the off-shell Z mass distribution.

References

[1] Emmy Noether. "Invariant variation problems". In: *Transport Theory and Statistical Physics* 1.3 (Jan. 1971), pp. 186–207. URL: http://dx.doi.org/10.1080/00411457108231446.

[2] Mark Thomson. *Modern Particle Physics*. University Printing House, Cambridge: Cambridge University Press, 2013. URL: https://cds.cern.ch/record/331068.

[3] M. Aker et al. "Direct neutrino-mass measurement with sub-electronvolt sensitivity". In: *Nature Phys.* 18.2 (2022), pp. 160–166. arXiv: 2105.08533 [hep-ex].

[4] "First measurement of neutrino oscillation parameters using neutrinos and antineutrinos by NOvA". In: *Phys. Rev. Lett.* 123 (15 Oct. 2019), p. 151803. URL: https://link.aps.org/doi/10.1103/PhysRevLett.123.151803.

[5] Robin Devenish and Amanda Cooper-Sarkar. *Deep Inelastic Scattering*. Oxford University Press, Nov. 2003. URL: https://doi.org/10.1093/acprof:oso/9780198506713.001.0001.

[6] R. S. Thorne A. D. Martin W. J. Stirling and G. Watt. "Parton distributions for the LHC". In: *The European Physical Journal C* 63.2 (July 2009), pp. 189–285. URL: https://doi.org/10.1140%2Fepjc%2Fs10052-009-1072-5.

[7] Richard D. Ball et al. "Parton distributions for the LHC run II". In: *Journal of High Energy Physics* 2015.4 (Apr. 2015). URL: https://doi.org/10.1007%2Fjhep04%282015%29040.

[8] C. S. Wu et al. "Experimental Test of Parity Conservation in Beta Decay". In: *Phys. Rev.* 105 (4 Feb. 1957), pp. 1413–1415. URL: https://link.aps.org/doi/10.1103/PhysRev.105.1413.

[9] M. Martinez et al. "Precision tests of the electroweak interaction at the Z pole". In: *Rev. Mod. Phys.* 71 (3 Apr. 1999), pp. 575–629. URL: https://link.aps.org/doi/10.1103/RevModPhys.71.575.

[10] Abdus Salam. "Weak and Electromagnetic Interactions". In: *Conf. Proc. C* 680519 (1968), pp. 367–377.

[11] Steven Weinberg. "A Model of Leptons". In: *Phys. Rev. Lett.* 19 (1967), pp. 1264–1266.

[12] Sheldon L. Glashow. "Partial-symmetries of weak interactions". In: *Nuclear Physics* 22.4 (1961), pp. 579–588. URL: https://www.sciencedirect.com/science/article/pii/0029558261904692.

[13] F. Englert and R. Brout. "Broken Symmetry and the Mass of Gauge Vector Mesons". In: *Phys. Rev. Lett.* 13 (1964). Ed. by J. C. Taylor, pp. 321–323.

[14] Peter W. Higgs. "Broken Symmetries and the Masses of Gauge Bosons". In: *Phys. Rev. Lett.* 13 (1964). Ed. by J. C. Taylor, pp. 508–509.

[15] G. S. Guralnik, C. R. Hagen, and T. W. B. Kibble. "Global Conservation Laws and Massless Particles". In: *Phys. Rev. Lett.* 13 (1964). Ed. by J. C. Taylor, pp. 585–587.

[16] M. Mulders, ed. *2013 European School of High-Energy Physics: Paradfurdo, Hungary 5 - 18 Jun 2013. Proceedings, 2013 European School of High-Energy Physics (ESHEP 2013). Paradfurdo, Hungary, June 5-18, 2013. 2013 European School of High-Energy Physics*. 6 lectures, 333 pages, published as CERN Yellow Report https://e-publishing.cern.ch/index.php/CYR/issue/view/3. CERN. Geneva: CERN, 2015. URL: https://cds.cern.ch/record/1522578.

[17] "A combination of measurements of Higgs boson production and decay using up to 139 fb^{-1} of proton–proton collision data at $\sqrt{s} = 13$ TeV collected with the ATLAS experiment". In: (Aug. 2020).

[18] G. Aad *et. al.* "Observation of a new particle in the search for the Standard Model Higgs boson with the ATLAS detector at the LHC". In: *Physics Letters B* 716.1 (Sept. 2012), pp. 1–29. URL: https://doi.org/10.1016%2Fj.physletb.2012.08.020.

[19] S. Chatrchyan *et. al.* "Observation of a new boson at a mass of 125 GeV with the CMS experiment at the LHC". In: *Physics Letters B* 716.1 (Sept. 2012), pp. 30–61. URL: https://doi.org/10.1016%2Fj.physletb.2012.08.021.

[20] G. *et. al.* Aad. "Combined Measurement of the Higgs Boson Mass in pp Collisions at $\sqrt{s}$ =7 and 8 TeV with the ATLAS and CMS Experiments". In: *Phys. Rev. Lett.* 114 (19 May 2015), p. 191803. URL: https://link.aps.org/doi/10.1103/PhysRevLett.114.191803.

[21] "A detailed map of Higgs boson interactions by the ATLAS experiment ten years after the discovery". In: *Nature* 607.7917 (July 2022), pp. 52–59. URL: https://doi.org/10.1038%2Fs41586-022-04893-w.

[22] "A portrait of the Higgs boson by the CMS experiment ten years after the discovery". In: *Nature* 607.7917 (July 2022), pp. 60–68. URL: https://doi.org/10.1038%2Fs41586-022-04892-x.

[23] ATLAS Collaboration. *Measurement of the CP properties of Higgs boson interactions with τ-leptons with the ATLAS detector*. 2022. arXiv: 2212.05833 [hep-ex].

[24] R. L. Workman et al. "Review of Particle Physics". In: *PTEP* 2022 (2022).

[25] F. Zwicky. "Die Rotverschiebung von extragalaktischen Nebeln". In: *Helv. Phys. Acta* 6 (1933), pp. 110–127.

[26] Douglas Clowe et al. "A Direct Empirical Proof of the Existence of Dark Matter". In: *The Astrophysical Journal* 648.2 (Aug. 2006), pp. L109–L113. URL: https://doi.org/10.1086%2F508162.

[27] P. A. R. Ade et al. "Planck 2015 results. XIII. Cosmological parameters". In: *Astron. Astrophys.* 594 (2016), A13. arXiv: 1502.01589 [astro-ph.CO].

[28] Adam G. Riess et al. "Observational Evidence from Supernovae for an Accelerating Universe and a Cosmological Constant". In: *The Astronomical Journal* 116.3 (Sept. 1998), pp. 1009–1038. URL: https://doi.org/10.1086%2F300499.

[29] Stefano Profumo, Leonardo Giani, and Oliver F. Piattella. "An Introduction to Particle Dark Matter". In: *Universe* 5.10 (2019), p. 213. arXiv: 1910.05610 [hep-ph].

[30] Carlo Rovelli. "Notes for a brief history of quantum gravity". In: *9th Marcel Grossmann Meeting on Recent Developments in Theoretical and Experimental General Relativity, Gravitation and Relativistic Field Theories (MG 9)*. June 2000, pp. 742–768. arXiv: gr-qc/0006061.

[31] and K. Abe et al. "Constraint on the matterantimatter symmetry-violating phase in neutrino oscillations". In: *Nature* 580.7803 (Apr. 2020), pp. 339–344. URL: https://doi.org/10.1038%2Fs41586-020-2177-0.

[32] Raymond Davis Jr., Don S. Harmer, and Kenneth C. Hoffman. "Search for neutrinos from the sun". In: *Phys. Rev. Lett.* 20 (1968), pp. 1205–1209.

[33] Gian Francesco Giudice. "Naturally Speaking: The Naturalness Criterion and Physics at the LHC". In: *Perspectives on LHC Physics*. WORLD SCIENTIFIC, Jan. 2008, pp. 155–178. URL: https://doi.org/10.1142%2F9789812779762_0010.

[34] R Scrivens et al. "Overview of the status and developments on primary ion sources at CERN*". In: (2011). URL: https://cds.cern.ch/record/1382102.

[35] Michael Barnes et al. *The PS complex as proton pre-injector for the LHC: design and implementation report*. CERN Yellow Reports: Monographs. Geneva: CERN, 2000. URL: https://cds.cern.ch/record/449242.

[36] Daniel Boussard and Trevor Paul R Linnecar. *The LHC Superconducting RF System*. Tech. rep. Geneva: CERN, 1999. URL: https://cds.cern.ch/record/410377.

[37] Oliver Sim Brüning et al. *LHC Design Report*. CERN Yellow Reports: Monographs. Geneva: CERN, 2004. URL: https://cds.cern.ch/record/782076.

[38] Fabienne Marcastel. "CERN's Accelerator Complex. La chaîne des accélérateurs du CERN". In: (2013). General Photo. URL: https://cds.cern.ch/record/1621583.

[39] "Reconstruction of primary vertices at the ATLAS experiment in Run 1 protonproton collisions at the LHC". In: *The European Physical Journal C* 77.5 (2017). URL: https://doi.org/10.1140%2Fepjc%2Fs10052-017-4887-5.

[40] I. Zurbano Fernandez et al. "High-Luminosity Large Hadron Collider (HL-LHC): Technical design report". In: 10/2020 (Dec. 2020). Ed. by I. Béjar Alonso et al.

[41] Tony Affolder. "ATLAS Phase II Upgrade". In: (2022). URL: https://cds.cern.ch/record/2799535.

[42] The ATLAS Collaboration. "Public ATLAS Luminosity Results for Run-3 of the LHC". In: (2022). URL: https://twiki.cern.ch/twiki/bin/view/AtlasPublic/LuminosityPublicResultsRun3.

[43] G et. al. Aad. "The ATLAS Experiment at the CERN Large Hadron Collider". In: *JINST* 3 (2008). Also published by CERN Geneva in 2010, S08003. URL: https://cds.cern.ch/record/1129811.

[44] F Ragusa and L Rolandi. "Tracking at LHC". In: *New Journal of Physics* 9.9 (Sept. 2007), p. 336. URL: https://dx.doi.org/10.1088/1367-2630/9/9/336.

[45] M. Aaboud et al. "Performance of the ATLAS Transition Radiation Tracker in Run 1 of the LHC: tracker properties". In: *Journal of Instrumentation* 12.05 (May 2017), P05002–P05002. URL: https://doi.org/10.1088%2F1748-0221%2F12%2F05%2Fp05002.

[46] M Capeans et al. *ATLAS Insertable B-Layer Technical Design Report*. Tech. rep. 2010. URL: https://cds.cern.ch/record/1291633.

[47] *ATLAS level-1 trigger: Technical Design Report*. Technical design report. ATLAS. Geneva: CERN, 1998. URL: https://cds.cern.ch/record/381429.

[48] Peter Jenni et al. *ATLAS high-level trigger, data-acquisition and controls: Technical Design Report*. Technical design report. ATLAS. Geneva: CERN, 2003. URL: https://cds.cern.ch/record/616089.

[49] The ATLAS collaboration. "Operation of the ATLAS trigger system in Run 2". In: *Journal of Instrumentation* 15.10 (Oct. 2020), P10004–P10004. URL: https://doi.org/10.1088%2F1748-0221%2F15%2F10%2Fp10004.

[50] Paolo Nason. "A New method for combining NLO QCD with shower Monte Carlo algorithms". In: *JHEP* 11 (2004), p. 040. arXiv: hep-ph/0409146.

[51] Stefano Frixione, Paolo Nason, and Carlo Oleari. "Matching NLO QCD computations with Parton Shower simulations: the POWHEG method". In: *JHEP* 11 (2007), p. 070. arXiv: 0709.2092 [hep-ph].

[52] Simone Alioli et al. "A general framework for implementing NLO calculations in shower Monte Carlo programs: the POWHEG BOX". In: *JHEP* 06 (2010), p. 043. arXiv: 1002.2581 [hep-ph].

[53] Enrico Bothmann et al. "Event Generation with Sherpa 2.2". In: *SciPost Phys.* 7.3 (2019), p. 034. arXiv: 1905.09127 [hep-ph].

[54] Torbjorn Sjöstrand, Stephen Mrenna, and Peter Z. Skands. "A brief introduction to PYTHIA 8.1". In: *Comput. Phys. Commun.* 178 (2008), pp. 852–867. arXiv: 0710.3820 [hep-ph].

[55] *ATLAS Computing: technical design report*. Technical design report. ATLAS. Geneva: CERN, 2005. URL: https://cds.cern.ch/record/837738.

[56] G. Aad et al. "The ATLAS Simulation Infrastructure". In: *Eur. Phys. J. C* 70 (2010), pp. 823–874. arXiv: 1005.4568 [physics.ins-det].

[57] S. Agostinelli et al. "Geant4a simulation toolkit". In: *Nuclear Instruments and Methods in Physics Research Section A: Accelerators, Spectrometers, Detectors and Associated Equipment* 506.3 (2003), pp. 250–303. URL: https://www.sciencedirect.com/science/article/pii/S0168900203013688.

[58] J. Allison et al. "Recent developments in Geant4". In: *Nuclear Instruments and Methods in Physics Research Section A: Accelerators, Spectrometers, Detectors and Associated Equipment* 835 (2016), pp. 186–225. URL: https://www.sciencedirect.com/science/article/pii/S0168900216306957.

[59] J. Allison et al. "Geant4 developments and applications". In: *IEEE Transactions on Nuclear Science* 53.1 (2006), pp. 270–278.

[60] Ferruccio Feruglio. "Flavour Physics 1". In: *PoS* CORFU2014 (2015), p. 016.

[61] Nima Arkani-Hamed et al. "Flavor at the TeV scale with extra dimensions". In: *Phys. Rev. D* 61 (2000), p. 116003. arXiv: hep-ph/9909326.

[62] *Performance of the ATLAS Silicon Pattern Recognition Algorithm in Data and Simulation at $\sqrt{s} = 7$ TeV*. Tech. rep. All figures including auxiliary figures are available at https://atlas.web.cern.ch/Atlas/GROUPS/PHYSICS/CONFNOTES/ATLAS-CONF-2010-072. Geneva: CERN, 2010. URL: https://cds.cern.ch/record/1281363.

[63] Rudolf E. Kalman. "A new approach to linear filtering and prediction problems". In: *Journal of Fluids Engineering* 82 (Mar. 1960), pp. 35–45.

[64] T Cornelissen et al. *Concepts, Design and Implementation of the ATLAS New Tracking (NEWT)*. Tech. rep. All figures including auxiliary figures are available at https://atlas.web.cern.ch/Atlas/GROUPS/PHYSICS/PUBNOTES/ATL-SOFT-PUB-2007-007. Geneva: CERN, 2007. URL: https://cds.cern.ch/record/1020106.

[65] Priyanka Mukhopadhyay and Bidyut B. Chaudhuri. "A survey of Hough Transform". In: *Pattern Recognition* 48.3 (2015), pp. 993–1010. URL: https://www.sciencedirect.com/science/article/pii/S0031320314003446.

[66] Georges Aad et al. "Muon reconstruction and identification efficiency in ATLAS using the full Run 2 pp collision data set at $\sqrt{s} = 13$ TeV". In: *Eur. Phys. J. C* 81.7 (2021), p. 578. arXiv: 2012.00578 [hep-ex].

[67] *Optimisation and performance studies of the ATLAS b-tagging algorithms for the 2017-18 LHC run*. Tech. rep. All figures including auxiliary figures are available at https://atlas.web.cern.ch/Atlas/GROUPS/PHYSICS/PUBNOTES/ATL-PHYS-PUB-2017-013. Geneva: CERN, 2017. URL: https://cds.cern.ch/record/2273281.

[68] Simone Alioli et al. "NLO vector-boson production matched with shower in POWHEG". In: *JHEP* 07 (2008), p. 060. arXiv: 0805.4802 [hep-ph].

[69] ATLAS Collaboration. "Measurement of the Z/γ^* boson transverse momentum distribution in pp collisions at $\sqrt{s} = 7$ TeV with the ATLAS detector". In: *JHEP* 09 (2014), p. 145. arXiv: 1406.3660 [hep-ex].

[70] Hung-Liang Lai et al. "New parton distributions for collider physics". In: *Phys. Rev. D* 82 (2010), p. 074024. arXiv: 1007.2241 [hep-ph].

[71] Richard D. Ball et al. "Parton distributions for the LHC Run II". In: *JHEP* 04 (2015), p. 040. arXiv: 1410.8849 [hep-ph].

[72] ATLAS Collaboration. *ATLAS Pythia 8 tunes to 7 TeV data*. ATL-PHYS-PUB-2014-021. 2014. URL: https://cds.cern.ch/record/1966419.

[73] ATLAS Collaboration. *Studies on top-quark Monte Carlo modelling for Top2016*. ATL-PHYS-PUB-2016-020. 2016. URL: https://cds.cern.ch/record/2216168.

[74] Torbjörn Sjöstrand et al. "An introduction to PYTHIA 8.2". In: *Comput. Phys. Commun.* 191 (2015), p. 159. arXiv: 1410.3012 [hep-ph].

[75] Stefano Frixione, Giovanni Ridolfi, and Paolo Nason. "A positive-weight next-to-leading-order Monte Carlo for heavy flavour hadroproduction". In: *JHEP* 09 (2007), p. 126. arXiv: 0707.3088 [hep-ph].

[76] "Alignment of the ATLAS Inner Detector in Run-2". In: *Eur. Phys. J. C* 80.12 (2020). 61 pages in total, author list starting page 45, 26 figures, 4 tables, published in EPJC. All figures including auxiliary figures are available at http://atlas.web.cern.ch/Atlas/GROUPS/PHYSICS/PAPERS/IDTR-2019-05, p. 1194. arXiv: 2007.07624. URL: https://cds.cern.ch/record/2724037.

[77] *Muon Momentum Resolution in First Pass Reconstruction of pp Collision Data Recorded by ATLAS in 2010*. Tech. rep. All figures including auxiliary figures are available at https://atlas.web.cern.ch/Atlas/GROUPS/PHYSICS/CONFNOTES/ATLAS-CONF-2011-046. Geneva: CERN, 2011. URL: https://cds.cern.ch/record/1338575.

[78] *Preliminary results on the muon reconstruction efficiency, momentum resolution, and momentum scale in ATLAS 2012 pp collision data*. Tech. rep. All figures including auxiliary figures are available at https://atlas.web.cern.ch/Atlas/GROUPS/PHYSICS/CONFNOTES/ATLAS-CONF-2013-088. Geneva: CERN, 2013. URL: https://cds.cern.ch/record/1580207.

[79] The ATLAS collaboration. "Resolution of the ATLAS muon spectrometer monitored drift tubes in LHC Run 2". In: *Journal of Instrumentation* 14.09 (2019), P09011–P09011. URL: https://doi.org/10.1088%2F1748-0221%2F14%2F09%2Fp09011.

[80] *Performance of the muon spectrometer alignment in 2017 and 2018 data*. Tech. rep. All figures including auxiliary figures are available at https://atlas.web.cern.ch/Atlas/GROUPS/PHYSICS/PUBNOTES/ATL-MUON-PUB-2021-002. Geneva: CERN, 2021. URL: https://cds.cern.ch/record/2753329.

[81] M. J. Oreglia. *A study of reactions $\psi\prime \to \gamma\gamma\psi$*. PhD thesis, Univ. Stanford, 1980. SLAC-R-0236, Appendix D.

[82] Max Baak et al. "Interpolation between multi-dimensional histograms using a new non-linear moment morphing method". In: *Nucl. Instrum. Meth. A* 771 (2015), pp. 39–48. arXiv: 1410.7388 [physics.data-an].

[83] ATLAS Collaboration. *Studies of the muon momentum calibration and performance of the ATLAS detector with pp collisions at $\sqrt{s}$=13 TeV*. 2022. arXiv: 2212.07338 [hep-ex].

[84] Georges Aad et al. "Muon reconstruction performance of the ATLAS detector in protonproton collision data at $\sqrt{s}$ =13 TeV". In: *Eur. Phys. J. C* 76.5 (2016), p. 292. arXiv: 1603.05598 [hep-ex].

[85] CDF Collaboration. "High-precision measurement of the W boson mass with the CDF II detector". In: *Science* 376.6589 (2022), pp. 170–176. eprint: https://www.science.org/doi/pdf/10.1126/science.abk1781. URL: https://www.science.org/doi/abs/10.1126/science.abk1781.

[86] Jose R. Espinosa. *Implications of the top (and Higgs) mass for vacuum stability*. 2015. arXiv: 1512.01222 [hep-ph].

[87] Tommi Markkanen, Arttu Rajantie, and Stephen Stopyra. "Cosmological Aspects of Higgs Vacuum Metastability". In: *Frontiers in Astronomy and Space Sciences* 5 (2018). URL: https://www.frontiersin.org/articles/10.3389/fspas.2018.00040.

[88] Tommi Markkanen, Arttu Rajantie, and Stephen Stopyra. "Cosmological Aspects of Higgs Vacuum Metastability". In: *Front. Astron. Space Sci.* 5 (2018), p. 40. arXiv: 1809.06923 [astro-ph.CO].

[89] Gino Isidori, Giovanni Ridolfi, and Alessandro Strumia. "On the metastability of the standard model vacuum". In: *Nucl. Phys. B* 609 (2001), pp. 387–409. arXiv: hep-ph/0104016.

[90] Georges Aad et al. "Measurement of the Higgs boson mass from the $H \to \gamma\gamma$ and $H \to ZZ^* \to 4\ell$ channels with the ATLAS detector using 25 fb^{-1} of pp collision data". In: *Phys. Rev. D* 90.5 (2014), p. 052004. arXiv: 1406.3827 [hep-ex].

[91] Vardan Khachatryan et al. "Precise determination of the mass of the Higgs boson and tests of compatibility of its couplings with the standard model predictions using proton collisions at 7 and 8 TeV". In: *Eur. Phys. J. C* 75.5 (2015), p. 212. arXiv: 1412.8662 [hep-ex].

[92] M. Aaboud *et. al.* "Measurement of the Higgs boson mass from the $H \to \gamma\gamma$ and $H \to ZZ^* \to 4\ell$ channels with the ATLAS detector using 25 fb^{-1} of pp collision data". In: *Physics Letters B* 784 (Sept. 2018), pp. 345–366. URL: https://doi.org/10.1016%2Fj.physletb.2018.07.050.

[93] Albert M *et. al.* Sirunyan. "A measurement of the Higgs boson mass in the diphoton decay channel". In: *Phys. Lett. B* 805 (2020). Replaced with the published version. Added the journal reference and the DOI. All the figures and tables can be found at http://cms-results.web.cern.ch/cms-results/public-results/publications/HIG-19-004 (CMS Public Pages), p. 135425. arXiv: 2002.06398. URL: https://cds.cern.ch/record/2709657.

[94] ATLAS Collaboration. *Luminosity determination in pp collisions at $\sqrt{s} = 13$ TeV using the ATLAS detector at the LHC*. 2022. arXiv: 2212.09379 [hep-ex].

[95] ATLAS Collaboration. "The ATLAS Simulation Infrastructure". In: *Eur. Phys. J. C* 70 (2010), p. 823. arXiv: 1005.4568 [physics.ins-det].

[96] S. Agostinelli et al. "GEANT4 – a simulation toolkit". In: *Nucl. Instrum. Meth. A* 506 (2003), p. 250.

[97] ATLAS Collaboration. *The Pythia 8 A3 tune description of ATLAS minimum bias and inelastic measurements incorporating the Donnachie–Landshoff diffractive model*. ATL-PHYS-PUB-2016-017. 2016. URL: https://cds.cern.ch/record/2206965.

[98] Richard D. Ball et al. "Parton distributions with LHC data". In: *Nuclear Physics B* 867.2 (Feb. 2013), 244?289. URL: http://dx.doi.org/10.1016/j.nuclphysb.2012.10.003.

[99] D. J. Lange. "The EvtGen particle decay simulation package". In: *Nucl. Instrum. Meth. A* 462 (2001), p. 152.

[100] Keith Hamilton, Paolo Nason, and Giulia Zanderighi. "MINLO: multi-scale improved NLO". In: *JHEP* 10 (2012), p. 155. arXiv: 1206.3572 [hep-ph].

[101] Keith Hamilton et al. "Merging H/W/Z + 0 and 1 jet at NLO with no merging scale: a path to parton shower + NNLO matching". In: *JHEP* 05 (2013), p. 082. arXiv: 1212.4504 [hep-ph].

[102] Stefano Catani and Massimiliano Grazzini. "An NNLO subtraction formalism in hadron collisions and its application to Higgs boson production at the LHC". In: *Phys. Rev. Lett.* 98 (2007), p. 222002. arXiv: hep-ph/0703012.

[103] Keith Hamilton et al. "NNLOPS simulation of Higgs boson production". In: *JHEP* 10 (2013), p. 222. arXiv: 1309.0017 [hep-ph].

[104] Keith Hamilton, Paolo Nason, and Giulia Zanderighi. "Finite quark-mass effects in the NNLOPS POWHEG+MiNLO Higgs generator". In: *JHEP* 05 (2015), p. 140. arXiv: 1501.04637 [hep-ph].

[105] Jon Butterworth et al. "PDF4LHC recommendations for LHC Run II". In: *J. Phys. G* 43 (2016), p. 023001. arXiv: 1510.03865 [hep-ph].

[106] U. Aglietti et al. "Two loop light fermion contribution to Higgs production and decays". In: *Phys. Lett.* B595 (2004), pp. 432–441. arXiv: hep-ph/0404071 [hep-ph].

[107] Marco Bonetti, Kirill Melnikov, and Lorenzo Tancredi. "Higher order corrections to mixed QCD-EW contributions to Higgs boson production in gluon fusion". In: *Phys. Rev. D* 97.5 (2018). [Erratum: Phys. Rev.D97,no.9,099906(2018)], p. 056017. arXiv: 1801.10403 [hep-ph].

[108] Stefano Actis et al. "NNLO computational techniques: The cases $H \to \gamma\gamma$ and $H \to gg$". In: *Nucl. Phys. B* 811 (2009), pp. 182–273. arXiv: 0809.3667 [hep-ph].

[109] Stefano Actis et al. "NLO electroweak corrections to Higgs boson production at hadron colliders". In: *Phys. Lett. B* 670 (2008), pp. 12–17. arXiv: 0809.1301 [hep-ph].

[110] Alexey Pak, Mikhail Rogal, and Matthias Steinhauser. "Finite top quark mass effects in NNLO Higgs boson production at LHC". In: *JHEP* 02 (2010), p. 025. arXiv: 0911.4662 [hep-ph].

[111] Robert V. Harlander et al. "Higgs production in gluon fusion at next-to-next-to-leading order QCD for finite top mass". In: *Eur. Phys. J.* C66 (2010), pp. 359–372. arXiv: 0912.2104 [hep-ph].

[112] Robert V. Harlander and Kemal J. Ozeren. "Top mass effects in Higgs production at next-to-next-to-leading order QCD: Virtual corrections". In: *Phys. Lett. B* 679 (2009), pp. 467–472. arXiv: 0907.2997 [hep-ph].

[113] Robert V. Harlander and Kemal J. Ozeren. "Finite top mass effects for hadronic Higgs production at next-to-next-to-leading order". In: *JHEP* 11 (2009), p. 088. arXiv: 0909.3420 [hep-ph].

[114] Falko Dulat, Achilleas Lazopoulos, and Bernhard Mistlberger. "iHixs 2 – Inclusive Higgs cross sections". In: *Comput. Phys. Commun.* 233 (2018), pp. 243–260. arXiv: 1802.00827 [hep-ph].

[115] Charalampos Anastasiou et al. "Higgs Boson Gluon-Fusion Production in QCD at Three Loops". In: *Phys. Rev. Lett.* 114 (2015), p. 212001. arXiv: 1503.06056 [hep-ph].

[116] Charalampos Anastasiou et al. "High precision determination of the gluon fusion Higgs boson cross-section at the LHC". In: *JHEP* 05 (2016), p. 058. arXiv: 1602.00695 [hep-ph].

[117] Paolo Nason and Carlo Oleari. "NLO Higgs boson production via vector-boson fusion matched with shower in POWHEG". In: *JHEP* 02 (2010), p. 037. arXiv: 0911.5299 [hep-ph].

[118] M. Ciccolini, Ansgar Denner, and S. Dittmaier. "Strong and Electroweak Corrections to the Production of a Higgs Boson + 2 Jets via Weak Interactions at the Large Hadron Collider". In: *Phys. Rev. Lett.* 99 (2007), p. 161803. arXiv: 0707.0381 [hep-ph].

[119] Mariano Ciccolini, Ansgar Denner, and Stefan Dittmaier. "Electroweak and QCD corrections to Higgs production via vector-boson fusion at the CERN LHC". In: *Phys. Rev. D* 77 (2008), p. 013002. arXiv: 0710.4749 [hep-ph].

[120] Oliver Brein, Robert V. Harlander, and Tom J. E. Zirke. "vh@nnlo – Higgs Strahlung at hadron colliders". In: *Comput. Phys. Commun.* 184 (2013), pp. 998–1003. arXiv: 1210.5347 [hep-ph].

[121] Robert V. Harlander et al. "vh@nnlo-v2: new physics in Higgs Strahlung". In: *JHEP* 05 (2018), p. 089. arXiv: 1802.04817 [hep-ph].

[122] Oliver Brein, Abdelhak Djouadi, and Robert Harlander. "NNLO QCD corrections to the Higgs-strahlung processes at hadron colliders". In: *Phys. Lett. B* 579 (2004), pp. 149–156. arXiv: hep-ph/0307206.

[123] Oliver Brein et al. "Top-quark mediated effects in hadronic Higgs-Strahlung". In: *Eur. Phys. J. C* 72 (2012), p. 1868. arXiv: 1111.0761 [hep-ph].

[124] Ansgar Denner et al. "Electroweak corrections to Higgs-strahlung off W/Z bosons at the Tevatron and the LHC with HAWK". In: *JHEP* 03 (2012), p. 075. arXiv: 1112.5142 [hep-ph].

[125] Ansgar Denner et al. "HAWK 2.0: A Monte Carlo program for Higgs production in vector-boson fusion and Higgs strahlung at hadron colliders". In: *Comput. Phys. Commun.* 195 (2015), pp. 161–171. arXiv: 1412.5390 [hep-ph].

[126] M. L. Ciccolini, S. Dittmaier, and M. Krämer. "Electroweak radiative corrections to associated WH and ZH production at hadron colliders". In: *Phys. Rev. D* 68 (2003), p. 073003. arXiv: hep-ph/0306234 [hep-ph].

[127] Lukas Altenkamp et al. "Gluon-induced Higgs-strahlung at next-to-leading order QCD". In: *JHEP* 02 (2013), p. 078. arXiv: 1211.5015 [hep-ph].

[128] Robert V. Harlander et al. "Soft gluon resummation for gluon-induced Higgs Strahlung". In: *JHEP* 11 (2014), p. 082. arXiv: 1410.0217 [hep-ph].

[129] Heribertus B. Hartanto et al. "Higgs boson production in association with top quarks in the POWHEG BOX". In: *Phys. Rev. D* 91.9 (2015), p. 094003. arXiv: 1501.04498 [hep-ph].

[130] W. Beenakker et al. "NLO QCD corrections to $t\bar{t}H$ production in hadron collisions". In: *Nucl. Phys. B* 653 (2003), pp. 151–203. arXiv: hep-ph/0211352.

[131] S. Dawson et al. "Associated Higgs production with top quarks at the large hadron collider: NLO QCD corrections". In: *Phys. Rev. D* 68 (2003), p. 034022. arXiv: hep-ph/0305087.

[132] Yu Zhang et al. "QCD NLO and EW NLO corrections to $t\bar{t}H$ production with top quark decays at hadron collider". In: *Phys. Lett. B* 738 (2014), pp. 1–5. arXiv: 1407.1110 [hep-ph].

[133] S. Frixione et al. "Electroweak and QCD corrections to top-pair hadroproduction in association with heavy bosons". In: *JHEP* 06 (2015), p. 184. eprint: 1504.03446.

[134] M. Wiesemann et al. "Higgs production in association with bottom quarks". In: *JHEP* 02 (2015), p. 132. arXiv: 1409.5301 [hep-ph].

[135] S. Dawson et al. "Exclusive Higgs boson production with bottom quarks at hadron colliders". In: *Phys. Rev. D* 69 (2004), p. 074027. arXiv: hep-ph/0311067.

[136] Stefan Dittmaier, Michael Krämer, and Michael Spira. "Higgs radiation off bottom quarks at the Tevatron and the CERN LHC". In: *Phys. Rev. D* 70 (2004), p. 074010. arXiv: hep-ph/0309204.

[137] Robert Harlander, Michael Krämer, and Markus Schumacher. "Bottom-quark associated Higgs-boson production: Reconciling the four- and five-flavour scheme approach". In: (2011). arXiv: 1112.3478 [hep-ph].

[138] Federico Demartin et al. "Higgs production in association with a single top quark at the LHC". In: *Eur. Phys. J. C* 75 (2015), p. 267. arXiv: 1504.00611 [hep-ph].

[139] Federico Demartin et al. "tWH associated production at the LHC". In: *Eur. Phys. J. C* 77.1 (2017), p. 34. arXiv: 1607.05862 [hep-ph].

[140] T. Gleisberg et al. "Event generation with SHERPA 1.1". In: *JHEP* 02 (2009), p. 007. arXiv: 0811.4622 [hep-ph].

[141] Tanju Gleisberg and Stefan Höche. "Comix, a new matrix element generator". In: *JHEP* 12 (2008), p. 039. arXiv: 0808.3674 [hep-ph].

[142] Fabio Cascioli, Philipp Maierhofer, and Stefano Pozzorini. "Scattering Amplitudes with Open Loops". In: *Phys. Rev. Lett.* 108 (2012), p. 111601. arXiv: 1111.5206 [hep-ph].

[143] Morad Aaboud et al. "Electron reconstruction and identification in the ATLAS experiment using the 2015 and 2016 LHC proton-proton collision data at $\sqrt{s} =$ 13 TeV". In: *Eur. Phys. J. C* 79.8 (2019), p. 639. arXiv: 1902.04655 [physics.ins-det].

[144] *Improved electron reconstruction in ATLAS using the Gaussian Sum Filter-based model for bremsstrahlung*. Tech. rep. All figures including auxiliary figures are available at https://atlas.web.cern.ch/Atlas/GROUPS/PHYSICS/CONFNOTES/ATLAS-CONF-2012-047. Geneva: CERN, 2012. URL: https://cds.cern.ch/record/1449796.

[145] *Electron and photon reconstruction and performance in ATLAS using a dynamical, topological cell clustering-based approach*. Tech. rep. All figures including auxiliary figures are available at https://atlas.web.cern.ch/Atlas/GROUPS/PHYSICS/PUBNOTES/ATL-PHYS-PUB-2017-022. Geneva: CERN, 2017. URL: https://cds.cern.ch/record/2298955.

[146] M. Aaboud et. al. "Electron and photon energy calibration with the ATLAS detector using 20152016 LHC proton-proton collision data". In: *Journal of Instrumentation* 14.03 (2019), P03017–P03017. URL: https://doi.org/10.1088%2F1748-0221%2F14%2F03%2Fp03017.

[147] Georges Aad et al. "Higgs boson production cross-section measurements and their EFT interpretation in the 4ℓ decay channel at $\sqrt{s}$ =13 TeV with the ATLAS detector". In: *Eur. Phys. J. C* 80.10 (2020). [Erratum: Eur.Phys.J.C 81, 29 (2021), Erratum: Eur.Phys.J.C 81, 398 (2021)], p. 957. arXiv: 2004.03447 [hep-ex].

[148] Lukas Adamek et al. *Measurement of the Higgs boson mass in the $H \to ZZ(*) \to 4\ell$ channel at $\sqrt{s}$=13 TeV with the 139 fb^{-1} with the ATLAS detector*. Tech. rep. Geneva: CERN, 2020. URL: https://cds.cern.ch/record/2697141.

[149] Syed Haider Abidi et al. *Event selection and background estimation in the HZZ4l channel at $\sqrt{s}$=13TeV - Final Run 2 Analysis*. Tech. rep. Geneva: CERN, 2018. URL: https://cds.cern.ch/record/2651267.

[150] ATLAS Collaboration. *Measurement of the Higgs boson mass in the $H \to ZZ^* \to 4\ell$ decay channel using 139 fb^{-1} of $\sqrt{s} = 13$ TeV pp collisions recorded by the ATLAS detector at the LHC*. 2022. arXiv: 2207.00320 [hep-ex].

[151] Dan Guest, Kyle Cranmer, and Daniel Whiteson. "Deep Learning and Its Application to LHC Physics". In: *Annual Review of Nuclear and Particle Science* 68.1 (2018), pp. 161–181. eprint: https://doi.org/10.1146/annurev-nucl-101917-021019. URL: https://doi.org/10.1146/annurev-nucl-101917-021019.

[152] Martin Abadi et al. *TensorFlow: Large-Scale Machine Learning on Heterogeneous Systems*. Software available from tensorflow.org. 2015. URL: https://www.tensorflow.org/.

[153] François Chollet et al. *Keras*. https://keras.io. 2015.

[154] The ATLAS Collaboration. "Event selection and background estimation in the $H \to ZZ* \to 4l$ decay channel with $\sqrt{s} = 13$ TeV". In: (2019). URL: https://cds.cern.ch/record/2651267/files/ATL-COM-PHYS-2018-1710.pdf.

[155] Kyle S. Cranmer. "Kernel estimation in high-energy physics". In: *Comput. Phys. Commun.* 136 (2001), pp. 198–207. arXiv: hep-ex/0011057.

[156] A. Bredenstein et al. "Precision calculations for the Higgs decays H $\to$ ZZ/WW $\to$ 4 leptons". In: *Nuclear Physics B - Proceedings Supplements* 160 (Oct. 2006), pp. 131–135. URL: https://doi.org/10.1016%2Fj.nuclphysbps.2006.09.104.

[157] Stefano Boselli et al. *Higgs boson decay into four leptons at NLOPS electroweak accuracy*. 2015. arXiv: 1503.07394 [hep-ph].

[158] Stefano Boselli et al. "Higgs decay into four charged leptons in the presence of dimension-six operators". In: *Journal of High Energy Physics* 2018.1 (Jan. 2018). URL: https://doi.org/10.1007%2Fjhep01%282018%29096.

[159] *Measurement of the Higgs boson mass and width using the four leptons final state*. Tech. rep. Geneva: CERN, 2023. URL: https://cds.cern.ch/record/2871702.

[160] *Letter of Intent for the Phase-I Upgrade of the ATLAS Experiment*. Tech. rep. Geneva: CERN, 2011. URL: https://cds.cern.ch/record/1402470.

[161] Marco Trovato. *FELIX: The New Readout System for the ATLAS Detector*. Tech. rep. Geneva: CERN, 2019. URL: https://cds.cern.ch/record/2704279.

[162] T Kawamoto et al. *New Small Wheel Technical Design Report*. Tech. rep. ATLAS New Small Wheel Technical Design Report. 2013. URL: https://cds.cern.ch/record/1552862.

[163] Sinem Simsek. *The ATLAS RPC upgrade project for the High Luminosity LHC program*. Tech. rep. Geneva: CERN, 2022. URL: https://cds.cern.ch/record/2805182.

[164] *ATLAS Liquid Argon Calorimeter Phase-II Upgrade: Technical Design Report*. Tech. rep. Geneva: CERN, 2017. URL: https://cds.cern.ch/record/2285582.

[165] Ralf Spiwoks et al. *Continuous Integration for the Software and the Firmware of the new ATLAS Muon-Central-Trigger-Processor Interface (MUCTPI)*. Tech. rep. Geneva: CERN, 2022. URL: https://cds.cern.ch/record/2823852.

[166] Paula Agnieszka Erland. *Overview of ATLAS Forward Proton Detectors for LHC Run 3 and Plans for the HL-LHC*. Tech. rep. Geneva: CERN, 2022. URL: https://cds.cern.ch/record/2838869.

[167] ATLAS Collaboration. *Measurement of the $H \to \gamma\gamma$ and $H \to ZZ^* \to 4\ell$ cross-sections in pp collisions at $\sqrt{s} = 13.6$ TeV with the ATLAS detector*. 2023. arXiv: 2306.11379 [hep-ex].

[168] D. de Florian et al. "Handbook of LHC Higgs Cross Sections: 4. Deciphering the Nature of the Higgs Sector". In: 2/2017 (Oct. 2016). arXiv: 1610.07922 [hep-ph].

[169] Georges Aad et al. "Measurements of the Total and Differential Higgs Boson Production Cross Sections Combining the H→$\gamma\gamma$ and H→ZZ*→4ℓ Decay Channels at $\sqrt{s}$=8 TeV with the ATLAS Detector". In: *Phys. Rev. Lett.* 115.9 (2015), p. 091801. arXiv: 1504.05833 [hep-ex].

[170] Georges Aad et al. "Measurement of the total and differential Higgs boson production cross-sections at $\sqrt{s} = 13$ TeV with the ATLAS detector by combining the H → ZZ*→ 4ℓ and H → $\gamma\gamma$ decay channels". In: *JHEP* 05 (2023), p. 028. arXiv: 2207.08615 [hep-ex].

[171] Georges Aad et al. "Measurement of the Higgs boson mass in the $H \to ZZ^* \to 4\ell$ decay channel using 139 fb^{-1} of $\sqrt{s} = 13$ TeV pp collisions recorded by the ATLAS detector at the LHC". In: *Phys. Lett. B* 843 (2023), p. 137880. arXiv: 2207.00320 [hep-ex].

[172] Halina Abramowicz et al. "The International Linear Collider Technical Design Report - Volume 4: Detectors". In: (June 2013). Ed. by Ties Behnke et al. arXiv: 1306.6329 [physics.ins-det].

[173] Michael Benedikt et al. *FCC-ee: The Lepton Collider: Future Circular Collider Conceptual Design Report Volume 2. Future Circular Collider*. Tech. rep. 2. Geneva: CERN, 2019. URL: https://cds.cern.ch/record/2651299.

[174] The CEPC Study Group. *CEPC Conceptual Design Report: Volume 1 - Accelerator*. 2018. arXiv: 1809.00285 [physics.acc-ph].

[175] Alain Blondel and Patrick Janot. "FCC-ee overview: new opportunities create new challenges". In: *Eur. Phys. J. Plus* 137.1 (2022), p. 92. arXiv: 2106.13885 [hep-ex].

[176] Paolo Azzurri et al. "A special Higgs challenge: measuring the mass and production cross section with ultimate precision at FCC-ee". In: *Eur. Phys. J. Plus* 137.1 (2022), p. 23. arXiv: 2106.15438 [hep-ex].